# Activity and selectivity loss modelling on Co based Fischer-Tropsch catalysts

Stefan Kocic

N°d'ordre NNT : xxx

**THESE de DOCTORAT DE L'UNIVERSITE DE LYON**
opérée au sein de
**l'Université Claude Bernard Lyon 1**

**Ecole Doctorale** N° 206
**Ecole Doctorale de Chimie de Lyon**

**Spécialité de doctorat** :
**Discipline** : Chimie

Soutenue publiquement le 06/11/2019, par :
**Stefan KOCIĆ**

---

# La perte d'activité et de sélectivité des catalyseurs Fischer-Tropsch à base de Cobalt

---

Devant le jury composé de :

| | | |
|---|---|---|
| Loubière, Karine | Directrice de Recherche CNRS, LGC Toulouse | Rapporteure |
| Saeys, Mark | Professeur, Ghent University | Rapporteur |
| Costa, Dominique | Directrice de Recherche CNRS ENSCP Paris | Examinatrice |
| Tronconi, Enrico | Professeur, Politecnico di Milano | Co-directeur de thèse |
| Fongarland, Pascal | Professeur Université Lyon 1, LGPC | Examinateur |
| Schweitzer, Jean-Marc | Ingénieur de Recherche IFPEN, Solaize | Directeur de thèse |
| Corral Valero, Manuel | Ingénieur de Recherche IFPEN, Solaize | Invité |

[NOM DE LA SOCIETE]

# Activity and selectivity loss modeling on Co-based Fischer-Tropsch catalysts

**Microsoft Office User**

**17/06/2019**

## Résumé

La perte d'activité et de sélectivité en fonction du temps sous charge du catalyseur de Fischer-Tropsch (FT) à base de cobalt constituent les principales limitations pour l'industrialisation de ce procédé. La bibliographie montre qu'il n'y a pas de consensus. Différentes causes sont proposées pour expliquer la désactivation du catalyseur et plusieures voies vers ces phénomènes inévitables ont été discutées. Parmi celles-ci, les hypothèses les plus répandues sont l'oxydation et la carburation de la phase active. De plus, la baisse d'activité des catalyseurs en fonction du temps ne presente pas un comportement uniforme, indiquant que ce phénomène est probablement dû à plusieurs voies concurentielles.

Dans le cadre de cette thèse, on s'intéresse aux voies relatives à la phase active, plus particulièrement au dépôt des espèces hydrocarbonées, à la reconstruction de surface induite par celles-ci, ainsi qu'à l'oxydation de la phase active en fonction des effets de recouverement en H, O et C. En utilisant les calculs DFT périodiques, nous déterminons l'energie libre de Gibbs pour un large panel de réactions clés qui forment les éspèces de surface $C_\alpha H_\beta O_\gamma$ dans les conditions de FT. Nous identifions les intermédiaires et les états de transitions qui conduisent à la perte d'activité et de séléctivité du catalyseur. De ce fait, nous proposons dans ce travail d'étudier l'évolution de la structure de la surface en fonction des potentiels chimiques du C, de H et de O dans les conditions opératoires du procédé FT. La prise en compte de l'H et l'O en tant qu'espèces de surface a été intégrée à nos calculs et a permis de modéliser la structure des précurseurs du coke identifiés experimentalement ainsi que d'identifier les conditions opératoires favorables à leur formation.

En fonction du recouverement (C,H,O), nous identifions trois domaines structurels contenant les espèces de surface liées aux tendances d'évolution de l'activité et de la séléctivité discutées dans la bibliographie: tout d'abord, dans un domaine de faible

recouvrement en C, où les monomères $CH_\beta$ sont formés, l'impact des atomes d'O est le plus important et mène aux CO, OH et $H_2O$ adsorbés, ainsi qu'à l'oxydation des sites actifs Co. Un deuxième domaine de recouvement moyen en C, où des hydrocarbures linéaires et ramifiés sont formés, et où la reconstruction de Co peut avoir lieu lors de la migration du C vers la sous-surface. Enfin un domaine de recouverement élevé en C a été identifié, où de plus longues chaines d'hydrocarbures ramifiées sont formées. Dans ce domaine, c'est la formation d'une sur-couche de C (similaire à du coke graphitique) qui devrait être la raison principale de la désactivation. Concernant le recouverement intermédiaire et élevé en C, l'impact des atomes d'oxygène sur la surface est plus faible, et son dépôt se produit sur C sans contact direct avec les sites actifs du cobalt.

En s'appuyant sur les calculs DFT périodiques et la modélisation micro-cinétique, nous proposons de nouvelles visions et idées relatives aux mécanismes de désactivation dus au C. Notre travail montre que les espèces de surface CCH peuvent être considérées comme les précurseurs de désactivation les plus plausibles d'un point de vue thermodynamique et cinétique. Par ailleurs, nous proposons la cycloaddition 2+2+2 et quelques réactions de couplage $CH_\beta/CH_\beta$ comme mécanismes parasites pour la formation du coke, conduisant à la désactivation progressive par blocage des sites actifs. Le mécanisme de désactivation proposé a été integré dans un modèle micro-cinétique initialement dépourvu de la prise en compte de ces phénomènes. Le modèle complet comprenant deux sites actifs a été optimisé et comparé à des observations expérimentales.

Ainsi, cette étude apporte un point de vue nouveau sur des questions complexes et débattues au sein de la communauté FT. Une cinétique de désactivation est proposée, et permet de donner des pistes de développement de nouveaux catalyseurs industriels.

**Mots clés:** Fischer-Tropsch, désactivation, précurseurs de coke, eau, recontruction, oxydation, DFT, modélisation micro-cinétique, modélisation multiéchelle, Cobalt.

## Abstract

Loss of catalyst activity and selectivity with time-on-stream are one of the greatest limitations for the Fischer-Tropsch (FT) industrial process. There is a lack of consensus about the reasons leading to catalyst deactivation and many different paths towards those inevitable events have been evoked in the literature. Among them, some of the most common hypotheses are oxidation and carburation of active sites. Besides, the diminution of Co catalyst activity during time-on-stream exhibits non-uniform behavior, indicating that this phenomenon might be a result of multiple distinctive events.

In this thesis, we concentrate on those paths that concern the active phase only, particularly hydrocarbon-species deposition, active phase oxidation and hydrocarbon-induced surface reconstruction as a function of hydrogen, oxygen and carbon coverage effects. With the aid of periodic Density Functional Theory (DFT) calculations, we determine the Gibbs free energy for a large set of key reactions leading to the formation of $C_\alpha H_\beta O_\gamma$ surface species on the Co(111) surface uner FT reaction conditions and we identify intermediates and transition states that may lead to activity and selectivity loss of Co-based catalysts. Hence, we propose here to study how the structure of the cobalt surface evolves as a function of the carbon, hydrogen and oxygen chemical potentials under FT reaction conditions. These calculations allowed us to propose an atomistic structure of some experimentally identified coke precursors and to identify favorable reaction conditions towards their formation.

Depending on the (C, H, O) coverages, we identify three structural domains containing surface species related with activity and selectivity trends discussed in the literature so far: firstly, a low C coverage domain, where $CH_\beta$ monomers are formed, the impact of O atoms is the strongest and leads to adsorbed CO, OH or water as well as to oxidized Co sites; an intermediate C coverage domain, where $C_\alpha H_\beta$ linear oligomers and branched hydrocarbon

chains are formed and where reconstruction of Co may take place upon subsurface C migration; and thirdly, a high C coverage domain, where we find the formation of longer branched hydrocarbon chains together with the genesis of a carbon overlayer (graphitic coke-like) that is expected to be the main source of deactivation. For intermediate and high carbon coverages, the impact of O atoms on the surface is weaker and its deposition occurs on top of the carbon overlayer without direct contact with Co sites.

With the aid of periodic DFT transition state calculations and microkinetic modeling, we offer some new understandings and ideas related to the mechanism of a carbon induced deactivation phenomenon. Our study shows that surface ethynyl species CCH may be regarded as thermodynamically and kinetically the most plausible deactivation initiators. Moreover, we propose 2+2+2 cycloaddition and some $CH_\beta$ / $CH_\beta$ reactions as a mechanism for detrimental coke formation leading to a progressive deactivation by a site-blocking effect. This deactivation mechanism has been integrated to an existing deactivation-free micro-kinetic scheme from the literature. The resulting, two-site deactivation model has been optimized and compared to some experimental observations.

Our multiscale (DFT and microkinetic model) reproduces well known experimental trends. Hence, we expect that our work will provide the FT community some valuable insights into this intricate and elusive problem, the kinetics of deactivation, as well as some rational guidelines about how to optimize the catalyst process.

**Keywords:** Fischer-Tropsch, deactivation, coke precursors, water, reconstruction, oxidation, density functional theory, micro-kinetic modeling, multiscale modeling, Cobalt.

## Introduction

Diversification of energy sources is a great challenge of modern society that confronts depletion of the natural reserves and growing demand for low-cost energy and fuels while maintaining efficient production and minimal impact on the environment. Excessive use of the limited amount of crude oil as a raw material due to its high-energy content began almost a century ago and continues nowadays. However, in the decades to come, non-renewable natural resources such as coal, petroleum (crude oil) and natural gas will be gradually substituted with alternative, clean and renewable energy sources such as solar, wind, wave, biomass and geothermal derived energies. Thus, to satisfy the needs of modern society in terms of its energy demands, the progressive change from crude oil, whose reserves become less accessible, towards advanced renewable energy sources is inevitable. Although all those clean and low carbon technologies have been known for a long time, their regular use remains limited due to either inefficiency or cost. Hence, an abrupt transition to those advanced technologies is practically impossible, and a transition time involving the use of more abundant non-renewable sources such as natural gas and coal is expected.

Depletion of fossil fuels, geopolitical events and the impact on the environment have activated worldwide energy consumers and producers towards a diversification of their "energy mix" and in particular towards the development of synthetic fuels. This renewed the interest in Fischer-Tropsch (FT) technology. Although the FT process has been known for almost a century, it remains challenging in many ways. In particular, applied research in this area tries to unravel some technical and fundamental issues that render the FT process uneconomical compared to conventional non-renewable energy resources. Some of these are within the scope of this Ph.D. thesis, as it will be shown below. The Fischer-Tropsch synthesis (FTS) reaction is a metal-catalyzed polymerization reaction in which adsorbed molecules of syngas mixture, carbon monoxide, and hydrogen, are transformed into a mixture

of hydrocarbons, water and oxygenates through adsorption, chain initiation, propagation and termination steps. The overall reaction mechanism of this chemical transformation is still not fully understood, and there is an intense debate in the literature. Nevertheless, n-paraffins and α-olefins are considered the major products of the Fischer-Tropsch transformation, although measurable quantities of branched hydrocarbons and oxygenated species such as aldehydes and fatty acids can be found. Apart from industrially valuable products (n-paraffins and α-olefins), FTS can also give unwanted products such as methane and coke by some reaction pathways. The effects of some of those reactions are still not understood, although there is an agreement that most of them are involved with catalyst activity and selectivity loss. It is therefore essential to understand those reaction pathways in order to optimize the catalyst lifetime and to ensure both financial and environmental viability to the Fischer-Tropsch process. Moreover, the fact that many side reactions and accordingly reaction products are involved is the reason why Fischer-Tropsch kinetics is an extremely complex and debated subject.

Among FT active metals, Co and Fe are common on a commercial scale due to their high stability and FTS activity, [1,2] and low methane selectivity [3]. The former metal is used in the Low-temperature High Pressure (LTHP) FT and the latter in the High-Temperature Low pressure (HTLP) FT processes.[4] The metal phase is usually deposed on the support by impregnation techniques and activated with hydrogen. Different types of supports and promoters are used due to economic reasons and improved physicochemical properties.

Nevertheless, all catalysts deactivate over time [5]. During the deactivation phenomenon, the activity and selectivity of catalysts are reduced. Hence, catalysts stability is one of the main issues in the industrialization of this process. Thus, there is a necessity to establish how operating conditions affect the deactivation and understand how it can be minimized.

In this thesis, we aim at describing the deactivation phenomenon at the atomistic scale using a multi-scale approach combining kinetic modeling with computational chemistry calculations. In **Chapter** 1 we describe some general aspects of the FTS reaction and in **Chapter** 2 we present up to date literature data on several aspects of the FTS reaction: thermochemistry, kinetics, impact of operating conditions and deactivation causes reported in the literature. In this chapter, we also present the reaction mechanisms of the FTS reaction proposed in the literature and we focus on the one developed by Tronconi and co-workers used throughout this thesis. In **Chapter 3** we present the methods used in this work. The results of our theoretical calculations are presented in **Chapter 4**. These results are used to provide insights into the elementary steps of deactivation and propose different deactivation pathways that could be implemented in a micro-kinetic model. These different deactivation pathways are assessed in **Chapter 5** and some of them implemented in an existing microkinetic model in **Chapter 6**. Moreover, in **Chapter 6** the modified micro-kinetic model is fitted to available experimental data and used to provide some insights on the most common experimental observations concerning the catalyst deactivation. In this chapter, micro-kinetic model predictions are confronted with some experimental findings described in **Chapter 2**. Finally, also in **Chapter 6,** we try to identify the operating conditions leading to minimal deactivation and long-lasting Co-based Fischer-Tropsch catalysts.

# 1 General Aspects of the Fischer-Tropsch Synthesis reaction

## 1.1 Some Historical facts

This chapter represents a very brief presentation of some historical facts based on the non-exhaustive list of references[6–10,1].

The origins of what is today called Fischer-Tropsch technology dates back to about a century ago. It begun with Sabatier and Senderens discovery of the methane formation reaction from carbon monoxide and hydrogen over different metal catalysts. Although still controversial, the first qualitative official report, in the form of a patent on liquid hydrocarbon formation at 120 atm and 300-400ºC over cobalt oxide, was given by Badische Anilin-und Soda-Fabrik (BASF) in 1913. Ten years afterward, with an intent to verify BASFs claims, Franz Fischer and Hans Tropsch reported the production of a mixture of oxygen-containing compounds called Synthol starting from synthesis gas over alkalized iron at severe conditions: 100-150 atm and 400-450 ºC. Fischer and Tropsch failed to obtain hydrocarbons in this test. Later, in 1925, additional studies of Fischer and Tropsch over the cobalt-iron catalyst at 250-300 ºC and 1 atm had shown the production of hydrocarbon liquids and gasses but also of solid paraffin molecules at conditions milder than previous experiments. Thus, 1925, represents **the official birth of Fischer-Tropsch technology**.

To expand the fruitful knowledge obtained from discoveries reported in those publications, the first small-scale pilot plant in Mulheim was constructed in 1932. In 1934, after Ruhrchemie acquired the patent rights, a large-scale pilot plant was built in Oberhausen-Holten and operated under the same conditions as a plant in Mulheim with a capacity of 7,240 bbl/year. The nickel catalyst used in this plant was soon replaced with a more active and expensive cobalt catalyst due to overheating, catalyst lifetime, and regeneration issues with nickel catalysts. After the plant success in 1935 in Oberhausen-Holten with cobalt-based Fischer Tropsch catalyst, nine commercial power plants were constructed by the end of the

second world war (WWII) that used the same metal at either atmospheric or medium 5-15 atm pressure and 180-200 ºC. Synthetic fuel and products obtained in those nine plants were valuable assets during WWII as they represented one-fifth of overall gasoline produced. After the end of WWII, industrial plants were shut down. Hence, the period between the end of WWII and the official discovery of the Fischer-Tropsch synthesis reactions marked **the commercial development of the FTS process**.

Due to the expected shortage of global supply in oil at that time, America and Britain showed a deep interest in the German, pre-war, Fischer-Tropsch technology. They sent scientific teams to Germany with a mission to gather the knowledge that Germany had collected and to consult engineers and scientists from that time. That research led to the construction of the GTL-FT plant in Brownsville, Texas, 1951, with a capacity of 7.000 bbl/day, which was shut down later in 1957 due to a sharp natural gas price increase and to the availability of cheaper petroleum from the Middle East. In 1955, the world first coal-to-liquids (CTL) complex (Sasol 1) at Sasolburg, South Africa, started producing synthetic fuels and chemicals, benefiting from large deposits of low-valued coal in that country. In response to several international oil crisis that took place in the 1970s and consequently, the economic benefit of the FTS process, Sasol expanded its fuel production by constructing another two CTL complexes (Sasol 2 and Sasol 3) at Secunda, South Africa, with an overall capacity of about 120 000 bbl/day.

Though still an interesting process, soon after the period of oil crisis had passed, between the 1980s and 1990s, the amount of research devoted to Fischer-Tropsch technology diminished due to a lack of political and industrial financial support. This fact is the reason why the period between 1975 and 1990 is the so-called period of the **rediscovery of Fischer-Tropsch technology**. During this time, much of the work done was a reassessment of earlier work, although significant progress was made in relating catalyst physicochemical properties

with activity and selectivity. At that time, several major oil companies: Gulf oil, Exxon, Shell, and Statoil were the leaders in developing high activity, noble-metal-promoted $Co/Al_2O_3$ catalysts. Those industrial processes and other research done at that time constitute the foundations of the advanced Fischer-Tropsch catalyst reactors and processes in use nowadays.

The so-called fifth period of Fischer-Tropsch technology begins with the commissioning of the world's first commercial plants that used natural gas as a raw material for syngas production (Bintulu, Malesia in 1993 by Shell and Mossel Bay City in 1992 by Mossgas presently PetroSA), both based on Sasol technology. **This is a landmark for the initiation and development of the FT GTL commercial era**. In 2006, Sasol's and Qatar's Petroleum (QP) Oryx-GTL plant started operating, with a daily capacity of approximately 34000 bbl. The largest GTL plant in the world is a production sharing agreement signed between Qatar Petroleum (QP) and Shell. This agreement gave birth to the Pearl GTL plant in Ras Laffan Industrial City, Qatar, in 2011 with a daily capacity of 140 000 bbl.

## 1.2 Overview of FT process technology

Synthesis gas used in FTS reaction is a mixture of $H_2$ and CO, and its production can be achieved in different manners depending on the choice of the initial carbonaceous feedstock. Development of technologies that transform coal, natural gas, organic matter (biomass) or even wastes (such as wood residues and plastics) to synthesis gas, established **C**oal-to-Liquid (**C**TL), **G**as-to-Liquid (**G**TL), **B**iomass-to-Liquid (**B**TL) and **W**aste-to-liquids (**W**TL) processes, respectively.

In processes that use solid feedstock such as CTL, BTL and WTL, syngas production is principally achieved by a gasification process which consists in cracking thermally the initial feed [11–13]. In the gasifier reactor, whose properties are determined based on the size and the chemical composition of solid feedstock, the gasifying agent (steam, air, and oxygen) is introduced and exposed to high pressure and temperatures. In GTL that uses gas feedstock,

low-weights hydrocarbons can be converted to syngas by different routes [13–18] such as steam methane reforming SMR, auto-thermal reforming (preferred one) ATR, non-catalytic and catalytic partial oxidation POX and CPO, respectively, heat exchange and compact reforming HEP and CPR, respectivley[19]. The syngas obtained in all those processes is usually not suitable due to its composition, and thus, the purification (impurities elimination such as HCl, $H_2S$, nitrogen compounds, particulates …) and conditioning (regulating composition) of the syngas are necessary before FT reaction. It is important to stress that syngas obtained from coal and natural gas are considered as non-renewable feeds, but their higher abundance and availability (relatively to the crude oil) make them very attractive for softening the transition period between non-renewable and renewable energy sources. Thus, synthetic fuels have been identified as a promising alternative [20,21].

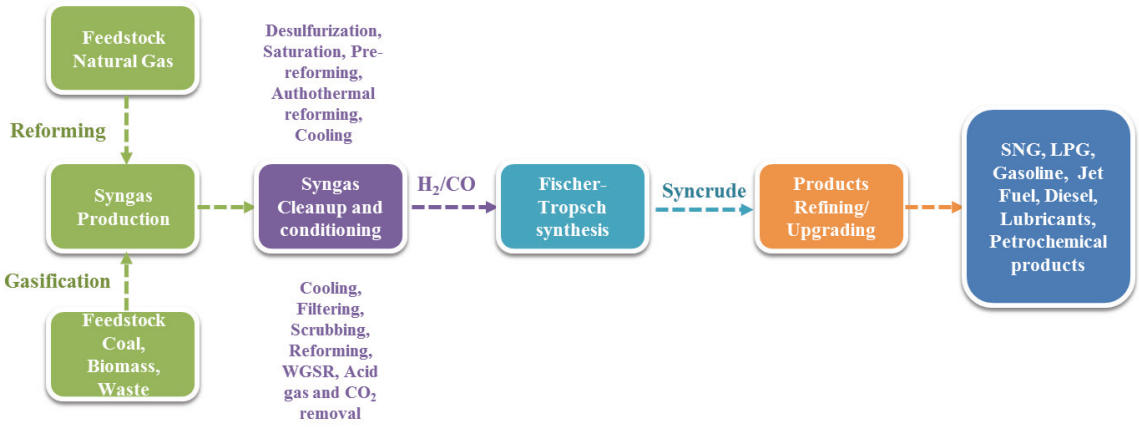


**Figure** 1. General scheme of XTL process and its principal components. Reproduced from [5,19]

There are two distinct operating modes related to the FT synthesis: the high-temperature FT (HTFT) mode employing Fe-based catalysts operating at <320° and the low-temperature FT (LTFT) employing mainly Co-based but also Fe-catalysts operating between 170 and 270 °C. Specific characteristics of the products obtained are depicted in **Table** 1 **.**

**Table** 1. Products overview in HTFT and LTFT. Reproduced from [5,19]

| Product Fraction | C range | Compound Class | Syncrude composition (mass%) | | |
|---|---|---|---|---|---|
| | | | **Fe-HTFT** | **Fe-LTFT** | **Co-LTFT** |
| Tail gas | $C_1$ | Alkane | 12.7 | 4.3 | 5.6 |
| | $C_2$ | Alkene | 5.6 | 1.0 | 0.1 |
| | | Alkane | 4.5 | 1.0 | 1.0 |
| LPG | $C_3$-$C_4$ | Alkene | 21.2 | 6.0 | 3.4 |
| | | Alkane | 3.0 | 1.8 | 1.8 |
| Napthha | $C_5$-$C_{10}$ | Alkene | 25.8 | 7.7 | 7.8 |
| | | Alkane | 4.3 | 3.3 | 12.0 |
| | | Aromatic | 1.7 | 0 | 0 |
| | | Oxygenate | 1.6 | 1.3 | 0.2 |
| Distilate | $C_{11}$-$C_{22}$ | Alkene | 4.8 | 5.7 | 1.1 |
| | | Alkane | 0.9 | 13.5 | 20.8 |
| | | Aromatic | 0.8 | 0 | 0 |
| | | Oxygenate | 0.5 | 0.3 | 0 |
| Residue/Wax | $>C_{22}$ | Alkene | 1.6 | 0.7 | 0 |
| | | Alkane | 0.4 | 49.2 | 44.6 |
| | | Aromatic | 0.7 | 0 | 0 |
| | | Oxygenate | 0.2 | 0 | 0 |
| Aqueous product | $C_1$-$C_5$ | Alcohol | 4.5 | 3.9 | 1.4 |
| | | Carbonyl | 3.9 | 0 | 0 |
| | | Carboxylic acid | 1.3 | 0.3 | 0.2 |

Several important factors need to be considered in the optimization of the FT synthesis such as reactor type, reaction phase, mass and heat transfers, hydrodynamics, catalyst strength, catalyst/product separation, per pass conversion and reactor configuration [5,22,23].

In the next paragraph, we describe some conventional reactor types used in the FT synthesis. Although the objective of this thesis is to model the active-phase only, notwithstanding, different reactor configuration may influence the deactivation phenomenon [24–26]. For instance, Chambrey et al. showed that a deactivation phenomenon is more pronounced in slurry-type than in the milli-fixed reactor. Therefore, it seems crucial to summarize briefly some current reactor technologies and in order to relate them with literature results.

### 1.2.1 FT reactor types

The primary concern in the design of commercial reactors is the highly exothermic nature of the FT reaction as we will discuss in **Chapter 2**. This fact requires an effective heat

removal from the reactor since high temperatures incite deactivation, which is a highly undesirable phenomenon that significantly affects operational costs. The characteristics of some FT reactor configurations are available in the literature [5,27–30,18]. A brief overview of those characteristics is presented in **Table** 2. Briefly, there are four broad categories of reactors in commercial use: Circulating Fluidized bed, Fluidized bed, Tubular Fixed bed, and Slurry phase reactor technologies. The choice of the reactor is usually determined based on the operating mode, the catalyst used, the envisaged products and building costs. Two major types of plant reactors are utilized in HTFT for the production of gasoline and higher-value chemicals. Those are fixed fluidized bed (FFB) and circulating fluidized beds (CFB) [4,23]. The FFB reactor scheme is usually preferred over CFB due to smaller construction costs, homogeneity of the reaction throughout the catalyst charge, and the lower catalyst consumption. In LTFT, diesel and waxes are produced in Multi-Tubular Fixed-Bed (MTFB) and slurry bubble column reactors [4]. In MTFB's, the syngas flows downstream inside the reactor filled with catalyst and with a cooling medium on the sides. In the slurry reactors, the reaction feed is bubbled upstream through a suspension of finely divided catalyst particles. The syngas then diffuses from the bubbles to the catalyst surface where the FT reaction occurs. The FT products are continuously separated from the catalyst using sieves. The main advantages of slurry over multitubular reactors are the low investment cost, low heat-transfer limitations, lower gas compression costs, lower catalyst consumption, higher conversion and longer reactor runs. However, the separation of the products from catalyst particles is one of the main problems of this reactor type. In LTFT synthesis, microchannel fixed-bed reactor types are currently being developed by some groups [31,32]

**Table** 2. Current reactor-technology properties used in HTFT and LTFT. Reproduced from[5].

| **Description** | **Fixed-bed** | | **Slurry** | **Fluidized-bed** | |
|---|---|---|---|---|---|
| | **Multitubular** | **Microchannel** | | **Fixed-fluidized** | **Circulating** |
| **Nature** | **PFR[a]** | **PFR[a]** | **CSTR[b]** | **CSTR[b]** | **CSTR[b]** |
| Reaction phase | g or g+l | g or g+l | g+l | G | g |
| Catalyst Particle size (mm) | >2 | <0.1 | <0.1 | <0.1 | <0.1 |
| Mass Transfer Limitation | High | Low | Medium | Medium-Low | Medium-Low |
| Heat Transfer Limitation | High | Low | Low | Medium-Low | Medium-Low |
| On-line catalyst replacement | No | No | Possible | Possible | Possible |
| Catalyst Mechanical Strength | Low | Low | Medium | High | High |
| Catalyst/Products Separation | Easy | Easy | Difficult | Fairly easy | Fairly easy |
| Feed poisoning | Local | Local | Global | Global | Global |
| Feed turn down limitation | None | None | Catalyst settling | Defluidization | Defluidization |

[a] Plug-Flow Reactor.

[b] Continuous Stirred Tank Reactor.

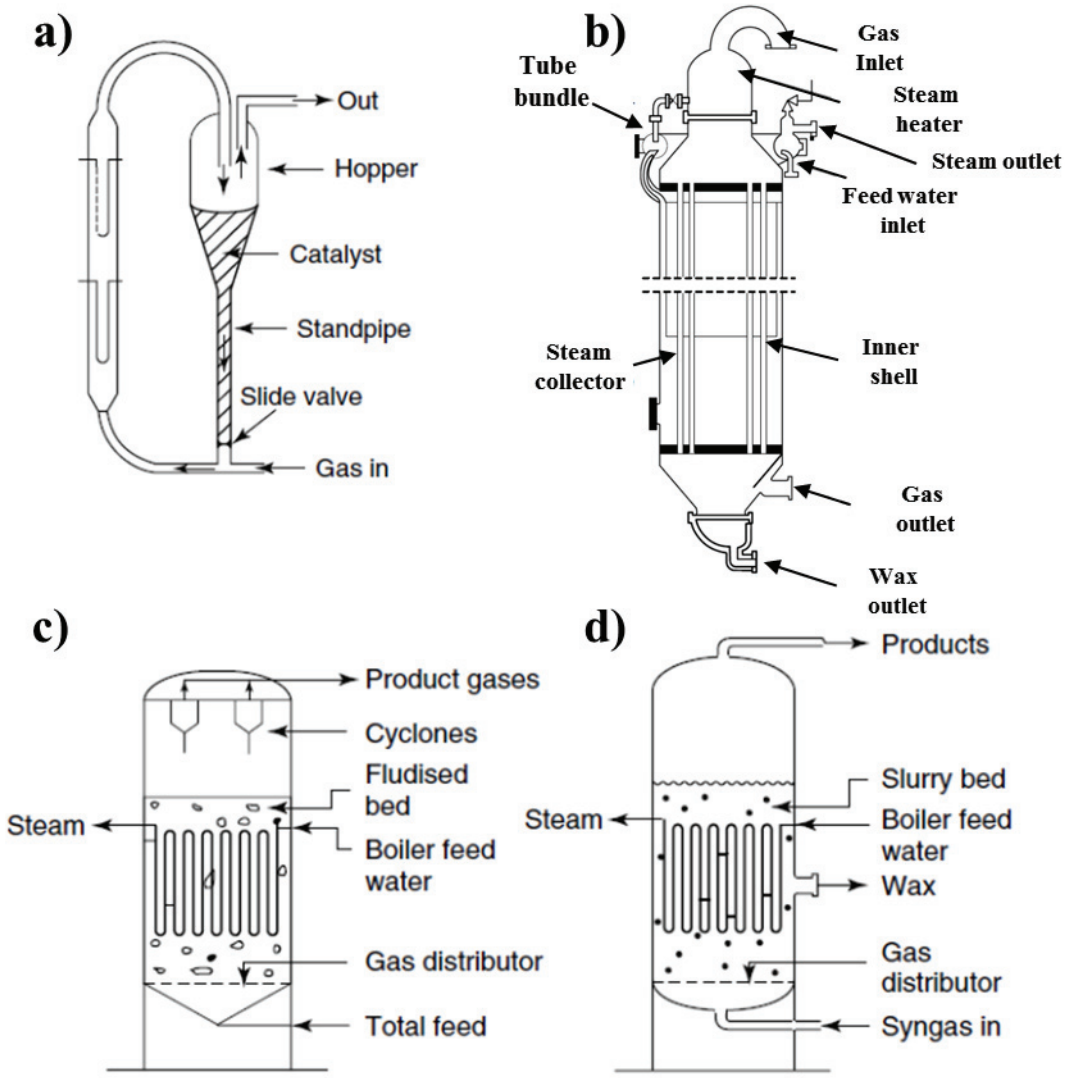


**Figure** 2. a) two-phase circulating fluidized beds (CFB) b) Multitubular fixed-bed reactor (MTFB) c) two-phase fixed fluidized bed (FFB) d) Three-phased slurry phase bubbling bed. Taken from [4]

Thus, each reactor configuration has its own technical and physical specificities, which, along with the catalyst employed, should be well studied and optimized towards maximizing the capacity of syngas conversion and products yield [17].

### 1.2.2 FT catalysts formulation and properties

The FT catalysts are mostly composed of small metallic particles, the active phase, dispersed throughout the support used to increase the number of active surface sites for the reaction to occur. In general, a metal oxide support[33] is used ($Al_2O_3$, $SiO_2$, $TiO_2$ …) to

increase active phase dispersion, stability, and improve the performance of the overall process. In addition to the support, some noble metals can be used to promote the catalyst while increasing catalytic performance. Detailed reviews of Co and Fe catalysts synthesis methods and the impact of promoters are given in references [23,18].

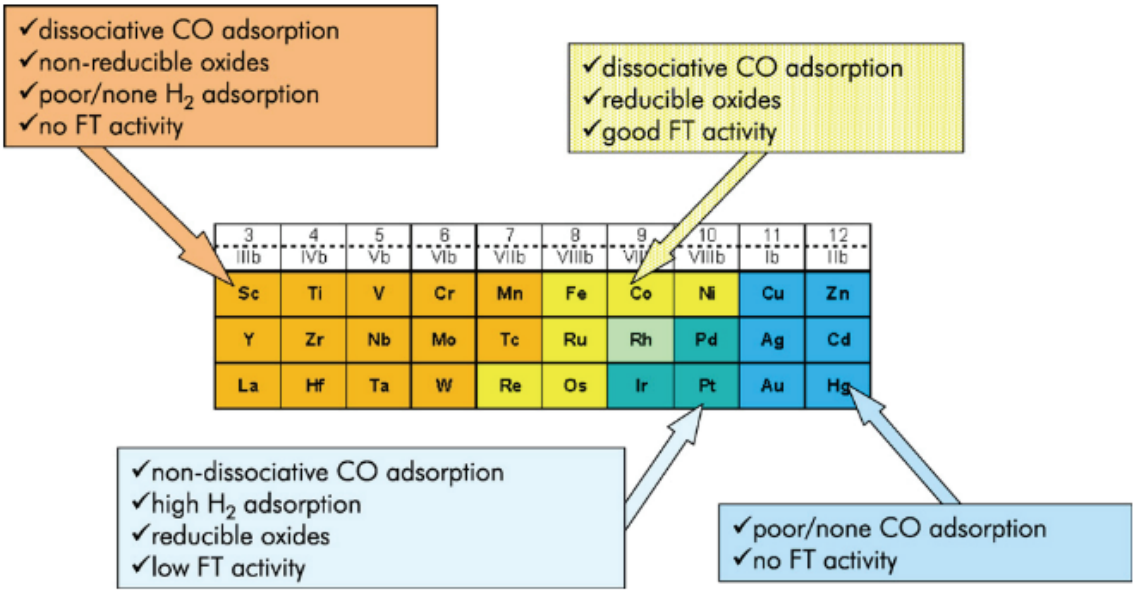


**Figure** 3. Physicochemical properties of different transition metals, according to Perego et al [33].

One of the characteristics of a suitable FT catalyst is the ability to adsorb and dissociate hydrogen and CO and, at the same time, easy reducibility of its oxide form. As a consequence, very few metals are FT active [33], and their properties can be discussed in terms of hydrogenation activity, Water-Gas Shift reaction activity (WGS; see below), sensitivity to promoters, stability, … [5,34] According to the Sabatier principle, the catalytic rate is maximized for the optimal (neither weak nor strong) interaction strength between adsorbate and catalyst surface. [35] Thus the interaction of reactants with the metallic surface is crucial for understanding the efficiency of the catalyst used, products properties, and the advantage of one catalyst formulation over another. The common metals showing the FT activities are the transition metals (see **Figure** 3) such as Fe, Co, Ni, Rh, Re, and Os. However, for commercial

use, only Fe and Co are suitable. The choice of the catalyst is related to the temperature mode, the origin of the synthesis gas, the price of the metal and wanted products [36,18].

The hydrogenation activity of metallic surface determines the nature of FTS products. Among conventional FT catalysts, the hydrogenation activity increases in the following order Fe<Co<Ni<Ru, making Ni and Ru highly methanazing catalysts compared to Fe and Co at the same temperature[5]. At similar reaction conditions, Fe is more selective to oxygenates than Co due to the differences in hydrogenation activities[5].

The WGS reaction ($CO + H_2O \leftrightarrow CO_2 + H_2$) activity of a FT catalyst is a very important property. Among the two most commonly employed catalysts, Fe and Co, high activity of WGS reaction is only observed for Fe whereas on Co catalysts this reaction is practically inactive. This catalyst property affects the choice of feed: due to WGS activity, Fe catalysts perform the best with a syngas of ratio 0.6-1.5, typical for coal and biomass derived syngas [33] whereas Co is considered more suitable closely stoichiometric ratios 1.9-2.2 characteristic for natural gas[36].

The catalyst used in the GTL industry is preferentially Co in LTFT, and preferentially in fixed-bed, slurry or micro-channel reactors. Co-catalysts have great stability, efficiency, high selectivity towards long-chained hydrocarbons, and low selectivity to the WGS reaction. There is a consensus in the literature that the active phase is the cobalt metal[37–39] contrary to Fe, where the active phase is iron-carbide. The properties of Co and other metallic catalysts mentioned above are potentially influenced by synthesis methods, the nature of support and promoters, operating conditions employed… Cobalt in its bulk form can appear in two unique crystallographic structures: face-centered cubic (fcc) and hexagonal (hcp). Since the phase transition hcp→ fcc takes place at a temperature around 450°C[40,41] they are both observed in FT[42]. Also, it is well known [43,41] that the size of particles can affect the transition between the two phases.

It is generally accepted that cobalt-based FT catalysts tend to lose their activity and selectivity while operating, although the exact mechanism towards deactivation is unknown. There are several deactivation hypotheses reported [44] in the literature for the FT catalysts and in particular for Co-based FT catalysts[45]. Among many assumptions evoked, we find sintering, poisoning, active metal re-oxidation, metal/support compound formation, reconstruction, and the deposition of carbon species as the most studied ones. In order to make the FT process economically attractive, catalyst deactivation has to be controlled.

Since FT catalyst deactivation is a slow process, we expect its mechanism to be slow and mainly driven by thermodynamics. This is the reason why, in our work, we make particular attention to the thermodynamic properties of the FTS reaction and the energy balance between reagents, products and the expected surface intermediates.

## 1.3 Thesis Aim

The present thesis has as an objective to verify some of the hypotheses evoked in the literature concerning the deactivation of Co-based FT catalysts, especially those that concern the active phase (metallic cobalt Co°): oxidation, carburization and surface reconstruction. We will attempt at describing the mechanism of the deactivation process, by a micro-kinetic model based on Density Functional Theory (DFT) calculations performed by us and by other groups, which offers a valuable asset towards the investigation of the preferential deactivation pathways. DFT methods will be used as a tool to investigate the structure and the energy of surface intermediates that may lead to deactivation. The result of those calculations will be used to construct the reaction network producing the deactivation phenomenon that we will implement in the current micro-kinetic model scheme. To the best of our knowledge, there exists no micro-kinetic model in the public literature aiming to describe the deactivation phenomenon due to the modification of the active phase. For instance, many experimental and

theoretical studies bring a hypothesis of possible surface species that take part in the deactivation mechanism, but they fail to produce a clear, step-by-step, mechanistic picture exploitable for micro-kinetic models. Besides, none of those studies confronts hypothetical deactivation intermediates therein with the experimental observations following the deactivation phenomenon. We hope that this combined DFT and micro-kinetic approach will be successful in describing the deactivation phenomenon, investigating the degree to which C and O deactivate Co-based FTS catalysts, those phenomena and, finally, to find the conditions at which those phenomena are minimized. The final goal of this work is, thus, to facilitate using this combined modeling approach, the optimization of industrial FT processes.

# 2 State of the art

## 2.1 Thermochemical aspects of Fischer-Tropsch Synthesis

Based on equation (1) in **Table** 3, the standard enthalpy change per carbon atom for the production of a given organic molecule can be derived. This quantity represents a measure of the thermodynamic feasibility and the direction of the spontaneity in the reaction that yields hydrocarbons from syngas. In **Figure** 4, Gibbs free energy change normalized to the carbon number in the produced molecules is presented at different reaction temperatures. The reaction enthalpy of individual reaction steps that can occur during the overall Fischer-Tropsch process is negative, and its average value is of the order of -150 kJ/mol [46] (see **Table** 3). **Figure** 4 reveals that production of methanal ($CH_2O$), methanol ($CH_3OH$), and ethyne $C_2H_2$ is unfavorable for all reaction conditions presented here. However, methane, ethane, and elemental carbon are very likely to appear as the products among which methane is the most favored product. Interestingly, lower temperatures seem to favor both long chained hydrocarbons and methane, demonstrating the negative entropy change in hydrocarbon formation. The formation of atomic carbon by the so-called Boudouard reaction ($2CO \rightarrow C + CO_2$) is also favored at low temperatures, although it is less favorable compared to the formation of either ethane or methane. An increase of chain length shifts the origin of the corresponding n-paraffin curve in the direction of higher free energy change whose limit is represented by the lower edge of the $C_{20}$ curve. Inversely, 1-olefins and oxygenates curves are shifted toward lower free energy changes and approach the origin of the $C_{20}$ curve. Hence, the paraffin content decreases as temperature increases, whereas the olefin and oxygenates content increases with temperature. In summary, the thermodynamic stability of product formation raises in the following order: oxygenates < olefins < paraffin < methane [47].

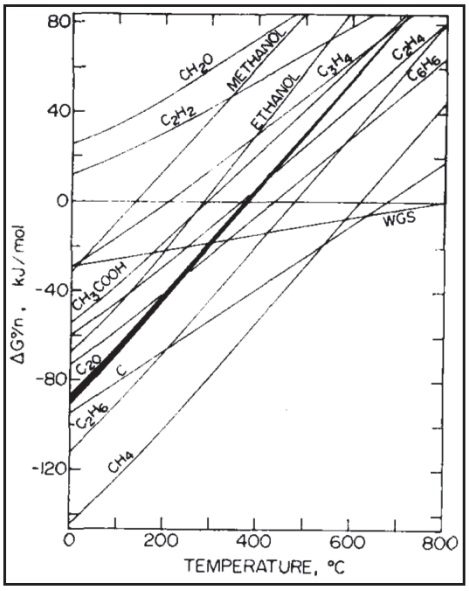


**Figure** 4. Gibbs energy change of hydrogenation of CO reaction normalized per carbon atom calculated based on the stoichiometry of equation (1) in **Table** 1. Taken from [48].

**Table** 3. Some stoichiometric reactions for the formation of $-(CH)_2-$ monomer unit and corresponding enthalpies under FTS relevant conditions [49,50].

| **$-(CH)_2-$ formation reaction** | **$\Delta H_r$ (500K) / kJmol$^{-1}$** | **Eq. number** |
|---|---|---|
| $CO + 2H_2 \rightarrow \mathbf{-(CH)_2-} + H_2O$ | -165.0 | (1) |
| $2CO + H_2 \rightarrow \mathbf{-(CH)_2-} + CO_2$ | -204.7 | (2) |
| $3CO + H_2 \rightarrow \mathbf{-(CH)_2-} + 2CO$ | -244.5 | (3) |
| $CO_2 + 3H_2 \rightarrow \mathbf{-(CH)_2-} + 2H_2O$ | -125.2 | (4) |

Although methane is thermodynamically the most favored product in the FTS reaction, catalyst type, operating conditions, kinetic limitations, and side reactions can have a profound influence on the real distribution of reaction products as reported by Anderson [51], Pichler [52] and Storch [53]. The actual product distribution of the Fischer-Tropsch reactions is considerably different from the distribution estimated based on the above thermodynamic calculations, and it is therefore of great importance to obtain kinetic insights concerning the reactions that lead to FTS products. Some side reactions in FTS are presented in **Table** 4 and **Table** 5.

**Table** 4. Stoichiometry of some side reactions that are considered undesirable for FTS [50,47].

| Reaction | Stoichiometry | $\Delta H_r$ (500K) / kJmol$^{-1}$ | Eq. number |
|---|---|---|---|
| Methane formation | $CO + 3H_2 \rightarrow CH_4 + H_2O$ | -214.8 | (5) |
| | $2CO + 2H_2 \rightarrow CH_4 + CO_2$ | -254.1 | (6) |
| | $CO_2 + 4H_2 \rightarrow CH_4 + 2H_2O$ | -175.0 | (7) |
| The Boudouard reaction | $2CO \rightarrow C + CO_2$ | -134.0 | (8) |
| Water Gas Shift reaction | $CO + H_2O \leftrightarrow CO_2 + H_2$ | -39.8 | (9) |

**Table** 5. Some side reactions that involve catalyst modification and that are supposed undesirable for FTS.

| Reaction | Stoichiometry | Eq. number |
|---|---|---|
| Oxidation/Reduction of catalyst | $M_xO_y + yH_2 \leftrightarrow yH_2O + xM$ | (10) |
| | $M_xO_y + yCO \leftrightarrow yCO_2 + xM$ | (11) |
| Bulk carbide formation | $yC + xM \leftrightarrow M_xC_y$ | (12) |

## 2.2 Kinetic aspects of Fischer-Tropsch Synthesis

Effluents from the FT reactor contain many different products. However, the product distribution follows a simple mathematical law as most polymerization reactions. A stepwise insertion of a $C_1$ monomer unit, $-CH_2-$ to the growing hydrocarbon chain $C_n$ at the surface of the metal is the most accepted scheme of Fischer-Tropsch reactions and it was firstly proposed in 1946 by Herington [54] and later promoted by Anderson [55]. Anderson described the product distribution in terms of the chain growth probability, $\alpha_{ASF}$, and today the distribution of hydrocarbons is described by the Anderson-Schulz-Flory (ASF) law. This law is based on the assumption that propagation and termination reactions solely affect the terminal carbon group in the growing chain. Herington [54] first defined an approximately constant parameter $\beta_n$ in order to characterize the distribution of hydrocarbons as the ratio of termination and propagation rates. For a given chain length $n$:

$$\beta_n = \frac{r_t}{r_p} \qquad \textbf{Eq.}\ 1$$

In **Eq.** 1, $r_t$ and $r_p$ are the rate of the termination and propagation reactions, respectively. Anderson [55] later improved the definition of this parameter in order to explain the molar product distribution and defined another characteristic parameter, $\alpha_{ASF}$ , as:

$$\alpha_{ASF} = \frac{r_p}{r_t + r_p}. \qquad \textbf{Eq.}\ 2$$

$\alpha_{ASF}$ can thus be interpreted as the probability of chain growth with respect to growth and termination events. Since Anderson and coworkers' publication was based on earlier work on polymer kinetics by Flory, [56] the product distribution is referred to as the Anderson-Schulz-Flory (ASF) distribution law and relates the mass fraction of given chain length $n$ product with ASF parameter $\alpha_{ASF}$ as:

$$W_n = n(1-\alpha_n)^2 {\alpha_{ASF}}^{n-1}. \qquad \textbf{Eq.}\ 3$$

After transformation of both sides, **Eq.** 3 becomes:

$$\ln(W_n/n) = \ln\frac{(1-\alpha_{ASF})^2}{\alpha_{ASF}} + n\ln(\alpha_{ASF}). \qquad \textbf{Eq.}\ 4$$

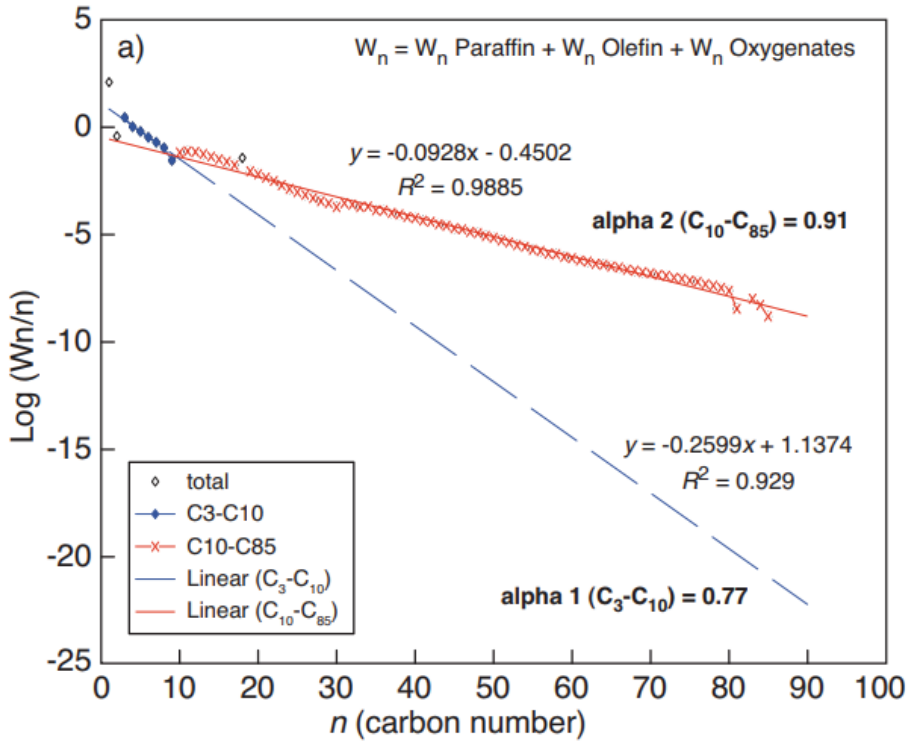


**Figure** 5. Illustration of the ASF distribution. The overall product distribution is described using two ASF coefficients. Taken from [57].

The chain growth probability $\alpha_{ASF}$ is assumed to be constant for every chain length of the reaction product ("ideal polymerization"), which allows representing with a straight line plot ln $(W_n/n)$ versus $n$ in **Eq.** 4. Experimentally however, the ideally linear behavior is not observed and some deviations to the ASF law have been reported for short chain hydrocarbons such as methane and ethane [58,46,59] (see **Figure** 5 and **Figure** 6**)**. This is the reason why the FTS is usually denoted as a "non trivial polymerization reaction"[60]. In order to describe the overall products distribution correctly, two ASF coefficients are estimated based on **Eq.** 4; one for low-molecular weight C species (usually up to ~10 C atoms) and one high-molecular weight species (>10 C atoms). Nevertheless, **Eq.** 4 is the most commonly used in experiments to estimate the chain growth probability $\alpha_{ASF}$.

Experimental mass fractions of products and chain growth probability $\alpha_{ASF}$ do not necessarily coincide with those predicted by the ASF law[60]. "Deviations" of experimental from theoretically predicted mass fraction for a given chain growth probability ($\alpha_{ASF}$)

regularly reported in a literature include underestimated theoretical selectivity of methane, overestimated theoretical selectivity of $C_2$ species, and incorrect olefin to paraffin ratio suggesting that the underlying assumption of independent from C number chain-growth probability in the ASF law is violated (see **Figure** 6). Different explications of those experimental deviations exist [61,62], however, the most plausible one so far, that reaches to explain all of them at once is the re-adsorption and subsequent secondary reaction of olefins [63–65,58]. This concept is related to all Fischer-Tropsch catalysts and it is reported that the extent of secondary reactions generally increases in the order Fe < Ru < Co, making cobalt the most susceptible to these secondary reactions [66–68]. Longer olefin chains are more likely to re-adsorb, due to their higher residence time, and to take part into secondary reactions. Those secondary reactions usually lead to longer olefins that can re-adsorb too. When those effects are important, complex Fischer-Tropsch reaction schemes such as the one by Horiuti-Polanyi can be envisaged (see below). This mechanism contains steps for hydrogenation, dehydrogenation and H exchange, and a bond-shift mechanism for isomerization [63]. Considering a deviation of ethylene, the simplest olefinic molecule, from the ASF distribution, we will consider its secondary reactions as a possible initial step in a deactivation phenomenon in **Chapter 5.**

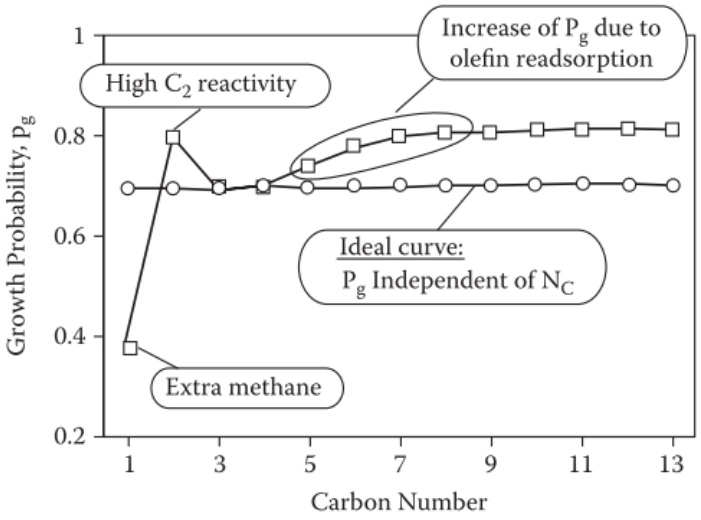


**Figure** 6. Illustration of ideal (chain size independent) and non-ideal chain growth. Taken from [69,70].

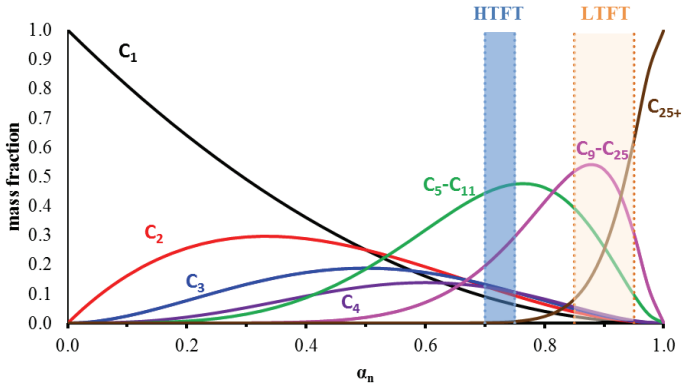


**Figure** 7. The product mass fraction as a function of chain growth probability α_ASF assuming ideal ASF kinetics. Shaded areas show typical $\alpha_{ASF}$ values for HTFT and LTFT catalysts.

For chain growth probabilities $\alpha_{ASF}$ that are close to 0, light molecular fractions are highly expected while for $\alpha_{ASF}$ that are close to one, heavy hydrocarbon molecular fractions are formed. In order to make the Fischer - Tropsch process economically feasible, operating under the high probability of chain growth ($\alpha_{ASF} > 0.9$) [58] is preferred in order to maximize the yield of high-valued products such as diesel fuel and waxes. It is very important to stress that selectivity, and therefore the chain growth probability $\alpha_{ASF}$, are highly dependent on operating conditions, but also on the type of reactor, the catalyst used and the way it is activated [71,61]. Dry reported ranges of $\alpha_{ASF}$ for cobalt, iron, and ruthenium catalysts of 0.70-0.80, 0.50-0.70, and 0.85-0.90, respectively. As for the influence of other parameters, Schulz

[72] reported a brief overview later reviewed by de Klerk [19,5]. Before we comment with more detail the effects of operating conditions on product selectivity, we present a summary of the different reaction mechanisms proposed in the literature.

## 2.3 The Fischer-Tropsch reaction mechanism

In our work, we use a micro-kinetic modeling approach in order to link the catalyst activity and product distribution under various reaction conditions. In this approach, a set of elementary reactions is thought to be relevant and representative for the overall chemical reactions taking place.

Micro-kinetic models are based on an in-depth mechanistic picture of a given chemical reaction and assumptions about active sites and elementary steps such as reactant adsorption, chain initiation, growth, termination and product desorption steps. In this approach, rate equations are usually derived by the Langmuir-Hinshelwood-Hougen-Watson (LHHW) rate theory, which allows rate prediction over a extensive range of conditions due to the fundamental theory underlining the model. This approach, however, demands knowledge of the detailed reaction mechanism and product selectivity. There are several mico-kinetic models proposed in the literature for the FTS reaction. In the following section, we present the main ones and focus our attention in the one developed by Tronconi and co-workers used in our work.

In this thesis, retrieve information about the deactivation of the Co based FT catalyst from DFT calculations. Hence, the final goal is to use DFT as a guideline towards the identification of deactivation phenomena and proposal of new elementary steps in the overall mechanism that lead to deactivation by carbon and oxygen. We believe that our approach is likely to reveal the actual kinetics of deactivation, which is of great concern in the industry.

### 2.3.1 The FTS reaction as a polymerization process

The FTS reaction can be rationalized as a polymerization process. In the following subsections, we will briefly describe initiation, propagation, and termination steps of the proposed reaction schemes for the FT polymerization reaction. We will also refer to some key DFT results in this area, in particular about the so-called site sensibility of the FT reaction. Although the investigation of the FT reaction mechanism is not the primary goal of our work, their consideration is needed to propose a sensible deactivation mechanism. We will finish this section by summarizing the reaction scheme proposed by Tronconi et al. [73,74], which is used in this work as it successfully explains most of the experimental observations.

Fischer-Tropsch polymerization reaction mechanism can be divided in the following subsets [47]:

- Adsorption of reactants CO and $H_2$,
- Chain initiation (start) – Creation of $C_1$ intermediate (chain initiator),
- Chain growth (propagation) – Insertion of monomer in the growing chain,
- Termination – Formation of the molecule and successive desorption,
- Secondary reactions of formed molecules (e.g., formation, desorption and readsorption of olefins).

The complete mechanism of the Fischer-Tropsch synthesis reaction remains still a subject of ongoing debate within the scientific community [75–77]. This fact is partly due to obstacles encountered when tracing the evolution of species that can appear on the catalyst surface during the reaction, half-life, reactivity of surface intermediaries and the liquid state of final products. A full review of the literature concerning the FT reaction mechanism is beyond the scope of our work. Here we put particular emphasis on theoretical results in line with our work. DFT is used to explore the Potential Energy Surface (PES) of the species on the catalyst surface. For more details on the concept of the PES, the equations derived in DFT theory and their applications, the reader is referred to **Chapter 3**. At this point, it suffices to understand

that the result of those calculations are reaction energies of hypothetical reactions and the structure of surface species that can be used to obtain insights in the catalyst surface composition and discriminate between different reaction mechanisms.

As proposed by Cheng et al.[78] and Dry[9], one of the main concerns in the experimental work in this domain is the fact that key-intermediates observed experimentally may be spectators and not the actual significant intermediates whose presence can help to unravel the exact mechanism of the FTS reaction. Besides, reactive species that cannot be determined experimentally may be key intermediates that allow the discrimination among mechanisms proposed for FT [78]. Moreover, there is evidence that the FTS reaction is site-sensitive, that is, different reaction pathways are possible according to the structure of the active sites. This will be commented with more detail below.

The adsorption and dissociation of hydrogen is not a concern in studies of the FT reaction mechanism, as hydrogen adsorption on the surface of most of transition metals is usually followed by spontaneous dissociation and an energy release as shown by numerous theoretical and experimental studies[79,80]. As for CO, authors in [81] reported non-activated reversible adsorption of CO of variable stoichiometry (0.4 to 2.3 molecules of CO/$Co_s$ atoms[1]) depending on the support, metal loading, and preparation method.

There is a great interest in understanding the dissociation of CO, especially since it is often considered as the rate-limiting step in the overall FT mechanism [82]. There are two hypotheses for the activation of CO. Some works propose direct dissociation of CO molecules [83–85] on steps and subsequent hydrogenation that gives $CH_x$ species on the catalyst surface. Other theoretical [78,86–94] and experimental [95,89,90] works suggest an alternative and energetically more favorable dissociation of CO that proceeds through hydrogen-assisted intermediates $CH_xO$ on terraces. Iglesia et Mavrikakis [96] provided both experimental and

[1] $Co_s$- Cobalt Surface Atom

DFT-based results on the significance of hydrogen in the supposed rate-limiting[82] CO dissociation step for Fe and Co catalysts. They concluded that H-assisted CO is preferred over the direct dissociation pathway. Similar results were found for Co by Saeys et al. [94]. Hence, CO dissociation is considered to be a *site sensitive.* It is predominantly on the initiation step that authors put more emphasis on this concept. We present site size-sensitivity in more detail below.

Production of long chains of hydrocarbons would not be possible without C-C coupling. Therefore, this is a crucial step in the overall Fischer-Tropsch process. Due to the complexity and somewhat limited possibilities to study surface intermediates during FT synthesis, propagation of carbon chains is elusive and is a subject of debate. Several mechanisms for propagation reactions have been proposed. It is also assumed that there are parallel reaction pathways that co-occur on the catalysts surface [97–99]. Starting from the discovery of Fischer-Tropsch synthesis reactions until today, proposed chain growth mechanisms to explain observed products can be roughly divided into five categories:

- Alkyl (carbide),
- Vinyl (alkenyl) mechanism,
- CO-insertion (hydro-formilation) mechanism,
- Enol (hydroxicarbene, hydroxymethylene) mechanism,
- Alkylidene mechanism.

### 2.3.2 Structure sensitivity of Co

There is evidence of structure sensitivity on the reaction mechanism of Co-based FT catalysts. The real catalyst surface does not correspond to the structure found in the bulk metal. One of the reasons for this behavior can be found in the trends of surface Gibbs free energies as a function of particle number size [100]; facet ratios between the (100) and (111) fcc surface structures, concentration of kinks and steps, coordination number of exposed metal

sites depend on the particle size (**Figure** 8). Moreover, since the real catalyst particle size is not uniform but rather dispersed over a particular range, the catalyst surface structure is primarily influenced by the size distribution of the catalyst particles (size sensitivity). Besides, the thermodynamic and kinetic properties of some elementary reactions are impacted by the nature of the catalytic site (Structure sensitivity) as it has been explained in detail by the works of van Santen et al. [77].

Thus, considering the realistic catalyst sample and its non-uniformity in terms of size, but also the chemical reactions that take place on the catalyst surface, the concept of size/structure sensitivity is often evoked in the literature. The catalysts of interest in this work are Co-based FT catalysts whose crystallites are with a diameter less than 100 nm and therefore exhibits Co (fcc) structure according to reference [100]. Also, considering the catalyst particle dispersion in a realistic sample, other metastable phases may exist [100]. A very interesting molecular dynamics simulation study was published to understand the effects of particles size and crystal phases on the distribution of surfaces sites in FT catalysts [101]. Van Santen et al.[102,103] discussed in detail this structure/size sensitivity phenomenon. Briefly, depending on the size of metal particles, there are multiple regimes presented in **Figure** 8. Another interesting view on the surface sensitivity is given by Liu et al.[104], who discussed this phenomenon qualitatively in terms of electronic and geometrical considerations.

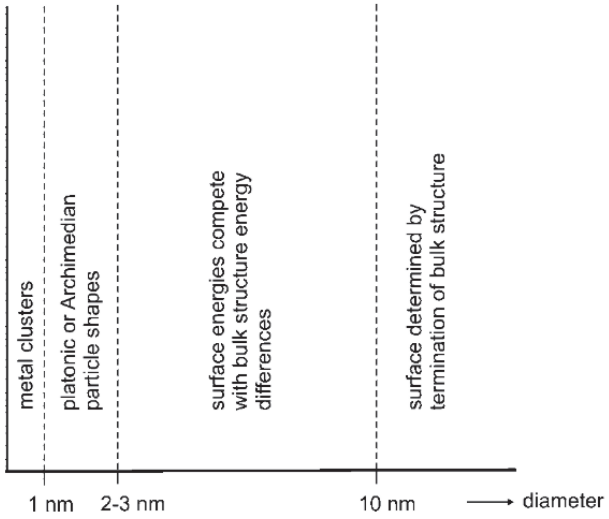


**Figure** 8. Schematic representation of size sensitivity for metallic particles and corresponding structures. Reproduced from [102].

Detailed theoretical studies were conducted on Co-based catalysts in ref. [105,106]. Many scientific groups discuss the reaction mechanism assuming "ideal" flat surface models (called terraces) but also "non-ideal" defect-containing surface (step-edges, kinks, B5 sites …) such as those reported in **Figure** 9 and **Figure** 10. Hence, this and the concept of structure sensitivity divided the scientific community into, on the one hand, those who argue in favor of the direct CO[42,88,106] dissociation mechanism on defected (B5 step-edge sites shown in **Figure** 9 and **Figure** 10), on the other hand, those in favor of the hydrogen-assisted[96,107,92] CO dissociation in ideal flat (terraces) sites. Based on DFT results reported by Cheng et al. [108], propagation reaction is also structure sensitive and according to that work more favorable on stepped than on flat surfaces as discussed previously[77]. Moreover, it was shown on corrugated Ru surfaces that propagation occurs more likely on different step-edge site[109]. Notwithstanding, $CH_y$ hydrogenation, as well as termination reactions, are assumed to be structure-insensitive [104]. Therefore, when discussing the mechanism of the FT reaction in details, the size sensitivity phenomenon should be kept in mind.

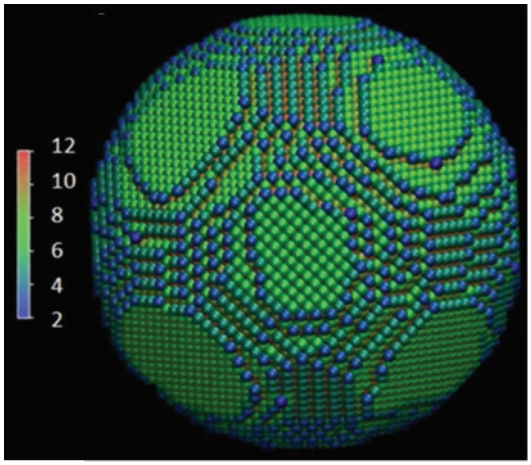


**Figure** 9. Structure of modeled 10 nm fcc nanoparticle of Co. edge/kink atoms (coordination number <7) are shown in blue; terrace atoms (CN=8-9) are shown in green. Taken from[101].

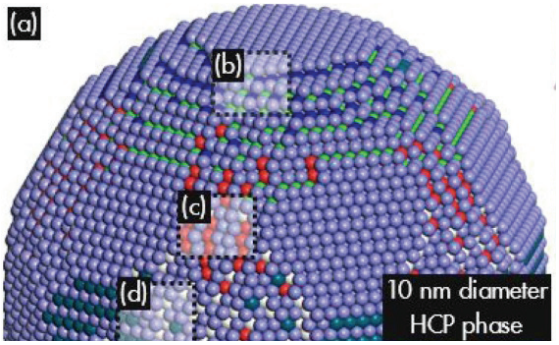


**Figure** 10. a) Structure of modeled 10 nm hcp nanoparticles and different type of B5 sites identified (shown in b), c) and d)). Taken from [101].

### 2.3.3 Alkyl mechanism

The alkyl mechanism, initially proposed by Fischer and Tropsch [110], assumes a direct dissociative chemisorption pathway of carbon monoxide on the catalyst surface and subsequent hydrogenation of carbon to form $CH_2$ monomer species, whose oligomerization allows for the formation of higher hydrocarbons through propagation reactions [111]. Cheng et al. [112], Zuo et al. [113]and Michaelides and Hu [114] studied the stability of $CH_y$ species and carbon hydrogenation energies on different stepped metal surfaces using DFT. In these works, C is the most stable surface specie based on its adsorption energy. Zuo et al. [113,115] determined that stability of different surface species increases in the following order: $CH_4<CH_3<H<CH_2<CH<C$. Those results thus can explain the existence of the surface

monomer and initiator species in the alkyl mechanism. They independently brought the conclusion that the rate determent step in C hydrogenation is the $CH_3$ hydrogenation step. Besides, Cheng et al. studied [108,78] C-C coupling mechanisms using DFT on different flat and defected stepped-metal surfaces and concluded that the barriers of C-C coupling are strongly dependent on the metal surface. The primary chain growth mechanisms identified on Co stepped-surface were $CH_2/CH_2$ and $C/CH_3$ and concluded that step sites are more favorable than terraces for those coupling reactions. Hence, these results infer that $(CH_2)_{ads}$ may be the most favored monomer species for Co catalysts, which is consistent with the alkyl mechanism proposal. However, the identification of the exact coupling species ($CH_3/CH_2$ coupling in alkyl mechanism) is still debated from the perspective of DFT calculations considering the results reported by Hu et al. [108,78,116], Huo et al. [93,117] for other FT catalysts considering the lower activation barriers of some other coupling reactions. Besides, there is a disagreement reported with $(CH_2)_{ads}$ as the monomer species based on the fact of its favorable decomposition to more stable surface species such as methylidyne $(CH)_{ads}$ [118,82]. Shetty et al. concluded that it is unlikely that $CH_2$ and $CH_3$ act as a building block for chain growth [109]. As for termination, the growing chain undergoes its termination either by β-carbon dehydrogenation or α-carbon hydrogenation leading to α-olefins and n-paraffins, respectively, as schematized in **Figure** 11 and **Figure** 12**.** The surface species involved in the alkyl mechanism have been experimentally detected on many metallic surfaces [119,97].

This reaction pathway explains neither the formation of branched hydrocarbons nor that of oxygenates that have been confirmed experimentally. Although the readsorption of 1-olefins is evoked to explain the formation of branched hydrocarbons, it is reported that this pathway solely cannot hold and some authors argued that additional paths are required to elucidate the presence of branched hydrocarbons[97]. Based on experimental findings, Schultz and al [120,121] proposed the supplementary reaction pathways schematized in **Figure** 13 to

explain previous discrepancies between theory and experiments. According to previous publications, the increase in hydrogen, CO, and water partial pressure reduces branching on cobalt [122].

As for alcohol production, chain termination is explained by the hydroxylation of growing chains, yielding 1-alcohols as products. However, the experimental confirmations of this reaction pathway are absent.

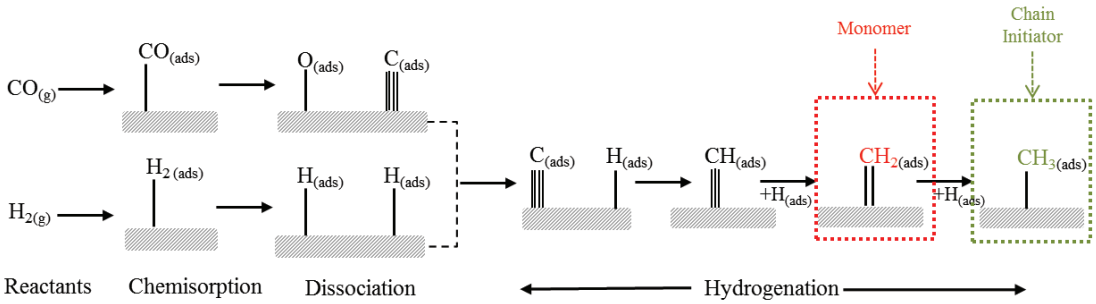


**Figure** 11. Schematic presentation of chain initiation step in the alkyl mechanism that leads to the formation of monomer units. Reproduced from[97].

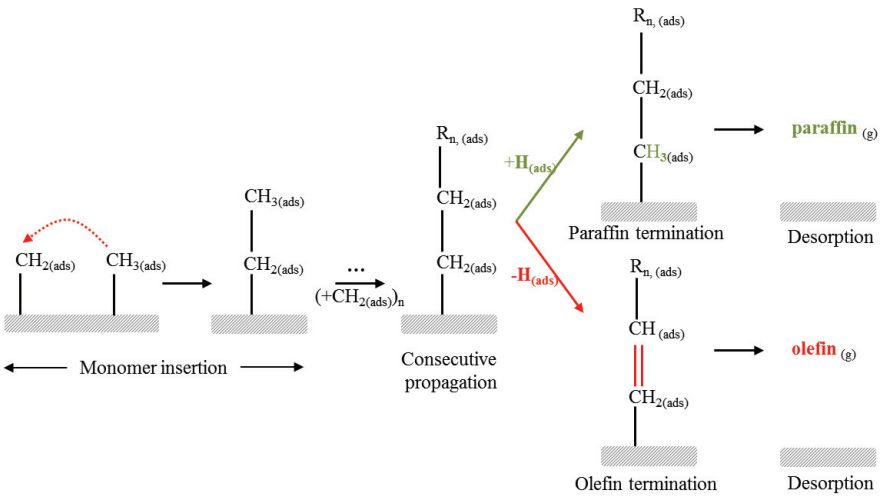


**Figure** 12. Schematic presentation of chain propagation step in the alkyl mechanism that leads to main product formation. Reproduced from[97].

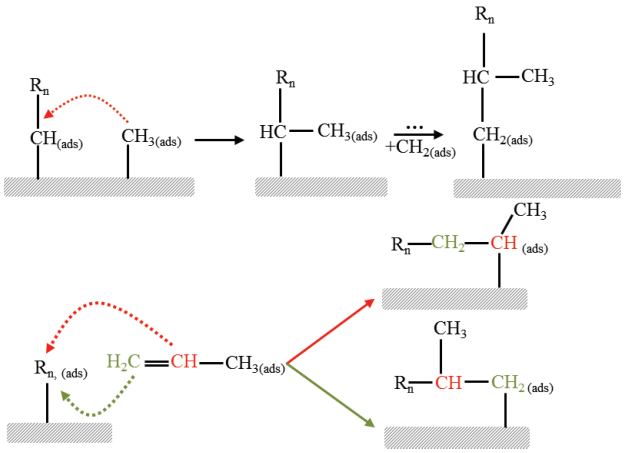


**Figure** 13. The possible pathway toward branched species formation, according to Schulz. Reproduced from[97].

### 2.3.4 Vinyl (alkenyl) mechanism

Maitlis et al.[123] pointed out to numerous reports of other authors mentioning that the coupling of two formally $sp^3$ hybridized carbon atoms, as proposed by alkyl mechanism, is unfavorable due to the kinetic barrier for the reorientation of two highly directional $sp^3$ orbitals [97]. Additionally, some studies show lower activation barriers for $sp^2$ coupling with either $sp^2$ or $sp^3$ hybridized C atoms compared to $sp^3$-$sp^3$ carbon coupling stressing the importance of vinyl species in the Fischer-Tropsch reaction. More precisely, the first C-C bond is created by coupling methylidyne $(CH)_{ads}$ and methylene $(CH_2)_{ads}$ to obtain surface vinyl groups $(CH_2{=}CH)_{ads}$ (chain initiator) (**Figure** 14). Coupling of vinyl groups with monomer units (methylene), gives surface allyl species $(CH_2{=}CHCH_2)_{ads}$ that isomerase to surface alkenyl species $(CH_3CH{=}CH)_{ads}$. The chain continues to grow with the subsequent addition of more methylene $(CH_2)_{ads}$ groups until the former binds some surface hydride $(H)_{ads}$ and desorbs as an olefin (**Figure** 15). This mechanism is supported by $^{13}C$ labeling experiments[95] and experiments with model catalysts[123]. Various modifications of the alkenyl mechanism were proposed, but most of them were not based on Co catalysts or other FT active metals. Besides, we did not find any DFT data that could support this mechanism. One

of the drawbacks of the proposed reaction scheme is its inability to describe paraffin formation as primary products. However, the vinyl mechanism can account for the production of branched hydrocarbon species as the isomerization of allylic intermediates.

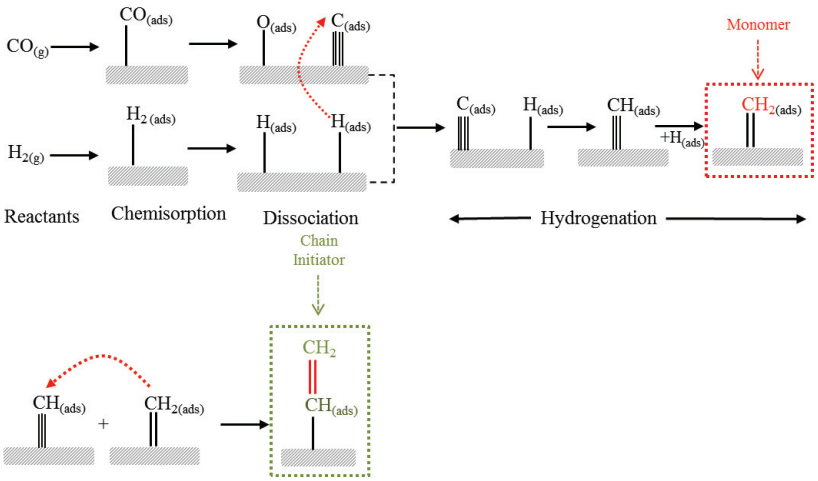


**Figure** 14. Schematic presentation of chain initiation step in the Vinyl mechanism that leads to the formation of the monomer unit. Reproduced from [97].

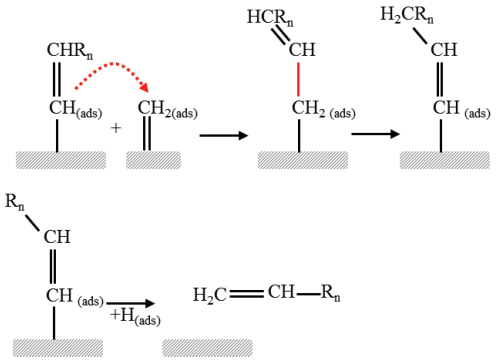


**Figure** 15. Schematic presentation of chain propagation step in the Vinyl mechanism that leads to primary product formation. Reproduced from[97].

### 2.3.5 Enol mechanism

Contrary to previously described mechanisms, the enol mechanism[124] accounts for the formation of oxygen-containing surface species obtained by hydrogenation of non-dissociated CO [53,125,124,97] $(CHOH)_{ads}$. This mechanism seems reasonable, at least for Co catalysts, according to the work of Balaji Gupta et al.[126]. They studied simultaneous adsorption of

hydrogen and carbon monoxide (different $CO/H_2$ mixtures) at different temperatures up to 100 °C. Their results suggest higher adsorption of CO and $H_2$ from syngas mixtures than from pure their pure counterparts. Besides, regardless of the initial gas composition, they have determined that the surface composition of the adsorbed phase is CO: $H_2$ = 1:1, which, according to them, suggests the formation of chemisorbed COH2 complexes, which is a monomer unit (and initiator) in the enol mechanism, presented in **Figure** 16**.** On the contrary, it was showed that aldehydes and alcohols are weak initiators for Co-based catalysts[127] and that they cannot act as the propagators[128], thus questioning the validity of this mechanism scheme for Co-based catalysts where CHOH acts as both chain initiator and monomer specie.

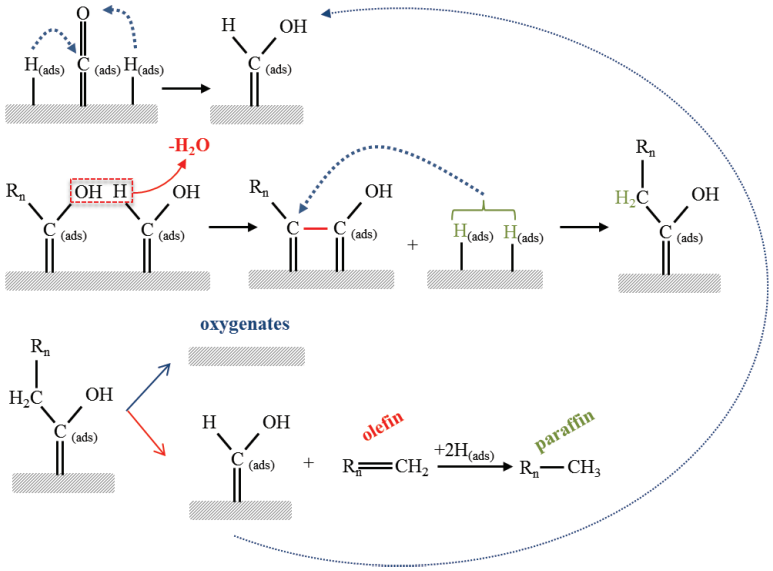


**Figure** 16. Schematic presentation of chain initiation and propagation step in the enol mechanism that lead to main product formation. Reproduced from[97].

The condensation of those enol complexes on the surface, after elimination of water molecules, represents the chain-building step of this polymerization reaction mechanism. Termination and desorption of obtained product can give different oxygenated species,, and olefins; further hydrogenation of the latter yields n-paraffins. Although surface science experiments suggest that there is little oxygen on the surface and that the kinetics of its

desorption as a water molecule is rapid, some co-feeding experiments with radioactive labeled propane 1 and 2-ol studies[97] support this mechanism.

### 2.3.6 CO insertion mechanism

The monomer unit in CO-insertion mechanisms is molecularly chemisorbed CO itself. [30,52,59,70]. As in the alkyl mechanism, the main assumption lays on the fact that the chain initiator is the surface methyl group. Oxygen release takes place after a hydrogenation step. Incorporation of additional carbon monoxide molecules occurs in the propagation step by giving acyl intermediate whose further hydrogenation and dehydration (removal of oxygen) enable the chain to grow. Organometallic chemistry and homogenous catalysis concepts strongly support this part of the reaction scheme. Chain termination reactions that lead to common Fischer-Tropsch products, n-paraffin, and α-olefin are identical to those described for the alkyl-mechanism. Many oxygenated species can also be formed starting from oxygenated surface species as partly presented in **Figure** 17 . Inderwildi et al. determined that initiation step in alkyl mechanism is not plausible for Co catalysts and that alternative pathways via hydrogenated forms of CO such as $(CHO)_{ads}$[95] and $(CH_2O)_{ads}$[107,96] are more plausible[86] in agreement with experimental studies of Weststrate et al. [129], Todić et al. [130]. Bhatelia et al. [131] performed a thorough study of different kinetic schemes proposed in the literature and discussed above and showed, for Co catalysts, that the CO insertion mechanism model the most consistent with respect to physicochemical and statistical tests.

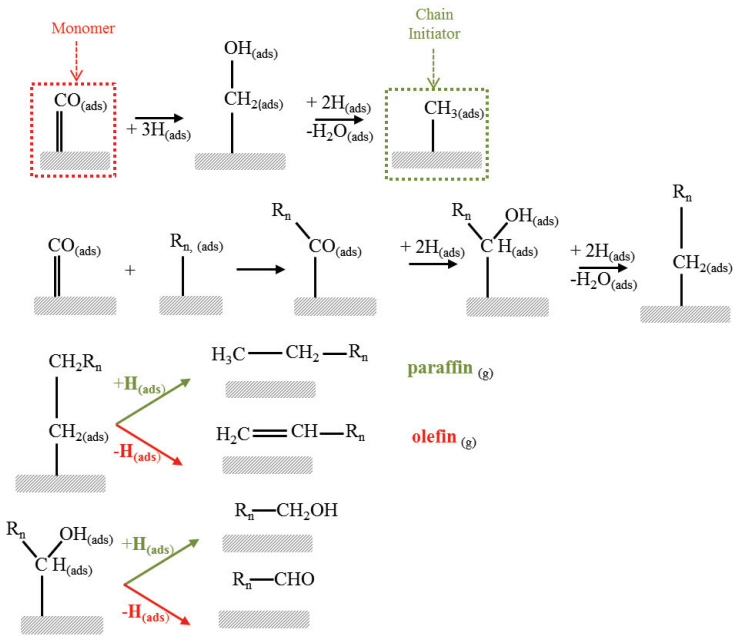


**Figure** 17. Schematic presentation of chain initiation and propagation steps in the CO-insertion mechanism. Reproduced from[97].

### 2.3.7 Alkylidene mechanism

As it was discussed by Shi et al.[132], mechanisms presented above fail to describe the most apparent experimental facts such as the underestimated compared to the ASF distribution selectivity of methane, the underestimated selectivity of ethane and the mechanism of formation of branched carbon species. Those observations led to new mechanism proposals such as the one from Shi et al. [133,134] based on deuterium tracer studies on Co catalysts, from Gaube and Maitlis[135,123] and Ciobîcă et al. [82]. According to Shi et al. [133,134], CH surface species is the product of CO hydrogenation (supported by the DFT calculations of Liu et al. on Ru[116] and Co[136,137] surfaces), which is the monomer in the chain growth reactions presented in **Figure** 18 . Coupling of monomers yields ethylidene species, as shown in **Figure** 19 **.** Moreover, complete hydrogenation of surface species CH leads to methane. Besides, the coupling of monomers can be responsible for ethylidene species growth to some higher alkylidene species such as propylidene, etc. According to Shi et al. [133,134], alkylidene species formed may be dehydrogenated or hydrogenated, leading to olefin and paraffin products, respectively, as presented in **Figure** 20. However, desorbed olefins can be

readsorbed, leading to the reformation of alkylidene surface species that can also lead to branched C species. This mechanism can explain the presence and the distribution of branched C species in the FTS products as well as previously reported deviations in the ASF distribution.

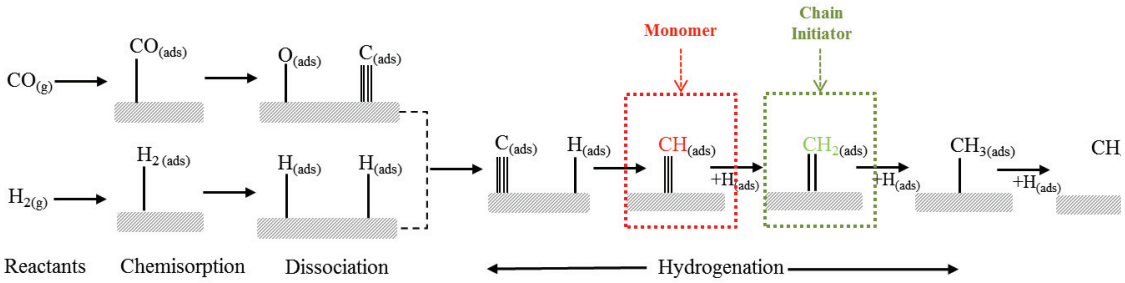


**Figure** 18. Schematic presentation of the formation of chain initiator and chain growth monomer species in alkylidene mechanism, according to[138,132] .

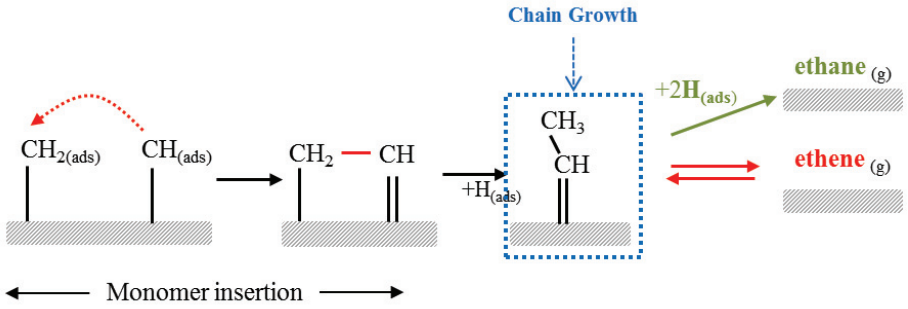


**Figure** 19. The initial phase of chain growth and ethane readsorption in alkylidene mechanism, according to[138,132] .

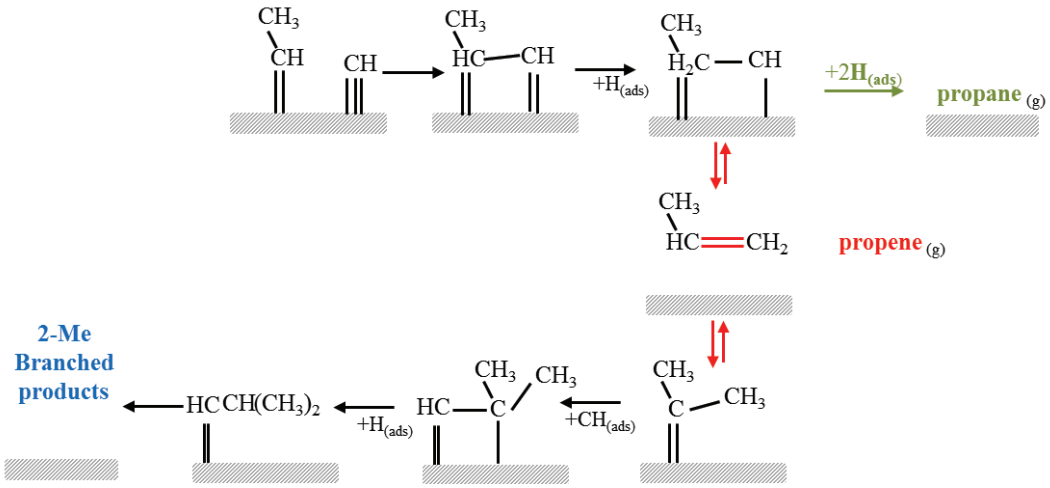

**Figure** 20. Chain growth towards paraffin, olefin, and 2-Methyl branched species in alkylidene mechanism, according to[138,132] .

### 2.3.8 Secondary reactions

Most of the reaction mechanisms previously discussed were developed to describe the selectivities of the main FT products: olefins (more specifically 1-olefins and olefins with internal double bonds). However, depending on the reaction conditions and catalyst properties, side reactions leading to different families of molecules can be activated. Those side reactions are believed to be involved in the production of oxygenates (alcohols, aldehydes, ketones, carboxylic acids) and branched carbon species (mainly mono-methyl branched)[97]. The exact mechanism of these transformations is widely discussed in the literature but still unknown[139,140,131]. Hence, in short, 1-olefin readsorption has been frequently reported. It is alleged that (re)adsorbed olefins may take part in several reactions such as: hydrogenation (to paraffin), double bond shift (thus isomerase to olefin with an internal double bond), incorporation into growing chains, hydroformylation (to alcohols and aldehydes) and hydrogenolysis of $O_n$ (n-length olefin chain to methane and $O_{(n-1)}$)[97]. Those secondary reactions are believed to be chain-length dependent due to the carbon number dependency of diffusivity and solubility in liquid products and physisorption energies of products on the catalyst surface, which increase the residence time of longer chains[97,141]. Selectivity models based on the above physical principles are out of the scope of this work. However, considering the observed product distribution of this family of molecules, and in particular ethylene, it seems reasonable to question their possible involvement in a deactivation too. Besides, as we will discuss in **Section 2.6.4**, hydrocarbon molecules, and ethylene above all[142,143], are frequently employed as precursors in a synthesis of carbon materials such as graphene. In those studies, hydrocarbon molecules are thermally

decomposed on a transition metal surfaces yielding various $C_\alpha H_\beta$ considered envolved in the nucleation and growth of graphene islands[144].

As for oxygenated products, those are assumed to be formed from the CO insertion mechanism[52,59,70,30] described above, leading mainly to alcohols and aldehydes. Another possible and assumed minor route for oxygenates formation, in addition to CO-insertion, is hydroformylation of olefins. This route has been proven to take place in Co catalysts with co-feeding experiments[140]. However, the fraction of oxygenated products is typically very low for Co-based catalysts.

Branched-carbon products have also been identified (up to around 5 mol % in the total hydrocarbon fraction)[145] in the product mixture of FT synthesis with Co catalysts. Shi et al. [145] showed that reaction conditions and formulation of catalysts have a substantial impact on the iso/normal hydrocarbons rations. Schulz et al.[122] underlined that in cobalt catalysts branching phenomena is very sensitive to reaction parameters and proposed that the "stationary state of the Co catalyst surface appears more dynamic than that of Fe catalysts". Besides, they showed that hydrogenating conditions reduce the extent of branching. Interestingly, CO and $H_2O$ partial pressure increase also reduces branching phenomenon. Schulz et al. [121] pointed out that surface segregation may play an essential role in explaining the surface chemistry of FT and pointed out how C-branching evolves with the self-organization of Co-based FT catalysts. Considering the low selectivity of branched products in Co catalysts, the scientific literature lacks information on reaction mechanisms for the formation of branched products.

### 2.3.9 Summary of mechanisms

As it can be seen from the reaction mechanisms briefly described above, different species on the catalyst surface have been proposed to take part in the overall mechanism of the Fischer-Tropsch synthesis reaction (**Table** 6). A key point in providing an overall mechanism and consequently, the mechanical description of the distribution of different

products of some reaction, is knowing the structure and energy of intermediaries that can intervene. This is often the scope of theoretical calculations in this field.

**Table** 6. A summary of the FTS reaction mechanisms presented in **Chapter** 2.

| Reaction mechanism | Initiator | Monomer unit | Chain propagation | Chain termination |
|---|---|---|---|---|
| **Alkyl** | $M=CH_3$ | $M=CH_2$ | Alkyl/$CH_2$ Coupling. | Hydrogen addition and elimination, leading to n-paraffins and α-olefins. No oxygenates. |
| **Alkenyl** | M-$CH=CH_2$ | $M=CH_2$ | $CH_2$-insertion into vynil giving allyl species. Allyl-vynil isomerates to alkenyl | Hydrogenation of alkenyl gives α-olefins |
| **Enol** | $M=COH_2$ | $M=COH_2$ | Condensation of surface $M=COH_2$ species followed by elimination of water. | Desorption yields α-olefins and oxygenates. Secondary paraffin formed from α-olefins. |
| **CO-insertion** | M-R | M-CO | CO-insertion into M-R, giving surface acyl, followed by hydrogenation and dehydration. | Hydrogen addition and elimination, leading to n-paraffins and α-olefins. Oxygenated surfaces species give oxygenates. |
| **Alkylidene** | $M-CH_2$ | M-CH | CH/$CH_2$ Coupling. | Alkylidene species hydrogenation/ dehydrogenation |

## 2.4 Tronconi and co-workers micro-kinetic scheme

The micro kinetic model used for Co based catalysis at IFPEN comes from Tronconi et al. [74,73]. This model, in its current state, can predict the activity and paraffin product distribution as a function of reaction conditions. However, it is not capable of predicting or describing the kinetics of deactivation in its current state. This is due to the lack of elementary steps in the micro-kinetic model that would take into account deactivation phenomena. The goal of this thesis is, therefore, upgrading this micro-kinetic model by introducing the elementary steps that lead to deactivation.

As it was described in the previous section, there are many propositions for the chain initiation and propagation steps in FT reaction mechanism studies. In the reaction scheme proposed by Tronconi et al. [73] the proposal for the chain initiation step is fully supported by

kinetic and DFT studies on Co [96,86]. This model is developed for hydrocarbons (paraffin and olefin molecules) up to 49 carbon atoms. Species that contain more than 50 atoms of carbon are considered as $C_{50+}$. The formation of oxygenated compounds is not taken into consideration due to their relatively low abundance for Co-based catalysts. Overall, 103 molecular and 56 radical species are considered in this model.

**Table** 7 shows individual elementary steps that constitute a micro-kinetic model of depart. The initiation step in this model is composed of dissociative adsorption of $H_2$ and molecular (non-dissociative) reversible adsorption of $CO$. Molecularly adsorbed $CO-\sigma$ is hydrogenated to formyl and hydroxyl-methylene intermediates, respectively, and then dissociates (hydrogen-assisted dissociation) to $CH-\sigma$ and $OH-\sigma$. The former is hydrogenated to give a chain monomer and an initiator similar as to the alkyl mechanism, $CH_2-\sigma$ and $CH_3-\sigma$, respectively. The latter is hydrogenated to water molecules. Addition of chain monomers $CH_2-\sigma$ to a chain initiator $R_n-\sigma$ constitutes the subset of propagation reactions. Addition and rejection of hydrogen atoms constitute the termination of growing chains that give paraffinic and olefinic products, respectively. $\beta$- hydride elimination is regarded as a reversible process in agreement with experimental results of olefin readsorption[63,146].

In contrast to some kinetic modelling approaches, micro-kinetic models allow the prediction of the influence of working conditions on methane, paraffin and olefin yields as well as their selectivity in terms of ASF coefficient α. WGS reaction and alcohol formation are not taken into account in this model.

**Table** 7. Elementary steps involved in the FTS over Co-based catalysts according to[74,73].

| El. Step number | El. Step Name | Elementary Step reaction | Kinetic/Equilibrium expression |
|---|---|---|---|
| **1** | Initiation | $H_2 + 2\sigma^* \leftrightarrow 2H - \sigma$ | $K_{H_2} = x_{H_2}^{-1}\theta_*^{-2}\theta_{H*}^2$ |
| **2** | | $CO + \sigma^* \leftrightarrow CO - \sigma$ | $K_{CO} = x_{co}^{-1}\theta_*^{-1}\theta_{CO*}$ |
| **3** | | $CO - \sigma + H - \sigma \leftrightarrow HCO - \sigma + \sigma^*$ | $K_{HCO} = \theta_{HCO*}\theta_*\theta_{CO*}^{-1}\theta_{H*}^{-1}$ |
| **4-6** | Methylene species formation | $HCO - \sigma + H - \sigma \rightarrow HCOH - \sigma + \sigma^*$<br>$HCOH - \sigma + \sigma^* \rightarrow CH - \sigma + OH - \sigma$<br>$CH - \sigma + H - \sigma \rightarrow CH_2 - \sigma + \sigma^*$ | $r_m = k_m\theta_{HCO*}\theta_{H*}$ |
| **7** | Water formation | $OH - \sigma + H - \sigma \rightarrow H_2O + 2\sigma^*$ | |
| **8** | Initiator formation | $CH_2 - \sigma + H - \sigma \rightarrow CH_3 - \sigma + \sigma^*$ | $r_{in} = k_{in}\theta_{CH_2*}\theta_{H*}$ |
| **9** | Propagation | $R_n - \sigma + CH_2 - \sigma \rightarrow R_{n+1} - \sigma + \sigma^*$ | $r_{prop,n} = k_{prop}\theta_{R_n*}\theta_{CH_2*}$ |
| **10** | Termination to paraffin for $n = 1$ | $CH_3 - \sigma + H - \sigma \rightarrow CH_4 + 2\sigma^*$ | $r_{CH_4} = k_{CH_4}\theta_{CH_3*}\theta_{H*}$ |
| **11** | Termination to paraffin $\forall n \in \{2,50\}$ | $R_n - \sigma + H - \sigma \rightarrow P_n + 2\sigma^*$ | $r_{par,n} = k_{par}\theta_{R_n*}\theta_{H*}$ |
| **12** | Termination to olefin for $n = 2$ | $C_2H_5 - \sigma \leftrightarrow C_2H_4 + H - \sigma$ | $r_{C_2H_4} = k_{O,dx}\theta_{C_2H_5*} - k_{C_2H_4*}x_{C_2H_4}\theta_{H*}$ |
| **13** | Termination to olefin $\forall n \in \{3,50\}$ | $R_n - \sigma \leftrightarrow O_n + H - \sigma$ | $r_{ol,n} = k_{O,dx}\theta_{R_n*} - k_{O,sx}x_{ol,n}\theta_{H*}$ |

In previously published studies, [147,96] adsorption steps of both CO and $H_2$ are assumed to approach thermodynamic equilibrium under working conditions of FTS (which allows writing equilibrium expressions for elementary steps (1) and (2) as discussed by Visconti et al. [73]). In their model, elementary step (3) is also at thermodynamic equilibrium whereas the second hydrogenation step (4) is a rate-determining step (**RDS**) in the series of steps (4) –(7). Rate constants that describe elementary steps for the chain growth of the adsorbed species (9), (11), and (13) are assumed independent of the carbon atom number of the involved intermediates $R_n - \sigma$.

This model is fitted with in-house experimental data[148] obtained for a $CoPt/Al_2O_3$ catalyst in the fixed-bed configuration over various experimental conditions ($H_2$/CO feed ratio

= 1.85-2.4, GHSW= 3.93-25.86, T=210-230°C and P=10-30 bar). The results of those fits were used in this work as a starting point in our work and are presented in **Chapter 6**.

## 2.5 Operating Conditions Impact on main FT observables

In industry, the most important descriptor of the properties of the FT process is the quality of the product distribution of the hydrocarbon mixture produced (paraffin and olefin molecules) usually defined with $\alpha_{ASF}$ coefficient. The operating conditions are described in term of temperature (T), pressure (P), space velocity (usually defined in terms of GHSV: Gas Hourly Space Velocity=Volumetric flow velocity of gas/ Volume of catalyst[2]) and syngas ratio. Although the relationships between observables and operating parameters are in principle very complex, there exist some empirical rationalizations summarized in **Table** 8. In the micro-kinetic model we use, we take into account those empirical observations in the fitting procedure to experimental data. Acquisition of experimental data we used for the fitting procedure was not the subject of this thesis. However, the most essential features of those catalytic tests are described in **Section 8.8**.

**Table** 8. Influence of some controllable parameters on some selected observables according to [5].

| Observable | Operating Parameter being increased | | | |
|---|---|---|---|---|
| | T | P | GHSV | $H_2/CO$ |
| C number distribution | Lower α | Higher α | No Change [c)] | Lower α |
| S[b)]($CH_4$) | Increases | Decreases | Decreases | Increases |
| S [b)] ($O_n$) | NaN[a)] | NaN [a)] | Increases | Decreases |
| S [b)] (oxygenates) | NaN [a)] | Increases | Increases | Decreases |
| S [b)] (aromatics) | Increases | NaN [a)] | Decreases | Decreases |
| Conversion | Increases | Increases | Decreases | NaN [a)] |

[a)] The direction of change depends on a more complex relationship.
[b)] Selectivity
[c)] Change is possible if secondary reactions are significant.

It should be kept in mind that the observations reported in **Table** 8 are not general. Those depend on the large extent on the catalyst used, reactor technology but also time. FT catalysts deactivate over time, and therefore, products selectivity in terms of main operating

[2] GHSV is the ratio of gas flow rate in standard conditions divided by the volume of the catalytic bed.

conditions can only be discussed adequately if the former are de correlated from deactivation. Also, the impact of deactivation on product selectivity, which is very important from the economic point of view should also be discussed if de correlated from other influences.

## 2.6 Catalyst deactivation and modified product selectivity

The economic feasibility of the Fischer - Tropsch process is greatly influenced by the cost of catalyst replacement due to the loss of its activity and selectivity with time on stream. The deactivation process seems to be inevitable, although the rate at which it occurs varies greatly[44,149]. Therefore, studies on catalyst deactivation such as ours, aim at minimizing those unfavorable events towards stable, long-lasting catalyst and commercially competitive FT processes. Van Berge and Everson [150] showed that for Co-based FT catalysts, two regimes of deactivation can be observed; the first one associated with a reversible process (period **A**) and the second one with irreversible deactivation (period **B**) as shown in **Figure** 21. Nevertheless, the overall mechanism of deactivation is still not well understood, although it is often agreed that it is an ensemble of deactivation mechanisms of different nature that co-occur with time on stream depending on the type of catalyst, nature of FT process, operating conditions, reactor configuration, etc. There are several deactivation paths reported [44] in the literature for FT and in particular for Co-based FT catalysts: sintering, poisoning, active metal re-oxidation, metal/support compound formation, carbonization, etc [45]. In this section, the main paths for deactivation and consequent, modified selectivity, will be presented.

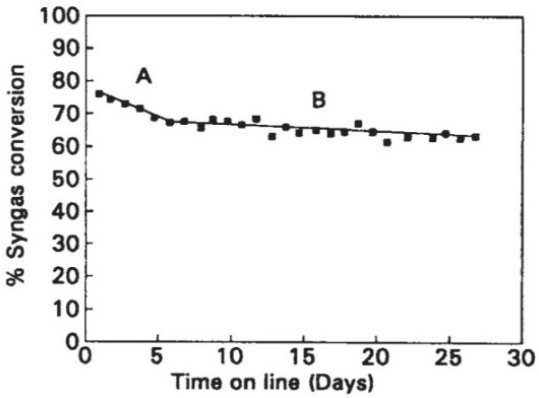


**Figure** 21. Common deactivation profile for cobalt catalysts in FTS[151,152].

### 2.6.1 Poisoning

Poisoning is a chemical process in which strong adsorption of some molecule (reactant, products, intermediates, impurities) occurs, on the catalytic site otherwise responsible for catalytic activity. The chemisorption of poison can have many unwanted consequences on the overall efficiency of process such as: **1)** physical blocking of active sites, **2)** electronic modification of metal/neighbor surface molecules as a result of strong chemisorption, **3)** modification of surface structure leading to loss of activity for surface-sensitive reactions and **4)** inhibition of surface diffusion of adsorbed reactants. Common poisons for Fischer-Tropsch reported in the literature are sulfur compounds, arsine, ammonia, and metal carbonyls. Due to the lack of relative importance of other poisons, only the general context of sulfur deactivation will be discussed.

Sulfur and its compounds are regarded as very poisonous species for most metallic surfaces used as a catalyst as they adsorb rapidly and irreversibly. Poisoning of the metallic surface with sulfur compounds is mostly studied on nickel catalysts, but it is believed that those results can be extrapolated at least qualitatively to other poison/metal systems. Bartholomew and al. [153] showed that poisoning with $H_2S$ is highly selective on Co, Ni, Fe, and Ru catalysts and that very low concentration of this poison (< 100 ppb) can diminish catalysts activities by several orders of magnitude. In other words, tolerance of those catalysts towards sulfur is extremely low. Visconti and al. [154] had confirmed the negative correlation between the sulfur presence and $Co/Al_2O_3$ catalyst reducibility, hydrogenation capability and activity, and that it has substantial effects on the product distribution leading toward lighter products as sulfur content increases. Other surface compounds can also have a significant impact on catalyst activity and selectivity as showed by co-feeding with COS and mercaptans. DFT simulations further support those experimental observations as they report large adsorption energies of sulfur on several sites of Co(111) [155] and Co(0001) surfaces [156,155].

Studies about the adsorption of sulfur on metal surfaces by McCarty and Wise [157–161] suggest that metal-sulfur bond strengths decrease in the following order Ni<Co<Ru<Fe, thus making Co vulnerable to sulfur. Since the content of sulfur in biomass and coal-derived syngas can be high, its purification based on sulfur compounds removal is mandatory. In this respect, the deactivation path is not considered in our work since it can be significantly reduced by the use of adsorbents[5].

### 2.6.2 Gas/vapor-induced chemical transformation

The vapor phase above the surface of a catalyst can lead towards chemically induced deactivation as it can induce changes that lead to **1)** inactive bulk and surface phases **2)** highly volatile compounds that leave the reactor **3)** catalytic solid/support and catalytic solid/promoter reactions and **4)** solid-state transformation of the catalytic phase itself during operation. The reactions of this type are not under the scope of this thesis. It suffices to say there are proofs that Fischer-Tropsch catalysts are susceptible to deactivation induced by vapor as it was shown for Fe, where the active carbidic phase is oxidized [162] and for $SiO_2$ supported Co, where breakdown of support and formation of inactive cobalt-silicates is observed [163] both at high conversions and therefore high partial pressure of water. Huber and al. [163] report results in agreement with those of Hilmen et al. [164,165] for Co/alumina, both showing loss of chemisorption surface area, the formation of a stable cobalt silicate or aluminate for high concentrations of steam leading to substantial loss of activity. It seems that this phenomenon is thermodynamically possible only for small cobalt crystallites, but it is nevertheless a slow process. Interestingly, Abi Aad et al. [166] provided an experimental confirmation of alumina degradation in hydrothermal conditions. Loss of activity due to the formation of volatile compounds and the solid-state transformation of the catalytic phase itself during operation seem not to be the essential deactivation pathways for Co-based Fischer-Tropsch catalysts.

### 2.6.3 Metal oxidation and sintering

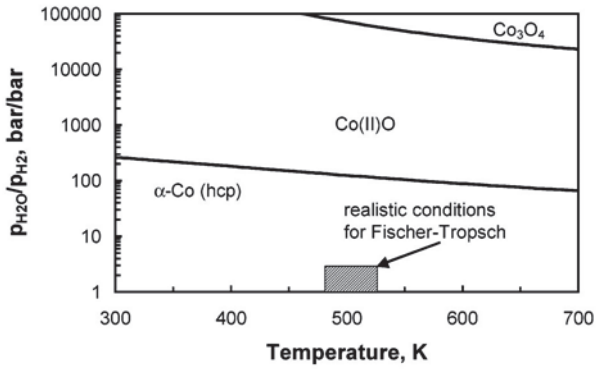


**Figure** 22. Stability diagram of bulk cobalt and different cobalt oxides over different temperatures and ratios of the partial pressure of water to hydrogen. The shaded area shows Fischer-Tropsch reaction conditions[100].

Oxidation of active sites of Co has been discussed extensively in the literature and is thought to be one of the main channels for deactivation [167,168,4,164,169,170] although there is no consensus in this matter. The risk for the oxidation of active sites is plausible due to water steam that happens to be one of the major products of Fischer-Tropsch synthesis reactions, acting as an oxidizing agent. Although there are several reviews[171–173] discussing the effect of steam water on Co-based FT catalysts, published reaction rate laws generally do not include a term quantifying the contribution of water species. Moreover, the impact of water on the activity is strongly influenced by catalyst composition, type of support, and catalyst synthesis method. Those are considered to be either negligible[174], beneficial[167], or detrimental[165,171]. In particular, operating at high CO conversion levels leads to high water vapor pressure and thus increases the risk of deactivation[175].

Nevertheless, thermodynamic calculations from van Steen and al.[100] showed that nano-sized Co crystallites of diameter above 4.4 nm are not expected to be susceptible to oxidation giving CoO. This has been confirmed by experimental results of Iglesia et al.[167] and Hilmen et al[165] who reported re-oxidation for diameter particles <5-6 nm, only. Those reports are also in agreement with some experimental results[165]. Therefore, there is evidence that at

FT conditions, bulk Co particles larger than 6 nm cannot oxidize[167,170,176]. Nevertheless, the risk of oxidizing Co nanoparticles is present in highly dispersed systems[4]. To oxidize bulk cobalt, a high excess of water compared to hydrogen partial pressure is needed, which is far from Fischer-Tropsch conditions and therefore, thermodynamically unfeasible (see **Figure** 22). In contrast, the stability to water of nano-sized Co crystallites is different from the stability for bulk metallic Co due to surface free energy differences. In addition to previous oxidation studies, recent thermodynamic calculations by Hou et al.[177] suggest that the surface of Co particles in contact with alumina can be oxidized by water where oxidation products are cobalt spinel- or aluminate-like products. Thus, there is a loss of active phase. Bukur et al. [175] presumed that Co metal was re-oxidized at high CO conversions due to high water partial pressures leading to deactivation. A summary of literature data on the effect of the water/hydrogen reactor ratio on directly measured oxidative properties of Co is reported by van de Loosdrecht et al. [172] and presented in **Figure** 23.

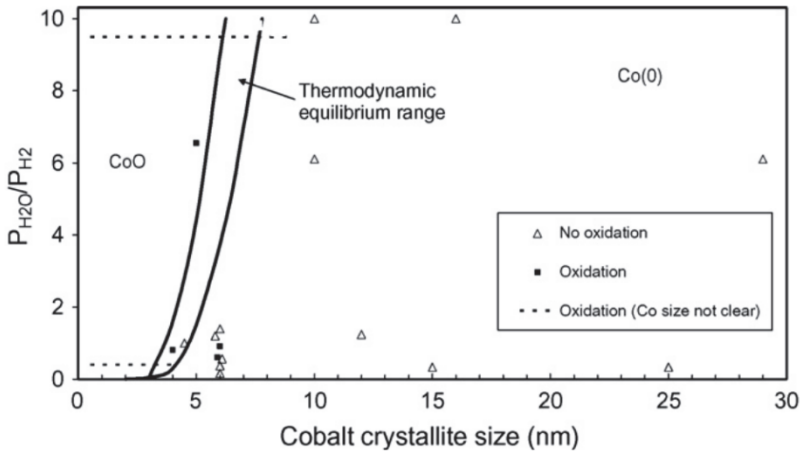


**Figure** 23. Summary of the effect of the water/hydrogen ration as a function of Co crystallite size on the oxidation properties of Co as given by van de Loosdrecht [172,178].

Although according to van Steen, [100] it is impossible to oxidize bulk Co particles, surface oxidation of Co-nanoparticles is probably possible and appears to be indirectly related to catalyst deactivation. Khodakov et al.[179–181] developed a mechanistic model and suggested that in the presence of water, sintering is enhanced. According to this study, sintering could

occur in three steps: diffusion, collision, and agglomeration, as shown in **Figure** 24. As suggested by Khodakov et al. [179–181], in the presence of water, sintering is facilitated since on the one hand, it reduces the particle surface energy and, on the other hand, Co nanoparticles diffusion rates are increased by surface oxidation. Those suggestions agree with previous experimental work[182,183] concerning sintering rates in the presence of water and also with findings that the surface energy of oxide nanoparticles is lower compared to metallic species[172]. This fact also suggests surface oxidation as the first step of Co sintering:

$$Co_s + H_2O \leftrightarrow Co_sO + H_2$$

In other words, the surface coverage of $Co_sO$ depends on partial pressures of water and hydrogen: $\theta(Co_sO) \approx K_{Co_sO}\frac{p(H_2O)}{p(H_2)}$.

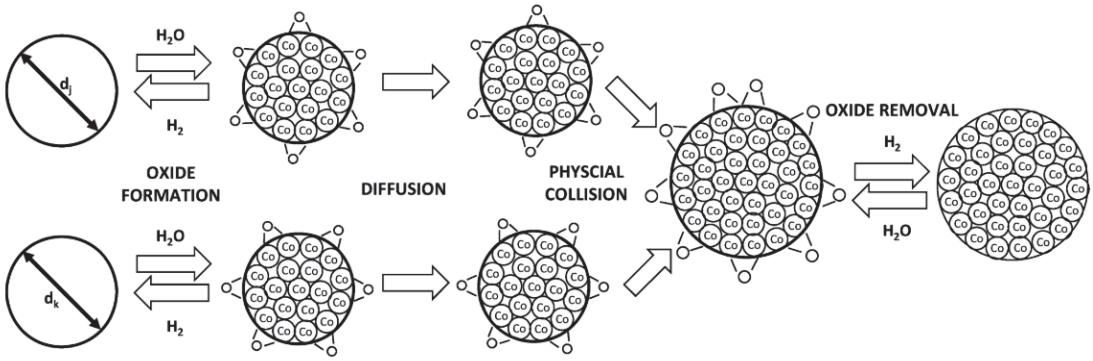


**Figure** 24. Sintering mechanism proposed by Khodakov et al. Once the particle surface is oxidized, the particle starts to grow, which lead to active site loss and catalyst deactivation. Reproduced from[179].

Simulations performed by Khodakov et al. suggest that sintering by water-assisted mechanism is the most important in the first several hours of time-of-stream and that its rate is strongly influenced by the $\frac{p(H_2O)}{p(H_2)}$ ratio inside the reactor. After crystallite growth stabilizes, sintering is no longer the most dominant effect and other deactivation mechanisms can be more important (such as deposition of carbon species). Severe deactivation effects were observed for very high water partial pressures i.e. $\frac{p(H_2O)}{p(H_2)} \approx 3$ .

Previously reported[184,185] experimental studies of water/Co systems provide limited information on the water adsorption and reaction behavior and in particular under FT reaction conditions. As a consequence of technological advances, some new experimental[186], and theoretical[187–189] works emerged towards a fundamental understanding of $H_2O$ interaction with Co and the microscopic role of water in the mechanism of Co surface-catalyzed reactions. In those works, the interaction of water with Co is found to be structure- and morphology-sensitive. Ma et al.[187,188] studied extensively using DFT the adsorption and decomposition of water monomers and dimers on various clean, O and OH pre-covered Co surfaces. They showed that water binds only weakly with clean Co surface and that it can be easily desorbed from it. In contrast, their study reveals the thermodynamically favorable dissociation of water monomers on oxygen pre-covered surfaces resulting in the formation of OH fragments. Therefore, this study shows that oxygen can be deposed on the surface in the form of OH fragments. Thus, those recent DFT studies reveal a mechanistic path in which oxygen accumulation on the surface may be achieved.

Severe deactivation effects were observed for very high water partial pressures. Scanning transmission electron microscopy (STEM) results published by Lancelot et al.[190] show that surface oxidation of Co particles occurs at FT relevant conditions. They report that the surface oxidation phenomenon in the presence of high partial pressure of water produced by FT reaction and low partial pressure of hydrogen characteristic for high CO conversions. STEM electron energy loss spectroscopy (EELS) results also reveal that Co particle core remains metallic in nature and therefore completely unaffected by oxidation, notwithstanding the surface of Co particle that is oxidized. This observation is consistent with a recent DFT study on the effect of oxygen adsorption on cobalt surface, which revealed the substantial reconstruction of the oxidized cobalt surface at oxygen surface concentration beyond 5/4 ML[191] .

The general trends concerning the effects of water on the selectivity are the following: higher $C_{5+}$ selectivity, lower methane selectivity, increased chain growth and sometimes and a slight increase in $CO_2$ selectivity generally independent on the choice of support and promoter. The effect of water on $C_2$-$C_4$ selectivity depends somewhat on the type of support and promoters but is absent for $Al_2O_3$ supported catalysts [192].

Therefore, there is no consensus about the effect of water on the catalyst activity and product selectivity, mostly due to the use of different types of catalyst used for studies in the literature. Although it is clear that high partial pressures of water can, in principle, lead to oxidation, it does not seem to be the main deactivation pathway under FT reaction conditions. Moreover, the influence of support or promoters in the oxidation phenomenon is not fully understood. Besides, water-induced sintering appears to take part in the overall deactivation process at the same time as oxidation, thus making a clear distinct analysis of both phenomena difficult. Hence, there is a need for a quantitative explanation for those phenomena and a mechanistic picture of the chemical transformations that take place.

### 2.6.4 Carbon deposition

Although deposition of carbon on the catalyst surface is a thermodynamically favored process, an excess of these species is considered to affect the catalyst lifetime negatively as they adsorb strongly and block reactants on the surface, encapsulate catalyst particles and consequently deactivate it or restrict access of reactants to metal active sites by plugging catalyst pores. Different deleterious carbon species are reported to be formed during realistic FT processes such as bulk or surface metal carbides formation and the deposition of amorphous carbon and graphite-like surface species[45]. Even though Fischer-Tropsch is somewhat regarded as a coke insensitive reaction due to the rich hydrogen environment, there are many indications that the above carbon species are indeed responsible for catalyst

deactivation (see Saib et al. for a review [155,193]). Possible carbon deposition pathways for Co-based FT catalyst are reported by Bartholomew [44] and are presented in **Figure** 25.

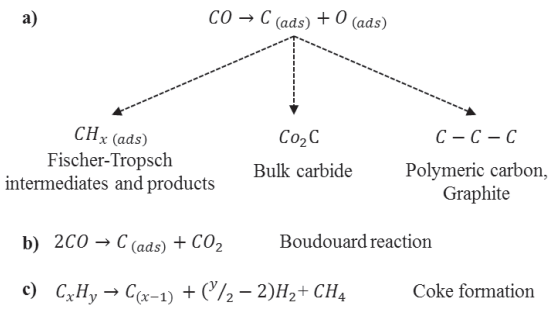


**Figure** 25. Some carbon deposition pathways for Co-based FT catalyst [44].

The most common techniques employed to study the deposition of different carbon species on the surface are temperature-programmed experiments. [194,195] The principle of those techniques is treating deactivated catalysts with hydrogen at elevated temperatures and tracing the evolution of methane at different temperatures. However, more sophisticated experimental methods such as Auger electron spectroscopy (AES), TOF-SIMS, XPS, and XRD have also been used.[196–199] Due to the air-sensitivity of Co catalysts and the wide range of carbon products present on the surface, experimental identification of the nature of deleterious carbon species and their potential precursors has proven to be very challenging.

Thermodynamic calculations show that bulk Co carbide formation is unfavorable at FT relevant conditions[200], yet some authors report its presence using different techniques, mostly XRD, XPS, XANES, and EXAFS[182,201,202]. Ducreux et al.[203] showed that bulk cobalt carbide can be decomposed, reporting also the formation of the hcp Co phase when treated with hydrogen. Deactivation due to bulk $Co_2C$ formation was also proposed due to the decline of activity and reported $Co_2C$ XRD peaks on alumina-supported catalysts. Another link between deactivation of Co-based FT catalyst and bulk carbide formation was proposed by Karaca et al. who reported low and high-intensity XRD peaks of $Co_2C$ after extended exposure to syngas and pure CO, respectively[182]. High-molecular-weight hydrocarbons,

although highly desired products in FT synthesis, can accumulate and block catalyst pores that furthermore limit the accessibility of catalytically active sites. Those polymeric amorphous carbon species are produced during both main and side reactions of the FT reaction mechanism and may accumulate on the surface, delaying the rate of diffusion of the reactants[162]. Moreover, carbon atoms may bind and form coke or graphite-like structures that cover the catalyst surface and act as poison[45]. It is generally agreed that those two species are directly linked with the phenomena of deactivation[44] although the exact mechanism for their formation is still unknown.

Lee et al. [194] suggested two sorts of carbon species, atomic and polymeric carbon, by using a combination of temperature-programmed reduction and AES techniques when studying the disproportionation of CO on $Co/Al_2O_3$ samples at different temperatures. Higher temperatures were positively correlated with the amount of total carbon content on the catalyst surface and activity loss but negatively correlated with the amount of atomic carbon on the surface. Consequently, they have suggested that polymeric and graphitic carbon deactivate the catalyst by the pore diffusion-inhibiting effect of those carbon species.

Moodley et al. [195] identified at least three main sorts of carbon species on dewaxed Pt promoted $Co/Al_2O_3$ catalysts with temperature-programmed hydrogenation and oxidation techniques (see **Figure** 26). Different peaks were attributed to different species found on the catalyst surface. The third peak was attributed to high molecular weight carbon species, of polymeric nature and amorphous structure. The nature of proposed carbon species was confirmed by electron microscopy (HR-TEM) and carbon mapping **E**nergy-**F**iltered **T**ransmission **E**lectron **M**icroscopy (EF-TEM). According to those results, carbon species can be found both on cobalt and on the alumina support, the latter being reached by migration from cobalt sites. Finally, it has been suggested that the long-term deactivation process is a

consequence of polymeric carbon accumulation and contemplated that its removal may result in a significant increase of FT activity.

Peña et al. [196] identified and characterized, using different techniques, carbonaceous species that are formed on the surface of used $Co/Al_2O_3$ catalysts under different operating conditions (syngas composition, GHSV) and questioned their role in catalyst deactivation. They showed, using TPH experiments, that three types of carbonaceous species exist: residual waxes, strongly adsorbed hydrocarbon fragments, and amorphous (polymeric) carbon. Peña et al. did not detect graphene/graphite-like structures nor cobalt carbide even for high $CO/H_2$ ratios.

Due to the numerous carbon products present on the surface, the identification of their nature is very challenging. Many computational chemistry studies focus on the effect of C species produced by the FTS reactions[191,204–209]. Using DFT calculations, Swart et al.[208,209] found that, at low coverages up to 1 ML, carbon atoms are very mobile and that atomic carbon species build up on the surface in order to create both linear and branched hydrocarbons with the former being energetically more stable. The subsequent increase in carbon coverages leads to the formation of aromatic clusters and stable graphene structures. Structures for graphene on fcc Co(111) surface are given in **Figure** 27.

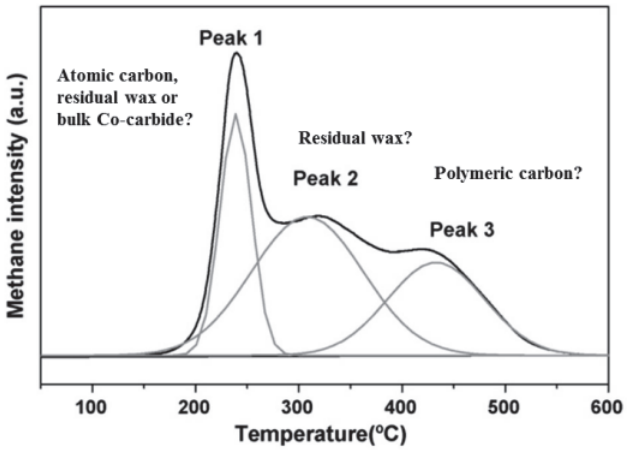


**Figure** 26. The TPH spectrum after deconvolution suggests three different carbon species present on the surface of Co-based FT catalyst [196].

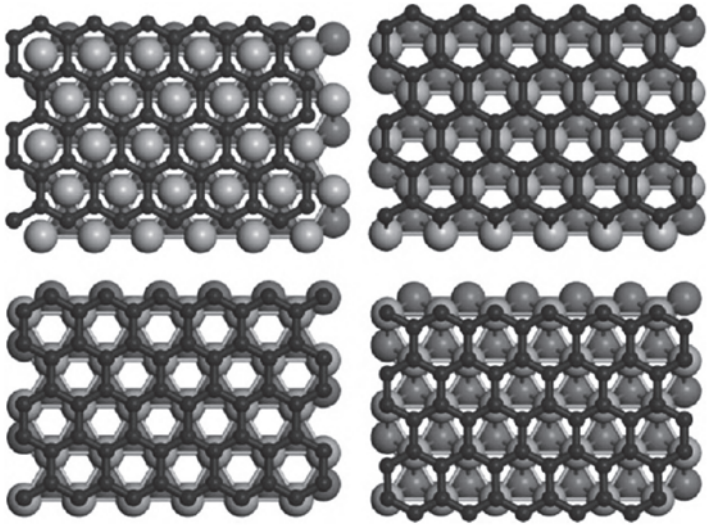

**Figure** 27. Graphene structures on the Co (111) surface obtained with DFT [208] .

Corral Valero and Raybaud[205] presented a thermochemical model that predicts the Gibbs free energy of formation of different Co surfaces with different carbon coverages and identified stability domains of carbon species on Co surfaces in FT reaction conditions. They showed that a graphene-covered Co(111) surfaces (with C coverage of 2 ML) are always the most stable in standard FT reaction conditions thus proposing this structure as a model representation of deactivated catalyst. Moreover, they found a reconstructed Co(111) surface

with 1 ML coverage of carbon and suggested a close relationship between the reconstructed surface and selectivity losses.

Many surface science studies try to unravel the impact of carbon on the activity of FT catalysts. In those studies, the catalyst surface is pre-treated with a carbon-containing molecule (carbon precursor) that is decomposed and transformed into polymeric and graphitic carbon. Finally, performances of such pre-treated catalysts are sometimes evaluated and discussed in terms of activity and selectivity towards different products during realistic FT conditions. The most common carbon precursors used for this procedure are CO molecule[194,199], that is directly transformed to atomic carbon through the Boudouard reaction ( $2CO \rightarrow C + CO_2$ ) described in **Section 2.1**, and ethylene[210,211] whose decomposition mechanism is still debated but it is agreed that its low decomposition temperature is favourable towards graphene formation. Regardless of the carbon precursors used, all such studies inferred a strong impact on the catalyst activity and selectivity towards long-chain hydrocarbons which reflects the strong deactivating potential of carbon species in agreement with previous DFT studies presented in this section. However, those studies do not explain how such deleterious carbon species can be formed in the realistic FT environment.

In contrast to the formation of deleterious carbon species through CO decomposition, ethylene decomposition seems more plausible due to experimental observations we discussed above: 1) Cobalt-based catalysts are considered selective for olefinic products $C_2H_4$ included (**Section 2.2**) 2) olefins are prone to re-adsorb (**Section 2.3.8**) 3) ethylene selectivity shows deviations from the ideal-polymerization case as predicted by the ASF distribution and discussed in **Section 2.2** suggesting the amplified reactivity of this molecule under a realistic FT environment. In **Chapter 5**, devoted to the search of a "deactivation initiator", we revisit some of these observations search of "deactivation initiator".

Weststrate et al.[198,211,212], studied in a combined experimental and DFT approach the decomposition of ethylene on the Co surface. They reported two distinct ethene transformation steps with gradual heating of ethene-covered Co(0001) surface, around 180 and 400 K. They concluded that at the former temperature, ethylene dehydrogenates to acetylene whereas at the later dehydrogenation of acetylene occurs yielding atomic carbon. The last conclusion was made based on the similarity of the C 1s core-level spectrum with previously reported Ni(111) surface [213]. Thus, the argumentation is that ethylene decomposition leads to atomic C species in the realistic FT conditions that may act as monomer specie for deleterious carbon species such as polymeric C and graphene species. According to them, the C/C coupling reaction of those species may be considered as a possible deactivation mechanism. Besides, authors of that work showed that the chemistry of ethylene decomposition is highly coverage-dependent.

In contrast to catalyst treated with ethylene only, the gradual heating of co-adsorbed ethylene and hydrogen led to the formation of ethylidene species which resulted in authors support for alkylidyne mechanism for chain growth[212] also supported for Ni(111) surface[214] . However, in that work, the authors did not evaluate the performances of such differently prepared catalysts. Besides, they did not suggest a possible explanation towards deactivation that includes this ethylidene species. In contrast to studies of Weststrate et al.[198,211], Ramsvik et al.[215] and Vaari et al. [216] performed acetylene decomposition experimental study that showed acetylene transformation at around 450 K to predominantly polymeric carbon species. As suggested by Weststrate et al.[198,211], those differences can be explained in terms of acetylene surface coverage-dependent reaction mechanism: for low surface coverage, decomposition of acetylene leads to atomic carbon species whereas for high surface coverages acetylene transforms to polymeric carbon species. Those observations are also in line with the experimental results of Xu et al. [142,217]. In contrast, joint experimental and theoretical studies

of Wang et al. on Rh(111) surface [218] suggest ethylene decomposition yielding ethylidyne specie that can engage in surface assisted $C_2+C_2+C_2$ trimerization reactions through $C_4$ intermediate when heated to around 470 K. Interestingly, Xu et al. [217] identified using an X-ray Photoelectron Spectroscopy (XPS) different types of carbon species formed on Co(0001) surface upon heating the decomposition of ethylene pre-covered surface. According to their results, ethylene pre-covered surface heated above 500K transforms into surface $C_2$ cluster, and graphitic carbon resulted from dehydrogenation and the cyclopolymerization/ dehydrogenation reactions, whereas a direct decomposition at 500K leads to the formation of surface atomic carbon.

An interesting DFT study of ethylene decomposition over on flat and stepped Co(0001) was performed recently[219] aiming to understand the initial steps to graphene formation. They concluded that CHCH and CHC species might be regarded as the key precursors of low-temperature graphene formation through cyclotrimerization and dehydrogenation reactions. Besides, as we discussed above, ethylene can be readily decomposed to acetylene, and the latter can undergo those cyclotrimerization reactions on some metallic surfaces[220,221]. A similar approach will be used in this work to model the growth of deleterious carbon species from readsorbed ethylene.

### 2.6.5 Carbon induced surface reconstruction

According to reports in the literature, reconstruction phenomena in Co-based FT catalysts is a thermodynamically driven phenomenon, alters catalyst behavior by changing the nature of active sites and therefore induces activity and selectivity variations[205,222,223,193]. Reconstructed surfaces can, in principle, lead to sites that are more sensitive concerning chemical transformations that lead to deactivation phenomena. Those changes can have consequences on the adsorption of different species that can normally be found on the surface during FTS reactions such as CO, O, N, S, some carbon intermediates, and even FT

products[224]. As it is a dynamic process, observation of surface reconstruction is technologically challenging to achieve and therefore, either model compounds, or computational approaches are required.

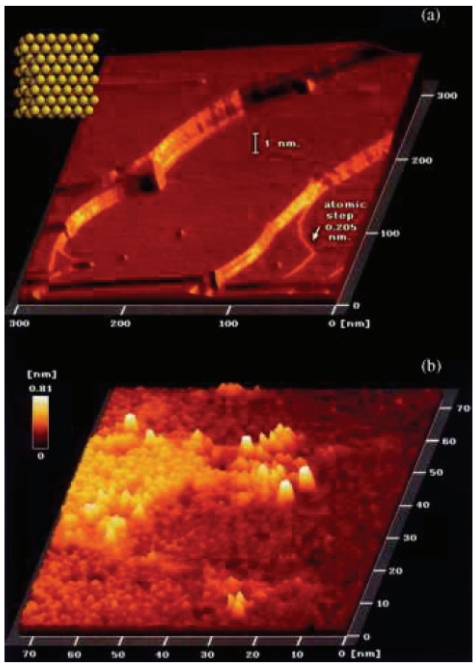


**Figure** 28. Reconstruction of flat Co surface to islands observed with STM microscopy[225].

For the CO hydrogenation reaction, Sautet and Cinquini showed that subsurface carbon is stable in the case of cobalt[226]. Ciobîcă et al. [223] reported quantum chemistry results on fcc cobalt surfaces with surface coverages of 50% atomic carbon and a reconstruction similar to that observed for Ni(111). Reconstruction stabilizes adsorption of carbon by approximately 15 kJ/mol compared to non-reconstructed surfaces with a very low activation barrier (around 1 kJ/mol). Furthermore, by reconstructing itself, the surface induces a diminution in Co-C distances and an increase in the coordination number of Co atoms. Among many species suspected to cause surface reconstruction, only atomic carbon is found to be capable of doing so, which indicates that CO dissociation is required. According to work by Ciobîcă et al.[87,223], reconstruction phenomenon of Co surface is a thermodynamically driven phenomenon which alters catalyst behavior by changing the nature of active sites and may, therefore, induce activity and selectivity variations[45,155,205,223]. This is in line with

experimental results of Wilson and De Groot[225] who detected the reconstruction of flat Co(0001) surface to triangular Co islands at FT relevant conditions using in situ STM (see **Figure** 28). Besides, reconstruction phenomena for a similar model catalyst have also been confirmed by Beitel et al. [227,228] with infrared spectroscopy (PM-PAIRS). Moreover, Banerjee et al.[229] reported DFT results showing that massive surface reconstruction occurs under FT reaction conditions along with nano-island formation. They also explained the crucial role of aromatic square-planar $Co_4C$ motif in the activity, structure, and coverage of Co-based FT catalysts.

Although arguments on the damaging influence of carbon built-up find support in many experimental and theoretical works, there is little knowledge on the possible precursor(s) that lead to deleterious carbon species on the catalyst surface.

## 2.7 Thesis strategy

As we showed above, there is a lack of agreement within the scientific community about the reaction mechanisms and the preferential deactivation pathways for FT catalysts. This is commonly due to the difficulty to perform an experimental analysis to air-sensitive Co catalysts under realistic conditions. Additionally, ex-situ and surface science techniques are limited by the inaccessibility of the surface, which is covered with waxy FT products that need to be removed by a procedure that endangers the conservation of a realistic surface state of the catalyst. Clearly, an approach that lacks the above obstacles needs to be envisaged. In our view, first-principles calculations and in particular Density Functional Theory methods, represent a powerful tool in situations where experiments are difficult or impossible to be performed, when their results are inconclusive or when confirmation of those results is needed. As we pointed out above, many scientists recognized the necessity of using those methods from the reasons described above to unravel the reaction mechanisms and the deactivation phenomena of the FT catalysts.

Although DFT methods cannot provide an answer to every question, this methodology is capable of providing information about what is possible or not from a fundamental point of view and shed light to some issues such as the structure of carbon on the experimentally inaccessible surface, and the influence of water on the surface of Co catalysts. Despite numerous theoretical studies in the field, there is still need to quantify the stability domains of surface intermediates of the FT reaction and enlighten the structure of carbon species in the presence of hydrogen and oxygen over Co at FT reaction conditions. In this thesis, we thus propose a systematic study of the evolution of Co surface states, calculated with DFT based models, to extend our understanding of the deactivation by C and/or O and to identify the particular surface states that can lead to the deactivation of the catalyst. Although numerous experimental and DFT studies related to deactivation phenomena are reported in the literature, as we have shown in **Section 2.6**, to the best of our knowledge, they have not been applied in a micro-kinetic model to describe the deactivation process. In other words, the scientific literature lacks information on how the proposed experimental and theoretical deactivation intermediates are produced and transformed into deleterious species. As we will show in **Chapter 6,** this type of information is essential for constructing the deactivation mechanism and can only be accessed using ab-initio methods. However, thermodynamics alone cannot describe the kinetics of those transformations and their effects on the catalyst performance. In addition to the identification of deactivation intermediates based on their stability, no studies have reported the impact of the proposed intermediates on the performance of Co-based FT catalysts. Thus, the micro-kinetic modeling approach proposed by Tronconi et al. will be used to access this information and to study the implications of those surface state intermediates on the catalyst deactivation.

Our approach is hence, to supply the micro-kinetic model with elementary steps essential to describe the deactivation phenomena based on DFT results. We will use DFT to

test some of the hypothesis evoked in the literature, and specifically those that implicate deposition of carbon and oxygen, because of their potential effects in the long-term deactivation process (see **Figure** 21). Finally, we will aim at using the micro-kinetic model describing deactivation to find the conditions where those phenomena are minimized. Before proceeding to a discussion of our results in **Chapters** 4, 5 and 6, we will first explain some basic principles of computational chemistry calculations with an emphasis on DFT.

# 3 Methodology

## 3.1 Quantum chemistry calculations

In this chapter, the basis of quantum chemical calculations performed in this thesis is described. The underlying theory behind those calculations is described in details elsewhere.[230–232]

### 3.1.1 The Schrödinger equation

The Schrödinger equation is the fundamental dynamic equation of quantum mechanics that gives a complete description of the evolution of the given quantum system in time. That is to say, all the information regarding that given quantum system can be obtained if the equation is resolved. Both corpuscular and wave nature of the electron are deeply embedded into this equation linking the wave function $\Psi_{tot}(t)$ and the total energy of the system $E_{tot}$.

The time-dependent Schrödinger equation has a mathematical form similar to the diffusion differential equation and can be expressed as:

$$\widehat{H}\Psi_{tot}(\mathrm{t}) = i\hbar\frac{\partial\Psi_{tot}(\mathrm{t})}{\partial t}, \qquad \textbf{Eq. } 5$$

where $\widehat{H}$ is the Hamilton operator that contains all the energetic contributions in the system being described. The *time-dependent* wave function $\Psi_{tot}(\overrightarrow{R},\vec{r},\sigma_e,t)$ is a function of nuclear $\vec{R}$ and electron positions $\vec{r}$, electron spin $\sigma_e$ and time $t$. In atomic units and in the absence of external fields, an arbitrary system composed of $M$ atomic nuclei with a charge $Z$ and $N$ electrons has a Hamiltonian operator of the following form:

$$\widehat{H} = \hat{T} + \hat{V} \qquad \textbf{Eq. } 6$$

where

$$\hat{T} = -\frac{1}{2}\sum_{i=1}^{N}\nabla_i^2 - \frac{1}{2}\sum_{A=1}^{M}\frac{\nabla_A^2}{M_A} \qquad \textbf{Eq. } 7$$

is the operator of the kinetic energy of electrons and nuclei and $\hat{V}$ is the operator of potential energy, which can be decomposed in terms of nuclei-electrons, electron-electron, and nucleui-nuclei interactions and is given, respectively, by:

$$\hat{V} = -\sum_{i=1}^{N}\sum_{A=1}^{M}\frac{Z_A}{|r_i - R_A|} + \sum_{i=1}^{N}\sum_{j>I}^{N}\frac{1}{|r_i - r_j|} + \sum_{A=1}^{M}\sum_{B>A}^{M}\frac{Z_A Z_B}{|R_A - R_B|} = \hat{V}_{n,e} + \hat{V}_{e,e} + \hat{V}_{n,n}. \quad \textbf{Eq.}\ 8$$

Since the above Hamiltonian operator contains no explicit time dependency (not always the case), we can write the overall *time-dependent* wave function $\Psi(\mathrm{t})$ (in **Eq.** 5) as:

$$\Psi_{tot}(\mathrm{t}) = \psi_{tot} e^{-i\frac{E_{tot}t}{\hbar}}. \quad \textbf{Eq.}\ 9$$

In the above equation, $\psi_{tot}$ is the *time-independent* part of the overall *time-dependent* wave function $\Psi_{tot}(\mathrm{t})$ and once introduced in the Schrödinger equation becomes an eigenvalue equation whose solutions lead to eigenvectors (stationary states) for every energy eigenvalue. The Hamiltonian operates on the eigenfunction $\psi_{tot}$, giving a constant (the eigenvalue $E_{tot}$) times the same function $\psi_{tot}$. Hence, the Schrödinger equation can be expressed as:

$$\hat{H}\psi_{tot} = E_{tot}\psi_{tot}. \quad \textbf{Eq.}\ 10$$

#### *3.1.1.1 Born–Oppenheimer approximation*

The exact solution of the Schrödinger equation of a system of nuclei and electrons is generally unknown due to the mathematical complexity of the term $\hat{V}$ in **Eq.** 8, and approximate solutions are needed. One first step towards an approximate solution is described by the Born–Oppenheimer approximation. The Born–Oppenheimer approximation assumes the instantaneous adaptation of electrons on every nuclear movement due to the significantly higher mass of the nucleus with respect to electrons. As a result, in the simplified physical picture, electrons move in the potential of nuclei at rest. This approximation allows separating the motion of atomic nuclei and electrons. Mathematically, the second term in **Eq.** 7

disappears (zero kinetic energy of nuclei) and the third term in **Eq.** 8 becomes constant (nuclei-nuclei potential is constant as they do not move). This simplification leads to the so-called the *electronic* Hamiltonian and consequently, the *electronic* Schrödinger equation. **Eq.** 6 and **Eq.** 10 thus become:

$$\hat{H}_e = \hat{T} + \hat{V}_{ne} + \hat{V}_{ee} = -\frac{1}{2}\sum_{i=1}^{N}\nabla_i^2 - \sum_{i=1}^{N}\sum_{A=1}^{M}\frac{Z_A}{|r_i - R_A|} + \sum_{i=1}^{N}\sum_{j>i}^{N}\frac{1}{|r_i - r_j|} \qquad \textbf{Eq.}\ 11$$

$$\hat{H}_e\psi_e(r_i, R_A) = E_e(R_A)\psi_e(r_i, R_A). \qquad \textbf{Eq.}\ 12$$

The electronic wave function $\psi_e(r_i, R_A)$ depends only *parametrically* on the space configuration of electron and nuclei $(r_i, R_A)$. By varying positions $R_A$ in small steps and repeatedly solving the electronic Schrödinger equation (**Eq.** 12), one obtains $E_e$ (electronic energy) as a function of $R_A$. $E_e = f(R_A)$ definies the potential energy surface, PES (see **Section** 3.1.4). The form of **Eq.** 12 suggests that $\psi_e$ is the eigenfunction of electronic Hamiltonian $\hat{H}_e$. In case of one-electron, n-electron atoms and n-electron molecules, wave functions $\psi_e$ are called an orbital, an atomic and molecular orbital, respectively.

When the electronic Schrödinger equation is solved, nuclear motion is considered by reintroducing the (previously neglected) constant term $\hat{V}_{n,n}$ and then, the Schrödinger equation for nuclear motion is solved:

$$\left[\hat{V}_{n,n}(R_A) + E_e(R_A)\right]\psi_n(R_A) = E_{tot}\psi_n(R_A) \qquad \textbf{Eq.}\ 13$$

In the above equation $\psi_n(R_A)$ is the nuclear wave function that depends on the space configuration of nuclei. The overall energy of a system is thus given by the sum of $E_e(R_A)$ (the sum of kinetic, electron-nuclei, electron-electron energies) and potential energy of nuclei-nuclei repulsion, $\hat{V}_{n,n}(R_A)$, which is a constant. The overall wave function of the system is given by the product $\psi_{tot} = \psi_n(R_A)\psi_e(r_i, R_A)$. The state of a system with the lowest energy is called the ground state.

Note that if we knew the electronic wave function $\psi_e$ in **Eq.** 12 exactly, we could calculate the energy $E_e$ too. However, the form of $\psi_e$ is generally unknown and one has to choose how to represent it. The most common way of representing the molecular wave functions is to express them as a linear combination of one-electron atomic wave functions $\varphi_i$:

$$\psi = \sum_{i}^{N} c_i \varphi_i \qquad \textbf{Eq.}\ 14$$

where the set of N functions $\varphi_i$ is a so-called basis set and is associated with some coefficient $c_i$. Constructing the molecular orbital (MO) as in **Eq.** 14 is known as the linear combination of atomic orbitals (LCAO) method. Depending on the system of interest there are many choices for the exact mathematical form of orbitals $\varphi_i$ used to expand molecular ones such as Slater-type, Gaussian-type, plane waves ... A full review of those functions is out of the scope of this work. In **Section** 3.1.3 we will briefly explain the choice for plane wave functions commonly used to describe the periodic systems such as solids that are of interest in our work.

Once the MO are developed in the chosen basis as in **Eq.** 14, there is a need to assess and improve the quality of MO and the associated energy (**Eq.** 12). This is achieved using **the variation theory** that states that, for any trial function MO in **Eq.** 14, the eigenvalue of that trial wavefunction is always an upper bound to the true energy of the system $E_{trial} \geq E_{exact}$. The equality between the trial eigenvalue $E_{trial}$, obtained by solving **Eq.** 12 for $\psi_{trial}$, and $E_{exact}$ holds if and only if $\psi_{trial} = \psi_{exact}$.

Note that the electronic Hamilton operator in **Eq.** 11 depends only on spatial coordinates. However, the description of an electron is only complete if a spin coordinate is included. This quantity can have only two possible values +1/2 or -1/2. The introduction of a spin coordinate thus leads us to a definition of a spin-orbital $\phi(\vec{x})$ ($\vec{x} = \{\vec{r}, \sigma\}$) that takes into consideration both spatial $\vec{r}$ and spin $\sigma$ coordinates of an electron in atoms, molecules...

### *3.1.1.2 The Hartree–Fock (HF) approximation*

Although the Born–Oppenheimer approximation simplifies the Schrödinger equation, the latter is still very complicated, mostly due to the unknown electron-electron interaction term $\hat{V}_{e,e}$ in equation **Eq.** 8. This equation has to be resolved by iterative methods since, in order to find the eigenvalues in equation **Eq.** 12 ($\psi_e$), knowledge of $\hat{V}_{e,e}$ is required and the computation of this term is itself based on the eigenfunctions $\psi_e$. There are many different approaches employed towards the approximate solution of the Schrödinger equation.

In Hartree's method, the actual pair interaction of electrons is substituted with the approximated interaction of every individual electron with the averaged potential of the other electrons. In that manner, the *many-electron* wave function can be replaced with a product of orthonormal *one-electron* molecular orbitals. This implies that electrons move independently in the averaged field of the other electrons in the system. Hartree's wave function for the N-electronic system is a simple product of contributions from individual electrons:

$$\psi(\overrightarrow{r_1}, \overrightarrow{r_2}, \dots \overrightarrow{r_N}) = \chi_1(\overrightarrow{r_1})\chi_2(\overrightarrow{r_2}) \dots \chi_N(\overrightarrow{r_N}), \qquad \textbf{Eq. } 15$$

where $\chi_i(\overrightarrow{r_i})$ are the one-electron functions.

Although mathematically convenient, wave functions defined as above are physically incomplete since they do not include spin. The wavefunction given by **Eq.** 15, is not properly antisymmetric and thus doesn't conform Pauli's Exclusion Principle. Fock showed that Hartree's wave function can be modified to be asymmetric with respect to electron exchange and therefore follow Pauli's Exclusion Principle, by adding and subtracting permutations of Hartree's product. Slater later showed that the resulting mathematically and physically convenient Hartree-Fock's wave function can be expressed as a determinant:

$$\psi = \frac{1}{\sqrt{N!}} \begin{vmatrix} \phi_1(\overrightarrow{x_1}) & \dots & \phi_N(\overrightarrow{x_1}) \\ \vdots & \ddots & \vdots \\ \phi_1(\overrightarrow{x_N}) & \cdots & \phi_N(\overrightarrow{x_N}) \end{vmatrix} \qquad \textbf{Eq.}\ 16$$

Where $\phi_i(\overrightarrow{x_i})$ are the one-electron *spin-orbitals*, that is, a function of electron coordinate $\vec{r}$ and electron spin $\sigma$. Substitution of Hartree-Fock's (HF) wave function into the electronic Schrödinger **Eq.** 12 yields a system of n one-electron generalized Hartree-Fock equations:

$$\hat{F}(1)\phi_k(1) = \varepsilon_k\phi_k(1) \qquad \textbf{Eq.}\ 17$$

where $\hat{F}$ is the *one-electron* Fock operator defined as:

$$\hat{F}(1) = \hat{h}\,(1) + \hat{J}\,(1) - \hat{K}(1)\,. \qquad \textbf{Eq.}\ 18$$

In **Eq.** 18, $\hat{h}$ is a one electron core Hamiltonian, and $\hat{J}$ and $\hat{K}$ are terms that describe classical electron-electron repulsion interactions and the exchange term, respectively and $\varepsilon_k$ is the spin-orbital energy. The resulting Hartree-Fock system given by **Eq.** 17 is solved iteratively according to the variational principle i.e. parameters of a trial wavefunction ($\{c_i\}$ in **Eq.** 14) are adjusted until the energy of a corresponding wavefunction is minimized.

The HF method was the first numerical method developed to solve the Schrödinger equation and is the cornerstone of other theories developed after this first attempt to apply quantum theory to poly-electronic systems. Since HF theory considers that electrons interact with the mean-field caused by other electrons, this approach fails in taking into account the so-called correlation effects. That is, the dynamical perturbation of electrons due to the presence of other electrons. The neglect of those effects can lead to wrong qualitative and quantitative results.

HF method is not reliable when there is significant charge redistribution as it is a case when bond breaking/creation or where electron excitation take place. There are other quantum chemistry methods, called post-HF methods, based on approximation of the wave function as

a linear combination of Slater determinants (see **Eq.** 15) that include "virtual" (non-occupied) electron states to retrieve the correlation energy. However, solving the Schrödinger equation using those methods can be computationally expensive even for the smallest systems. Rather than approximating the electronic wave function as in **Eq.** 14, an alternative approach is to approximate the Hamiltonian in **Eq.** 6, which is the basis of **D**ensity **F**unctional **T**heory (**DFT**) methods.

### 3.1.2 Density functional theory

Methods based on **D**ensity **F**unctional **T**heory [233] (**DFT**) are successfully employed when dealing with many-electron systems, including solids, which are the subject of this thesis. According to this theory, the properties of the system in the ground state can be determined entirely using quantities that are a functional of electron density, which is a scalar quantity. Since the energy is calculated as a function of a scalar quantity, the dimensionality of the calculations is significantly reduced in terms of computational time. DFT and related methods are prevailing in the domain of solid-state physics and material science are applied to the study of molecular structure, thermodynamics, reaction mechanisms, etc.

The foundations of Density Functional Theory were established in 1964 by Hohenberg and Kohn in the form of two theorems. The electronic Hamiltonian given by **Eq.** 11 is expressed as:

$$\hat{H} = -\frac{1}{2}\sum_{i=1}^{N}\nabla_i^2 - \sum_{i=1}^{N}V_{ext}(r_i) + \sum_{i=1}^{N}\sum_{j>i}^{N}\frac{1}{|r_i - r_j|} = \hat{T} + \hat{V}_{ne} + \hat{V}_{ee} \qquad \textbf{Eq.}\ 19$$

In **Eq.** 19, $\hat{T}$ is the kinetic energy, $\hat{V}_{ne}$ is the N-electron potential energy from the external field and $\hat{V}_{ee}$ is the electron repulsion energy. $V_{ext}(r_i)$ represents the expectation value of the operator $\hat{V}_{n,e}$ in **Eq.** 19 and is usually called the *external potential* (potential felt by the electrons due to the presence of the nuclei). Mathematically,

$$V_{ext}(\vec{r}\,) = -\sum_{A=1}^{M} \frac{Z_A}{|r_i - R_A|} \qquad \textbf{Eq. } 20$$

The main question in DFT is to find a way of calculating electron density $\rho(\vec{r})$ in the ground state, if the potential felt by the electron is known. First, the relation between $\rho(\vec{r})$ and $V_{ext}(\vec{r}\,)$ is provided by ***The first Hohenberg-Kohn theorem*** where the overall energy is rewritten in terms of $\rho(\vec{r})$. Then, a recipe to calculate the ground state of the system by using a variational principle is specified under the the scope of ***The second Hohenberg-Kohn theorem***.

***The first Hohenberg-Kohn theorem*** claims that the external potential $V_{ext}(r_i\,)$ is, to within a constant, an unique functional of $\rho(\vec{r})$ for the non-degenerate ground state. In other words, $\rho(\vec{r})$ uniquely determines the Hamiltonian operator and thus all the properties of the system since $V_{ext}(\vec{r}\,)$ fixes $\hat{H}$ in **Eq.** 18. Thus, the expectation value of an arbitrary observable $\hat{O}$ ($\hat{T}, \hat{V}_{ne}, \hat{V}_{ee}$ in **Eq.** 18) in the ground state of a system is an unique functional of charge density $\rho(\vec{r})$ and thus $\rho(\vec{r})$ determines all the properties of the system. Mathematically, in Dirac "bra-ket" notation:

$$\langle\psi|\hat{O}|\psi\rangle = O[\rho(\vec{r})]. \qquad \textbf{Eq. } 21$$

Since $\rho(\vec{r})$ determines uniquely all the properties of the ground state, the total energy of a system (see **Eq.** 18) can be also expressed explicitly in terms of the electron density as:

$$\begin{aligned} E[\rho] &= V_{ne}[\rho] + (T[\rho] + V_{ee}[\rho]) = V_{ne}[\rho] + F_{HK}[\rho] \\ &= \int V_{ext}(\vec{r}\,)\rho(\vec{r})d\vec{r} + F_{HK}[\rho] \end{aligned} \qquad \textbf{Eq. } 22$$

where $V_{ne}[\rho]$ is system dependent (nuclei coordinates and on nuclear charges) whereas $F_{HK}[\rho]$ is system independent quantity since it is not a function of external potential $V_{ext}$. Hence, $F_{HK}[\rho]$ is *universal* functional of $\rho$ and it could be used in principle to describe any atomic, molecular or solid-state system of interest. However, the explicit form of both $T[\rho]$

and $V_{ee}[\rho]$ that compose $F_{HK}[\rho]$ is unknown. The latter, in turn, can be further decomposed in terms of classical (Coulomb) electron repulsion $J[\rho]$ and a non-classical exchange functional $E_{xc}[\rho]$:

$$F_{HK}[\rho] = J[\rho] + E_{xc}[\rho] \qquad \textbf{Eq. } 23$$

$E_{xc}$ is known as exchange-correlation energy.

***The second Hohenberg-Kohn theorem*** introduces the variational principle and claims that for a chosen trial charge density, $\tilde{\rho}(\vec{r})$, such that $\tilde{\rho}(\vec{r}) \geq 0$ and $\int \tilde{\rho}(\vec{r})d\vec{r} = N$ the following expression holds:

$$E_0 \leq E[\tilde{\rho}(\vec{r})] \qquad \textbf{Eq. } 24$$

where $E_0$ is the ground state of the system and $E[\tilde{\rho}(\vec{r})]$ is the energy obtained from the functional of the *trial* density that defines its proper (trial) Hamiltonian. Therefore, the electronic energy calculated with the chosen trial density is equal or bigger than the real electronic energy we wish to calculate. Hence, the second Hohenberg-Kohn theorem proposes searching the energy of a system applying the variational principle over electron density.

#### *3.1.2.1 The Kohn-Sham equations*

In order to solve the Schrödinger equation and overcome issues of finding the universal functional $F_{HK}[\tilde{\rho}(\vec{r})]$, Kohn and Sham proposed decomposing it in three terms by mapping the problem of the system of *interacting electrons* (real system characterized by $\rho(\vec{r})$) onto a (fictitious system characterized by $\rho_0(\vec{r})$) system of *non-interacting electrons* that has exactly the same density as the former one and whose exact ground state is a simple single Slater determinant (described in **Eq.** 16). The final aim is dealing with much simpler terms where all the complex (unknown) behavior is contained in only one term that can be

approximated. If charge density $\rho_0(\vec{r})$ is written in terms of the spin orbitals of the non-interacting system (Kohn-Sham orbitals):

$$\rho_0(\vec{r}) = \sum_{i=1}^{N} \sum_{\sigma} |\phi_i(\vec{r}, \sigma)|^2 \qquad \textbf{Eq. } 25$$

then, the electronic energy of a real (electron-interacting) system can be expressed by the following equation:

$$E[\rho(\vec{r})] = \underbrace{-\frac{1}{2}\sum_{i=1}^{N} \int \phi_i(\vec{r})(\nabla^2)\phi_i(\vec{r})d\vec{r}}_{T_0} + \underbrace{\frac{1}{2}\sum_{i,j=1}^{N} \iint \frac{\rho(\vec{r}_1)\rho(\vec{r}_2)}{\vec{r}_{1,2}} d\vec{r}_1 d\vec{r}_2}_{J} - \underbrace{\sum_{i=1}^{N} \int \sum_{A=1}^{M} \frac{Z_A}{|\vec{r}_{A,i}|} d\vec{r}_1}_{V_{ext}} + E_{xc}[\rho(\vec{r})] \qquad \textbf{Eq. } 26$$

In **Eq.** 26**,** the different contributions represent the kinetic energy of electrons in the fictitious system ($T_0$), Coulombian classical repulsion ($J$), nucleus-electrons attraction ($V_{ext}$) and exchange-correlation energy that contains all the non-classical electronic interaction ($E_{xc}$). In the sense of the Kohn-Sham approach developed in the beginning of this section, the exchange-correlation term is given by[3]:

$$E_{xc} = (T - T_0) + \left(V_{e,e} - J\right) \qquad \textbf{Eq. } 27$$

where $T$ and $T_0$ are the kinetic energies of electron-interacting and fictitious non-interacting system respectively, $V_{e,e}$ and $J$ are the total energy related to both classical (Coulombian) and non-classical electron-electron repulsion, respectively. Minimizing the above expression for total energy by means of the variation principle yields a set of one-electron equations known as Kohn-Sham equations that have to be solved iteratively:

$$\left(-\frac{1}{2}\nabla^2 + V_{eff}(\vec{r}_1)\right)\phi_i^{KS} = \varepsilon_i \phi_i^{KS} \qquad \textbf{Eq. } 28$$

In **Eq.** 28, the effective potential is given by:

[3] The dependencies on $\rho(\vec{r})$ are omitted in equation but are presumed.

$$V_{eff}(\vec{r}_1) = \int \frac{\rho(\vec{r}_2)}{\vec{r}_{1,2}} d\vec{r}_2 + V_{xc}(\vec{r}_1) - \sum_{A=1}^{M} \frac{Z_A}{|\vec{r}_{1,A}|}. \quad \textbf{Eq.}\ 29$$

$V_{xc}(\vec{r}_1)$ is the potential due to the exchange correlation energy, $E_{xc}$, whose explicit form we don't know. Hence, $V_{xc}$ it is simply defined as:

$$\hat{V}_{xc} \equiv \frac{\delta E_{xc}[\rho]}{\delta \rho} \quad \textbf{Eq.}\ 30$$

This approach offers the possibility of obtaining better results than the HF method still using a single determinant wave function (and without any overwhelming multi-determinant post-HF methods). "One-electron" wave functions, $\phi_i^{KS}$, has no physical meaning and under no circumstances represent the physical state of the electron itself. It describes a "quasi-electron" whose total density in the system is equal to the total (realistic) electron density of the system in its ground state. Hence, DFT can provide very good results for energies and structures in ground state systems. However, it has some drawbacks when applied to excited states, the determination of band gaps and it fails to take into account dispersion forces.

#### *3.1.2.2 Exchange-correlation functionals*

Although exact in principle, the KS theory is approximate due to the unknown exchange-correlation energy functional form. It is widely accepted that the **L**ocal **D**ensity **A**pproximation (**LDA**) gives a good guess. It is mathematically expressed as:

$$E_{xc}^{LDA} = \int \rho(\vec{r}) \varepsilon_{xc}(\rho(\vec{r}))\, d\vec{r}, \quad \textbf{Eq.}\ 31$$

where $\varepsilon_{xc}$ is the known density of exchange-correlation energy of a homogeneous electron gas. The integral in the above equation reveals the nature of this approximation: the real system is divided in an infinite number of subsystems that have constant charge density. Every infinitesimal part of the volume contains a homogeneous electron gas that has the same

density as the original electron gas and that contributes to the total exchange-correlation energy. This approximation holds well for systems with almost constant electron density.

The next step in improving the description of exchange-correlation effects lies in including not only the local density in a given volume but also contributions from its neighborhood. This is achieved by adding density gradients $\nabla\rho(\vec{r})$ that leads to the **G**eneralized **G**radient **A**pproximation, (**GGA**):

$$E_{xc}^{GGA} = \int \rho(\vec{r})\varepsilon_{xc}(\rho(\vec{r}, \nabla\rho(\vec{r}))\, d\vec{r}. \qquad \textbf{Eq. } 32$$

Contrary to LDA, GGA functionals can be theoretical but also semi-empirical with constants adjusted to reproduce experimental data such as atomization energies. In this thesis, we use the non-empirical Perdew-Burke-Ernzerhof (PBE) functional good for solids[234].

### 3.1.3 Periodic calculations, Plane waves and Pseudopotentials

The theory described above is somewhat general and can be applied to molecular systems. In order to study solid-state systems, periodic boundary conditions need to be applied. This approach allows us to model realistic systems by replicating a unit-cell of atoms in three dimensions. Due to the long-range order characteristic of a crystal structure, the molecular orbitals are expressed as the product of a lattice periodic function $u(\vec{r})$ and a plane wave $e^{i\,\vec{k}\vec{r}}$:

$$\phi_{i,\vec{k}}(\vec{r}) = u(\vec{r})e^{i\,\vec{k}\vec{r}} \qquad \textbf{Eq. } 33$$

where $\vec{k}$ is the crystal wave vector and $\phi_{i,\vec{k}}$ are the so-called Bloch wave functions[235] and represent a point of the system in reciprocal space. Since both energy and Bloch wave functions depend on the wave vector, the calculation of electron density requires, in principle, an infinite number of k-points:

$$n(r) = \sum_{i=1}^{n} \int \left|\phi_{i,\vec{k}}(\vec{r})\right|^2 d\vec{k}. \qquad \textbf{Eq. } 34$$

However, since $\phi_{i,\vec{k}}(\vec{r})$ varies slowly with $k$, in practice, the integral is replaced with summation over a wisely chosen discrete set of k-points:

$$n(r) = \sum_{i=1}^{n} \sum_{k=1}^{Nk} \left|\phi_{i,\vec{k}}(\vec{r})\right|^2. \qquad \textbf{Eq. } 35$$

The k-point set can be reduced even further by some symmetry operations. In this thesis, the Monkhorst-Pack scheme [236] is used to minimize the k-points set in the irreducible Brillouin zone (that is, the primitive cell in reciprocal space). The denser the grid, the finer and more accurate will be the sampling, although the appropriate size can be established using a convergence test (see **Chapter 8.1**)[236]. In terms of k-integration, metals are particularly different from insulators and are known to provoke instabilities in the algorithm due to the non-smooth form of Bloch functions at the Fermi level.

Although there are physical differences in KS and HF theories, expressions given by **Eq.** 28 and **Eq.** 17 are of the same mathematical form and can be solved similarly: one electron wave functions are represented in an expansion of some basis functions $\{\chi_\mu(\vec{r})\}$:

$$\phi_p(\vec{r}, s) = \sum_{\mu} C_{\mu p} \chi_\mu(\vec{r}) \qquad \textbf{Eq. } 36$$

The coefficients $(C_{\mu p})$ in the **Eq.** 36 are determined according to the variational principle.

Expansion in a basis set $\{\chi_\mu(r)\}$ reduces the system of KS equations to a mathematically simple eigenvalue problem. The quality of the expansion of one-electron wave functions depends on the form and number of basis functions. Mathematically the simplest form for a basis set is a set of orthogonal plane waves, which is also advantageous

since the accuracy of calculations can be better controlled. However, due to the high kinetic energy of electrons in the vicinity of the nuclei, wave functions are rapidly oscillating functions and a considerable number of plane waves is required to capture its behavior in contrast to regions far from nuclei characterized by a slowly-oscillating potential. This recalls the introduction of pseudopotentials, also called effective core potentials (see **Figure** 29**)** approximation. Such functions mimic the exact behavior of wave functions far from nuclei and are constant or slowly varying functions near the nuclei. The electronic wave functions near the nuclei are thus substituted with "atom-like" functions (atomic solution of the Schrödinger equation). In other words, the core electrons are "frozen", being considered together with the nuclei as rigid non-polarizable ion cores. This idea is physically reasonable since core electrons (in the vicinity of the nucleus) and nuclei itself are only marginally influenced by external forces. The consequence is the elimination of core electrons from the calculation and only valence electrons are treated exactly, which reduces the dimensionality of the problem significantly. The calculation parameter that divides those two regions in the calculations is the cut-off radius (and related cut-off energy); generally, the greater the cut off radius the greater the number of planewaves and thus the better the description of the electronic system is. There are two main criteria to judge the quality of a pseudopotential, these are softness and transferability. The soft pseudopotential requires few plane waves to describe the system of interest whereas the transferable pseudopotentials are applicable in whatsoever environment (solid, surface, molecules …). The pseudopotential approach has its drawbacks too since it is not possible to describe satisfactory changes in the electronic configurations of core electrons and consequently the hyperfine structure, excitation of core electrons and some other phenomena. In order to overcome those limitations, basis sets such as augmented-plane wave (APW), linearized augmented-plane wave (LAPW), augmented-

plane wave with additional local orbitals (APW+LO) and projector augmented wave (PAW) are developed.

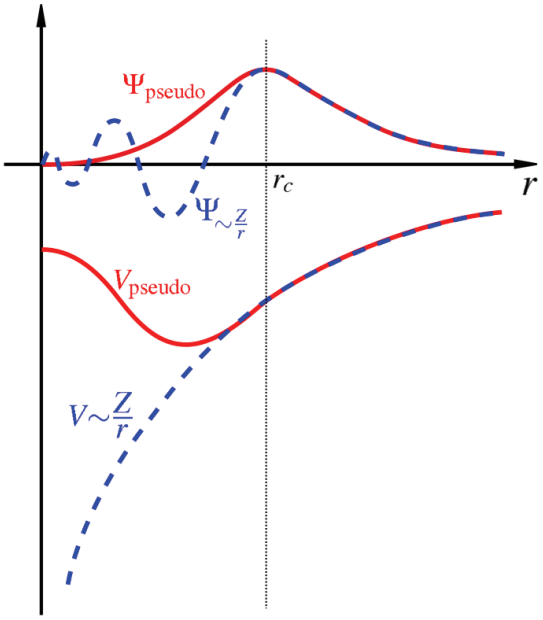


**Figure** 29. Schematic explanation of pseudopotentials. A wave function in the Coulomb all-electron potential of the nucleus (blue) versus the pseudo-potential (red). The real and the pseudo-wave function and potentials match above a certain cutoff radius that corresponds to the cut-off energy. Taken from [237].

### *3.1.3.1 Augmented-plane wave (APW) method*

Within the APW method, space is divided into spheres localized at each atom, the so-called muffin-tins (**MT**), and the remaining is interstitial space. Inside each MT sphere of radius $r_{mt}$ the potential is spherical-symmetric similar to the potential of the atom (since the electrons behave as if they were in a free atom), thus the basis functions are obtained by integrating the radial part of the Schrödinger equation. On the other side, the interstitial space is usually described by a constant interstitial potential with smooth plane wave functions. This strategy is called *augmenting*. The APW approach hence, is able to treat highly localized atomic-like states, core states, but also delocalized states using Bloch wave functions. Basis functions in the interstitial area are augmented by the atom-like functions *inside* MT spheres. Although today the APW method is not of practical use, it is convenient to describe it since other methods such as PAW described below, are an advanced version of the APW method.

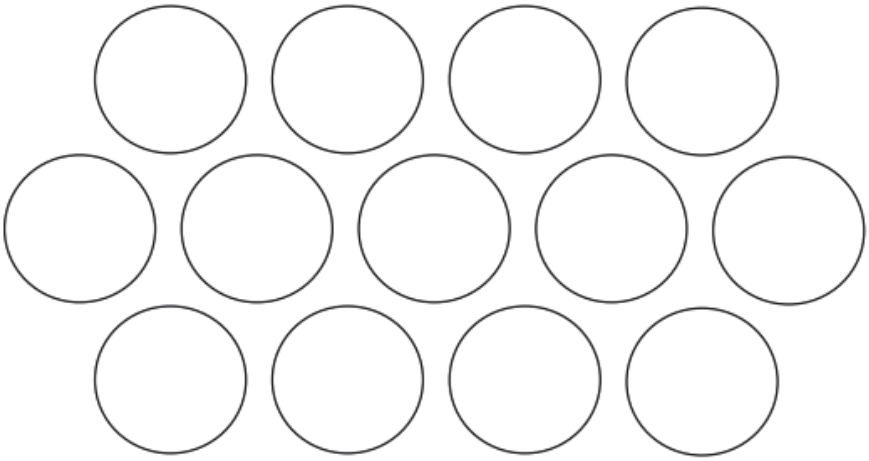

**Figure** 30. The "muffin-tin" division of space intra-atomic spheres and interstitial regions. This is the basis for representing wavefunction differently in the different regions used in all augmented formulations. Taken from [238].

An augmented plane wave that is used in the basis set expansion of a crystal structure is described as follows:

$$\phi_{\vec{k}}^{n}(\vec{r},E)=\begin{cases}\dfrac{1}{\sqrt{V}}e^{i(\vec{k}+\vec{K})\vec{r}} & ,\vec{r}\in I\\ \sum_{l,m}A_{l,m}^{\alpha,\vec{k}+\vec{K}}R_{l}^{\alpha}(r',E)Y_{m}^{l}(\theta',\varphi') & ,\vec{r}\in S_{\alpha}\end{cases} \qquad \textbf{Eq.}\ 37$$

This basis set depends on the reciprocal space vector $\vec{k}$ as it is a case with a plane wave. $V$ is the unit cell volume, $Y_m^l$ are spherical harmonics, $A_{l,m}^{\alpha,\vec{k}+\vec{K}}$ are expansion coefficients, $E$ is energy. $R_l^\alpha$ is the solution of the radial part of the Schrödinger equation that corresponds to the free atom $\alpha$ with energy $E$. $A_{l,m}^{\alpha,\vec{k}+\vec{K}}$ are the parameters determined by requiring the waves to match at the surface of the MT spheres.

The main drawback of the APW method is its energy dependence i.e. the resulting APW equations must be solved separately for each eigenstate i.e. the APW method is much slower than the pseudopotential method. For an iterative procedure that leads to the determination of eigenstates, it is essential to suppose the value of $E$ that is close enough to an eigenvalue, the energy we are actually looking for. When the energy is found for a given $\vec{k}$ the

procedure is repeated until the whole set $\{\vec{k}\}$, that has to be sufficiently dense to cover uniformly the first Brillouin zone, is depleted. Hence, the APW method is computationally extremely demanding.

### *3.1.3.2 The projector-augmented wave (PAW) method*

The PAW method [239] is a very general augmentation scheme that allows DFT methods to be performed with good computational efficiency and accuracy. The main purpose of this augmentation scheme is finding a transformation of the true all-electron wave function ($\psi_n$) to an auxiliary smooth wave function ($\tilde{\psi}_n$) that will not make the numerical treatment cumbersome due to previously mentioned rapid oscillations of true all electron wave function close to the nucleus. The true wave function is thus modified only close to the nuclei, since it is already smooth at a certain minimum distance from the core that corresponds to the radius of the augmentation sphere[238]. Thus, in the PAW context, one seeks to express the real all-electron (AE) wavefunction $\psi_n$ in terms of some carefully chosen functions:

1) The pseudo wave $\tilde{\psi}_n$ identical to the all electron KS wave function $\psi_n$ *except* inside the augmentation sphere

2) All-electron partial waves within the augmentation spheres.

3) Pseudo partial waves (pseudo versions of the all electron partial waves) inside and outside augmentation spheres. The latter are so-called projector functions.

Therefore, the real all-electron wavefunction (smooth everywhere except around the nucleus) is written as the sum of the pseudo wave function (smooth everywhere) $\tilde{\psi}_n$ and a steep function that is defined within the augmentation sphere from which we subtract the smooth part within the augmentation sphere [240] as shown in **Eq.** 38.

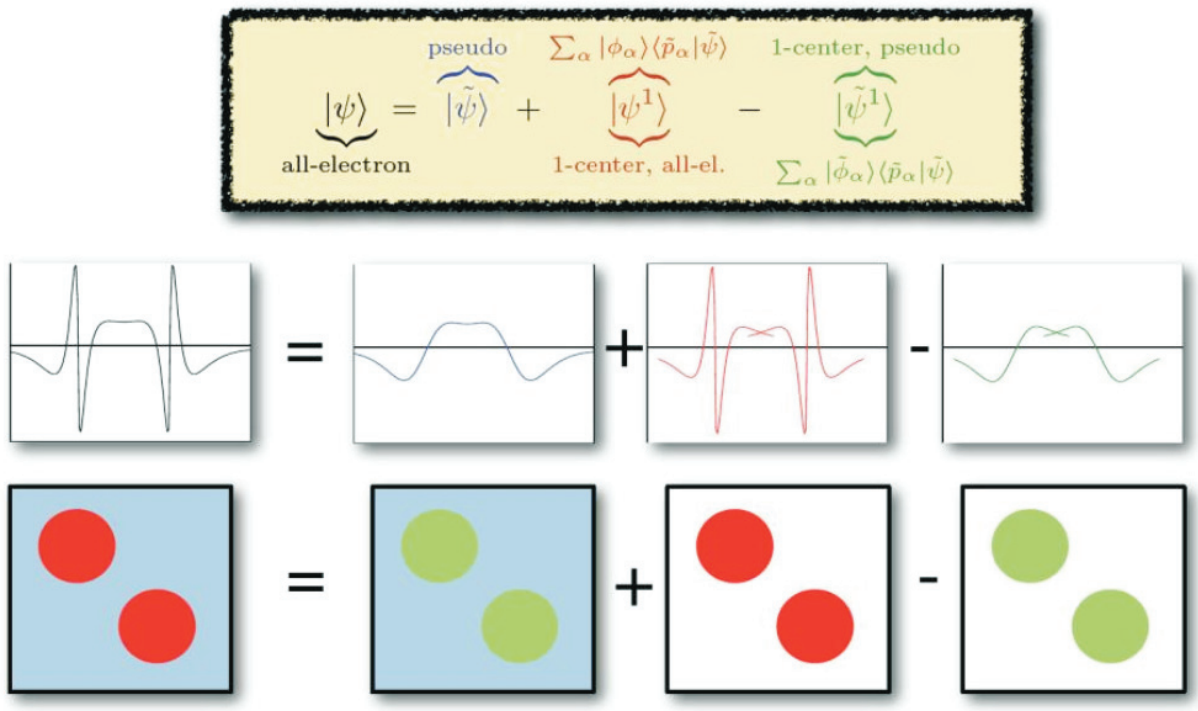


**Figure** 31. PAW augmentation scheme. Taken from [240]

$$\psi_n = \tilde{\psi}_n + \sum_i (\phi_i - \tilde{\phi}_i)\langle\tilde{p}_i|\tilde{\psi}_n\rangle. \qquad \textbf{Eq.}\ 38$$

In **Eq.** 38, $\phi_i$ are the partial waves, $\tilde{\phi}_i$ are the smooth partial waves, $\tilde{p}_i$ are the smooth projector functions, and $\langle\tilde{p}_i|\tilde{\psi}_n\rangle$ are the expansion coefficients (numbers). A decomposition according to **Eq.** 38 of the true all electron wave function ($\psi_n$) into smooth auxiliary wave functions and a contribution that contains rapid oscillation (that contributes only in small areas of space), allows treating these individually in a numerically convenient fashion.

### 3.1.4 Geometry optimization

One of the main objectives of quantum chemistry is the determination of molecular structures through geometry optimization methods, not only for stable molecules but also for transition states, the knowledge of which is highly desirable for the understanding of reactivity.

A geometry optimization process consists of an exploration of the potential energy surface (PES) of the molecular system of interest. The energy change that follows the transformation of a molecular structure is determined by its PES, which is a function of the positions of all the nuclei that compose the system. In the case of polyatomic systems and linear molecules, it is a $(3N-6)$ and a $(3N-5)$ dimensional hyper-surface, respectively. The topology of PES consists of several chemically relevant points:

a) The valleys, that correspond to the minima of the PES and that correspond to stable molecular structures related to reactants, products and chemical reaction intermediates.

b) First order saddle points, that is, points which are minimum in all the directions except one (where it is maximized) and that correspond to transition state (TS) structures. The height of this maximized peak of the transition state with respect to the minimum that corresponds to a stable molecular configuration is the activation barrier.

Since equilibrium structures correspond to a minimum of PSE, ab initio and DFT methods are used to find those chemically relevant structures. By calculation of the first (force) and the second derivative (Hessian) of the energy with respect to atomic displacement $(q = R - R_{equilibrium})$ from their equilibrium positions (in other words, energy gradients):

$$f_{i,j} = -g_{i,j} = -\left(\frac{\partial E}{\partial q_{i,j}}\right)_0, \qquad \textbf{Eq.}\ 39$$

$$H_{i,j} = -\left(\frac{\partial^2 E}{\partial {q_{i,j}}^2}\right)_0 : \qquad \textbf{Eq.}\ 40$$

In the case of more than one degree of freedom, **Eq.** 39 and **Eq.** 40 become matrices. For structures in a local or global minimum of the PES, $g_{i,j} = 0$ and $H_{i,j} > 0\ \forall i,j$, where all Hessian eigenvalues are positive. At first-order saddle points $g = 0\ \forall i,j$ and $H > 0$ for all but one $(i,j)$ which is negative.

At the end of each self-consistent field cycle, residual forces on the nuclei are calculated with the converged wave function by the Hellman-Feynman theorem:

$$-f_\alpha = \langle \Psi | \frac{\partial H}{\partial R_\alpha} | \Psi \rangle \qquad \textbf{Eq.}\ 41$$

Several reviews of geometry optimization procedures are reported in the literature. Some of the well-known analytical gradient methods are Newton, quasi-Newton, conjugate gradient methods, direct inversion of iterative subspace (DIIS), and geometric direct inversion in the iterative subspace (GDIIS).

In this thesis, all the geometry optimizations were done using the conjugate gradient method since this method generally performs better in regions far away from equilibrium geometries.

### 3.1.5 Transition state structures

The calculation of a transition state (**TS**) can provide essential information about an elementary step in a hypothetical reaction mechanism. This type of calculation gives us necessary parameters, such as activation barriers, that can be further used to determine rate constants and gives us insight into the most probable steps in the overall reaction mechanism. There are two prevailing approaches for obtaining the TS that connects two local minima (one for reactants, one for products), the Nudged Elastic Band (NEB), [241–243] which is used for obtaining the energy profile of a reaction (minimum energy paths), and the dimer method, [244] which is used for obtaining the energy and structure of a TS.

NEB operates by optimizing simultaneously a given number of intermediate images along the reaction path that are obtained by progressive movement of atoms from a given reactant to a given product structure. Every image structure is, therefore, optimized while preserving equal spacing between neighbor images. During calculations, this restriction is imposed by adding artificial spring forces $k$ between images, which is a parameter that should

be carefully chosen in the calculation. To start a NEB calculation, an interpolation between initial $R_0$, and final states $R_N$ is needed. In this thesis, we used the Opt'nPath software [245] for a linear interpolation and images generation (imaginary intermediates). In order to optimize images, $R_i(i = 1, \dots, (N-1))$, along the guessed reaction path, an objective function $F$ can be defined:

$$F(R_1 \dots R_N) = \underbrace{\sum_{i=1}^{N-1} E(R_i)}_{\left(\frac{\partial E(R_i)}{\partial R_i}\right)_{\parallel} + \left(\frac{\partial E(R_i)}{\partial R_i}\right)_{\perp}} + \underbrace{\sum_{i=1}^{N} \frac{k}{2}(R_i - R_{i-1})^2}_{\left(\frac{\partial E_{spring}}{\partial R_i}\right)_{\parallel} + \left(\frac{\partial E_{spring}}{\partial R_i}\right)_{\perp}} . \qquad \textbf{Eq.}\ 42$$

As it is schematically described in **Figure** 32, forces acting on the image can be decomposed to its parallel and perpendicular components, as suggested by **Eq.** 42. However, to preserve the equidistant distribution of images along the pathway but also to prevent an upward drift of the energy pathway along the perpendicular direction, forces $\left(\frac{\partial E(R_i)}{\partial R_i}\right)_{\parallel}$ and $\left(\frac{\partial E_{spring}}{\partial R_i}\right)_{\perp}$ need to be applied. However, only two components among the four above are taken into account when calculating NEB forces on an image:

$$F_k = -\left(\frac{\partial E(R_k)}{\partial R_k}\right)_{\perp} - \left(\frac{\partial E_{spring}}{\partial R_k}\right)_{\parallel}. \qquad \textbf{Eq.}\ 43$$

Another technique, complementary to NEB is the climbing-image NEB method (CI-NEB), [246] where the image with the highest energy is not subjected to a spring force from adjacent images and is therefore allowed to climb to the saddle point. The highest energy point of the (CI) NEB trajectory is closest to the saddle point. However, the (CI) NEB procedure tends to overestimate the energy of the saddle point, and TS structures need to be refined by a subsequent Steepest-Descent geometry optimization.

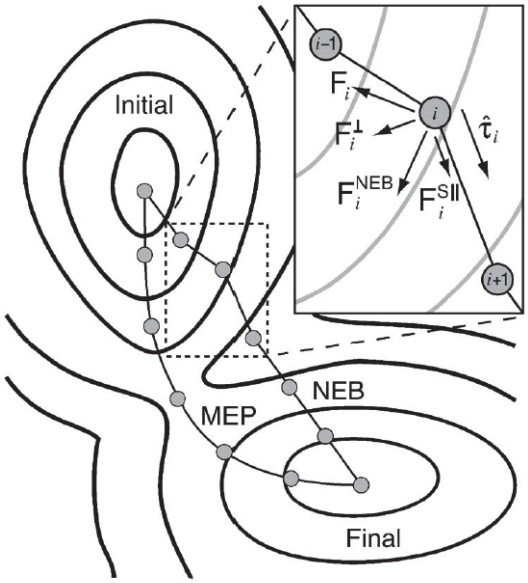


**Figure** 32. Potential energy surface scheme of an arbitrary chemical reaction with its minimum energy pathway (MEP) along with a Nudged Elastic Band (NEB) path. Neighbor images are "connected" with springs whose constant is *k* inducing an artificial spring force. [243]

In this thesis, both NEB and CI-NEB are used. After the search of the transition state is performed, a Steepest Descent geometry optimization is performed until a convergence criterion is reached. Then, the Hessian matrix is computed to verify that we have a transition state structure for which all but one Hessian eigenvalues are positive as described in **Section 3.1.4.**

### 3.1.6 The VASP code

The Vienna Ab initio Simulation Package (VASP) [247,248] is a software designed explicitly for first-principles modeling of materials with periodic boundary conditions. The electronic ground state of a system is determined using DFT calculations.

In this thesis, we use the VASP package and PAW pseudopotentials parametrized for the PBE functional [249] according to the Bloch formalism described previously. [250] Electron energy calculations were done with a constant energy cutoff of 400 eV. The Methfessel-Paxton smearing scheme [251] was used with a width of 0.01 eV. Reciprocal space sampling was done with fineness of 0.04 $Å^{-1}$ Electron energies were converged to $10^{-6}$ eV/unit cell.

Geometry optimizations were performed until all interatomic forces were below 0.02 eV $Å^{-1}$. To take into consideration the magnetic nature of Co, the spin-polarized mode was used. All input parameters were carefully chosen based on an optimization scheme. Details concerning optimization of parameters are given in **Section 8.1**.

### 3.1.7 Slab model representations used in this work

It is known that Co can exist in two different phases, hcp, and fcc, where a transition of the former to the later can be observed at 673K. Since FT catalysts are prepared at temperatures above 673K, the Co-fcc phase is present in a non-negligible amount in fresh supported Co catalysts. Besides, support effects are known to reduce the temperature of phase transition. [252,253] Moreover, nanometric-sized cobalt in the fcc structure is known to be more stable than hcp structure for particle sizes below 100 nm based on thermodynamic calculations. [100] The last condition is usually satisfied for Co-based FT catalysts. Hence, we decided to perform our calculations with fcc-Co.

A four-layer slab was used to model the Co(111) surface built from the fcc-Co bulk phase in the same spirit as in reference [254,205] from our group. The surfaces were represented by using p(2x2) surface unit cells. Those models have approximately a 15 Å empty layer to describe the vacuum and to minimize lateral interactions between the repeating unit cells. All the atoms in the configurations were allowed to relax upon optimization except those in the bottom two layers. For more information about the choice of these parameters, see **Chapter 8.1**.

## 3.2 Fixed Bed Reactors Modeling

In **Section 1.2.1**, we presented some typical reactor configurations employed in the industrial FT fuel production. Compared to other reactor configurations, fixed-bed reactor configurations are particularly suitable due to the ease of operation and simpler technology [255]. In the fixed-bed setting, mobile fluid (reactants) reacts over the catalyst surface in the immobile packed bed.

Mathematical modeling of conventional FT reactors is essential from both research and development and industrial perspective. On the one hand, it allows predicting the effects of operating conditions on economically relevant observables and on the other hand, it allows obtaining some fundamental insights of underlying phenomena. Hence, the development of generalized mathematical models requires the knowledge of many physical aspects, such as mass and heat transfer, hydrodynamics, phase equilibrium, chemical kinetics … as well as their mutual interactions. In order to study those effects, several modeling (see **Figure** 33) approaches are commonly employed for fixed-bed reactors. Those are mostly continuous models where the reaction mixture continuously enters and leaves the system in contrast to closed systems. In contrast to heterogeneous models, pseudo homogenous models do not account explicitly for the presence of solid phase and are usually adequate when the mass transfer limitations and the intra-particle heat are negligable[255]. In other words, it is assumed that the catalyst surface is covered with a fluid phase (homogenous) and negligible mass and heat transfer resistances. Hence, a chemical reaction takes place (homogenously) in the bulk of liquid covering the solid phase. Pseudo homogenous models are thus, the starting point in most of studies so far. In those models, a plug flow in the axial direction is adopted (because the real system is closed to the ideal case). The plug flow reactor model assumes flowing without any back mixing in the axial direction of the reactor (see **Figure** 34). A

comprehensive review of various studies on the mathematical models for the production of fuels by FT is given elsewhere [256].

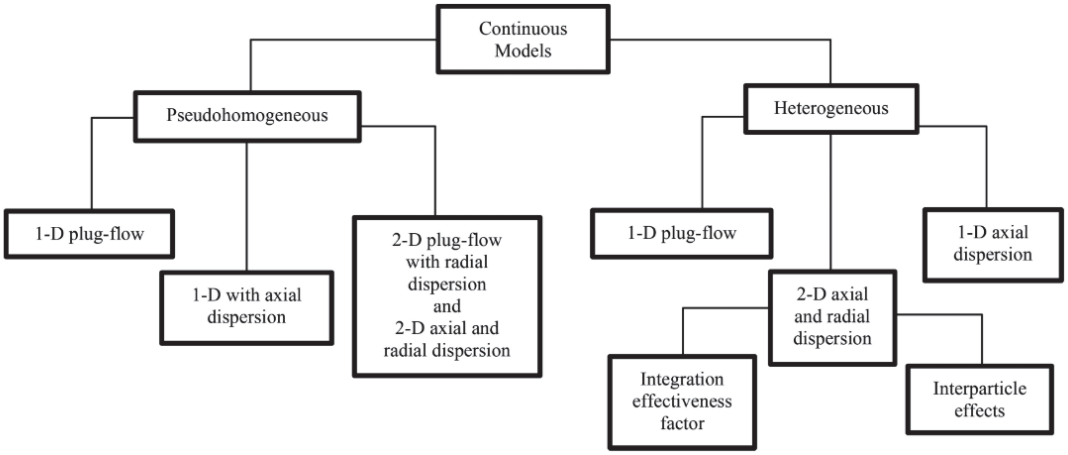


**Figure** 33**.** Classification of continuum models used to describe fixed-bed reactors.

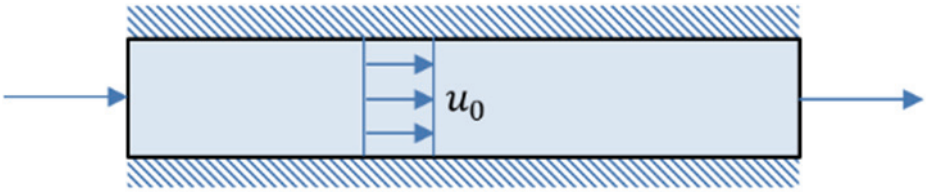


**Figure** 34**.** Schematic diagram of a 1D plug-flow reactor.

Conversion and selectivities at reactor outlet can be predicted by a reactor model. Mass balances for each compound is written assuming plug flow for hydrodynamics. These balances include kinetic source terms to describe species transformations due to chemical reactions. Hence, it is necessary to develop an accurate kinetic model validated on a wide range of operating conditions.

In this thesis, we use the detailed micro-kinetic model presented in **Section 2.4** in conjunction with a 1D heterogenous plug-flow fixed-bed reactor. Several assumptions have been adopted to undertake the modeling of a fixed-bed reactor:

1) We considered plug-flow velocity profile of fluid, i.e., the velocity of the fluid is assumed constant across any cross-section perpendicular to the axis of the reactor.

2) We adopt that the reaction medium is isothermal and isobaric. Therefore, no heat balance equations were introduced in our reactor model

3) We assume gas/liquid equilibrium for reactants and products.

### 3.2.1 Mass balances equations for molecular species

A mass balance on the differential volume of a fluid element on specie $i$ of axial length $dz$ between $z$ and $(z + dz)$ (see **Figure** 34) can be written in terms of input $F_i^{tot}$, output $F_i^{tot} + \frac{\partial F_i^{tot}}{\partial z} dz$, generation $\sum_j \nu_{i,j} r_j \rho_s \varepsilon_s S_r dz$ and accumulation $\frac{dn_i^{tot}}{dt}$. Hence, the overall mass balance equation of a specie $i$ ( $accumulation = input - output + generation$) is given by:

$$\frac{dn_i^{tot}}{dt} = -\frac{\partial F_i^{tot}}{\partial z} dz + \sum_j \nu_{i,j} r_j \rho_s \varepsilon_s S_r dz \qquad \textbf{Eq.}\ 44$$

In **Eq.** 44**,** $\varepsilon_s$ is the solid holdup (the volume of solid per reactor volume), $\rho_s$ is the solid density, $S_r$ is the reactor cross-section, $\nu_{i,j}$ is the stoichiometric coefficient of specie $i$ in the j[th] reaction, $r_j$ is the rate of reaction $j$, $F_i^{tot}$ and $n_i^{tot}$ are the total (gas and liquid) molar flowrate and the total amount of specie $i$, respectively. Note that $(S_r dz)$ has units of volume.

In order to obtain a master balance equation, $dn_i^{tot}$ in **Eq.** 44 is written explicitly in terms of $F_i^{tot}$. This is achieved by writing:

$$dn_i^{tot} = dn_i^{liq} + dn_i^{gas} = c_i^{liq} S_r dz \varepsilon_l + n_i^{gas} S_r dz \varepsilon_g \qquad \textbf{Eq.}\ 45$$

and

$$c_i^{liq} = \frac{F_i^l}{Q_l};\ c_i^{gas} = \frac{F_i^g}{Q_g} \qquad \textbf{Eq.}\ 46$$

Hence,

$$dn_i^{tot} = \left(\frac{F_i^l}{Q_l}\varepsilon_l + \frac{F_i^g}{Q_g}\varepsilon_g\right) S_r dz \qquad \textbf{Eq.}\ 47$$

In **Eq.** 47, $c_i$,$\varepsilon$ and $Q$ are concentrations, holdups and volumetric flow rates of fluid phase species. In order to express $dn_i^{tot}$ as a function of $F_i^{tot} = \left(F_i^l + F_i^g\right)$, we need to express both $F_i^l$ and $F_i^g$ in **Eq.** 47 as a function of $F_i^{tot}$. This is typically achieved using *G/L equilibrium* calculations using a given equation of state that yield the parameter $\alpha$, the ratio of (total) amount of gas in the gas/liquid mixture:

$$\alpha = \frac{F_g^{tot}}{F^{tot}}; (1-\alpha) = \frac{F_l^{tot}}{F^{tot}} \qquad \textbf{Eq.}\ 48$$

In addition to $\alpha$, the $K_{f,i}$-value (gas-liquid flowrate ratio) is defined (yet unknown due to $\frac{y_i}{x_i}$) as the ratios:

$$K_{f,i} = \frac{F_i^g}{F_i^l} = \frac{y_i F_g^{tot}}{x_i F_l^{tot}} = \frac{y_i \alpha}{x_i (1-\alpha)} \qquad \textbf{Eq.}\ 49$$

**Eq.** 49 yields species $i$ fluxes in both fluid phases in terms of unknown gas-liquid flowrate ratio $K_{f,i}$:

$$F_i^g = F_i^{tot} \frac{K_{f,i}}{1+K_{f,i}}; F_i^l = \frac{F_i^{tot}}{1+K_{f,i}} \qquad \textbf{Eq.}\ 50$$

whereas, equation **Eq.** 48 transforms $Q_l$ and $Q_g$ in equation **Eq.** 47 to:

$$Q_g = \frac{F_g^{tot}}{c_g^{tot}} = \frac{\alpha F^{tot}}{c_g^{tot}} = \alpha RT \frac{F^{tot}}{P_{tot}} \qquad \textbf{Eq.}\ 51$$

$$Q_l = \frac{F_l^{tot}}{c_l^{tot}} = \frac{(1-\alpha) F^{tot}}{c_l^{tot}} = (1-\alpha) M_w^l \frac{F^{tot}}{\rho_l} \qquad \textbf{Eq.}\ 52$$

In **Eq.** 51 and **Eq.** 52, $P_{tot}$ is the total pressure, $M_w^l$ is the specific-mass of the liquid phase, $T$ is the temperature and $\rho_l$ is the density of the liquid phase. Substitution of **Eq.** 49-**Eq.** 52 in **Eq.** 47 gives:

$$n_i^{tot} = \frac{F_i^{tot}}{F^{tot}(1+K_{f,i})}\left[\frac{\rho_l}{(1-\alpha)M_w^l}\varepsilon_l + \frac{K_{f,i}P_{tot}}{\alpha RT}\varepsilon_g\right]S_r dz = \beta_i F_i^{tot} dz \qquad \textbf{Eq.}\ 53$$

where

$$\beta_i = \frac{S_r}{F^{tot}(1+K_{f,i})}\left[\frac{\rho_l}{(1-\alpha)M_w^l}\varepsilon_l + \frac{K_{f,i}P_{tot}}{\alpha RT}\varepsilon_g\right] \qquad \textbf{Eq.}\ 54$$

Note that $K_{f,i}$ in equation **Eq.** 54, gas liquid flowrate ratio, is unknown and to be determined based on gas/liquid equilibrium described in **Section 3.2.3**. Now that we expressed $n_i^{tot}$ as a function of $F_i^{tot}$ and considering that $\beta_i$ is time-independent, mass balance equation **Eq.** 44 can be transformed to:

$$\boxed{\frac{\partial F_i^{tot}}{\partial t} = \frac{1}{\beta_i}\left(\sum_j \nu_{i,j} r_j \rho_s \varepsilon_s S_r - \frac{\partial F_i^{tot}}{\partial z}\right)} \qquad \textbf{Eq.}\ 55$$

### 3.2.2 Mass balance equations for adsorbed species

Material balance for adsorbed species (*) can be easily obtained using the same reasoning we developed for molecular species, after noting that there are no input and output terms and no mass transfer associated to them. Hence, **Eq.** 44 can be written as:

$$\frac{dn_i^*}{dt} = \sum_j \nu_{i,j} r_j \rho_s \varepsilon_s S_r dz \qquad \textbf{Eq.}\ 56$$

If we now express radical $i$ (*) mole number $n_i^*$ in terms of concentration per mass of catalyst $dn_i^* = c_i^* \rho_s \varepsilon_s S_r dz$, we obtain the master equation of radical material balance:

$$\boxed{\frac{dc_i^*}{dt} = \sum_j \nu_{i,j} r_j} \qquad \textbf{Eq.}\ 57$$

### 3.2.3 Thermodynamic model

The resolution of the gas/liquid equilibrium requires the knowledge of partition coefficients $K_i$ of every component $i$. The gas and the liquid composition profiles are determined by using a two-phase flash calculation and the Soave-Redlich-Kwong (**SRK**) equation of state for various operating conditions. It was shown that the composition does not affect partition coefficients $K_i$, hence, correlations are developed as a function of operating conditions using an Antoine equation[257,258]:

$$\log(P_{tot} K_i) = \frac{a_i}{T} + b_i \qquad \textbf{Eq.}\ 58$$

With partition coefficient defined as:

$$K_i = \frac{y_i}{x_i} \qquad \textbf{Eq.}\ 59$$

In **Eq.** 59 $y_i$ is the vapor molar fraction and $x_i$ is the liquid molar fraction. Thus, for each component, coefficients $a_i$ and $b_i$ in **Eq.** 58 have been determined and used to estimate $K_i$. Note that partition coefficients $K_i$ are related to Henry coefficients of each specie:

$$H_i = \frac{P_i}{c_i^l} = \frac{y_i P_{tot}}{x_i \sum_i c_i^l} = K_i \frac{P_{tot}}{c_{tot}^l} = K_i M_w^l \frac{P_{tot}}{\rho_l} \qquad \textbf{Eq.}\ 60$$

Determination of the unknown gas/liquid flowrate ratio $K_{f,i}$ in **Eq.** 49 is necessary to solve the mass balance **Eq.** 55**.** Hence, **Eq.** 49 can be written as:

$$K_{f,i} = \frac{y_i \alpha}{x_i (1-\alpha)} = \frac{H_i \rho_l}{P_{tot} M_w^l} \frac{\alpha}{(1-\alpha)} \qquad \textbf{Eq.}\ 61$$

### 3.2.4 Reaction rate equations

Based on the detailed micro-kinetic model presented in **Section 2.4**, the rate of reactions $r_j$ in equations **Eq.** 55 and **Eq.** 57 are given by a power law. Arrhenius law has been adopted for all rate constants in the micro-kinetic model including those for adsorption/desorption equilibrium:

$$k = A\, e^{-\frac{E_a}{RT}} \qquad \textbf{Eq.}\ 62$$

where, $A$ is the pre-exponential factor, and $E_a$ is the activation energy. Mathematical form of **Eq.** 62 involving exponentiation of the $\frac{1}{T}$, introduces a high correlation between $A$ and $E_a$ making a parameter estimation problem difficult to solve [259]. The most common way to overcome this numerical difficulty is to re parametrize the Arrhenius **Eq.** 62 in the more convenient form:

$$k = k_{T_{ref}}\, e^{-\frac{E_a}{R}\left[\frac{1}{T} - \frac{1}{T_{ref}}\right]} \qquad \textbf{Eq.}\ 63$$

where

$$k_{T_{ref}} = A\, e^{-\frac{E_a}{RT_{ref}}} \qquad \textbf{Eq.}\ 64$$

Hence, $k_{T_{ref}}$ , can be regarded as the specific reaction rate at the reference temperature. The reference temperature in this work was set to $T_{ref} = 493.15K$ close to the FT operating temperature in order to reduce the numerical sensitivity of the exponential part in Eq. 63. .

### 3.2.5 Numerical Methods

Livermore Solver for Ordinary Differential Equations (**LSODE**) stiff solver is applied to integrate the axially discretized differential equations **Eq.** 55 and **Eq.** 57 and generate

concentration profiles as a function of reactor length and time for a given input of reactor geometry, syngas composition and operating conditions. The complete model was implemented in object-oriented FORTRAN.

In order to fit the micro-kinetic model to experimental data, a numerical method was used based on a discretization scheme and the finite differences approximation. Second and first-order derivative terms were solved using a centered-discrete scheme and an upwind scheme, respectively. Time integration was performed using the Lsode solver.

The optimization method or parameter estimation method refers to minimizing the objective function that is the measure of correctness of the model data $R_j^{calc}$ with respect to a given experimental data $R_j^{exp}$ and is given by the following equation:

$$R^{obj} = \sum_{i=1}^{N_{exp}} w_i \sum_{j=1}^{NRS} w_j \left( \frac{R_j^{exp} - R_j^{calc}}{R_j^{exp}} \right)^2 \qquad \textbf{Eq. } 65$$

In the above equation, NRS represents the number of responses in the multi-response system, $w_i$ and $w_j$ represents the weight factor of $i$th experiment and $j$th response objective function. Weight factors for all experiments are set to unity i.e. $w_j = 1 \; \forall j$ . Weight factors for observables such as CO conversion and methane selectivity are set to unity whereas those of chain growth probabilities are set to100 due to differences in order of magnitudes. Due to time limitations, statistical analysis (F-test in particular) of our results have not been performed.

The micro-kinetic model described in **Section 2.4** contains several unknown independent parameters (rate/equilibrium constants, activation energy) which should be estimated by numerical adjustment. The kinetic parameters were optimized using an advanced local optimization method, the Levenberg-Marquardt (LM) algorithm[260], designed explicitly for nonlinear programming problem such as chemical reaction network described by the micro-kinetic model. This numeric minimization algorithm is designed to find the set of the

model parameters (subject to bounds) so that the sum of the squares of the individual deviations is minimized given a set of empirical observations. The problem is solved using iterative procedure based on an initial guess for the model parameters, whereas in each iteration step the function is approximated by its linearization by calculating the gradient and the Jacobian matrix. In this study, our starting point is micro-kinetic model parameters obtained by Visconti et al. The goal is, therefore, to acquire numeral values for those parameters (reaction rates, activation energies …) that give the best possible agreement with the experimental data. In this work, it is considered that one Co atom corresponds to one active site on which reactions take place. The experimental data for the fitting procedure are provided by IFP internal report of Hazemann [148] from catalytic tests performed during his thesis.

Several physicochemical criteria will be applied while optimizing to obtain accurate estimates for reaction rate constants, adsorption equilibrium constants, and activation energies. For example, kinetic rate and equilibrium constants will be limited to positive values and activation energies, in addition to that, will have to be in the range of some experimentally obtained values. The optimized model will not be validated with independent data due to the absence of such data during this thesis.

# 4 Surface speciation of Co-based Fischer-Tropsch catalyst

In this chapter, we present the results on the surface speciation of Co-based FT catalyst under realistic reaction conditions based on our thermodynamic model. Firstly, we compare deactivation by oxygen-containing species with that due to the formation of deleterious carbonaceous species. We then deduce the structure of some coke precursors leading to catalyst deactivation. In the following chapters, we propose a mechanism of their formation and a micro-kinetic model to depict the catalyst activity and selectivity loss due to the formation of those surface species.

## 4.1 Computational methods

### 4.1.1 Total Energy Calculations

All calculations in this chapter are performed using a periodic DFT approach with a plane wave basis set and pseudopotentials as implemented in the VASP code [247,248]. We used PAW pseudopotentials parametrized for the generalized gradient approximation (GGA) Perdew-Burke-Ernzerhof (PBE) functional [249]. The electron distribution at the Fermi level was modeled by the Methfessel and Paxton method [251] with $\sigma = 0.08\,eV$. In order to account for the magnetic properties of Co, we included spin-polarization.

A four-layer slab was used to model the Co(111) surface built from the fcc-Co bulk phase in the same spirit as in our previous work [205]. The surfaces were represented by using p(2x2) surface unit cells. Those models have approximately a 15 Å empty layer in the direction perpendicular of the surface to minimize lateral interactions in that direction. All the atoms in the configurations were allowed to relax upon optimization except from those in the bottom two layers. The k-point sampling was done using the Monkhorst-Pack [236] procedure with 7x7x1 meshes. The plane-wave basis set cutoff energy was set to 400 eV. According to

our benchmark calculations, the dipole correction is below 1 meV/atom in our models. Hence, we performed our calculations without this correction.

Using the Birch-Murnaghan equation of state, we obtained an equilibrium lattice constant of 3.524 Å (exp: 3.550 Å [261]). A magnetic moment of 1.65 $\mu_b$ per Co atom is obtained which is in good agreement with experimental results (exp: 1.70 $\mu_b$ [262]). Gas-phase molecules ($H_2$, CO and, $H_2O$) were calculated by placing the molecule in a cubic unit cell of 10x10x10 $Å^3$.

Surface coverages of C, H and O, are expressed with respect to the number of surface Co atoms in our unit cell: one monolayer (1 ML) of C, H or O corresponds to 4 atoms in our p(2×2) unit cell composed of 4 Co surface atoms. Note also that the energy values reported hereinafter will be expressed in eV per surface Co atom. In this work, we considered systematically all possible surface coverages of hydrogen and oxygen atoms up to 1ML and of carbon atoms up to 2 ML (including subsurface atoms in this case); we also tested different high symmetry adsorption sites for those atoms on the surface: on-top, bridge, 3-fold hcp hollow and 3-fold fcc hollow sites as well as subsurface sites for C atoms.

### 4.1.2 Thermodynamic model

The overall stoichiometry equation of the FT reaction producing the mixture of paraffin molecules can be written as follows:

$$CO + (3 - \alpha_{ASF})H_2 \rightarrow H_2O + (1 - \alpha_{ASF}) \sum_{i=1}^{n} x_i^{ASF} P_i \qquad \textbf{Eq.}\ 66$$

where $\alpha_{ASF}$ is the chain growth probability and $x_i^{ASF}$ is the mole fraction of paraffin $P_i(C_iH_{2(i+1)})$ composed of $i$ carbon atoms as defined by the ASF distribution: $x_i^{ASF} = \alpha_{ASF}^{(i-1)}(1 - \alpha_{ASF})$.

We aim at studying the chemical state of the Co surface, by calculating the energetics and the geometry of various surface $C_\alpha H_\beta O_\gamma$ intermediates that can be precursors of either the desired FT products (long chain paraffins) or of detrimental unwished ones such as coke or oxidized sites. Since we also want to take into account the FT reaction conditions, the general expression of the reaction of $C_\alpha H_\beta O_\gamma$ deposition on the surface can be written as:

$$Co + xCO + yH_2 + zH_2O + \sum_{i=1}^{n} \delta_i * C_i H_{2i+2} \rightarrow Co^* - C_\alpha H_\beta O_\gamma \qquad \textbf{Eq.}\ 67$$

where $x$, $y$, $z$ and $\delta_i$ are the stoichiometric positive or negative coefficients of the corresponding molecular species that can either appear as reactants or products, respectively. By considering the material balance in terms of carbon, hydrogen and oxygen atoms, the relationship between the surface composition $(\alpha, \beta, \gamma)$, and the stoichiometric $(x, y, z, \delta_i)$ coefficients is found as detailed in **Section 8.4.1** and shown in **Eq.** 96. In **Section** 8.4 we explain the full derivation of the expression for the Gibbs free energy of the deposition reaction corresponding to **Eq.** 67:

$$\Delta_r G^{p,T} = \frac{1}{N_{Co}^{Co(111)}}\Bigg(G_{Co-C_\alpha H_\beta O_\gamma} - G_{Co_{(111)}} - xG_{CO_{(g)}} - yG_{H_{2(g)}} - zG_{H_2O_{(g)}} - n_{tot}\sum_{i=1}^{n} x_i^{ASF} G_{P_{i(g)}}\Bigg)$$

$$= \frac{1}{N_{Co}^{Co(111)}}\Bigg[\Delta_r H^{0K} - x\Delta_{0K\to T}\overset{\circ}{h}_{CO_{(g)}} - y\Delta_{0K\to T}\overset{\circ}{h}_{H_{2(g)}} - z\Delta_{0K\to T}\overset{\circ}{h}_{H_2O_{(g)}} - n_{tot}\sum_{i=1}^{n} x_i^{ASF}\Delta_{0K\to T}\overset{\circ}{h}_{P_{i(g)}} + T\Bigg(x\overset{\circ}{S}_{CO_{(g)}}(T) + y\overset{\circ}{S}_{H_{2(g)}}(T) + z\overset{\circ}{S}_{H_2O_{(g)}}(T) + n_{tot}\sum_{i=1}^{n} x_i^{ASF}\overset{\circ}{S}_{P_{i(g)}}(T) - R\ \ln\Bigg(p_{CO}^{x}p_{H_2}^{y}p_{H_2O}^{z}\prod_{i=1}^{n} p_{P_i}^{n_{tot}x_i^{ASF}}\Bigg)\Bigg)\Bigg] \quad \textbf{Eq.}\ 68$$

In this equation, we consider that $\Delta_{0K\to T}\overset{\circ}{h}_{Co-C_\alpha H_\beta O_\gamma} - \Delta_{0K\to T}\overset{\circ}{h}_{Co_{(111)}} \approx 0$. The theoretical enthalpy of reaction at 0K $\Delta_r H^{0K}$ is given by:

$$\Delta_r H^{0K} = \Bigg(E_{Co-C_\alpha H_\beta O_\gamma} - E_{Co_{(111)}} - \alpha H_{C_{(g)}}^{0K,th*} - \frac{\beta}{2}H_{H_2}^{0K,th*} - \frac{\gamma}{2}H_{O_2}^{0K,th*} - x\left[\Delta_f H_{CO}^{exp} - ZPE_{CO}\right] - y\left[\Delta_f H_{H_2}^{exp} - ZPE_{H_2}\right] - z\left[\Delta_f H_{H_2O}^{exp} - ZPE_{H_2O}\right] - n_{tot}\sum_{i=1}^{n} x_i^{ASF}\left[\Delta_f H_{P_i}^{exp} - ZPE_{Pi}\right]\Bigg) \quad \textbf{Eq.}\ 69$$

In **Eq.** 68, $N_{Co}^{Co(111)}$ represents the number of surface Co atoms per unit cell, $\Delta_{0K\to T}\overset{\circ}{h}_i$ is the tabulated thermal correction to the enthalpy at given temperature $T$ relative to 0 K and obtained from experimental data bases at $p^\circ$=1 bar [263,264], $\overset{\circ}{S}_i(T)$ represents the tabulated [263,264] standard entropy of species $i$, $T$ is the temperature in K, $R$ is the universal gas constant and $p_i$ represents the partial pressure of species. In **Eq.** 69, $E_i$ are the absolute

electronic energies without zero-point (ZPE) corrections from our DFT calculations. Hence, $E_{Co^*-C_\alpha H_\beta O_\gamma}$ is the electronic energy of the slab with adsorbed $\alpha C$, $\beta H$ and $\gamma O$ atoms and $E_{Co_{(111)}}$ is the electronic energy of the bare Co(111) surface. $H_{C_{(g)}}^{0K,th*}$, $H_{H_2}^{0K,th*}$ and $H_{O_2}^{0K,th*}$are, respectively, the corrected references for carbon, hydrogen and oxygen (**Section 8.4.3** for the choice of our reference states). $\Delta_f H_i^{exp}$ is the experimental formation enthalpy of species at 0K (all paraffins assumed to be in the gas phase) and $n_{tot}$ is the total amount of hydrocarbon molecules used (or produced) during the deposition step. Notice that the choice of $H_{C_{(g)}}^{0K,th*}$, $H_{H_2}^{0K,th*}$ and $H_{O_2}^{0K,th*}$ is done so that experimental formation enthalpies can be used in **Eq.** 69 in a consistent way with DFT slab electronic energies and so that, at T= 0K, this equation yields the energy change of reaction at the DFT level of accuracy (see **Section 8.4.4**). Notice also that these reference states contain the ZPE of $H_2$ and $O_2$ molecules so that **Eq.** 69 assumes that the ZPE between reactants and products cancel out ($\Delta$ZPE ~0).

In this work, partial pressures of gas-phase reactants ($H_2$ and CO) are assumed to be constant and known from the experimental syngas composition. Water and hydrocarbons partial pressures on the other hand, depend on the reaction progress and chain-growth probability $\alpha_{ASF}$. They will be therefore estimated according to the approach described in reference[205].

In summary, we explored systematically all possibilities in a p(2×2) unit cell, in the range of surface coverages of carbon, oxygen and hydrogen considered in our work, and used $\Delta_r G^{p,T}$ to find the most plausible surface states. The Gibbs free energy of reaction we calculated is without presuming thermodynamic equilibrium, since it depends on the ASF coefficient. The minimum of $\Delta_r G^{p,T}$ is reached when $\alpha_{ASF} \to 0$ as shown by Masuku[265] and developed in **Section 8.4.6**. Explicit inclusion of $\alpha_{ASF}$ in our thermodynamic model not only

allows us to study the thermodynamics, but also to take the catalyst selectivity into consideration.

## 4.2 Key chemical reactions leading to $CH_\beta$, $OH_\beta$ ($\beta$=0, 1 and 2), CO and H adsorbed species at low coverages

The chemical transformation depicted by **Eq.** 67 suggests that, in general, not a single chemical reaction exists leading to the deposition of a given surface $(\alpha, \beta, \gamma)$ concentration of carbon, hydrogen and oxygen atoms. In this section, we first present some relevant competing pathways for simple relevant cases and we discuss their thermodynamic contributions with respect to available data published so far. For the sake of clarity, in this section we consider only the case where $\alpha_{ASF} \rightarrow 0$ so-called methanazing conditions. **Table** 9 lists the deposition reactions and corresponding energies for some surface states of interest.

**Table** 9 Different chemical pathways, calculated enthalpies at $0K$ and Gibbs free energies at $500K$ using **Eq.** 68 for deposing, on a bare Co surface, some surface species for $P = 20$ bar, $H_2/CO=2$, $\alpha_{ASF} \rightarrow 0$. One surface atom corresponds to 0.25 ML.

| Reaction **N (direct), N' (reverse)** ◦ | Final surface state | Chemical reaction | $\Delta_r H^{0K}$ (eV per surf. Co atom) | $\Delta_r G^{T,p}$ (eV per surf. Co atom) |
|---|---|---|---|---|
| **(1)** | $\{* C_1\}$ | $* + \boldsymbol{CO + H_2 \rightarrow \{* C_1\} + H_2O}$ | -0.18 | **-0.05** |
| **(2)** | | $* + \boldsymbol{CH_4 \rightarrow \{* C_1\} + 2H_2}$ | 0.52 | 0.48 |
| **(3)** | $\{* O_1\}$ | $* + \boldsymbol{CO + 2H_2 \rightarrow \{* O_1\} + CH_4}$ | -0.77 | **-0.51** |
| **(4)** | | $* + \boldsymbol{H_2O \rightarrow \{* O_1\} + H_2}$ | -0.07 | 0.02 |
| **(5)** | $\{* H_1\}$ | $* + \boldsymbol{\frac{1}{2}H_2 \rightarrow \{* H_1\}}$ | -0.13 | **-0.07** |
| **(6)** | | $\boldsymbol{\frac{1}{4}H_2O + \frac{1}{4}CH_4 \rightarrow \{* H_1\} + \frac{1}{4}CO + \frac{1}{4}H_2}$ | 0.05 | 0.07 |
| **(7)** | | $\boldsymbol{\frac{1}{2}H_2O + \frac{1}{2}CH_4 \rightarrow \{* H_1\} + \frac{1}{2}CO + 1H_2}$ | 0.22 | 0.20 |
| **(8)** | $\{* CH_1\}$ | $* + \boldsymbol{CO + \frac{3}{2}H_2 \rightarrow \{* CH_1\} + H_2O}$ | -0.40 | **-0.20** |
| **(9)** | | $* + \boldsymbol{CH_4 \rightarrow \{* CH_1\} + \frac{3}{2}H_2}$ | 0.31 | 0.33 |
| **(10)** | $\{* CH_2\}$ | $* + \boldsymbol{CO + 2H_2 \rightarrow \{* CH_2\} + H_2O}$ | -0.43 | **-0.17** |
| **(11)** | | $* + \boldsymbol{CH_4 \rightarrow \{* CH_2\} + H_2}$ | 0.28 | 0.36 |
| **(12)** | $\{* CH_3\}$ | $* + \boldsymbol{CO + \frac{5}{2}H_2 \rightarrow \{* CH_3\} + H_2O}$ | -0.58 | **-0.26** |
| **(13)** | | $* + \boldsymbol{CH_4 \rightarrow \{* CH_3\} + \frac{1}{2}H_2}$ | 0.12 | 0.27 |
| **(14)** | $\{* CO\}$ | $* + \boldsymbol{CO \rightarrow \{* CO\}}$ | -0.41 | **-0.19** |
| **(15)** | $\{* C\} + \{* O\}$ | $\boldsymbol{2 * + CO \rightarrow \{* C\} + \{* O\}}$ | -0.03 | 0.19 |
| **(16)** | $\{* H_2O\}$ | $* + \boldsymbol{CO + 3H_2 \rightarrow \{* H_2O\} + CH_4}$ | -0.76 | **-0.37** |
| **(17)** | | $* + \boldsymbol{H_2O \rightarrow \{* H_2O\}}$ | -0.06 | 0.16 |
| **(18)** | $\{* OH\} + \{* H\}$ | $\boldsymbol{2 * + CO + 3H_2 \rightarrow \{* OH\} + \{* H\} + CH_4}$ | -0.82 | **-0.43** |
| **(19)** | | $\boldsymbol{2 * + H_2O \rightarrow \{* OH\} + \{* H\}}$ | -0.12 | 0.09 |
| **(20)** | $\{* O\} + 2\{* H\}$ | $\boldsymbol{3 * + CO + 3H_2 \rightarrow \{* O\} + 2\{* H\} + CH_4}$ | -0.71 | **-0.32** |
| **(21)** | | $\boldsymbol{3 * + H_2O \rightarrow \{* O\} + 2\{* H\}}$ | 0.00 | 0.21 |

**Table** 9 shows that for surface state $\{* C_1\}$ the thermodynamically favorable pathway is achieved by deposing a single carbon atom from a $CO$ molecule (reaction **(1)**) rather than from methane decomposition (reaction **(2)**). Reaction **(2)**, that assumes carbon deposition from a paraffin molecule, methane in this case, is highly endothermic and therefore expected to be less favorable, as expected from chemical intuition. On the contrary, the formation of a paraffin molecule (methane) from this particular surface state $\{* C_1\}$ in the presence of hydrogen is highly exothermic ( $\Delta_r G^{T,p} = -0.48\, eV$ per Co surface atom). A similar conclusion can be drawn for reactions **(8)** to **(13)** comparing the deposition of $CH_\beta$ from either from $CO$ (and $H_2$) or from methane, showing that $CH_\beta$ formation occurs preferentially through C originating from $CO$ molecules.

Carbon stability on Co(111) and Co(0001) has been extensively studied using DFT calculations in the literature. In references[266,267,209], carbon deposition from CO molecules is studied, whereas reference[205] discusses also the elimination of carbonaceous surface species in the form of hydrocarbons through the reverse of reaction (**2**). Likewise, Tan et al.[204] studied the stability of different $CH_\beta$ species on Co(111) terraces by calculating the Gibbs free energies of reactions explicitly using equations **(1) (8)** and **(10)** in **Table** 9. Carbon deposition Gibbs free energy (reaction **(1)**) in that work[204] (-0.04 eV/Co surface atoms) is comparable with that in **Table** 9 and reference[205](-0.05 eV/Co surface atoms). Deposition energies of hydro carbonaceous species in reference[204] agree very well with the results for $\{* CH_1\}$ and $\{* CH_2\}$ presented in **Table** 9 (-0.18 and -0.17 compared to our -0.20 and -0.17 eV/Co surface atoms, respectively), despite different FT operating conditions. Moreover, the authors of that work chose purely DFT instead of our corrected DFT approach used here to calculate the Gibbs free energy (see **Sections** 8.4.2 and 8.4.3). Moreover, our enthalpies of reaction at $T = 0K$ agree with those from references[268,112] for the Co(0001) surface.

Thus, all deposition energies reported in what follows refer to the deposition of carbon from CO and not from hydrocarbon molecules unless otherwise stated.

Considering reaction **(4)**, oxygen deposition from a water molecule is exothermic ($\Delta_r H^{0K} = -0.07\ eV$ per Co surface atom) in accordance with previous DFT results [155,269] but endergonic under realistic FT conditions ($\Delta_r G^{T,p} = 0.02\ eV$). However, reaction **(3)** that produces identical surface state $\{* O_1\}$, shows that the deposition of oxygen can occur more readily from the dissociation of a CO molecule (as studied in [191]). Indeed, deposition energy of O from a CO molecule is ~0.5 eV per Co surface atom more exergonic under FT conditions than that from water (reaction **(4)**) and thus thermodynamically more favorable. Thus, from a thermodynamic point of view, CO molecules are stronger oxidizing agents than $H_2O$ molecules as shown in the recent study of Wolf et al. [270] using in situ magnetometry.

Similarly to previous works[271–274], adsorption of CO is studied according to reaction **(14)**. In this work, we find enthalpies for CO adsorption comparable to those reported in reference [271] (-1.63 eV in our current modified DFT approach compared to -1.7 eV in the literature). Besides, geometrical properties of adsorbed CO in both approaches are almost identical. According to our calculations, molecular adsorption of CO is -0.39 eV per Co surface atom more exergonic than dissociative adsorption in the form of $\{* C_1\} + \{* O_1\}$ surface state as shown by reaction **(15)** in **Table 9**.

Reactions **(16)** to **(21)** lead to several oxygenated surface states ($\theta(O) = 0.25$ and $\theta(H) = 0.50$ ML) and take into account different chemical pathways in which oxygen deposition occurs from either carbon monoxide or water molecules. The local structures of species in **Table** 9 are very close to those reported in reference[187]. In addition, reaction enthalpies of water adsorption (either dissociative or non-dissociative) in **Table** 9 are very close to those found in the literature[187] for $\{* H_2O\}$ (-0.06 eV/Co in the present work (reaction **(17)** compared to -0.07 eV in the literature). However, this reaction is endergonic under FT

conditions according to our model ($\Delta_r G^{T,p} = 0.16\, eV/Co$). In addition to the adsorption energy of water molecules, reaction enthalpies obtained for partial (reactions **(18)** and **(19)**) $H_2O$ atomization are comparable with those in reference [187] (-0.12 eV/Co for $\{*OH\} + \{*H\}$ deposition in reaction **(19)** compared to -0.08 eV/Co in [187]). Similarly to oxygen $\{*O\}$, water deposition reaction $\{*H_2O\}$ is exothermic no matter the chemical pathway considered (reaction **(16)** or **(17)**), but the latter (concerning the non-dissociative adsorption of water in reaction **(17)**) is endergonic. According to our thermodynamic model, deposition of $\{*OH\} + \{*H\}$ is preferred over $\{*H_2O\}$ and $\{*O\} + 2\{*H\}$. However, the complete dissociation of water (reaction **(20)**) is the least favorable surface state at $\theta(O) = 0.25$ and $\theta(H) = 0.50$ ML suggesting that surface OH fragments are thermodynamically preferred, as in reference[187]. In conclusion, the deposition of oxygen from a CO molecule and simultaneous desorption of methane (reactions **(3)**, **(16)**, **(18)** and **(20)**) is thermodynamically more favorable than the deposition of the same surface species from a water molecule (reactions **(4)**, **(17)**, **(19)** and **(21)**). Thus, all oxygen deposition energies reported below refer to oxygen surface deposition from CO and not from water unless otherwise stated. In summary, from a thermodynamic point of view, the CO molecule represents a common reservoir of carbon and oxygen atoms deposited on the surface.

The deposition of hydrogen from $H_2$, paraffin and water molecules are given by reactions **(5)**, **(6)** and **(7)** respectively. Results in **Table** 9 show that the latter two are not favored. The thermodynamics for the deposition of hydrogen given by reaction **(5)** has been studied previously[275,79,276] and our results are in reasonable agreement with those publications (-0.47 compared to -0.52 eV in the present work) considering differences in functionals and calculation parameters, dipole and ZPE corrections employed. Thus, all deposition energies reported in the present work refer to the hydrogen deposition from $H_2$ and not from water nor paraffin molecules.

### 4.3 Stability of carbonaceous species in presence of coadsorbed hydrogen

**Figure 35a** presents the Gibbs free energies, $\Delta_r G^{p,T}$, for the deposition of $C_\alpha H_\beta$ species (see **eq 3** for $\gamma = 0$) on the Co(111) surface as a function of surface coverages of carbon and hydrogen.

Starting from a completely fresh Co catalyst, the gradient of the surface free energy corresponds to the pathway leading to a completely deactivated catalyst by passing through different surface states, where C atoms are in some cases in subsurface positions (gray circles in **Figure 35a**). For $\theta(C) = 2.00\ ML$ the catalyst surface is completely covered with graphitic carbon, and there are no free Co sites available for the FTS reaction to occur. At this point, we consider the catalyst to be fully deactivated, although the deactivation process may have started at lower C coverage.

Considering the calculated structures of the corresponding surface states, the Gibbs free energy of the carbon and hydrogen co-deposition presented in **Figure 35a** can be divided roughly into three zones also represented in **Figure 36** with some key molecular structures of the surface**. Zone 1** corresponds to low and moderate surface coverages of carbon ($\theta(C) < 1.00\ ML$) where configurations with carbon atoms in both subsurface and surface positions are the most stable ones and where multiple hydrogenated carbons such as $\{C_{\alpha=1}H_\beta\}$, $\{C_{\alpha=2}H_\beta\}$ and $\{C_{\alpha=3}H_\beta\}$ may exist depending on C and H coverages. The amount of carbon atoms present in subsurface in **Zone 1** is not sufficient to induce the surface reconstruction phenomenon. Some FTS mechanisms proposed in the literature[74,73,108,277,278,141] consider that the species found in **Zone 1** are involved in chain initiation and chain growth. Hence, their existence and surface concentrations are crucial for the high activity and selectivity of Co catalyst. According to reference[204], the formation of $\{CH_1\}$ is as favorable as the formation of $\{CH_2\}$. This is in line with our results in **Table 9**. However, our most stable surface state for the later C and H coverages ($\theta(C) = 0.25$ and $\theta(H) = 0.50\ ML$) is not in the form of

$\{* CH_2\}$ but rather $\{C H_1 + H_1\}$ species, which is more stable than $\{CH_1\}$ by 0.6 eV/Co surface atom.

**Zone 2** ($\theta(C) \sim 1ML$) presents a decrease in the Gibbs free energy of deposition with multiple hydrogenated carbon atoms: chain initiator and monomer are still present but, some hydrogenated branched carbon chains are often close in energy ($\theta(C) = 1ML$) or even more stable ($\theta(C) = 1.25ML$). These molecular structures may contain ternary carbon atoms which seem more reluctant to hydrogenation (**Figure 36**). The gradient of Gibbs free energy for the deposition reaction in this zone suggests that increasing $\theta(C)$ in **Zone 2** is thermodynamically more favorable than increasing $\theta(H)$. Ternary C atoms in **Zone 2** cannot be hydrogenated according to our calculations since geometry optimization of initially hydrogenated branched C atoms leads to species where hydrogen moves to other C atoms that are not ternary. Therefore, we consider this type of carbon to be hydrogen-resistant. We should emphasize that Co-based FTS catalysts are not considered to be selective for branched C species. Hence, we expect these species to remain preferentially adsorbed on the surface and promote the increase of carbon coverage. In both **Zones 1** and **2**, it should be underlined that the amount of C atoms present in the subsurface is stabilized particularly for $\theta(H) \leq 0.50\ ML$ (**Figure 36** and **Figure** 95). Moreover, for $\theta(C) = 1.00\ ML$ and $1.25\ ML$, surface reconstructions occur in presence of such subsurface C atoms, which may lead to a deactivation pathway in H deficient reaction conditions. In our previous work[205], we showed that two opposite effects involving the interaction of C atoms with surface and subsurface sites are taking place: maximization of Co-C interactions and maximization of C-C interactions. As for the relative stability of C containing structures, adding hydrogen atoms stabilizes surface positions due to the formation of the more favorable C-H bonds with respect to Co-C bonds in the subsurface, whose energy does not compensate costs induced by the associated local distortion of the Co network and the energy barrier for carbon diffusion[279]. In other words, two opposite effects

are taking place in **Zones 1** and **2**: on the one hand, maximization of Co-C interactions and, on the other hand, maximization of *both* C-C and C-H interactions. The detailed effects of hydrogen on the relative stability of C atoms in the subsurface or on surface positions are further described in **Section** 8.5.

**Zone 3**, at $\theta(C) > 1.25\ ML$, exhibits a sharper decrease of the Gibbs free energy where the surface concentration of branched C atoms is increased and multiple hydrogenated carbon atoms are no longer present. Moreover, branched C atoms that compose those structures can be (mono)hydrogenated according to our calculations but they are less favorable compared to purely carbonaceous graphitic structures (see **Section 8.5**) as it can be seen from the evolution presented in **Figure 35**. Indeed, in **Zone 3**, hydrogenated carbon species are slightly destabilized by $\sim 0.14\ eV$ per Co surface atom and per hydrogen added with respect to non-hydrogenated structures. For example, at $\theta(C) = 2.00\ ML$, $\Delta_r G$ is -2.45 and -1.88 eV/Co for $\{C_8\}$ and $\{C_8H_4\}$ species respectively, and therefore the hydrogenation of $\{C_8\}$ species is endergonic. This result could be explained from the stability of aromatic coke precursors resistant to hydrogenation[280,209] (see **Section** 8.5 for a structural analysis). This behavior accounts for a second type of deactivation phenomenon induced by aromatic coke formation. Based on the strongly exergonic energy values involved in the formation of these surface species, we emphasize that, amongst all deactivation pathways mentioned here, this seems to be the major one as highlighted in the litterature[281,282].

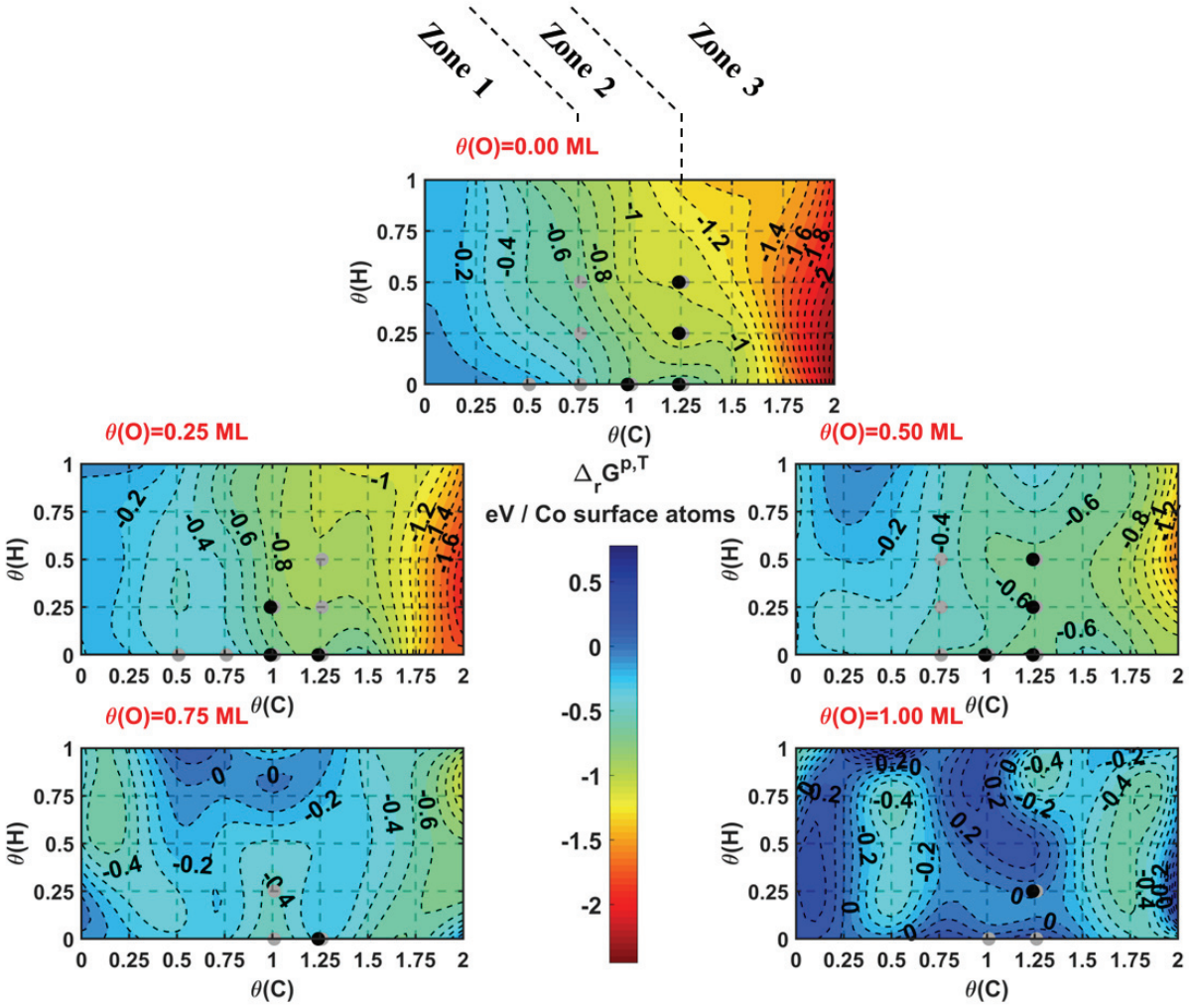


**Figure** 35. Evolution of $\Delta_r G^{p,T}$ at FT conditions ($\alpha = 0.90$, $T = 500\,K$, $P = 20$ bar, $H_2$/CO=2) for different surface coverages of oxygen: (a) $\theta(O) = 0.00$ (b) $\theta(O) = 0.25$ (c) $\theta(O) = 0.50$ (d) $\theta(O) = 0.75$ and (e) $\theta(O) = 1.00\,ML$. Gray and black dots correspond to structures where some C atoms are in subsurface positions; in addition, for black dots surface reconstruction occurs. Level step between successive contour plots is 0.1 eV/Co surface atoms. $\Delta_r G^{p,T}$ is plotted using discrete data points calculated at given surface coverages of carbon, oxygen and hydrogen and has been smoothen by using cubic *spline* data interpolation in Matlab.

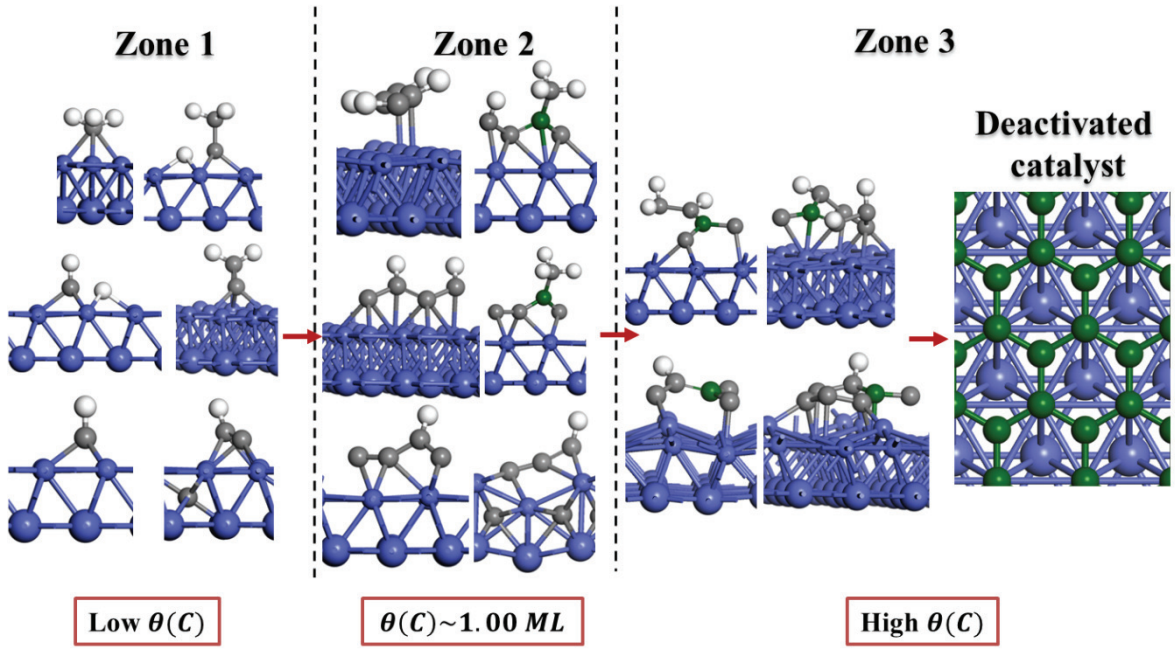


**Figure 36.** Some relevant structures in the three **Zones** of carbon coverages depicted in the manuscript. Ternary carbon atoms are shown in green.

Moreover, some authors[204,209] also found, in accordance with our results, that the most stable form of carbon on the surface is graphene. Weststrate et al.[198] showed that graphene formation is detrimental for catalyst activity and proposed a graphene growth mechanism on Co(0001).

The evolution of the surface states presented in **Figure 35** is based on thermodynamic considerations and cannot answer the question of how fast the transition from clean to the graphene-covered Co surface will occur. However, if we compare our thermodynamic results with the works of Hu et al.[93,117,283], where the activation barriers for different carbon-carbon coupling elementary steps are reported, the coupling reactions leading to the formation of hydrogen-resistant carbon are kinetically slow as they present high activation barriers due to the coupling of bare surface C atoms with other species. This explains the slow and irreversible deactivation profile of the catalyst usually reported in the literature.

Peña et al.[284,280,285] recently identified and characterized carbonaceous species on the surface of spent alumina supported cobalt catalysts using different experimental techniques. Using temperature-programmed hydrogenation-mass spectrometry (TPH-MS), it was shown that the surface of spent catalysts contained strongly adsorbed residual hydrocarbons and hydrocarbon fragments in agreement with both Moodley et al.[195] and Gruver et al.[286]. Indeed, in **Zone 2**, hydrogenated carbonaceous species can be regarded as hydrocarbon precursors of coke and/or hydrocarbon fragments that interact strongly with the surface. In the latter works, a high-temperature TPH-MS peak around $T = 450°C$ was attributed to polymeric (amorphous) carbon. Taking into consideration that the definition of polymeric carbon is somewhat vague, but also considering the results we presented for **Zone 3**, we could attribute that high temperature TPH-MS peak to hydrogenated carbonaceous structures with multiple ternary carbon atoms connected by covalent bonds and resistant to hydrogenation, as our thermodynamic analysis in **Figure** 35 suggests. Those species hinder the active surface sites and therefore deactivate Co-based[195,194,287] and Rh-based[288,289] FTS catalysts. In addition to that, Peña et al [280] also reported measurable amounts of 2-methyl branched carbon species adsorbed on the wax-extracted from spent Co-based FT catalyst using gas-chromatography-mass spectrometry (CG-MS). A small amount of branched hydrocarbons in the FT reaction products was found in[9,280], but they are predominantly mono-methyl species. The existence of those species on the surface of a spent catalyst suggests strong adsorption in accordance with our DFT calculations (see the simulated carbonaceous structures in **Zone 2** reported in **Figure 36**) and subsequent deactivation, although the activity decrease was not directly correlated with the quantity of branched species in Peña's work. Moreover, under extremely deactivating conditions, the formation of 6-membered ring (aromatic) compounds is reported in that work, which can be related to simulated structures found in **Zone 3** (**Figure 36**).

Moodley et al.[195] reported a hydrogen resistant polymeric type of carbon species and proposed chains of polymeric carbon species or hard to remove wax as detrimental for catalyst activity. Their study showed that there is an increase in hydrogen resistant carbon with increasing time on stream for wax-extracted Co catalysts, which can be related to the increase in the quantity of ternary-branched C atoms we found. Moreover, according to that study, those hydrogen resistant carbon species have similar reactivity to polymeric carbon. Further studies on the mechanism of the FTS on Co showed that there is a decrease in the probability of branching with time until the steady-state is reached, which might contradict our interpretation[69]. In addition, at steady-state, branching probability declines exponentially with carbon number (for larger $C_4$ chain length). In our opinion, those results can be attributed to the fact that, according to our study, branched carbon chains (**Zone 2**) could become a part of coke-like structures (**Zone 3**) on the surface of greater stability and thus remain undetected as ordinary FT products. This reinforces the idea that highly branched coke-like structures are not likely to be detected as a product in the transient experiments performed in reference[69]. It should also be noted that authors in that work do not report the (transient) quantities of carbon that remains on the surface. Therefore, the reported branching probability, in our opinion, refers only to desorbed products and not to the overall branching probability that also includes species that do not desorb from the surface.

These results can also help us to understand the selectivity loss issues of Co-based catalysts. In agreement with mechanisms of the FTS reaction reported in the literature[74,73], the evolution of surface states in **Figure 36** suggests that, in **Zone 3** ($\theta(C) > 1.25\ ML$) and partly **Zone 2** ($\theta(C) \sim 1.00\ ML$), propagation reactions are less prone to occur due to the lack of $CH_3$ and $CH_2$ species. In these regions, and more particularly in the absence of hydrogen, C atoms tend to couple and form linear chains on the surface while maintaining Co-C bonds whereas, in the presence of hydrogen they tend to be lifted from the surface (**Zone 2**, **Figure 36**)

indicating weaker interactions with the surface compared to linear chains found in previous works (see reference[209,205]). If $\theta(C)$ is increased, the formation of ternary carbon atoms increases. According to reference[209], high carbon coverages will result in the formation of oligomers involved in an island formation process as proposed by others[229,290,204]. Here, we propose that ternary carbon atoms may be regarded as the precursors of cyclic carbonaceous species and as coke precursors. Therefore, the evolution of the surface states from **Zone 1**, where $CH_3$ and $CH_2$ are dominant species, to **Zone 2,** where hydrogen resistant C atoms are dominant ones, can be at the origin of both the loss of free Co sites (leading to catalyst deactivation) and a depletion of species involved in the propagation mechanism of the FT reaction.

### 4.4 Stability of carbonaceous species in presence of coadsorbed hydrogen and oxygen

Regarding now the effect of oxygen, **Figure 35b-e** reveals that oxygen may impact significantly the overall stability of hydrocarbonaceous species previously identified. The key question is to determine whether this impact of oxygen is thermodynamically favored or not. For the lowest $\theta(O) = 0.25\ ML$, the trend for the overall evolution of the Gibbs free energy remains similar to the previous one in absence of adsorbed oxygen (**Figure 35a**). However, for $\theta(O) \leq 0.75\ ML$, the energy is shifted towards more positive (destabilization impact) and negative (stabilization impact) values in **Zones 3** and **1**, respectively, whereas **Zone 2** is less affected. For $\theta(O) = 1.00\ ML$, all three zones are shifted towards more positive energies thus suggesting that such a high surface coverage of oxygen is thermodynamically unfavored except for the case where $\theta(C) = 0\ ML$ with $\theta(H) = 1\ ML$ leading to the formation of OH groups. This analysis is summarized in **Figure 37** which reports the most stable oxygen coverages at a given $\theta(C)$ and $\theta(H)$ coverage, corresponding to the minimal value of energy,

i.e. $\min_{\theta(O)} \Delta_r G^{p,T} = f(\theta(C), \theta(H))$ . The corresponding reactions leading to this energy mapping are given in **Section** 8.7 .

This $\Delta_r G$ map, compared to the one of **Figure 35a**, in absence of O atoms co-adsorbed on the surface, clearly highlights that only **Zone** 1 and **Zone** 2, for $\theta(C) = 1.25\ ML$ and $\theta(H) = 0\ ML$ are affected by co-adsorbed O atoms.

Our results thus infer that at the early stages of the catalyst lifetime (**Zone 1**), oxygen has a significant impact on the stability of the hydrocarbonaceous species on the Co surface. However, in **Zone 3**, carbon preponderates over oxygen making **Zone 2** a transition zone between O rich and C rich surface coverage regimes. Moreover, **Figure 37** shows that the deposition of oxygen from CO is favorable roughly until $\theta(O) = 1.00\ ML$. However, the extent to which oxygen is deposed in the form of surface species depends on the amount of carbon and hydrogen atoms present on the surface.

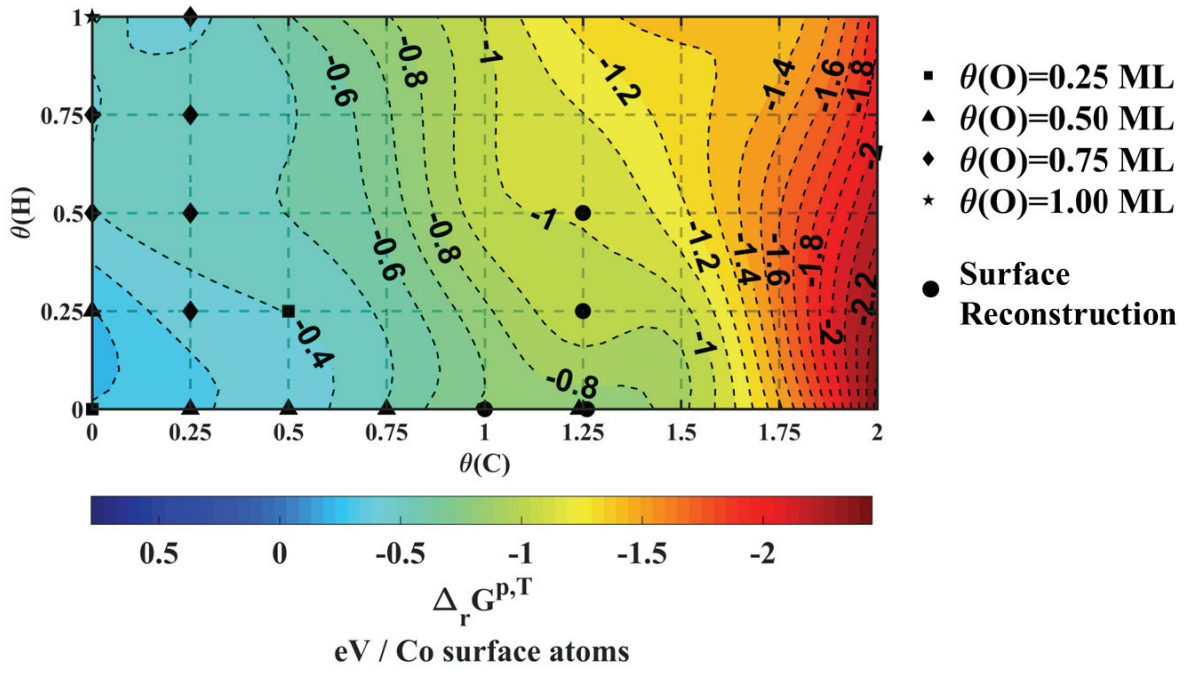


**Figure 37.** Most favorable oxygen coverages as a function of $\theta(C)$ and $\theta(H)$ and their associated $\Delta_r G$ at FT conditions ($\alpha = 0.90$, $T = 500\ K$, $P = 20$ bar, $H_2$/CO=2). Black dots correspond to surface reconstruction. Level step between successive contour plots is 0.1 eV/Co surface atoms. The reactions corresponding to each point of the energy grid are given in **Section 8.6**.

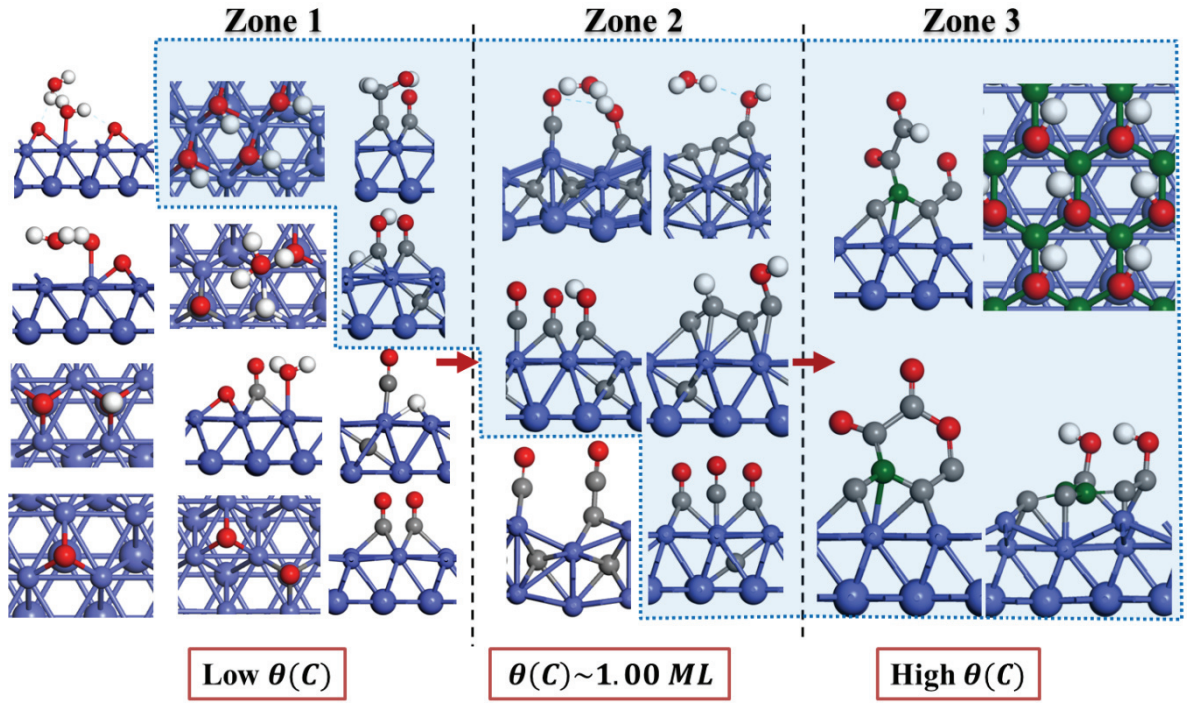


**Figure 38**. Some relevant oxygen-containing surface species in the three Zones of carbon coverages depicted in the manuscript. Ternary carbon atoms are shown in green. Shaded **Figures** represent structures that do not correspond to $\min_{\theta(O)} \Delta_r G^{p,T}$ but are thermodynamically metastable only in **Figure** 31b-e.

In **Zone 1,** for $\theta(C) = 0ML$ , (hydro)oxygenated surface states seem thermodynamically very favorable making CO a very strong oxidizing agent (since oxygen is deposed from this molecule and not from water according to our discussion in **Section 4.2**. The most abundant surface intermediates in **Zone 1** for $\theta(C) = 0\ ML$ are chemisorbed $\{* OH\}$ and/or $\{* O\}$ and physisorbed water $\{* H_2O\}$. Indeed, if no carbon is available on the surface, oxygen atoms interact with surface Co sites that become oxidized. Nevertheless, at higher hydrogen coverages ($\theta(H) \geq 0.5\ ML$), water formation is favored. Although water molecules (and oxygen atoms therein) may be considered in close contact with Co sites, surface oxidation (i.e. formation of Co-O bonds) at high hydrogen coverages is absent and the loss of activity due to oxidation seems unlikely compared to carbon deposition. The general trend in molecular structures involved in **Figure 37** is that for oxygen deposition in contact

with Co sites (in the form of $\{* O_\gamma\}$ and $\{* OH\}$) is only be achieved for very low surface coverages of oxygen ($\theta(O) < 0.5\, ML$) (**Figure 38**). For the highest surface coverage of oxygen, ($\theta(O) = 1\, ML$, no hydroxyl group is formed but rather physisorbed water and chemically adsorbed O which are thermodynamically favorable thus suggesting deactivation by oxidation in **Zone 1** ($\Delta_r G = -0.54$ eV/Co with $2\{O_1\}^* + 2\{H_2O\}^*$ as surface state). Deposition of water $\{H_2O^*\}$ in on-top sites of cobalt leads to structures where water is only physisorbed with an Co-O average distance of 2.33Å in agreement with previous studies [188,189,291,292]. Moreover, for $\theta(O) = 0.25\, ML$ and $\theta(H) = 0.50\, ML$ the most favorable surface state is $\{OH\}^* + \{H\}^*$ (**Figure 35b**) ($\Delta_r G = -0.15$ and 0.09 eV/Co surface atoms for CO hydrogenation and $H_2O$ dissociation pathway, respectively) also in line with previous works[188]. Thus, oxidation of active phase may be considered thermodynamically possible in **Zone 1** in particular for $\theta(O) > \theta(C) = 0$ due to favorable Co-O interactions in the absence of carbon, which itself represents a more favorable adsorption site for oxygen than that for Co as explained below. Thus, it seems that direct oxidation of Co sites (and formation of FT inactive cobalt oxide phases) whatever the path for oxygen deposition studied, is thermodynamically possible under FT conditions as long as no carbon atom is simultaneously deposited on the surface.

Increasing surface coverage of carbon on the surface expands the chemical diversity on the surface in **Zone 1** ($0 < \theta(C) < 1\, ML$). In this region, we obtained many surface states of involving numerous adsorbed CO molecules $\{* CO\}$. As soon as one O atom is deposited on the surface, it will preferentially bind to one C atom forming one adsorbed CO molecule. When sufficient C atoms are deposited together with O atoms, the formation of adsorbed CO molecules occurs in **Zone 1** and **Zone 2** which is consistent with previous works reporting the role of high surface coverages of CO during FT synthesis [293,273,107]. If an excess of O atoms

with respect to C atoms is achieved ($\theta(O) > \theta(C)$), the extra O atoms with respect to C form either $\{* O_\gamma\}$ or $\{* OH\}$ or water adsorbed on the surface.

We also obtained metastable $\{* COH + * H\}$, $\{COH - CH\}$ and $\{* COH\}$ surface states thus preserving strong C-O bonds and avoiding direct surface oxidation by O atoms. **Figure 37** and **Figure 38** also suggest that adsorbed COH and CO species represent the most stable "oxygenated" carbon species which may be related to the hydrogen-assisted CO activation mechanism proposed in the literature[96,94,283,86]. In **Zone 1**, oxygen atoms represent the preferential adsorption sites for hydrogen whereas carbon represent the preferential adsorption sites for oxygen thus leading either to the elimination of the surface oxygen atoms in the form of water (for low surface coverages of carbon) or to precursors of oxygenated species (for high surface coverages of carbon). Multiple oxygenated surface carbon atoms that are also metastable according to our energy values could be regarded as either the precursors of FT secondary products such as, $CO_2$ and/or carboxylic acid, or structures relevant to the regeneration of the Co catalyst by oxidation treatments rather than precursors of main FT products. Further work needs to be undertaken in order to confirm this hypothesis.

Among stable oxygenated structures in **Zone 1** and **2** (**Figure 38**) we also find structures with C in subsurface positions similarly to the previous case $\gamma = 0$. However, surface reconstruction and formation of carbide Co species may occur only in **Zone 2** as it requires the migration of about 0.50 ML of carbon atoms in subsurface positions. Thus, contrary to the effect of hydrogen on carbon showed in **Section 4.3** for the same $\theta(C)$, oxygen does not extract C from the subsurface. This is a rather interesting feature since it further confirms the fact that, at hydrogen poor conditions and also at high θ(CO) conditions, deactivation by Co-carbide formation and/or surface reconstruction may occur in line with previous works[202]. However, hydrogen addition (**Figure 37**-**Figure 38**) does not favor those Co-carbide structures where surface reconstruction occurs; instead, structures where some or

all C atoms are on the surface become thermodynamically the more favorable ones and thus deactivation by the formation of polymeric hydrocarbons occurs.

The structures obtained for the low surface coverages of carbon in the presence of both hydrogen and oxygen can be related to oxygenates detected by Peña et al. [280,294,285] and Pinard et al. [287] at high CO-conversion conditions on the surface of spent Co-based FT catalysts. In the latter works, the authors identified four different groups of species on the surface of spent Co-based FT catalysts. They identified hydrogen resistant alcohols and carboxylic acids ("soluble coke") on the surface of a spent catalyst, which can be related to some hydroxy carbene species found in **Zones 1** and **2**. According to these previous experimental works, under hydrogenating conditions, it was necessary to raise the temperature to 500°C to remove such species from the catalyst surface. Indeed, our calculations also show that those species are expected to be present as long as oxygen surface coverages are below 1 ML.

High surface coverages of carbon with co-adsorbed oxygen atoms (**Zone 3** in **Figure 38)** are thermodynamically stable but to a far lesser extent than the oxygen-free surface as described in **Section 4.3**. Increasing surface concentrations of oxygen destabilizes hydrocarbon chains in **Zone 3**. Moreover, oxygenated hydrocarbon chains for those structures present some significant differences compared to oxygen-free chains. As we showed in **Section 4.3,** the latter, interact with Co surface, thus blocking active sites, whereas the former ones are partially detached from Co surface, implying less Co-C bonds (see **Figure** 100). As shown by their Gibbs free energies, the structures in **Zone 3** with high surface coverages of oxygen are not stable under FT conditions, but they may be more relevant during catalyst regeneration when oxidation conditions are used to remove detrimental forms of carbon. Complementary work is required to confirm this hypothesis.

Several insights into the impact of oxygen on the stability of hydrocarbonaceous Co supported chains can be deduced from the structural analysis. Firstly, oxygen shows a preferential tendency to bind with C rather than with Co (**Figure 38**). Although Co-OH species are possible, in agreement with the literature [96,204,108,268], C always represents a more favorable binding site for oxygen than cobalt according to our calculations. The affinity of oxygen towards carbon could be because the strong CO bond is energetically more favorable even in the presence of other carbon and hydrogen atoms. As long there are free carbon atoms on the surface, oxygen tends to bind them, either alone (forming chemisorbed CO) or in the form of C-O-H fragments present in a bigger chain. Moreover, although we obtained adsorbed hydroxyl groups in many cases, they represent the most stable structures only when there are no carbon atoms on the surface. Besides, the deposition of higher quantities of OH groups on the surface of Co is energetically less favorable than water formation thus suggesting that their removal from the surface as a water by-product is preferred in agreement with the literature[96,199,295]. Besides, mechanistic studies concerning water elimination are limited and water formation remains elusive[269]. Our prediction of the surface coverages of $OH_\beta$ are in agreement with Van Helden et al.[296], who compared experimentally [297] obtained surface coverages of different species with different micro-kinetic models and reported $OH_\beta$ surface coverages in the range 10~20% for theoretical models, thus overestimating the experimental value of ~10% (**Figure 36-Figure 38** suggest that OH coverage can be upmost 0.25 $ML$). For $\theta(O) > 0.25$ ML, surface states with physisorbed water are preferred according to our calculations. Hence, those rather low surface concentration of oxygen in [296,297] could be associated with relatively fast water desorption. In addition, the possible CO coverages obtained by our analysis varies from $\theta(CO) = 0.25\ ML$ and $\theta(CO) = 0.50\ ML$ which is in reasonable agreement with the experimental values in the literature ($\theta(CO) = 40\%$ in ref. [297] and micro-kinetic predictions $\theta(CO)$ between 40% and 60% [296]). As for the position of

hydrogen atoms in the presence of O, they are stabilized either on carbon, oxygen or on free Co sites, which reveals the structural flexibility and mobility of H which is available to react with both C and O species during FT synthesis

## 4.5 Conclusions from thermodynamic calculations

In this section, we presented a thorough ab initio thermochemical investigation of the cobalt surface under FT reaction conditions. We quantified the stability domains of $C_\alpha H_\beta O_\gamma$ species formed on Co surface by calculating the Gibbs free energy of their deposition reactions, including the effects of (T, $CO/H_2$ pressures) and the Anderson-Schulz-Flory coefficient. We explore systematically different chemical reactions and identify the most thermodynamically favored according to their Gibbs free energies in order to analyze the possible deactivation routes. We systematically presented the molecular structures of the $C_\alpha H_\beta O_\gamma$ surface species that could be at the origin of the surface deactivation.

From this analysis, we identify three main zones of chemical surface speciation depending on the (C, H, O) coverages. In zone 1 ($\theta(C) \leq 0.75\ ML$ and $0 \leq \theta(H) \leq 1\ ML$) the nature of stabilized species present clearly correspond to $CH_x$ monomers required for FT synthesis. However, this zone is sensitive to the deposition of O atoms whose surface coverage may reach 0.75 ML by interacting with:

- C in undissociated CO adsorbed molecules,
- H atoms leading to OH or water molecules
- Oxidized Co sites

The latter case may be at the origin of some activity loss of Co sites. It is essential to notice that this oxidation route is thermodynamically driven by the dissociation of the CO molecule (with desorption of hydrocarbons) and not by water dissociation alone.

In **Zone 2** ($1 \leq \theta(C) \leq 1.25\ ML$ and $0 \leq \theta(H) \leq 1\ ML$), we found an increase in the oligomerization degree of $C_xH_y$ linear chains that are key intermediates for FT synthesis.

Simultaneously, these intermediates may compete with the formation of branched hydrocarbon chains exhibiting ternary carbons reluctant to hydrogenation. In this zone also, the reconstruction of the cobalt surface occur through the migration of C in metal subsurface sites. It must be underlined that in **Zone 2**, O atoms are only expected to have a weak effect on activity: due to the higher carbon surface coverage, O atoms are not allowed to interact directly with the Co sites, but they rather bind with the C over layer. Moreover, most of these cases where O atoms are present, are metastable with respect to other surface species.

In **Zone 3** ($1.5 \leq \theta(C) \leq 2\ ML$) the Co surface is predominantly covered by C atoms forming either multiple branched chains or a graphitic overlayer. This surface state can be defined as the ultimate deactivation state of the surface since graphitic coke is poisoning a large domain. The branched hydrocarbons (found in **Zone 2** and **3**) may be also considered as precursors of this graphitic over layer. As for **Zone 2**, no direct O-Co interaction is found to be stable: metastable O atoms are always located on top of the carbon overlayer.

Finally, regarding H atoms, it is generally found that they may be located either on C atoms, O or Co sites if available. The weak effect on the deposition energy implies that they are rather flexible to participate in other reaction mechanisms.

# 5 Deactivation Mechanism of Co-based FT catalysts

In **Chapter 4**, we identified three structural domains containing surface species related to activity and selectivity trends discussed in the literature. In terms of hydrocarbon species $C_\alpha H_\beta$ , we showed that in a low carbon coverage domain (**Zone 1**) different hydrocarbonaceous species can be formed in which C-C and C-H (and sometimes Co-C and Co-H) bonds are established (**Figure 36**). In **Zone 2,** linear and branched $C_\alpha H_\beta$ chains, considered as a polymeric hydrocarbon structures are favored. Finally, in **Zone 3**, the catalyst is considered deactivated since its surface sites are shielded with multiple branched chains or a graphitic overlayer. The exact mechanism and the kinetics of the evolution from the fresh catalyst, in **Zone 1**, to deactivated catalyst, in **Zone 3**, has not been considered. Moreover, no assumption has been made on the precursor of deleterious carbon in **Zone 3**. In order to improve the current micro-kinetic model and take into consideration the deactivation and selectivity losses, there is a need to describe the exact nature of all suface reaction intermediates involved and their transformation towards carbon overlayer deactivating the Co catalysts in **Zone 3**. To the best of our knowledge, literature data on the exact mechanism of such transformations does not exist.

In this chapter, we first put a brief emphasis on some experimental observations and mechanistic studies presented in **Chapter 2** and compare them with our findings in **Chapter 4**. Based on those publications, we propose a mechanistic pathway from **Zone 1** to **Zone 3,** i.e. a catalyst deactivation phenomena. Then, we substantiate the proposed deactivation mechanism by calculating both thermodynamic and kinetic properties of this scheme using molecular modeling techniques described in **Section 3.1.5**. Based on those results, we perform an analysis of the zones described in **Chapter 4** and we propose a microkinetic deactivation mechanism.

Compared to other metals such as Pd, Pt and Rh[298], studies involving Co surfaces are limited. Weststrate et al.[198,211,212] showed that ethylene pre-covered Co(0001) participates in dehydrogenation reactions and subsequent formation of polymeric C and graphene species. Although they identified some ethylene decomposition products and proposed a $C_2H_\beta$+ $C_2H_\beta$ + $C_2H_\beta$ cyclopolymerization mechanism for the formation of deleterious C species found in **Zone 3** in **Chapter 4**, the exact nature of the $C_2H_\beta$ surface species remains unknown. Vaari et al. [216] showed that acetylene pre-covered Co(0001) surface transforms at around 400K (thus below typical FT conditions) into a carbonaceous overlayer composed of graphitic carbon and a small amount of carbidic carbon. Ramsvik et al.[215] suggested that acetylene pre-covered $Co(11\bar{2}0)$ surface decomposes at around 300K to either $C_2H$ or $C_2$ fragments with subsequent formation of graphitic carbon when further heated. Those observations are also in line with the experimental results of Xu et al. [142,217]. Zhang et al. [219] performed a DFT study on the mechanism of ethylene decomposition over Co(0001) and concluded that acetylene CHCH and acetylide CHC species might be regarded as the key precursors of low-temperature graphene formation through cyclotrimerization and dehydrogenation reactions.

Hence, based on up to date experimental studies, it seems that ethylene decomposition products and subsequent reactions of those species can alter the catalytic performances negatively. However, there is no explicit agreement on the structure of $C_2H_\beta$ surface species that initiate the growth of deleterious carbon species. Besides, to our knowledge, proposed cyclopolymerization mechanism of the unknown $C_2H_\beta$ leading to the formation of deleterious carbon has never been examined using DFT methods. Considering proven olefin readsorption reactions described in **Section 2.3.8** and ethylene deviations from the ideal-polymerization case as predicted by the ASF distribution discussed in **Section 2.2,** in this chapter we hypothesize that an FT synthesis product, ethylene itself, can be considered as a coke precursor. By examining this hypothesis, we expect to obtain some valuable insights into the

coke formation mechanism and the conditions at which this pathway can be activated. Thus, in order to verify our hypothesis, we first carry out a DFT study in which we examine a reaction pathway of ethylene decomposition reactions on Co(111). Then, based on a micro-kinetic model of ethylene decomposition, we shed some light on kinetically and thermodynamically favorable ethylene decomposition product(s), some of them found in **Chapter 4**, that can be regarded as the deactivation initiator(s). Then, in a second time, we study using DFT a mechanistic pathway for the coupling reactions between deactivation monomer units leading to the formation of a cyclic coke seed (precursor) identified in **Zone 3 (Chapter 4).** Lastly, we propose a mechanism that allows coke-seed growing yielding eventually deactivated Co(111) surface due to active site-blocking effects.

## 5.1 Computational methods

Transition states of proposed reaction pathways are studied using periodic ab initio DFT calculations as implemented in the VASP code [247,248]. Details about total energy calculations can be found in **Section 4.1**.

A four-layer slab was used to model the Co(111) surface built from the fcc-Co bulk phase in the same spirit as in **Chapter 4**. In order to eliminate the influence of lateral interactions between large C-containing species as found in **Zone 3**, the surfaces were represented using p(4x4) surface unit cells. Hence, one atom in this unit cell corresponds to $\frac{1}{16}ML$ surface coverage in contrast to $\frac{1}{4}ML$ in **Chapter 4**. Those models have approximately a 15 Å empty layer between the repeating surfaces to describe the vacuum and to minimize lateral interactions. All the atoms in the configurations were allowed to relax upon optimization except from those in the bottom two layers. According to our benchmark calculations in **Section 8.3.2**, the dipole correction is negligible in our models. Hence, we performed our calculations without this correction.

Reaction pathways have been studied using Nudge Elastic Band (NEB) and the Climbing Nudge Elastic Band (CI-NEB). The initial reaction pathway is obtained using local reaction path generator, Opt'n Path[245] by introducing eight intermediate images to be optimized between initial and final states. The geometries of initial and final states computed previously in **Chapter 4** using p(2x2) were re-optimized using p(4x4) surface unit cell. Transition states have been refined by a subsequent Steepest-Descent geometry optimization and confirmed by the presence of a single imaginary vibration mode along the reaction coordinate.

Based on the DFT calculated energy profiles, a micro-kinetic model study has been conducted using the MKMCXX package created by the Inorganic Materials Chemistry group at the Eindhoven University of Technology [299]. In this package, the set of ordinary differential equations is solved using the Backward Differentiation Formula. The activation energy of all surface reactions are taken at $T = 0K$ and reaction rate constants are estimated within the context of transition state theory thus assuming the validity of Arhenius law. Pre-exponential factor mainly governed by $\frac{k_b T}{h}$ of all surface reactions is set to its typical value of $10^{13}$ (see [300]). Thus, no entalphy and entropy contributions are included in this work. In addition, zero-point energy corrections are neglected. For adsorption/desorption equilibrium of hydrogen, non-activated adsorption is assumed and the desorption rate constant is calculated assuming Hertz-Knudsen law of adsorption/desorption equilibrium:

$$k_{ads} = \frac{PAS}{\sqrt{2\pi m k_b T}} \qquad \textbf{Eq.}\ 70$$

$$k_{des} = \frac{k_b T^3}{h^3} \frac{A(2\pi m k_b)}{\sigma \theta_{rot}} e^{\left(\frac{-E_{des}}{k_b T}\right)} \qquad \textbf{Eq.}\ 71$$

In **Eq.** 70 and **Eq.** 71, $P$ is the partial pressure of the molecule in the gas phase, $A$ is the area of the surface site taken to be $10^{-19}$, m is the mass, $T$ is the temperature, $k_b$ is the Boltzman constant set to $1.381*10^{-23}$ $m^2kgs^{-2}K^{-1}$, $h$ is the Plank constant equal to $6.26*10^{-23}m^2kgs^{-1}$, $S$ is the sticking coefficient taken to be unity, $\sigma$ is the symmetry number, $\theta_{rot}$ is the rotational temperature calculated from statistical thermodynamics, $E_{des}$ is the desorption energy. Experimental desorption energy have been used for hydrogen [79,276] in order to account for lateral interactions of adsorbates in the experimental surface.

## 5.2 Identification of deactivation initiator

In this subsection, we test the hypothesis that ethane can be considered a coke precursor, considering recent experimental [198,211,212] and theoretical [219] results. As we showed in **Section 2.3.8,** olefins can undergo re-adsorption and further side-reactions on account of π-bond reactivity. Besides, ethene shows deviation from the ideal-polymerization case as predicted by the ASF distribution discussed in **Section 2.2**. Thus, it seems crucial to understand the type of reaction ethene molecule can undergo and provide an answer to its transformation reactions once readsorbed on Co(111) surface. A previous theoretical study[219] has shown that CC bond scission reactions of ethylene and its dehydrogenation products on the Co(0001) surface are energetically very demanding. Thus, in this work, we do not consider CC bond-breaking reactions. Wang et al. [218] proposed a pathway of ethylene transformation to graphene in which ethene is first dehydrogenated to ethylidyne $CCH_3$ species and proposed a 2+2+2 cycloaddition reaction of those species as responsible for the formation of cyclic $C_6H_\beta$ coke precursors. However, this reaction does not explain how tri hydrogenated carbon of ethylidyne species $CCH_3$ lose their terminal hydrogen in the formation of mono hydrogenated cyclic $C_6H_\beta$ coke precursors. Hence, here we focus on the calculation of C-H bond scission/formation but also H transfer reaction to account for dehydrogenation of ethylidyne species on the Co(111) surface, starting from the ethylene

molecule in gas-phase. Hence, we propose studying geometric and energetic characteristics of transformations depicted in **Figure 39**.

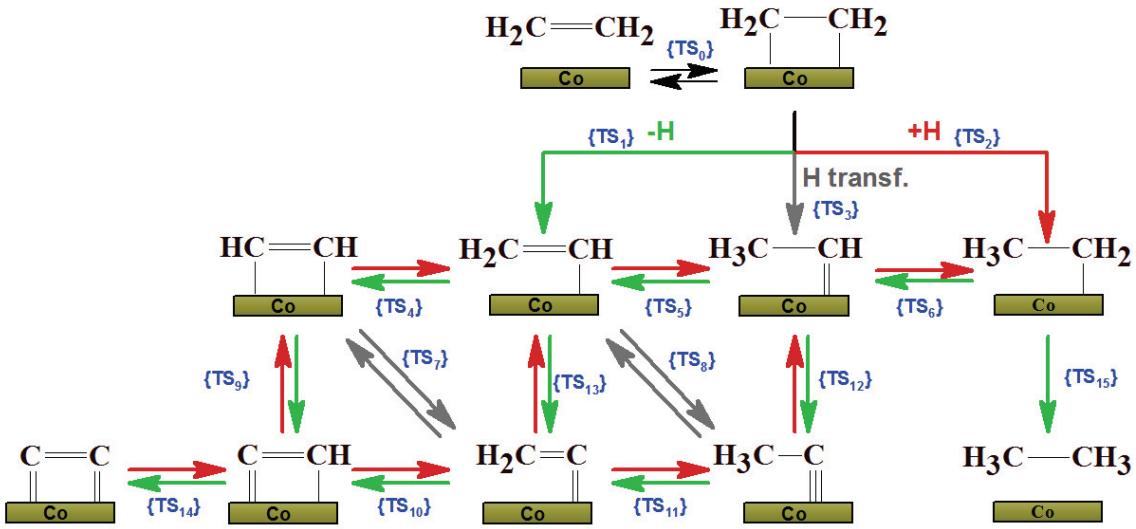


**Figure 39.** Schematic representation of ethylene transformations we proposed in this work. Dehydrogenation, hydrogenation and H transfer reactions are shown in green, red and gray, respectively. Note that hydrogenation and dehydrogenation reactions share the same transition state structure. Transition state labels are shown in blue.

### 5.2.1 Geometric and energetic properties of transition states

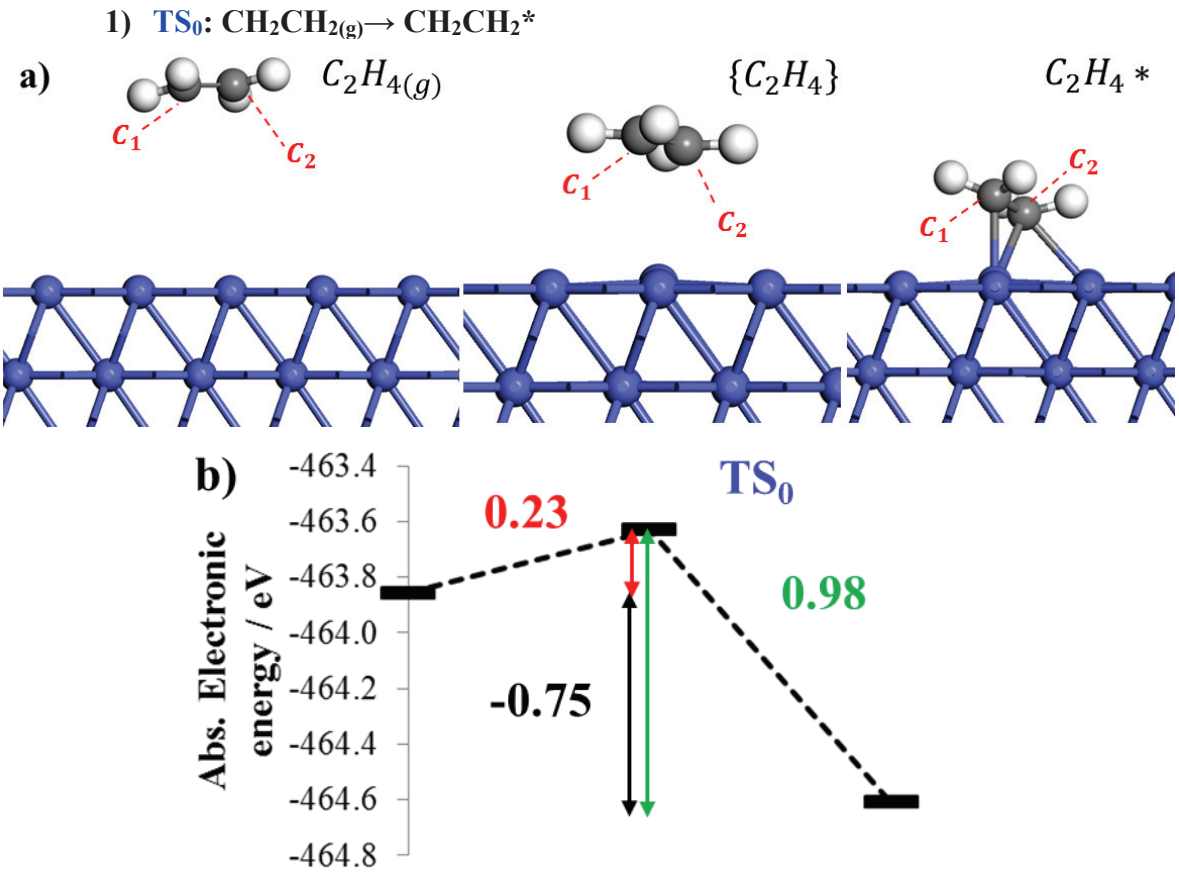

**Figure** 40**.** a) Geometric and b) energetic characteristics ethylene readsorption reaction.

Ethylene molecule initially present in the gas phase (d($C_1C_2$)=1.33Å) approaches a Co(111) on-top site. In the transition state, molecular $C_2$ axis that passes through both carbon atoms is approximately parallel to a Co surface. Transition state $TS_0$ was confirmed by a vibrational frequency calculation that gave one imaginary vibrational mode of $\tilde{\nu} = -83.6\ cm^{-1}$ in which C-C skeleton (d($C_1C_2$)=1.35 Å) moves in phase in the direction parallel to the surface normal vector, suggesting the existence of π-bond interaction of ethylene with Co electron-density. The result for this transition state, hence, can be related to Dewar-Chat-Duncanson model where π electron density is donated to the metal surface, whereas d-electron density of metal is back donated to an empty antibonding π* orbital of the hydrocarbon [301,142]. In its final state $CH_2CH_2$*, ethylene is adsorbed in the non-dissociative manner with one $CH_2$ fragment located at a on-top site ($C_1$) and the second one ($C_2$) located at an hcp site (d($C_1C_2$)=1.45 Å, d(C1Co)=2.02 Å, d($C_2$Co)=2.11 Å. The energy barrier of this reaction is 0.23 eV, suggesting kinetically fast ethylene readsorption. In addition, this reaction is highly exothermic which implies favorable thermodynamic properties for the deposition reaction. In contrast, the reverse reaction is both kinetically (0.98 eV barrier) and thermodynamically unfavorable ($\Delta E = +0.75\ eV$).

**2) $TS_1$: $CH_2CH_2$*+*→ $CH_2CH$* + H***

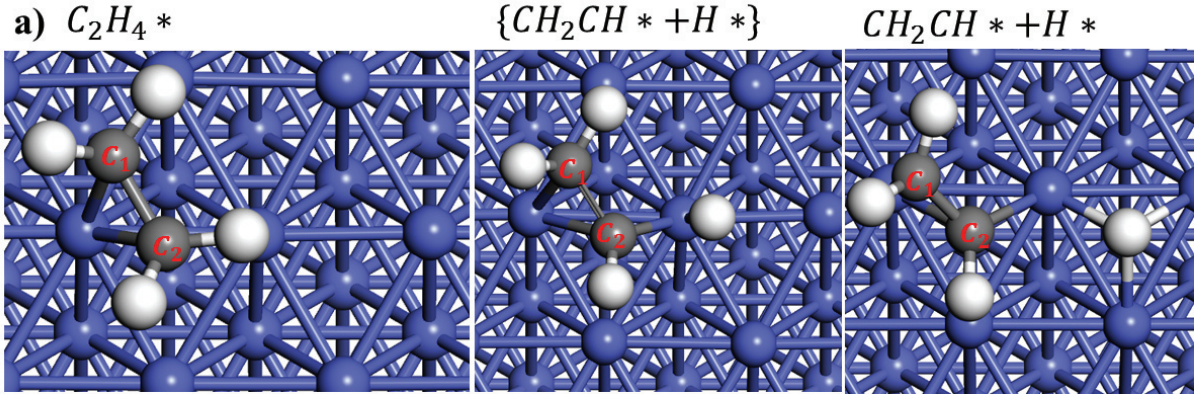

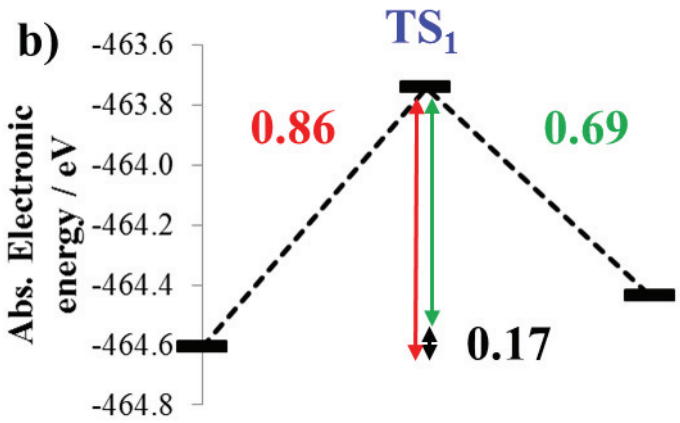


**Figure** 41**.** Geometric and energetic characteristics of the ethylene to vynil decomposition reaction.

Initially adsorbed ethylene molecule with d($C_1C_2$)=1.45 Å extends its CH bond from d($HC_2$)=1.13 Å to d($HC_2$)=1.70 Å in the transition state (stretching mode $\tilde{\nu} = -823.9\ cm^{-1}$). In the latter structure, outgoing hydrogen goes to a neighbor fcc hollow site by passing over an on-top Co site in the transition state (d(HCo)=1.53) Å. The activation energy for this deprotonation and protonation reactions are 0.86 and 0.69 eV, respectively, suggesting that the former is kinetically inhibited. Besides, deprotonation reaction is endothermic, indicating that the backward reaction is thermodynamically preferred.

**3) $TS_2$: $CH_2CH_2$*+ H*→ $CH_3CH_2$* +***

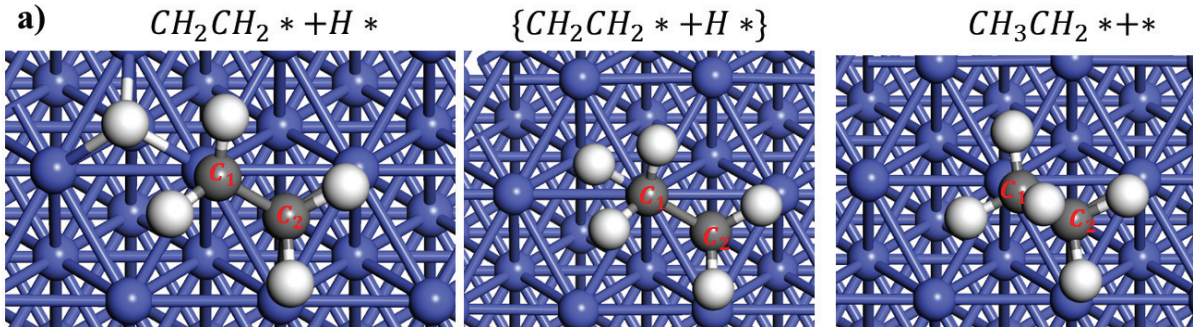

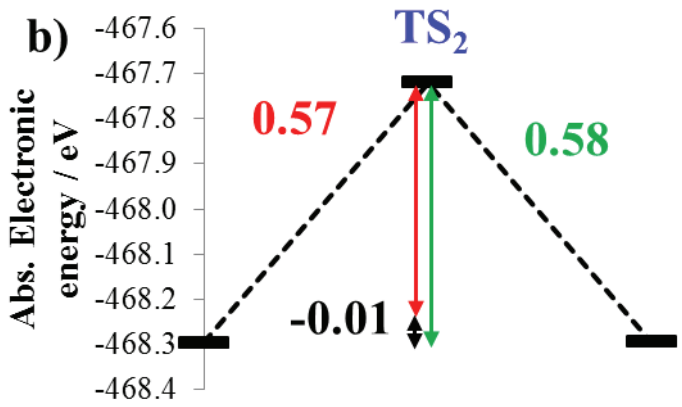


**Figure** 42. a) Geometric and b) energetic characteristics of hydrogenation of ethylene to ethyl reaction.

Surface hydrogen sat in the hcp-hollow site d(HCo)=1.68 Å approaches surface ethylene (d($C_1$Co)=2.07 Å, d($C_2$Co)=2.09 Å, d($C_1C_2$)=1.47 Å) over the on-top Co site below $C_1$ in the transition state where d(HCo)=1.60 Å (stretching mode $\tilde{\nu}(CH) = -892.5\ cm^{-1}$). $C_1$H bond legth shrinks from d($C_1$H)=1.50 Å in the transition state to d($C_1$H)=1.11 Å in the final state. The evolution from the transition to the final state modifies CC and CoC bonds from d($C_1$Co)=2.07, d($C_2$Co)=2.09, d($C_1C_2$)=1.47Å to d($C_1$Co)=2.76, d($C_2$Co)=2.15, d($C_1C_2$)=1.54Å. Note that hydrogenated carbon $C_1$ is pushed away from the surface due to hydrogenation and consequent weakening of the $C_1$Co bond. This, hydrogen-pulling ability has been previously demonstrated in **Chapter 4**. Backward and forward reactions have almost the same reaction barriers.

**4) $TS_3$:$CH_2CH_2$* → $CH_3CH$***

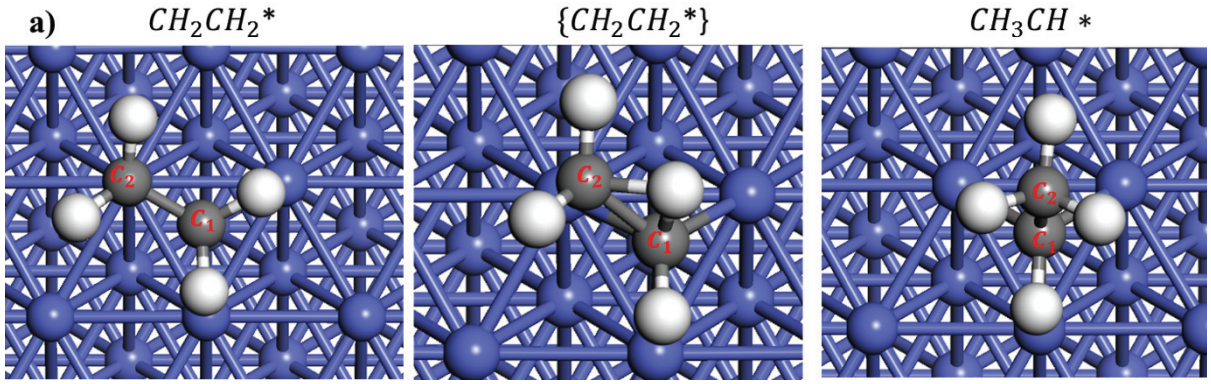

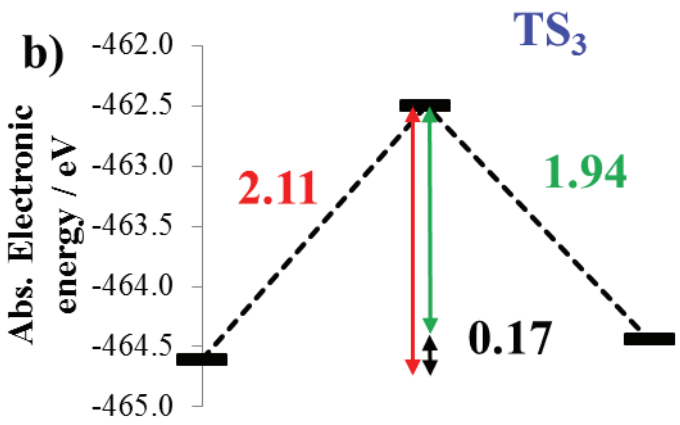


**Figure** 43. Geometric and energetic characteristics of H-transfer from ethylene to surface ethyl.

Hydrogen transfer reaction from CH bond ($d(HC_1)$=1.12Å, $d(HC_2)$=2.18Å, $d(C_1C_2)$=1.45Å) of initially adsorbed ethylene molecule to the transition state ($d(HC_1)$=1.31 Å, $d(HC_2)$=1.29Å, $d(C_1C_2)$=1.54Å) and then to the final state ($d(HC_1)$= 2.17Å, $d(HC_2)$=1.10, $d(C_1C_2)$=1.52Å) is kinetically the most demanding step we found so far similarly to Rh (2.15eV)[298]. In the H-transfer reaction, there is no involvement of Co surface sites and therefore, this reaction is not surface-mediated. To jump from one carbon $C_1$ to another $C_2$, the bending mode in CH vibrations has to be activated. δ(CH) bending mode in the transition state has an imaginary frequency of $\tilde{\nu} = -1121\ cm^{-1}$. In addition, the overall reaction is endothermic, suggesting that H-transfer reactions are unlikely to be important compared to hydrogenation/dehydrogenation reactions. Therefore, this is the reason why we did not evaluate barriers of other H-transfer reactions such as those in $TS_7$ and $TS_8$ of the scheme in **Figure 39**. Hence, we will consider H-transfer reactions negligible in the overall surface-ethylene transformation mechanism.

**5) $TS_4$: $CH_2CH^*+^* \rightarrow CHCH^*+H^*$**

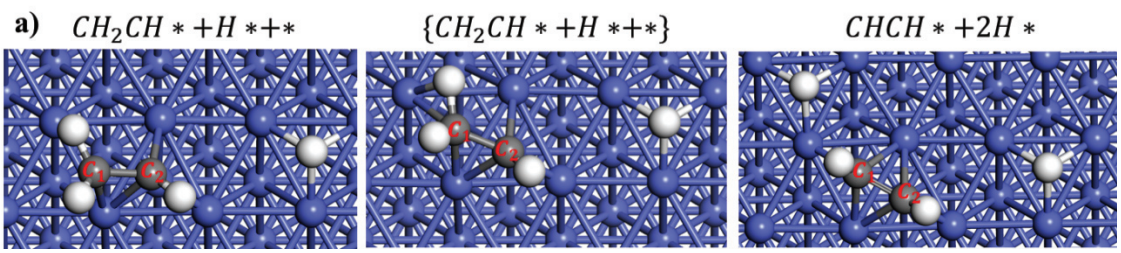

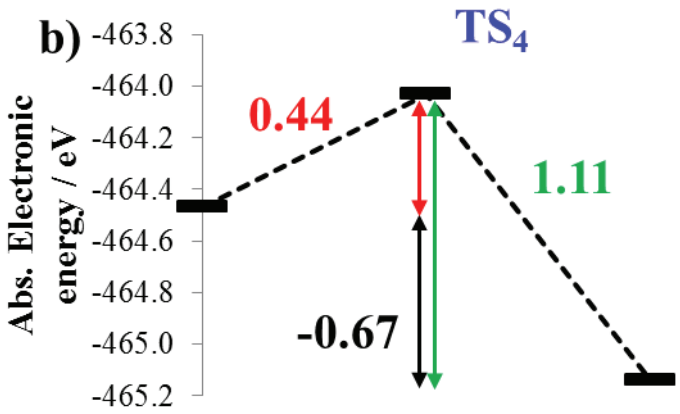


**Figure** 44. a) Geometric and b) energetic characteristics of dehydrogenation of vynil to acetylene reaction.

CH bond in the surface vinyl specie ($CH_2CH$), activated by the closest Co on-top site, stretches from d($HC_1$)=1.13 Å (d(HCo)=1.92 Å) to 1.29 Å (d(HCo)=1.77 Å) in the transition state whereas deprotonated $C_1$ atom from initial on-top position shifts towards a fcc hollow site (from d($CoC_1$)= 2.05 to 2.11 Å). From the transition state, hydrogen atom relaxes to a neighbor fcc-hollow site. The imaginary frequency of the activated mode is $\tilde{\nu} = -164.3\ cm^{-1}$ which corresponds to a complex movement of CC and CH bonds with respect to on-top Co. The activation barrier of 0.44eV and exothermic reaction energy of-0.67eV, suggest very fast deprotonation of $CH_2CH$ to acetylene.

**6) $TS_5$: $CH_3CH^*+^* \rightarrow CH_2CH^*+ H^*$**

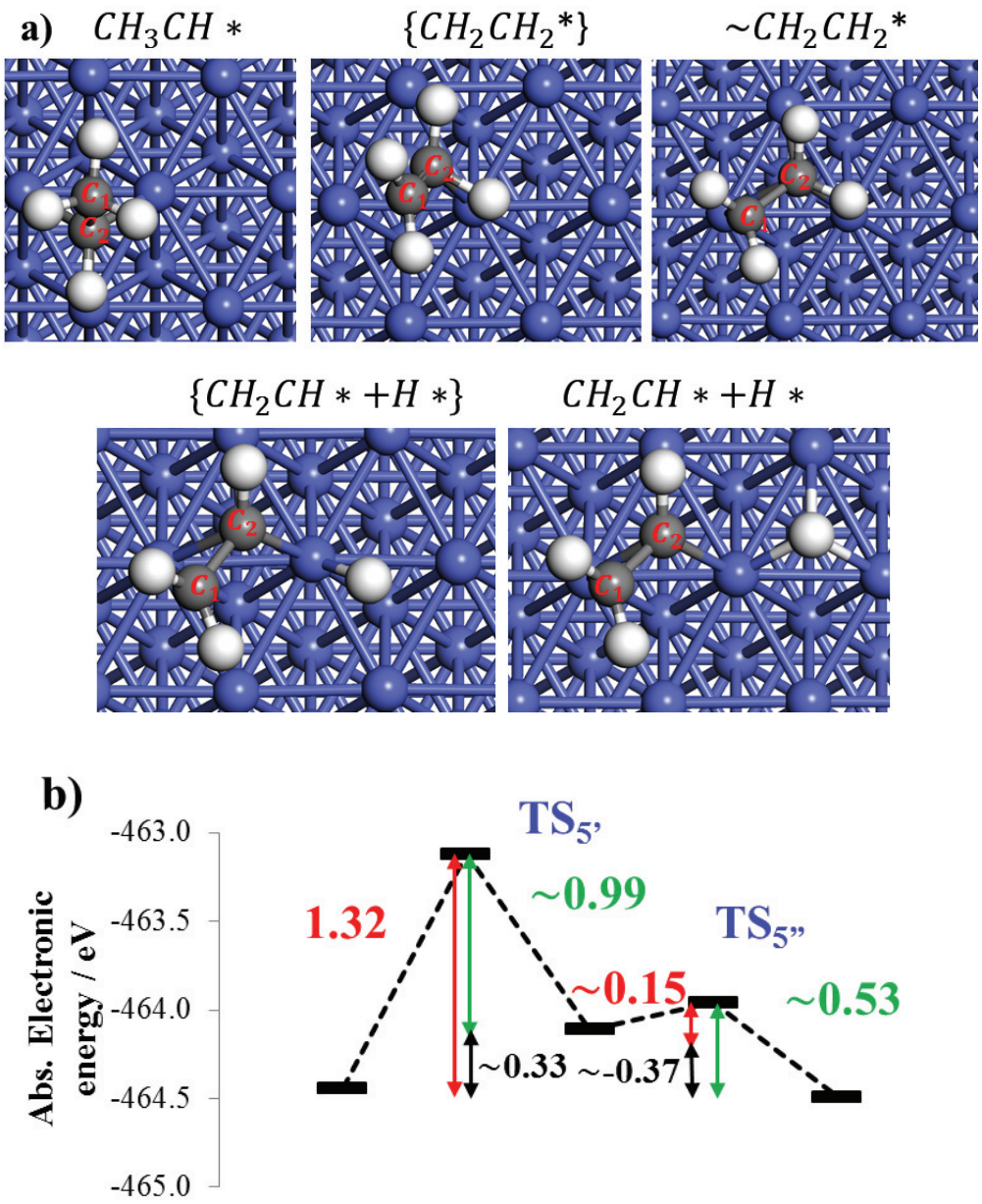


**Figure** 45. Geometric and energetic characteristics of ethylidene dehydrogenation reaction to surface vinyl.

For this transition state, we are presenting the results of CI-NEB calculation only and we explain below the reasons for not pursuing further calculations of this transition state. Regardless the mechanism of its formation, dehydrogenation of ethylidene ($d(C_1C_2)$=1.52 Å, $d(C_2Co)$=1.97 Å, $d(HC_2)$=2.17 Å, $d(HC_1)$=1.10 Å, d(HCo)=3.35 and $d(C_1Co)$=3.03 Å) to vynil is a two-step transformation. As we discussed previously, $C_1$ and hydrogens attached to it, are very far from the surface on-top site due to high hydrogenation degree of $C_1$ and the

hydrogen pulling effect. Therefore, in order to transform ethylidene to surface vinyl, H-transfer from $C_1$ to $C_2$ is necessary as it can be seen from the first ($TS_{5'}$) transition state we obtained. The first transition state of this two-step process was confirmed by a vibrational frequency calculation that gave one imaginary vibrational mode of $\tilde{\nu} = -92.73\ cm^{-1}$. Moreover, the structure of the first transition state (d($C_1C_2$)=1.38 Å, d($C_2$Co)=2.03, Å, d($HC_1$)=1.97 Å, d($HC_2$)=1.22 Å , d(HCo)=1.67, d($C_1$Co)=3.17 Å) suggests that the ongoing hydrogen atom is not shared between $C_1$ and $C_2$ as it was the case with $TS_3$. In this hydrogen-transfer transition state, H sits exclusively on $C_2$. We suspect that the initial number of images we used between reactant and product (eight) was not sufficient to obtain the transition state for H-transfer reaction in which H is shared between $C_1$ and $C_2$ as it has been shown for $TS_3$. This is also supported by the fact that the strong structural rearrangement of carbons and hydrogens occurred during the optimization, whereas the transition state have been obtained after two intermediate images between reactant, and the transition state. Geometry properties shown in **Figure** 45a) suggest that first transition state {$CH_2CH_2$*} corresponds to the relaxation of mono (CC axis perpendicular) to di-α-complexed ethylene (CC axis parallel to the surface) and not H-transfer reaction we wanted to obtain. Hence, we suspect that another transition state is hidden between images CH3C* and {$CH_2CH_2$*} in **Figure** 45a. The vibrational model of $TS_{5'}$ $\tilde{\nu} = -92.73\ cm^{-1}$ in which C-C skeleton (d($C_1C_2$)=1.38 Å) moves towards the on-top Co surface site, suggests the existence of π-bond interaction of (ethylene) with Co electron-density (similarly to $TS_0$). In the second transition state, di-α-complexed ethylene looses its hydrogen just as in $TS_1$. Energies reported in **Figure** 45 are only approximate since the intermediate specie in this two-step mechanism has not been optimized, as $TS_{5''}$ is the same as $TS_1$ we presented previously. From the same reason, steepest descent calculations have not been performed on identified TS structures. Considering the H-transfer reaction step in this reaction, we suspect that the actual transition state will posses high energy

barriers in accordance with the litterature[298] (as in $TS_3$ or $TS_{11}$) and is therefore of minor importance for our work.

**7) $TS_9$:CHCH*+*→ CCH*+H***

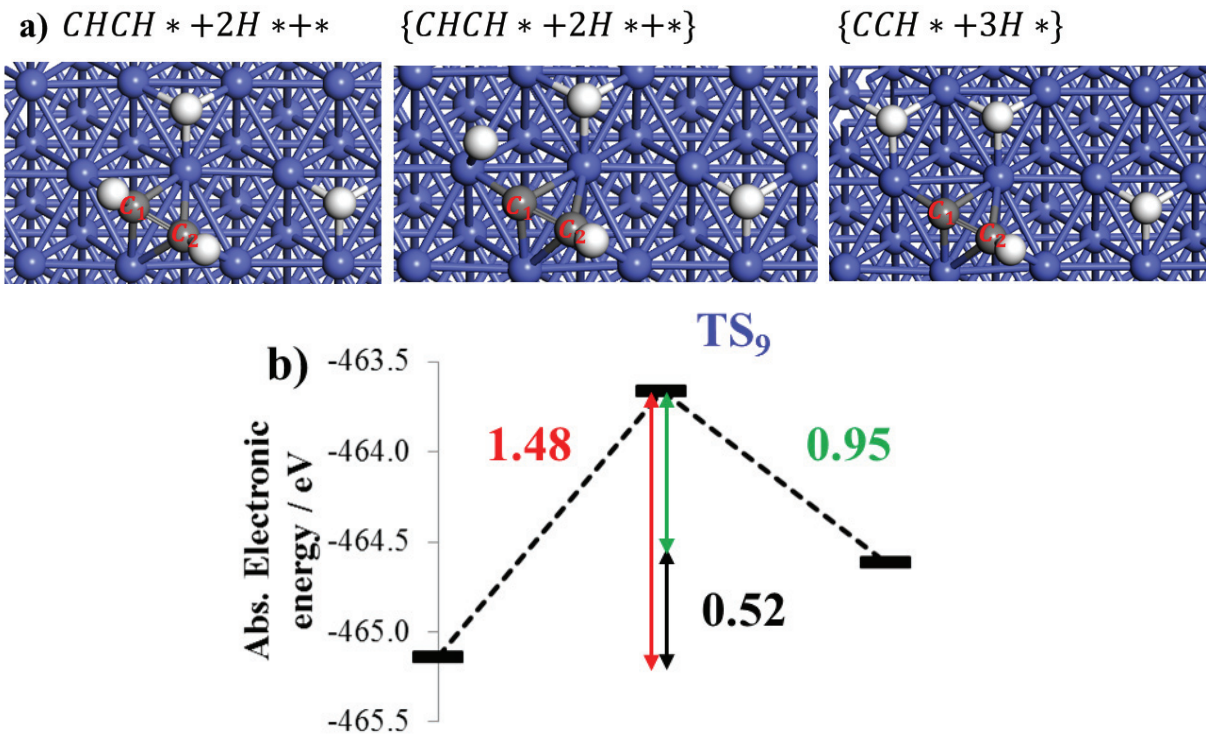


**Figure** 46. Geometric and energetic characteristics of acetylene dehydrogenation to surface ethynyl.

Acetylene CH bond (d($HC_1$)=1.09 Å), activated by the closest Co on-top site (d(HCo)=2.49 Å ) extends to d($HC_1$)=1.64 Å over Co site in the on-top position d(HCo)=1.54 Å. The outgoing H moves to fcc hollow site d(HCo)=1.71 Å. The imaginary frequency of the activated CH stretching mode is $\tilde{\nu} = -809.6\, cm^{-1}$. The overall activation barriers of 1.48 and 0.95 eV for forward and backward reactions, respectively, suggest that acetylene dehydrogenation is kinetically slower compared to the previous dehydrogenation reactions.

**8) $TS_{10}$: $CH_2C$*+*→ CHC*+ H***

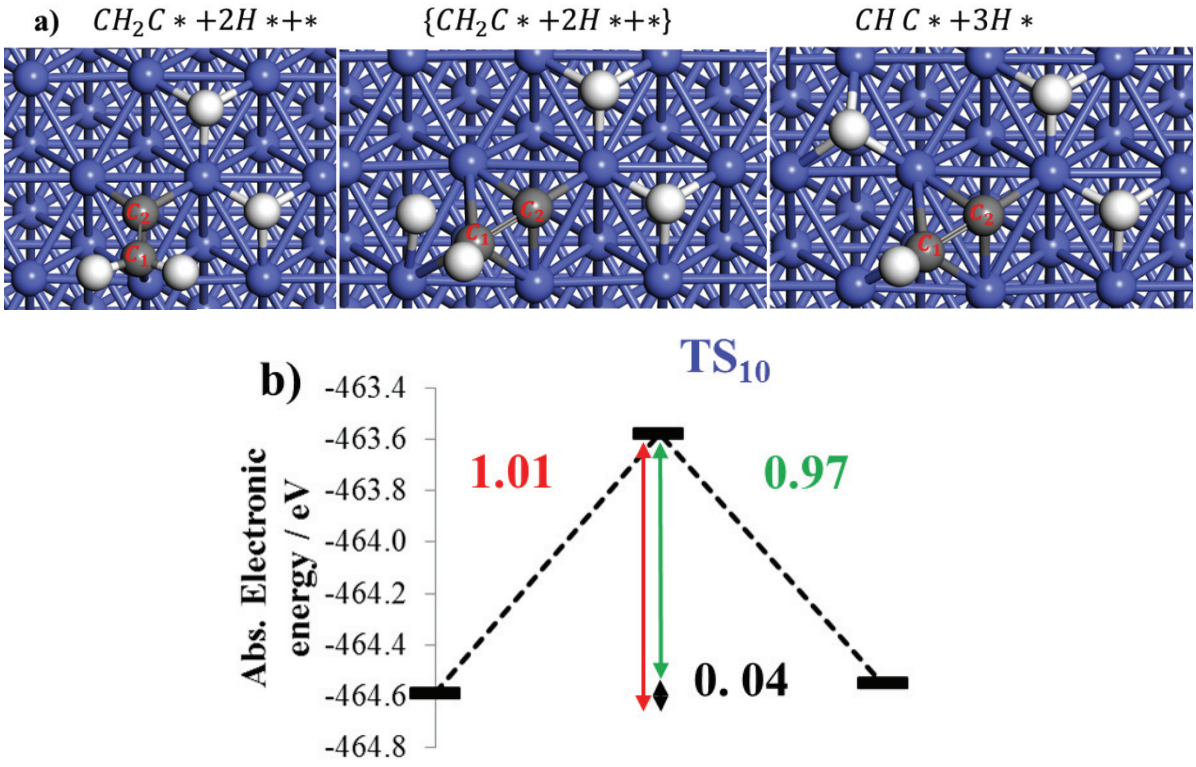


**Figure** 47. Geometric and energetic characteristics of vinylidene dehydrogenation to surface acetylide.

Vinylidene group $CH_2C$ ($d(C_1C_2)$=1.38 Å, $d(C_1Co)$=2.26 Å, $d(C_2Co)$=1.92 Å, $d(HC_1)$=1.14 Å) initially adsorbed with $C_1$ and $C_2$ on a on top and hollow Co site, respectively, moves its $C_1$ end to the nearest *hollow* site ensuring agostic interaction of departing H with the nearest on-top site ($d(C_1C_2)$=1.39 Å, $d(C_1Co)$=2.13 Å, $d(C_2Co)$=1.90 Å, $d(HC_1)$=1.34 Å). The imaginary frequency of the activated CH stretching mode is $\tilde{\nu} = -541.9\ cm^{-1}$. Outgoing hydrogen moves, via an on-top site to the nearest *hcp* hollow site. Forward and backward reactions have almost the same reaction barriers 1.01 and 0.97 eV, respectively.

**9) $TS_{11}$: $CH_3C^*+^*\rightarrow CH_2C^*+H^*$**

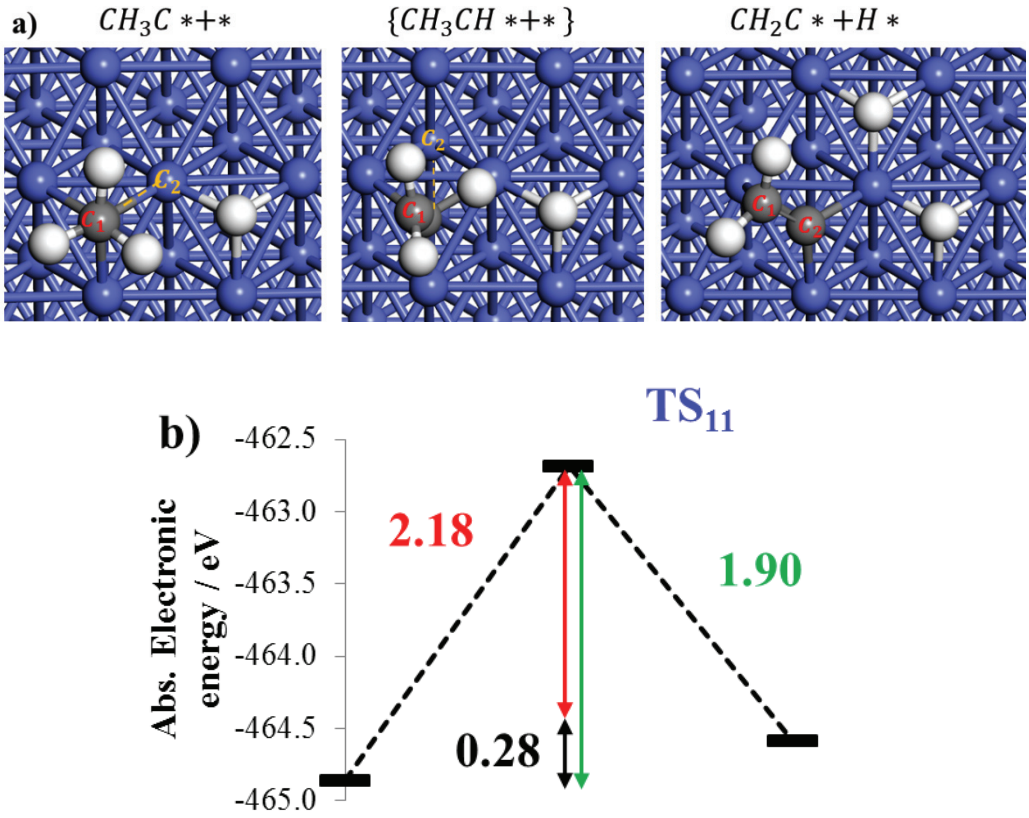


**Figure** 48. Geometric and energetic characteristics of ethylidyne dehydrogenation reaction to surface vinylidene.

Dehydrogenation of ethylidyne ($d(C_1C_2)$=1.49 Å, $d(C_1Co)$=3.07 Å, $d(HC_1)$=1.10 Å) to vinylidene ($d(C_1C_2)$=1.38 Å, $d(C_1Co)$=2.27 Å, $d(HC_1)$=3.13 Å) starts with $HC_1$ bond breaking. Outgoing hydrogen descends towards the closest Co on-top site ($d(C_1C_2)$=1.40 Å, $d(C_1Co)$=2.99 Å, $d(HC_1)$=1.59Å and $d(HC_2)$=1.34Å) and settles on the nearest fcc hollow site. In the final state, CC skeleton firmly descends towards a near on-top Co site where $C_1Co$ contact is established. The activation barrier of this endothermic transformation is 2.18 eV signifying a very slow dehydrogenation of the $C_1$ end in surface ethylidyne species.

**10) $TS_{12}$: $CH_3CH^*+^* \rightarrow CH_3C^* + H^*$**

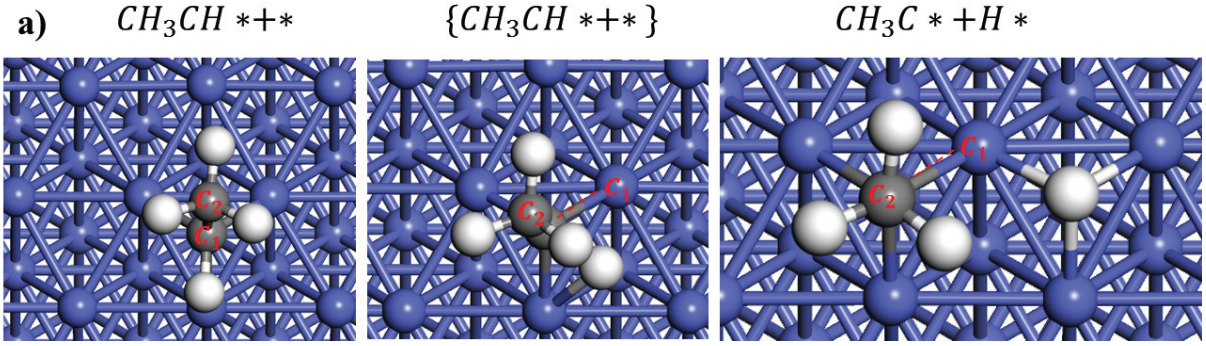

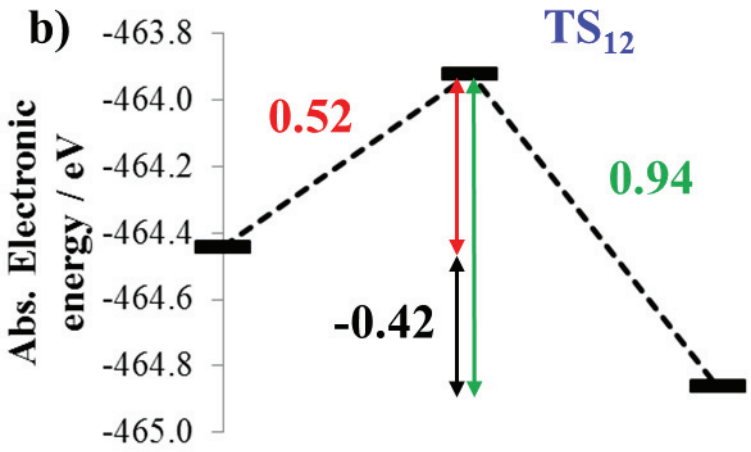


**Figure** 49. Geometric and energetic characteristics of ethylidene dehydrogenation reaction to surface ethylidyne.

Dehydrogenation of ethylidene (d($C_1C_2$)=1.52 Å, d($C_1$Co)=2.01 Å, d($HC_1$)=1.19 Å) to ethylidyne (d($C_1C_2$)=1.49 Å, d($C_1$Co)=1.89 Å, d($HC_1$)=2.62 Å) starts with the activation of low frequency $\tilde{\nu} = -223.4\, cm^{-1}$ δ(CH) bending mode towards the on-top Co site. In the transition state, carbon skeleton remains approximately unchanged d($C_1C_2$)=1.51 Å and d($C_1$Co)=1.99 Å whereas CH bond elongates to d($HC_1$)=1.26 Å after which the bond is broken. Outgoing hydrogen goes through on-top Co site to a neighbor fcc-hollow site. The activation barrier of this exothermic transformation is 0.52 eV signifying a rapid dehydrogenation of a $C_1$ end in surface ethylidene species.

**11) $TS_{13}$: $CH_2CH^*+^* \rightarrow CH_2C^*+H^*$**

**a)** $CH_2CH*+H*+*$ $\{CH_2CH*+H*+*\}$ $CH_2C*+2H*$

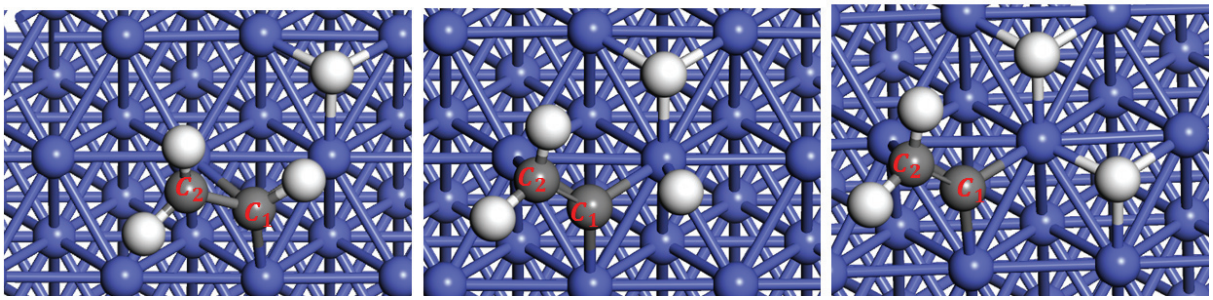

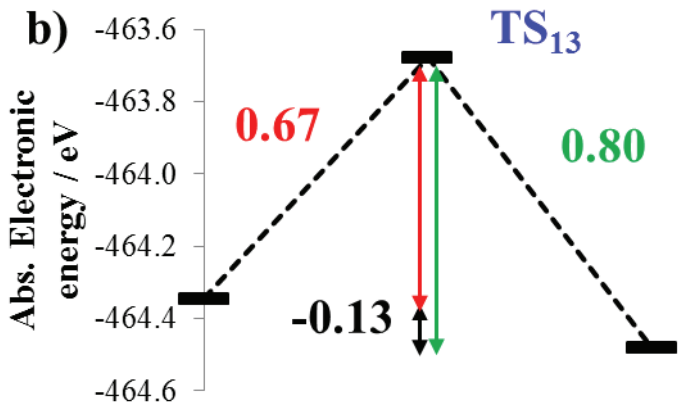


**Figure** 50. Geometric and energetic characteristics of vynil dehydrogenation to surface vinylidene.

$HC_1$ bond from vinyl group $CH_2CH$ (d($HC_1$)=1.14 Å, d(HCo)=1.93 Å) in agnostic interaction with the nearest Co on-top site stretches to d($HC_1$)=1.61 Å (d(HCo)=1.52 Å) in the transition state. The imaginary frequency of the activated CH stretching mode is $\tilde{\nu} = -810.5\ cm^{-1}$ similarly to some previous CH scission reactions. CC skeleton (d($C_1C_2$)=1.42 Å, d($C_2$Co)=2.12 Å, d($C_1$Co)=2.04 Å) initially adsorbed with the $C_2$ end on the on-top site and the $C_1$ end on the hollow site, descends its $C_1$ end, whereas the $C_2$ end rises (d($C_1C_2$)=1.38 Å, d($C_2$Co)=2.27 Å, d($C_1$Co)=1.93 Å) with respect to Co surface in the final state, indicating stronger interaction of dehydrogenated $C_1$-end with the surface. In addition, the energy barrier for the direct reaction is 0.67 eV compared to 0.80 eV for the reverse reaction suggesting that this reaction may occur readily.

**12) $TS_{14}$: CHC*+*→ CC*+ H***

**a)** $CH\,C*+3H*+*$ $\{CH\,C*+3H*+*\}$ $C\,C*+4H*$

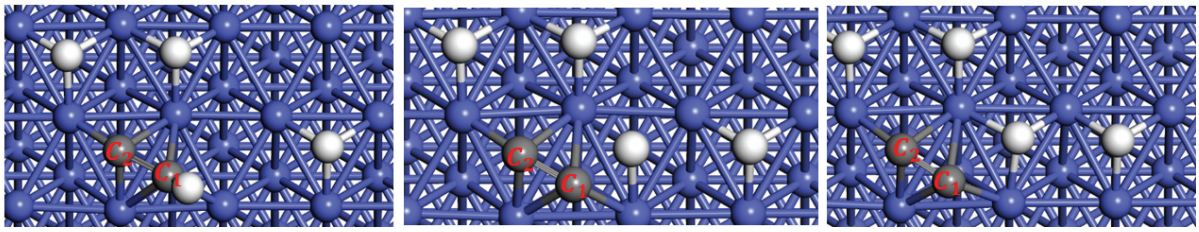

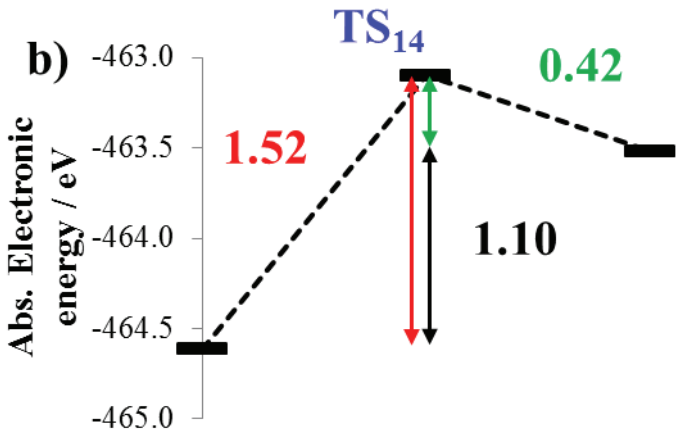


**Figure** 51. Geometric and energetic characteristics of acetylide dehydrogenation to surface di carbide.

Surface ethynyl (acetylide) CCH (d($C_1C_2$)=1.36 Å, d($C_2$Co)=2.10 Å, d($HC_1$)=1.09 Å, d(HCo)=2.59 Å) initially adsorbed on hollow sites with both $C_1$ and $C_2$ ends, extends its $HC_1$ bond to approximately d($HC_1$)=1.46 Å in the transition state due to interaction with the nearest Co site (d($C_1C_2$)=1.34 Å, d(HCo)=1.76 Å). Outgoing hydrogen diffuses to the nearest fcc-hollow site where d(HCo)=1.73 Å. In transition state $TS_{14}$, the imaginary frequency has been observed at $\tilde{\nu} = -787.3\ cm^{-1}$ which corresponds to a CH stretching mode. Regarding kinetics, results presented in **Figure 51,** the last dehydrogenation is expected to be slow compared to other dehydrogenation reactions in this study. Moreover, this reaction is endothermic, suggesting that this reaction may not occur at low temperatures.

Figure 52 presents the summary of transition states we are discussing in our further work considering low-energy barriers of steps associated with them. Note that transition state $TS_{15}$ has been already reported in the litterature[79] and therefore we did not evaluate it. All kinetically the most favorable steps in

Figure 52 represent hydrogenation/dehydrogenation steps leading to either FT products or hypothesized deleterious deactivation initiator surface species and are therefore of critical importance for understanding carbon-induced deactivation phenomenon.

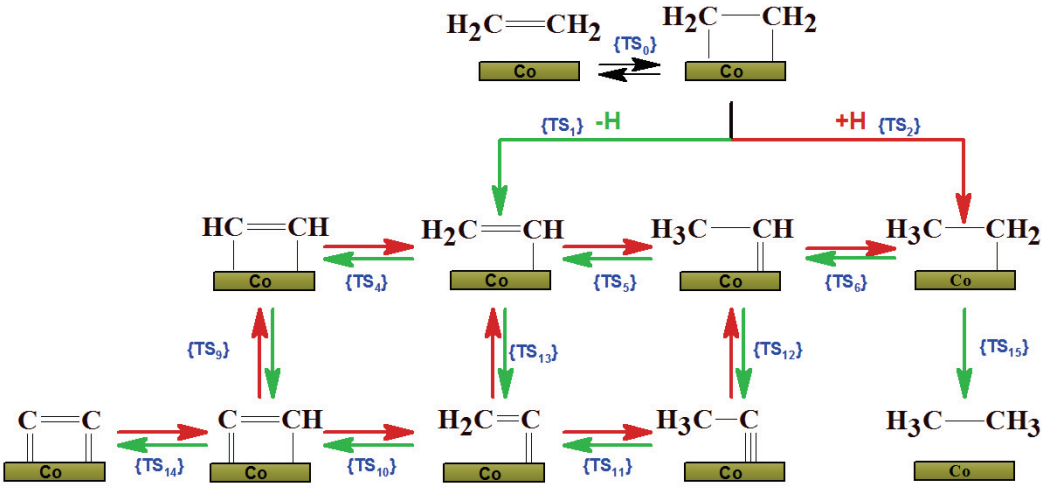


**Figure 52**. The summary of selected reaction pathways candidates for deactivation initiator formation.

### 5.2.2 Potential energy profile of ethylene decomposition

**Table** 10. Energy barriers of some ethylene decomposition reactions studied in this work.

| Notation | Reaction | $E_f$ / eV | $E_b$ / eV | ΔE / eV |
|---|---|---|---|---|
| $TS_0$ | $CH_2CH_2(g) \rightarrow CH_2CH_2*$ | 0.23 | 0.98 | -0.75 |
| $TS_1$ | $CH_2CH_2*+* \rightarrow CH2CH* + H*$ | 0.86 | 0.69 | 0.17 |
| $TS_2$ | $CH_2CH_2* + H* \rightarrow CH_3CH_2* +*$ | 0.57 | 0.58 | -0.01 |
| $TS_3$ | $CH_2CH_2* \rightarrow CH_3CH*$ | 2.11 | 1.94 | 0.17 |
| $TS_4$ | $CH_2CH*+* \rightarrow CHCH*+ H*$ | 0.44 | 1.11 | -0.67 |
| $TS_5$ | $CH_3CH*+* \rightarrow CH_2CH* + H*$ | / | / | ~-0.05 |
| $TS_6$ | $CH_3CH_2*+* \rightarrow CH_3CH*+ H*$ | / | / | / |
| $TS_7$ | $CHCH* \rightarrow CH_2C*$ | / | / | / |
| $TS_8$ | $CH_2CH* \rightarrow CH_3C*$ | / | / | / |
| $TS_9$ | $CHCH *+* \rightarrow CCH*+ H*$ | 1.48 | 0.95 | 0.52 |
| $TS_{10}$ | $CH_2C *+* \rightarrow CHC*+ H*$ | 1.01 | 0.97 | 0.04 |
| $TS_{11}$ | $CH_3C*+* \rightarrow CH_2C* + H*$ | 2.18 | 1.90 | 0.28 |
| $TS_{12}$ | $CH_3CH*+* \rightarrow CH_3C* + H*$ | 0.52 | 0.94 | -0.42 |
| $TS_{13}$ | $CH_2CH*+* \rightarrow CH_2C*+ H(ads)$ | 0.67 | 0.80 | -0.13 |
| $TS_{14}$ | $CHC*+* \rightarrow CC*+ H*$ | 1.52 | 0.42 | 1.1 |
| $TS_{15}$ | $CH_3CH_2*+ H* \rightarrow CH_3CH_3(g)+2*$ | / | / | / |

The summary of reactions we have studied is presented in **Table 10**. We have shown that H-transfer reaction (one-step H-transfer reaction $TS_3$) is kinetically very unfavorable in agreement with the litterature[298]. Hence, we did not evaluate transition states $TS_7$ and $TS_8$. Moreover, we have shown that certain, one-step dehydrogenation reactions, such as those characterized by $TS_7$ and $TS_{11}$ in **Figure 39**, are in fact two-step reactions composed of an H-

transfer and a subsequent dehydrogenation reaction. We have reached this conclusion by taking into account the geometrical considerations and the reactant structure whose terminal carbon $CH_\beta$ atoms to be dehydrogenated are very far from the surface. Thus, H sitting on carbon sites are geometrically constrained and therefore cannot undergo the agostic interaction with near-surface Co site that would lead to a simple one-step dehydrogenation reaction. However, this does not mean that ethylidyne $CH_3C^*$ and ethylidene $CH_3CH^*$ species do not take part in the overall decomposition scheme. For instance, the reaction pathway through $TS_2$ and $TS_6$ could lead to such species. Note, however, that those paths require the presence of adsorbed hydrogen. Due to time limitations, we did not examine $TS_6$ and $TS_{15}$ reaction pathways. Based on results reported by Chen[302], those reactions seem to be thermodynamically and kinetically very favorable. However, considering high hydrogen content of terminal C in those species, high energy barriers for deprotonation reactions in terminal $CH_3$ groups, but also the fact that the most stable species in **Zone** 3 (presented in **Chapter** 4) contain no such highly hydrogenated carbons, we assume that ethylidyne $CH_3C^*$ and ethylidene $CH_3CH^*$ species either act as spectator species in ethylene decomposition reactions or they take part in further hydrogenation reactions leading to ethane. Thus, we do not consider them as plausible deactivation initiators.

Based on the transition state calculations we performed, we can now construct the potential energy profiles of the various reactions involved in ethene decomposition reaction on the Co(111) surface. Those results are presented in **Figure 53**.

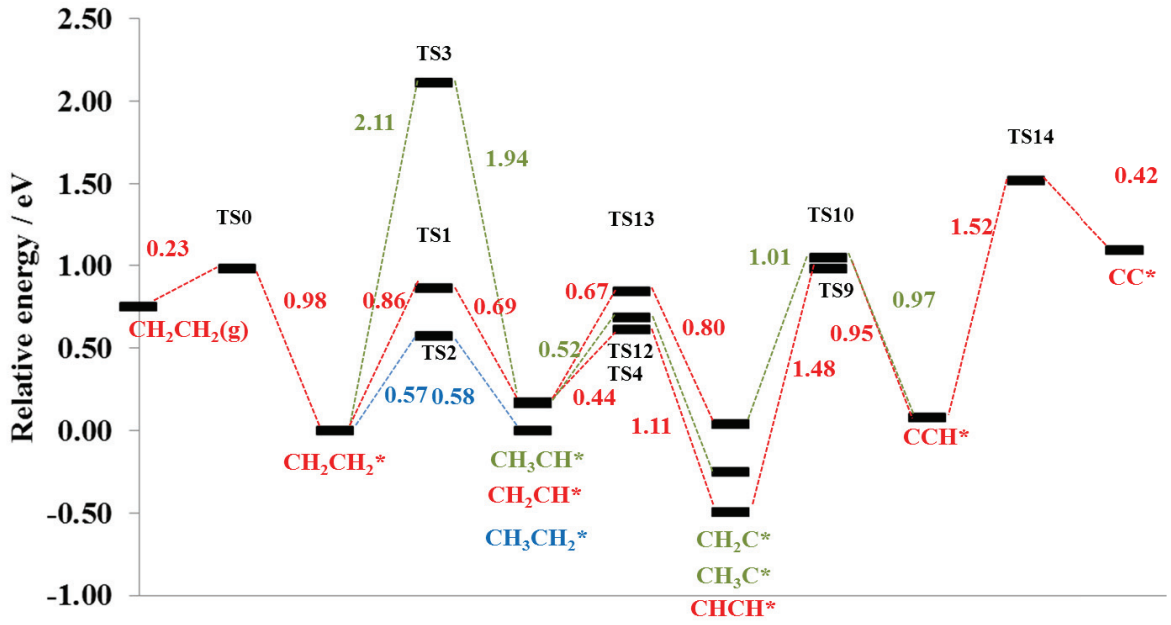


**Figure 53.** Ethylene decomposition pathways on Co(111) studied in this work.

Potential energy profiles for some ethylene decomposition reactions have been already studied using DFT on Co(0001) [219] and Co(111) surfaces[302]. Although (111) and (0001) surfaces are expected to have different reactivity, we will use results in[302,219] for comparing trends. Thermodynamic analysis of the energy profile in **Figure 53**, indicates that the most favorable surface species, products of ethylene decomposition are surface acetylene CHCH, ethynyl CCH, vinyl $CH_2CH^*$ and vinylidene $CH_2C^*$ species. Acetylene CHCH and ethynyl CCH surface species have been also proposed as a precursor of cyclopolymerization-dehydrogenation reactions in graphene formation[219]. Thus, they represent thermodynamically the most probable candidates for deactivation initiators in our study. This is also in line with our results from **Section 4.3** where we showed that low hydrogenated forms of coke (θ(C)=2 ML and θ(H) up to 1 ML) represent the most stable surface states for Co(111) surfaces and that stability of those species increases as θ(H) decreases. In contrast, although we cannot exclude entirely ethylene decomposition into dicarbide CC* as a possible deactivation initiator, thermodynamic analysis depicted in **Figure 53** suggests that dicarbide CC* is less stable than ethylene molecule in the gas-phase. Hence, the graphitic phase at θ(C)=2 ML in

**Section 4.3**, ur model system of deactivated Co(111), seems thermodynamically less likely to be formed from dicarbide than from acetylene CHCH and ethynyl CCH species. Besides, $CH_\beta/CH_\beta$ coupling reactions are kinetically more favorable compared to C/C reactions [108]. For instance, cyclic coke precursors may be formed in two-step reaction mechanism where hydrogen-containing species such as acetylene CHCH and ethynyl CCH couple and form hydrogen-containing cyclic species (found in **Section 4.3 for** θ(H) up to 1 ML and θ(C)=2 ML**)**, and the latter can be dehydrogenated to form hydrogen-free cyclic species (found in **Section 4.3** θ(C)=2 ML**).** Further analysis is needed to test the proposed reaction mechanism.

The energy profile depicted in **Figure 53** suggests that adsorption and dehydrogenation reaction of ethylene to CHCH and $CH_2C$ can occur readily from both thermodynamic and kinetic point of views. For instance, ethylene adsorbed on the surface can easily dehydrogenate and hydrogenate to $CH_2CH$ and $CH_3CH_2$, respectively. By comparing barriers for those two reactions, we can conclude that they compete. In other words, if surface hydrogens are locally present, the pathway through $TS_2$ that leads essentially to ethane[302] can readily occur, whereas in the absence of free hydrogens, the $TS_1$ pathway leading to $CH_2CH$ occurs. Note, however, that the only source of hydrogen in the context of ethylene decomposition experiments[198,211,212] is ethylene itself. Hence, hydrogens produced in dehydrogenation reactions may desorb from the surface, if the temperature of experiments allows it before the formation of ethane. In contrast, in the context of the FT synthesis, surface H are expected in the non-negligible concentrations, thus both pathways (through $TS_1$ and $TS_2$) are thermodynamically and kinetically favorable. This result is in line with the observation that hydrogen-poor conditions accelerate deactivation phenomenon[199,45,280]. Thus, the $TS_1$ pathway seems to be responsible for deactivation initiator formation considering that the $TS_2$ leads to non-reactive FTS product (ethane).

Once formed, surface species $CH_2CH$ can dehydrogenate through $TS_4$ but also $TS_{13}$ with a low energy barrier with the former being kinetically and thermodynamically more favorable leading to surface acetylene species (CHCH). Hence, our kinetic and thermodynamic analysis shows that once formed, $CH_2CH$ is more likely to decompose to CHCH. Surface acetylene CHCH represents thermodynamically and kinetically the most favorable decomposition product of ethylene as suggested by the overall potential energy profile in **Figure 53**. This is also in line with a previous Co(0001) [219] and Co(111) [302] studies. Dehydrogenation of $CH_2CH$ through $TS_{13}$ leads to a surface vinylidene $CH_2C$ species also found very stable in the previous work on Co(0001)[219]. In contrast, our results are not in agreement with calculations performed on Co(111) by Chen et al. [302] . In that work, authors reported an activation barrier close to 0 eV for this reaction.

Considering thermodynamic stability of surface acetylene species, its decomposition to CCH through $TS_9$ seems kinetically more demanding than a decomposition of $CH_2C$ through $TS_{10}$ (1.48 vs. 1.01 eV). Thus, $TS_{10}$ and $TS_9$ activated pathways may be considered as a low-temperature (kinetically less demanding) and high-temperature (kinetically more demanding) parallel pathways towards a common deactivation initiator species CCH*. The final dehydrogenation pathway towards di-carbide seems kinetically demanding and therefore possible only for high temperatures such as those found in surface annealing experiments [218].

Therefore, two ethylene decomposition pathways can be proposed based on our calculations: $CH_2CH_{2(g)} \rightarrow CH_2CH_2^* \rightarrow CH_2CH^* \rightarrow CHCH^* \rightarrow CCH^* \rightarrow CC^*$ and $CH_2CH_{2(g)} \rightarrow CH_2CH_2^* \rightarrow CH_2CH^* \rightarrow CH_2C^* \rightarrow CCH^* \rightarrow CC^*$. Those two reaction pathways are in full agreement with the findings of Zhang et al. on Co(0001) [219]. Further investigations are needed to explain a possible involvement of multiple (and highly) hydrogenated $C_2$ structures such as ethylidene ($CH_3CH$), ethylidyne ($CH_3C$), vynil ($CH_2CH$) and vinylidene $CH_2C$ type species on Co(111) surface. Although we cannot refute their

involvement in the ethylene decomposition reaction, we assume that their participation in the formation of experimentally detected coke is unlikely for Co(111). Two possible explanations are underlying this hypothesis:

Firstly, highly hydrogenated C atoms, as shown in our previous calculations in **Section 4.3** but also in **Section 5.2.1** are lifted from the surface due to H pulling effect, and thus hydrogen atoms attached to carbon are inaccessible for Co surface. As we have seen in **Section 5.2.1**, the necessary condition for CH bond scission reactions is a close neighbor Co site. Besides, calculations of Kang et al. [303] showed a similar trend on Pt(111) and stressed that the lowest energy barriers are achieved for CH bonds that "point at" the surface metal atoms (i.e. agostic interaction of H with surface metal site). In addition to that, we have also seen that cyclic structures (θ(C)=2 ML) presented in **Section 4.3** do not contain multiple hydrogenated C atoms as this is thermodynamically less favorable. It seems reasonable to assume that, even if ethylidene, ethylidyne, vynil and vinylidene species are somehow involved in ethylene decomposition reactions, it is unlikely that they are involved in the formation of deleterious carbon species on Co(111) presented in **Figure 36** in **Section 4.3** for θ(C)=2ML. Interestingly, ethylidyne species have been previously reported as the intermediate of ethylene decomposition on Pt(111), however, according to Carter et al.[304], it undergoes decomposition to surface dicarbide $C_2$ or ethynyl CCH.

Secondly, all ethylidene, ethylidyne, vynil and vinylidene species can be further hydrogenated[302] if hydrogen surface concentrations allow that (leading to non-reactive ethane) or dehydrogenated leading to surface species whose transformations we discussed previously (see $TS_5$ and $TS_{11}$). Moreover, if such dehydrogenation reactions were studied on Co(111) in more details, we believe that they would follow a two-step mechanism scheme where 1,2H-transfer and then CH bond scission reactions occur. Considering this, such reactions are

kinetically hindered as they involve H-transfer reaction in line with the literature for Rh(111) [298].

### 5.2.3 Impact of temperature on the structure of deactivation initiator

In **Section 5.2.2**, we have shown that the surface acetylene CHCH and ethynyl CCH species represent possible decomposition products of ethylene. Surface science experiments have been widely used to identify the mechanism of ethylene decomposition by investigating the structure of species that intervene [198,211,218].

In works of Weststrate et al. [211,198], decomposition of ethane adsorbed at 90K was investigated using a combination of experimental techniques such as XPS, work-function change measurements ΔWF, temperature-programmed desorption TPD of hydrogen when **gradual heating** was applied. In order to examine the impact of temperature on the formation of polymeric carbon precursors, and relate our findings in **Section 5.2.2** with experimental studies, we propose performing a micro-kinetic calculation based on scheme presented in **Table 11**. We are therefore interested in investigating how an ethylene pre-covered surface evolves when temperature is applied. More specifically, we set the initial surface coverage of ethylene to 0.2 ML similarly to [211,198]. In addition, no other species (except for the free surface sites) are present at the beginning in this micro-kinetic calculation. Note however, that we added hydrogen adsorption/desorption equilibrium ($TS_H$) and ethane desorption ($TS_{16}$) steps to account for experimentally detected gas-phase products. Considering that those steps were not evaluated in our work, we propose taking values in the litterature[79,305]. We have also added decomposition of dicarbide to carbide since this is also a suggested ethylene decomposition product. This reaction pathway energy is calculated by us and given in **Table 11**. The micro-kinetic model in **Table 11** was solved using MKMCXX [299,306,300] with activation energies from **Table 11**. For Arrhenius type reactions (**Section 3.2.4**) the pre-exponential factor was taken to be $10^{13}$ for all surface reaction (see [300]) except for the

backward step of ethane formation where we have taken $10^4$ as in reference [91] considering the the-gas phase specie reaction has been represented using Arrhenius law. The total pressure is set to 0 bar (i.e., there are no gas-phase species at the beginning of "experiment") following low-pressure surface science experiments we are comparing with. The results of this micro-kinetic model should provide an answer on the most favorable product of ethylene decomposition product for the given temperature and therefore clarify the impact of the temperature on the structure of ethylene decomposition product and deactivation initiators in FTS. Moreover, by investigating the transient responses of our model, we can verify which pathways in **Figure 53** are activated towards the formation of the plausible deactivation precursors.

**Table** 11**.** Elementary steps used in the micro-kinetic model to simulate decomposition of ethylene on the Co(111) surface.

| Notation | Reaction Type | Stoichiometry | $E_f$/ eV | $E_b$/ eV |
|---|---|---|---|---|
| $TS_H$[a)] | Hertz-Knudsen | $H_2 + 2^* <-> 2\ H^*$ | 0 | 0.69 |
| $TS_1$ | Arrhenius | $CH_2CH_2^* + * <-> CH_2CH^* + H^*$ | 0.86 | 0.69 |
| $TS_4$ | Arrhenius | $CH_2CH^* + * <-> CHCH^* + H^*$ | 0.44 | 1.11 |
| $TS_{13}$ | Arrhenius | $CH_2CH^* + * <-> CH_2C^* + H^*$ | 0.67 | 0.80 |
| $TS_{10}$ | Arrhenius | $CH_2C^* + * <-> CHC^* + H^*$ | 1.01 | 0.97 |
| $TS_9$ | Arrhenius | $CHCH^* + * <-> CHC^* + H^*$ | 1.48 | 0.95 |
| $TS_{14}$ | Arrhenius | $CHC^* + * <-> CC^* + H^*$ | 1.52 | 0.42 |
| $TS_C$ | Arrhenius | $CC^* + * <-> 2\ C^*$ | 2.05 | 0.86 |
| $TS_2$ | Arrhenius | $CH_2CH_2^* + H^* <-> CH_3CH_2^* + *$ | 0.58 | 0.57 |
| $TS_{15}$[b)] | Arrhenius | $CH_3CH_2^* + H^* <-> CH_3CH_3 + 2^*$ | 0.69 | 0.49 |

a) Based on reference [79].
b) Based on references [305,91].

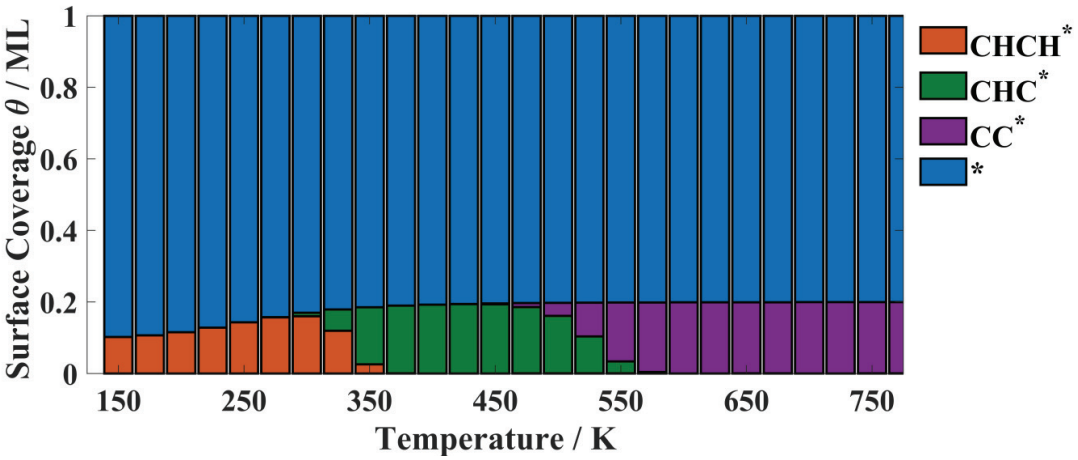


**Figure 54.** The most abundant products of 0.2ML ethylene pre-covered Co (111) surface decomposition reaction for a given temperature at the end of simulation.

**Figure 54** presents the evolution of the surface coverages of different decomposition products of ethylene pre-covered surface for a given constant temperature based on transition-state calculations presented in **Section 5.2**. Results in **Figure 54** infer that regardless of the temperature applied, ethylene preadsorbed on Co surface decomposes. Thus, this implies that ethylene is highly unstable. In addition, no surface carbide C* has been detected in our simulations even for temperatures higher than typical FT conditions (>500K). Our microkinetic results in **Figure 54** also infer that there are three critical temperature intervals for the formation of coke precursor: 150-300K, 300-500K, and >500K. We discuss those temperature intervals below.

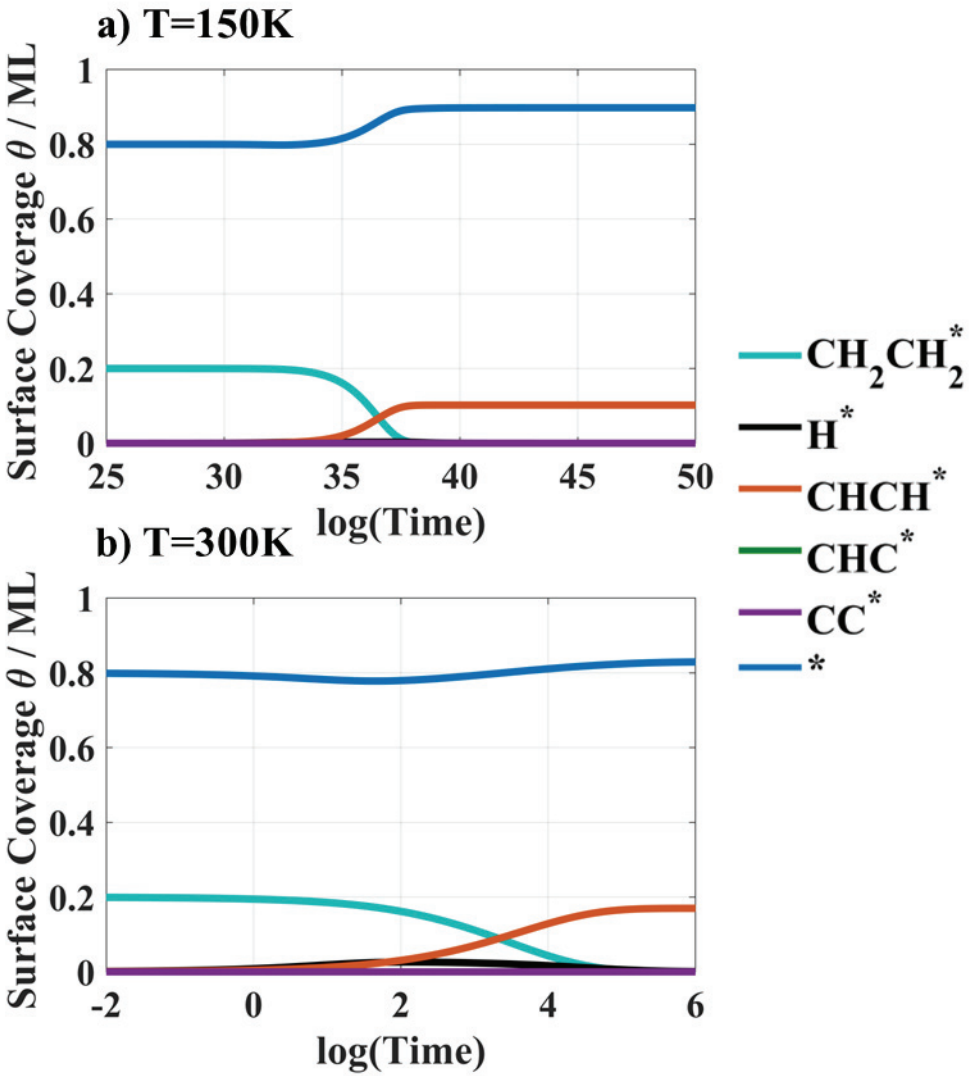


**Figure** 55**.** Surface coverage transient responses of products of ethylene pre-covered Co(111) surface decomposition a) at T=150K b) T=300K.

**Figure 55** presents transient surface coverage of (0.2 ML) ethylene decomposition products in the first temperature interval of interest (150-300K). Results presented in **Figure 55** suggest that after sufficiently long times, the surface composition is essentially the same at T=150 and 300K, although higher temperatures favor faster changes in the surface composition. For this temperature interval, pre-adsorbed ethylene decomposes rapidly on surface vynil and acetylene in agreement with low energy barriers for $TS_2$ and $TS_4$ presented in **Figure 42** and **Figure 44**, respectively. Besides, by decomposing itself at T=150K, pre-adsorbed ethylene leaves some surface hydrogens that are consumed in two parallel reactions:

one in which surface hydrogens recombine and desorb from the surface (through $TS_H$) and the second one in which adsorbed ethylene is hydrogenated to give gas-phase ethane (through $TS_2$ and $TS_{15}$). This is especially pronounced for low-temperature limit at 150K where we see that initial 0.2 ML of ethylene is decomposed to around 0.1 ML of acetylene yielding approximately 0.1ML of ethylene evacuated from the surface through $TS_2$ and $TS_{15}$. For the high-temperature limit at 300K, this is less likely to happen considering the low energy barrier for $TS_4$ reaction where almost an instant transformation of ethylene to acetylene occurs. For this temperature, 0.2ML of initially deposed ethylene transforms to approximately 0.16ML of acetylene. Besides, Weststrate et al. [211] found that ethene-covered Co(0001) surface decomposes between 120-200K to produce acetylene. Our results also infer that acetylene formation occurs readily at low temperature. In conclusion, in the low-temperature interval up to 300K, the following reaction occurs $CH_2CH_2^* \rightarrow CH_2CH^* \rightarrow CHCH^*$. Weststrate et al. [211] do not report ethane desorption for this temperature interval. The possible explanation for this disagreement may be found in the nature of the experiment compared to the simulation. In the experiment [211], a gradual heating of 0.5K/s is applied on ethylene pre-covered surface. Thus, decomposition and desorption products are identified under dynamic temperature conditions i.e. $T = f(time)$. In contrast to experiments, the micro-kinetic simulation shows dynamic decomposition and desorption products for static, temperature-given conditions i.e., $T \neq f(time)$. In dynamic temperature conditions found in experiments, hydrogen may be constantly desorbing in this temperature interval and hence there are no surface hydrogens to produce ethane through $TS_2$ and $TS_{15}$. Thus, the information about the competition for the formation of gas-phase hydrogen and ethane is lost. A second possible explanation is that ethylene theoretical desorption barriers we took from the literature are too low compared to experimental hydrogen adsorption/desorption equilibrium; i.e., the actual ethane desorption energy may be higher (see **Table** 11). Further work is needed to confirm this hypothesis.

Nevertheless, the final surface composition in both static (theoretical) and dynamic (experimental) temperature studies is practically the same.

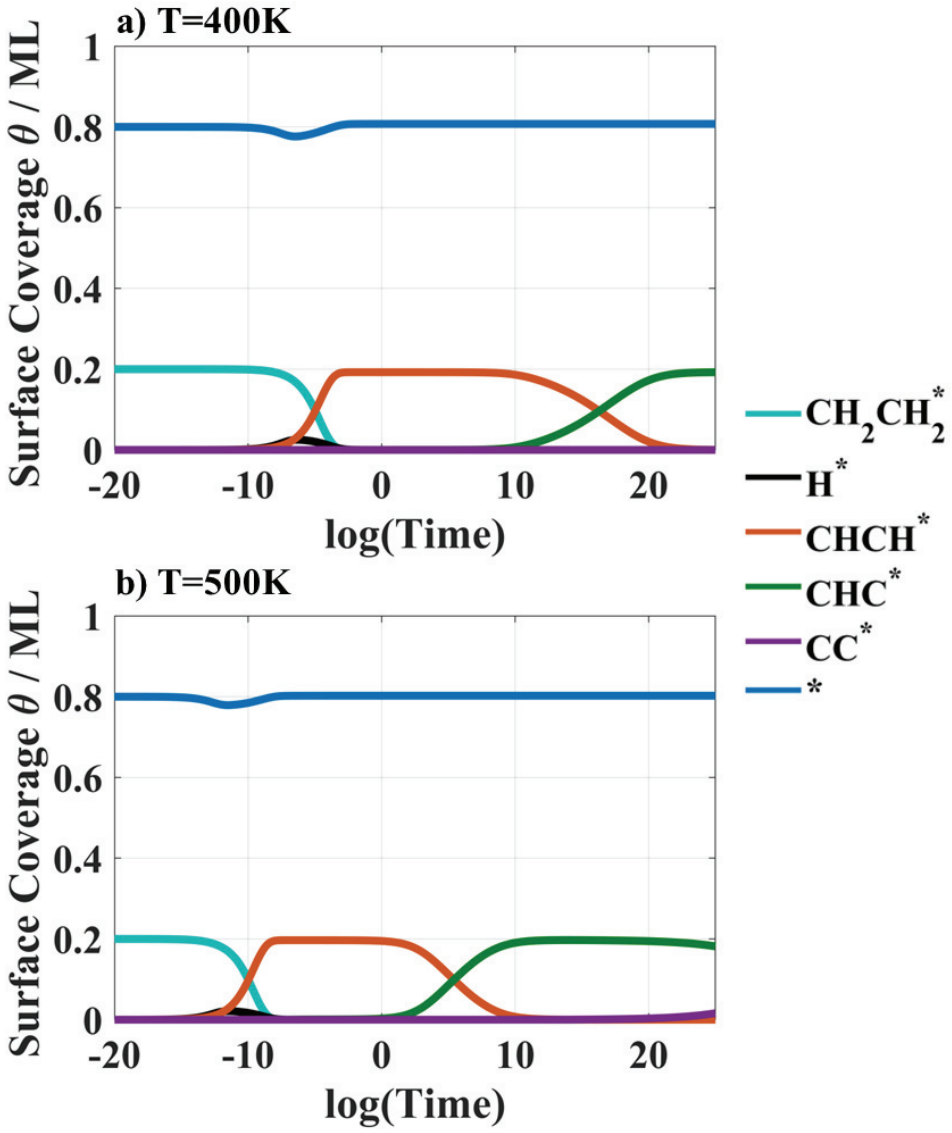


**Figure 56.** Surface coverage transient responses of products of ethylene pre-covered Co(111) surface decomposition a) at T=400K b) T=500K.

**Figure 56** presents transient surface coverage of (0.2 ML) ethylene decomposition products in the second temperature interval of interest (300-500K). Compared to the first temperature interval, here, we see that surface ethylene decomposes faster to surface acetylene species. Moreover, our results suggest that in this temperature range surface acetylene can decompose to surface ethynyl CCH through $TS_9$ (CHCH* + * <-> CHC* + H*),

which is not the case for the low-temperature interval previously discussed. Therefore, in the second temperature interval, partial dehydrogenation of acetylene to surface ethynyl CCH occurs. Higher temperatures (T=500K) facilitate earlier partial decomposition to acetylene compared to lower temperatures (T=400K). Weststrate et al. [211] found that acetylene covered surface is stable up to 400K. This is in reasonably good agreement with our results where we find that at steady-state conditions and T>300K, acetylene partially dehydrogenates to surface ethynyl CCH. Note that, specifically for T=500K, a small amount of dicarbide CC* can also be observed for long runs and therefore, a second dehydrogenation step of acetylene also occurs at this temperature. In the experiment, a gradual heating rate of 0.5K/s was applied, suggesting that the overall investigation was conducted for (400-200)/0.5K/s=400 seconds between the surface state where acetylene is detected as stable (200K) and where it started to decompose (400K). Besides, in our micro-kinetic study, the initial surface state is always a 0.2ML ethylene pre-covered surface, whereas, in those experiments, the initial surface state evolves in time due to the previously mentioned dynamic temperature conditions. Nevertheless, Weststrate et al. [211] found that the ethylene-saturated surface heated above 400K produces atomic carbon based on the similarity of double peak structure of Co(0001) 1s core-level XPS spectrum with previously studied Ni(111)[307]. However, our results do not support the presence of atomic carbon on the surface. In conclusion, in the temperature interval 300-500K, the following transformations occur according to our micro-kinetic results $CH_2CH_{2(ads)} \rightarrow CH_2CH(ads) \rightarrow CHCH_{(ads)} \rightarrow CCH_{(ads)} \rightarrow CC_{(ads)}$.

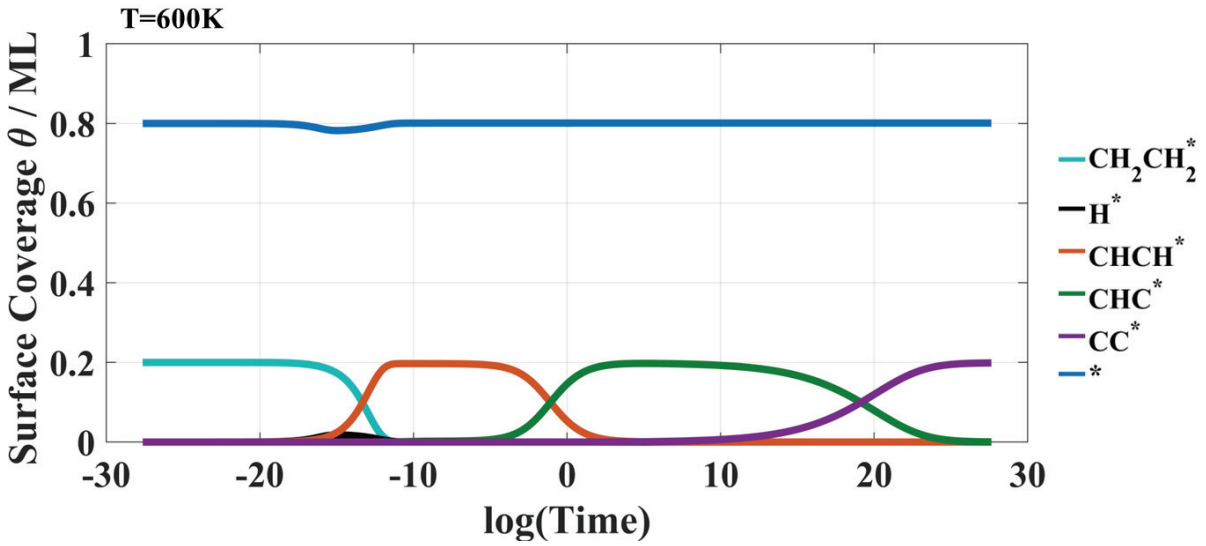


**Figure 57.** Surface coverage transient responses of products of ethylene pre-covered Co(111) surface decomposition at T=600K.

**Figure 57** presents transient surface coverage of (0.2 ML) ethylene decomposition products in the third temperature interval (>500K). Compared to the previous temperature ranges, **Figure 57** suggests that surface ethynyl CCH dehydrogenates completely for T>500K giving surface dicarbide CC. In other words, initially formed acetylene dehydrogenates in a two-step manner where, surface ethynyl CCH and dicarbide CC are formed, respectively. Note that even at the high-temperature interval, carbon-carbon bond in surface dicarbide remains intact according to our calculations. Xu et al. [142] found that ethylene pre-covered surface decomposition depends on the amount of vacant site available on clean (0001) Co surface. When heated at 424K they found the formation of graphite carbon with hydrogen desorption. However, according to them, graphitic carbon forms from carbide C rather than dicarbide $C_2$. Chen et al. [308] studied within DFT calculations the energetics and kinetics of C nucleation in the early stages of graphene growth on different metal surfaces. They found that both surface dicarbide CC (observed in this work) and carbide C may be involved in the initial stages of graphene growth depending on the strength of surface C/metal bond. According to them, if C/metal bonds are very strong, the dimer formation is not energetically favorable. In contrast, if C/metal bonds are weak, the formation of dicarbide is preferred.

Furthermore, they categorized several closed-pack metal surfaces in terms of metal/C bond strengths and suggested that on Co monomer formation is preferred. Although they did not give details on the structure of Co (hcp or fcc), they did explain that their results may be modified due to the variation in the binding nature due to geometrical effects. Thus, according to these authors, Co(111) and Co(0001) surface may behave differently, although cobalt crystallites with a diameter less than 100 nm fcc is the thermodynamically preferred phase[100]. We also point to the fact that in that work, $CH_\beta$-$CH_\beta$ scission reactions that produce monomer units $CH_\beta$ that could eventually dehydrogenate and give surface carbide C were not studied. In conclusion, the high-temperature range we considered in this study >500K, the following reaction pathway of ethylene decomposition occurs $CH_2CH_{2(ads)} \rightarrow CH_2CH(ads) \rightarrow CHCH_{(ads)} \rightarrow CCH_{(ads)} \rightarrow CC_{(ads)}$ according to our micro-kinetic calculations.

In this section, we showed in detail the plausible mechanisms of ethylene decomposition once readsorbed on the Co(111) surface by combined DFT and micro-kinetic calculations. Our study infers that the most favorable final decomposition product of ethylene at temperatures >500K on Co(111) is dicarbide surface species (CC*).

We did not address many open questions in this study due to time limitations: 1) we did not take into account reactions in which ethylidyne species are involved. However, we explained why those reactions may not represent the principal pathway for the formation of deactivation initiator; 2) coverage-sensitivity phenomena have not been studied in-depth, i.e., decomposition of ethylene has not been examined for different surface coverages of spectator atoms/molecules. 3) the structure-sensitivity phenomena needs to be further investigated. Although our calculations have been performed on Co(111) surface, we believe that other close-packed surfaces and step-surfaces behave differently in terms of the decomposition of ethylene. For instance, we think that ethylidyne species decomposition on the step sites may readily occur. 4) we did not examine $CH_\beta$-$CH_\beta$ scission reactions although it has been shown

on Co(0001) surfaces that those barriers are significantly higher than barriers of dehydrogenation reactions[219]. Further analysis needs to be undertaken to verify if the same holds for Co(111) surface. Results presented by Peng et al. [210] suggest that this may not be the case for Co(111). If those barriers are found comparable to barriers of dehydrogenation reactions presented in **Section 5.2**, one may think of some more favorable pathways for deactivation initiator formation that do not require ethylene to be readsorbed. Thus, we cannot exclude the importance of some $C_1H_\beta$ species in the formation of deleterious forms of carbon.

Nevertheless, our results strongly infer that the most favorable surface species produced in ethylene re-adsorption and subsequent decomposition are surface acetylene CHCH, ethynyl CCH, and dicarbide CC species. Using a combined DFT and microkinetic model presented above, we estimated that surface ethylene will most likely decompose to surface ethynyl species CCH seeing that surface acetylene decomposes to a lower temperature and that the energy barriers for CH-bond scission in CCH are high. In our opinion, $C_2H_\beta$ with low $\beta$ represent ideal candidates for deactivation initiators. Firstly, our results in **Section 4.3** show that the stability of polymeric forms of carbon and coke is reduced when hydrogenated. Secondly, polymeric hydrocarbons $C_\alpha H_\beta$ with low $\beta$ ensure a "close contact" of carbon with Co surface as we have shown in **Section 4.2**. Increase in hydrogen ($\beta\uparrow$) tends to detach C from the surface while forming multiply hydrogenated $CH_\beta$ species due to H pulling effect. Thus, carbon/metal surface contact is ensured in hydrogen deficient conditions in line with the observed deactivation phenomenon. We therefore expect those $C_\alpha H_\beta$* species to have high residence times on the surface and high probabilities to undergo $CH_\beta$ / $CH_\beta$ coupling reactions that would allow deleterious C to grow. Thirdly, $C_2H_\beta$ species represent more favorable deactivation initiators considering that a stronger hydrogenating environment is needed to evacuate them from the surface compared to $CH_\beta$ species. In other words, in order to eliminate $C_2H_\beta$ species, we expect greater H surface concentration to form the specie that can desorb.

In conclusion, surface ethynyl CCH can be regarded as the representative deactivation initiator based on our combined DFT and micro-kinetic study and considering thermodynamic, geometric, and kinetic considerations we presented above. Surface ethynyl CCH will be used below to model the formation of deleterious forms of carbon we found in **Chapter** 4.

## 5.3 Deleterious carbon seed formation-Cyclotrimerization mechanism in CC coupling

According to the literature[217] (**Section 2.6.4)**, when heated, ethylene pre-covered surface transforms in different forms of carbon considered damaging for the activity of FTS catalysts. Although there is no consensus on the exact structure of the deactivation initiator species, in several independent works on Rh(111)[218] and Co(0001) [211,212,198] it was suggested that a surface cyclotrimerization reaction of some $C_2H_\beta$ species occurs. Cyclotrimerization reactions have been extensively studied in the literature on some non-cobalt catalysts such as Cu[309,220] and Pd [310–312]. Interestingly, it was found[311] that the selectivity towards cyclotrimerization reaction increases in the following order of facets (111):(110):(100)=100:18:5 making (111) surfaces particularly interesting for studying those reactions. In the work of Wang et al. [218] cyclotrimerization of *ethylidyne* was proposed as a key step in the mechanism of graphene formation, whereas Weststrate et al. [198] proposed the cyclotrimerization reaction of *acetylene* on Co(0001). In this section, we wish to analyze the feasibility of this type of reaction and we suggest studying the cyclotrimerization reaction of surface ethynyl CCH we previously identified as the most abundant, thermodynamically and kinetically favorable ethylene decomposition product. Therefore, similarly to the work of Weststrate et al. [198] and Wang et al. [218], we wish to form cyclic structures, identified in **Chapter 4**, that block catalytic sites thus initiating the deactivation phenomenon. The cyclotrimerization reaction is going to be studied as a two-step reaction in which first, a $C_4H_2$ polymeric species are formed. In a second step, the latter is coupled with a third surface

ethynyl CCH species to create a $C_6H_3$ cycle considered as a harmful carbon seed structure in this study. Hence, two reactions will be studied, $CCH + CCH \rightarrow HCCCCH \equiv C_4H_{2_{(poly)}}$ and $CCH + C_4H_2 \rightarrow C_6H_{3(cycl)}$.

### 5.3.1 Formation of $C_4$ intermediate

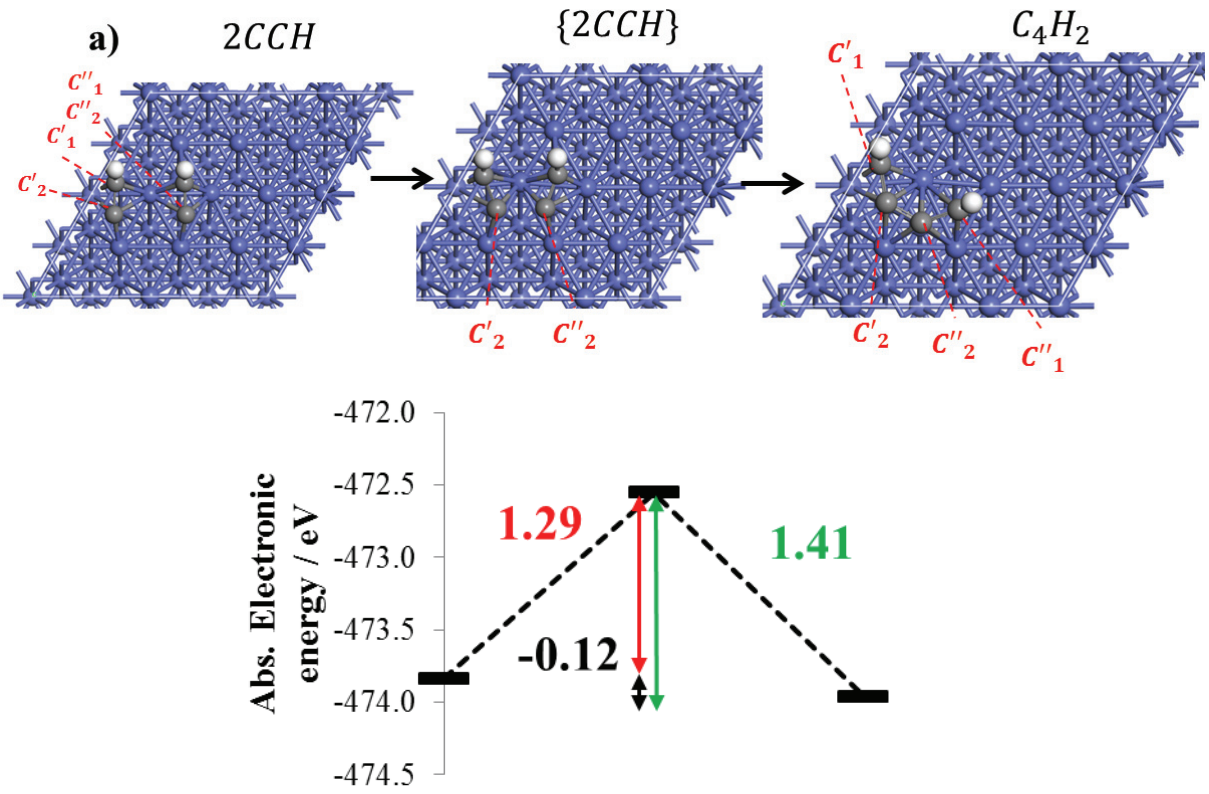


**Figure** 58. a) Structural and b) energy properties of $C_4$ intermediate formation reaction starting from two surface ethynyl units previously identified as plausible deactivation initiators.

Starting from two surface ethynyl species (d($C_1C_2$)=1.37Å in both of them and d(C'$_2$C''$_2$)=3.06 Å), terminal carbon atoms initially sitting in hollow sites, approach each other through Co bridge positions where d(C'$_2$C''$_2$)=1.88 Å. In this transition state, one imaginary frequency has been obtained that corresponds to CC stretching of C'$_2$C''$_2$ one towards another ($\tilde{\nu} = -485.5\ cm^{-1}$). Once the CC bond is formed, C'$_2$ and C''$_2$ both initially in Co bridge positions, relax so a polymeric carbon species is formed on the surface. The

energy barrier for the forward reaction is 1.29 eV and it is higher than most CH bond scission reactions we studied previously, suggesting that a formation of this $C_4H_2$ polymeric intermediate may be a rate-determinating step for deactivation. Note, however, that we have chosen to bring two (hydrogen free) $C_2$ ends to form a C/C bond whereas, as suggested by Hu et al. [108] hydrogenated ends i.e., $C_1$'C''$_2$ , $C_2$'C''$_1$ ($C_1$'C''$_2H_\beta$ etc.) may be kinetically more favorable. In other words, our calculation may be regarded as the worst-case scenario for polymeric carbon formation i.e., kinetically the most exigent reaction, for $C_4H_2$ intermediate formation. Dimerization of surface ethynyl species $2CCH \rightarrow C_4H_2$ is an exothermic reaction according to our calculations and hence, thermodynamically favorable. No studies in the literature were found to compare the structure of our theoretical $C_4$ intermediate with those hypothesized in [198,218].

### 5.3.2 Step-wise formation of a cyclic $C_6$ intermediate

According to our calculations, 4+2 cycloaddition reaction of surface ethynyl species with the previously formed $C_4$ intermediate is a four-step reaction. In a first step, CC coupling reaction occurs, resulting first in a *bent* $C_6$ polymeric species. In a second step, bent $C_6$ polymeric species relax to an energetically more favorable (also bent) isomer structure that further undergoes a CC bond coupling and cyclization reaction (third step). In the last step, cyclic $C_6$ species relax to an energetically more stable cyclic $C_6$ species. The overall step-wise formation of a cyclic intermediate can be thus represented using the following reaction set: $CCH + (C_4H_2)_{poly} \rightarrow (C_6H_3)_{bent_1} \rightarrow (C_6H_3)_{bent_2} \rightarrow (C_6H_3)_{cycl_1} \rightarrow (C_6H_3)_{cycl_2}$ . These elementary steps are discussed below.

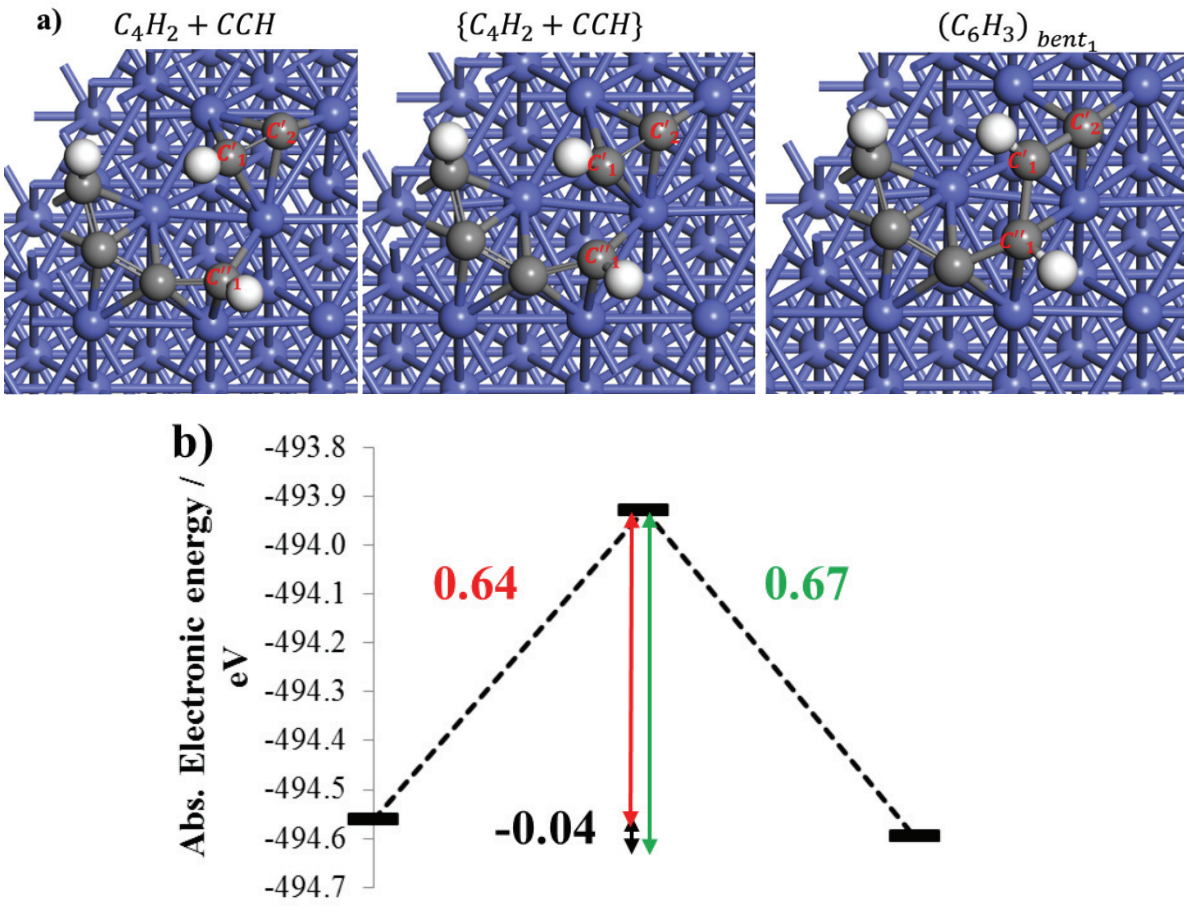


**Figure** 59. a) Structural and b) energy properties of 4+2 cycloaddition reaction of surface $C_4H_2$ intermediate and ethynyl specie resulting in the formation of polymeric $(C_6H_3)_{bent1}$.

Surface ethynyl species, sitting initially with its C'$_1$ (hydrogenated) and C'$_2$ end in the bridge and hollow position, respectively, approaches with its hydrogenated C'$_1$ to the hydrogenated C''$_1$ end of surface $C_4H_2$ intermediate (d(C'$_1$C''$_1$)=2.61 to 1.85Å in the transition state). In the transition state, one imaginary frequency has been identified ($\tilde{\nu} = -361.5\ cm^{-1}$), corresponding to a C'$_1$C''$_1$ stretching mode. Transition state structure then relaxes to a structure where all carbon atoms are approximately in hollow sites except for hydrogenated C'$_1$ that is too far from the surface to establish a contact with Co. The low energy barrier for this exothermic transformation suggests that the formation of polymeric $(C_6H_3)_{bent_1}$ can readily occur under FTS conditions.

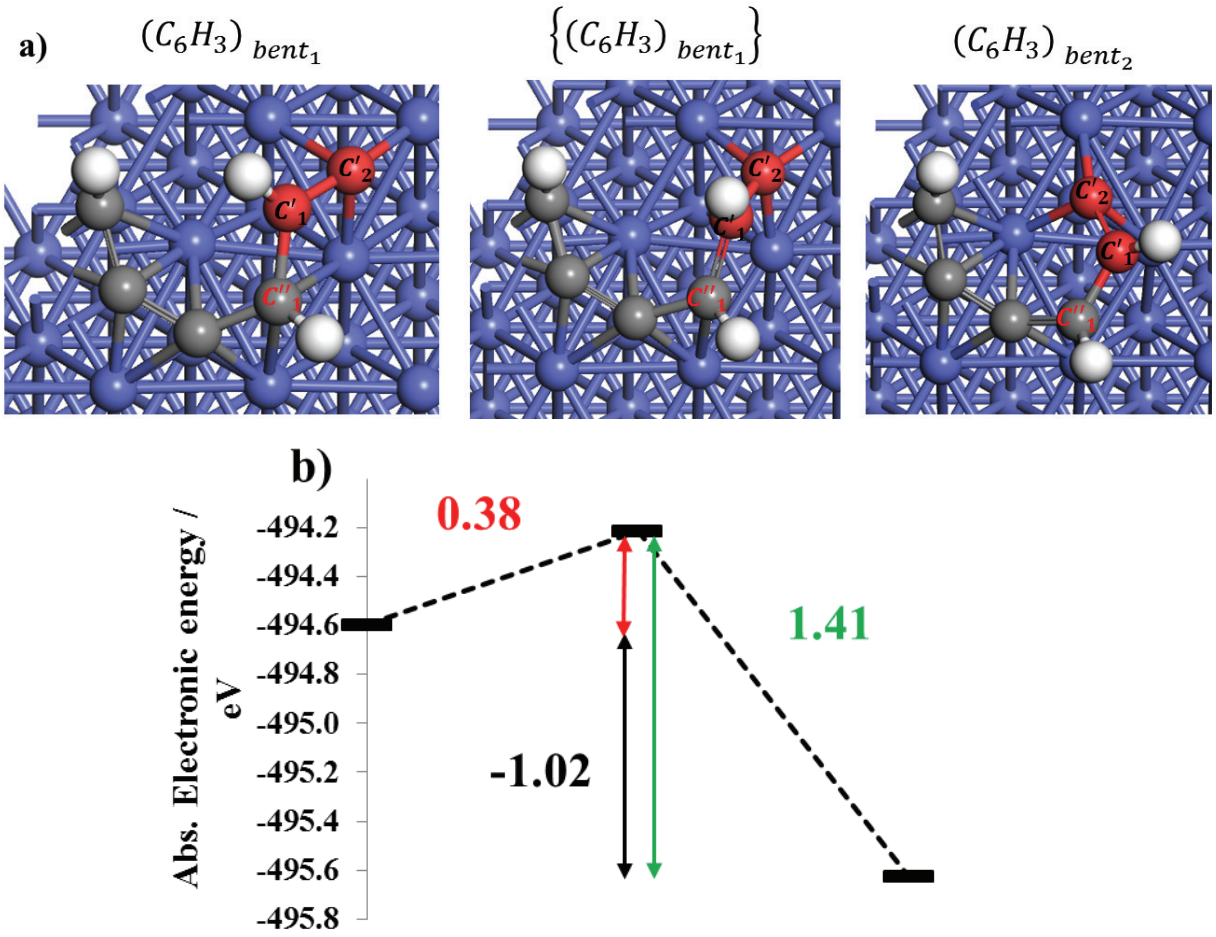


**Figure** 60. a) Structural and b) energy properties of isomerization of polymeric $(C_6H_3)_{bent_1}$ to $(C_6H_3)_{bent_2}$ reaction.

Polymeric $(C_6H_3)_{bent_1}$ surface species previously formed in $C_4$+$C_2$ addition reaction (d(C'$_1$C''$_1$)=1.53 and d(C'$_1$C'$_2$)=1.38Å) rearrange its C'$_2$ unit by switching place from one hollow site to another producing a 1.02 eV more stable polymeric form of carbon $(C_6H_3)_{bent_2}$ (d(C'$_1$C''$_1$)=1.45 Å and d(C'$_1$C'$_2$)=1.42 Å). One imaginary frequency was identified ($\tilde{\nu} = -257.0\ cm^{-1}$) that corresponds to a C'$_1$C'$_2$ stretching mode, confirming that it is a transition state structure. This isomerization reaction is highly exothermic and kinetically very fast, suggesting that it may occur readily under FTS conditions once polymeric $(C_6H_3)_{bent_1}$ is formed.

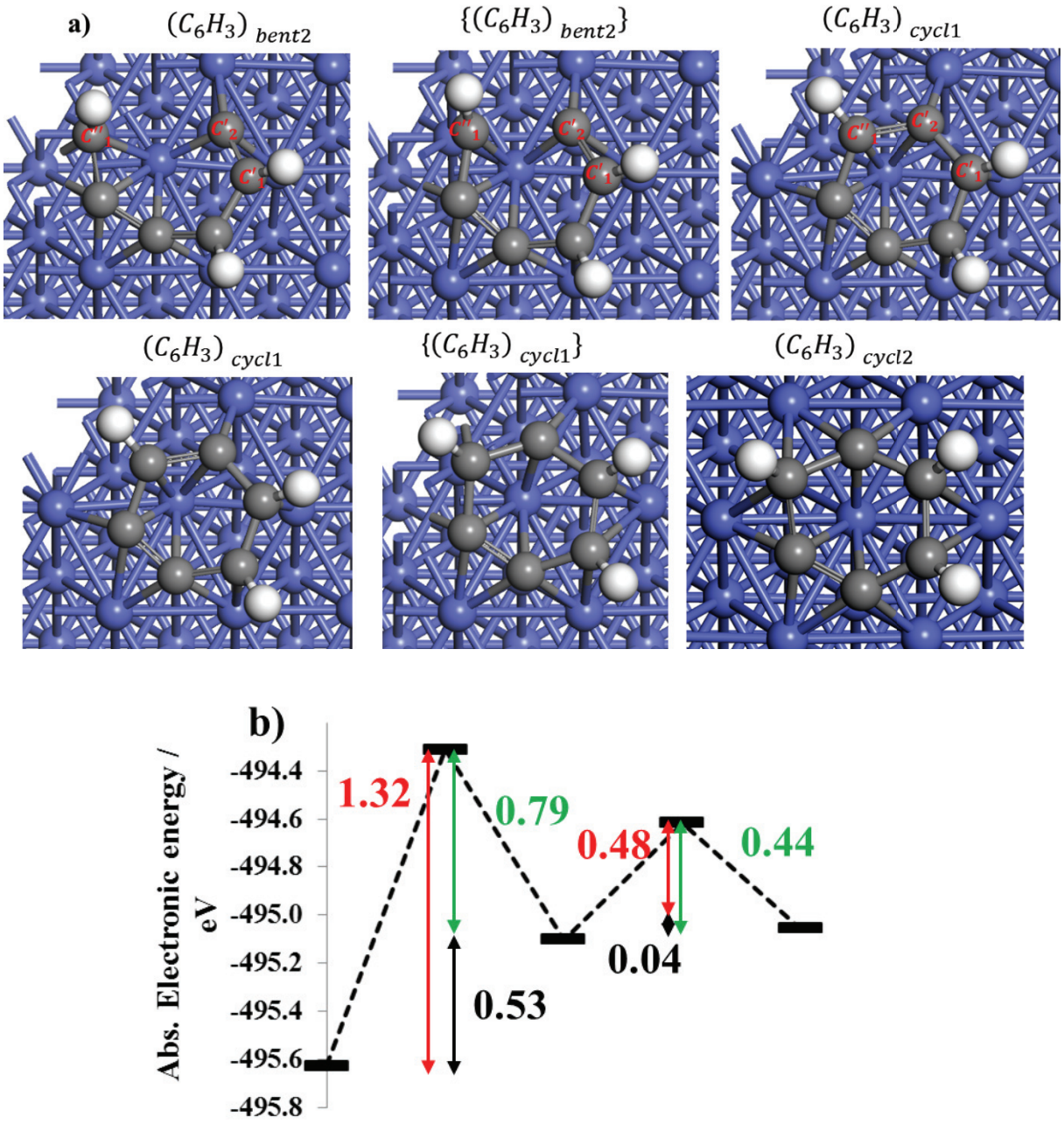


**Figure** 61. a) Structural and b) energetic properties of cyclization of polymeric carbon specie and a cycle relaxation reaction.

Initially formed bent $(C_6H_3)_{bent_2}$ (d(C$_1$''C$_2$')=2.9) undergoes a cyclization reaction in which coupling of C$_2$' approaching from a Co bridge site to C$_1$'' and a formation of $(C_6H_3)_{cycl_1}$ occurs. In the transition state d(C$_1$''C$_2$') shortens to 2.09. One imaginary frequency corresponding to a HC-C stretching mode was identified ($\tilde{\nu} = -397.5\ cm^{-1}$). In the final state, $(C_6H_3)_{cycl_1}$, d(C$_1$''C$_2$')=1.46. The energy barrier of this endothermic

cyclization reaction is somewhat high, suggesting that this step may represent a rate-determinating step in the overall coke seed formation. The previously formed cyclic intermediate $(C_6H_3)_{cycl_1}$ undergoes a structural rearrangement, once again through Co bridge positions, in which *all* C are relaxed to Co hollow positions. Those surface species $(C_6H_3)_{cycl_2}$ can be considered as a *coke seeds* that may continue to grow. Our results suggest that, although it is an endothermic reaction, it may occur with a very low energy barrier of 0.48 eV suggesting that this transformation is fast.

The results we presented in this section confirm that cyclotrimerization reactions of surface ethynyl species are both kinetically and thermodynamically possible. Hence, those represent a plausible but slow, low-temperature pathway for deleterious carbon species formation. A *coke-seed* that is, species that we believe can continue to grow in condensation reactions. Our results are in line with Weststrate et al. [198] who brought up the hypothesis that such cyclotrimerization reactions occur with surface acetylene species. However, no specific reaction pathways have been given. In fact, to the best of our knowledge, this pathway has never been studied using DFT methods. Although we cannot exclude either surface acetylene or ethylidyne species as deactivation monomers in line with previous studies, we believe that those species could readily undergo the C-C or C-CH coupling reactions we studied here. Below we address the issue of the fate of such coke-seed species.

### 5.3.3 Coke seed growth reactions

Once formed, the cyclic structure presented above may continue to grow according to our hypothesis. In the view of Weststrate et al. [198], acetylene species could be incorporated effectively in the structure of such cyclic species. Although we share this view, recent findings of Xu et al. [313] suggest that it is kinetically more favorable for $C_1$ species to be incorporated into the existing graphene-like structure. In that work, authors studied the

kinetics and thermodynamics of $C_1$ and $C_2$ coupling to graphene on a graphene-like pre-covered Co(0001) surface. It was found that the apparent energy barrier for $C_1$ coupling to graphene is lower than the corresponding energy for $C_2$ incorporation to graphene. They suggested that both transformation reactions proceed via a carbon cluster attachment mechanism[313]. Interestingly, Weststrate et al. [198]also found "occasional incorporation of atomic carbon". Considering that surface species $C_1H_\beta$ are part of all conventional mechanisms proposed for the FTS reaction, but also findings of Xu et al. [313] we propose studying here coke-growth reactions by incorporating $C_1H_\beta$ species with low β into the existing coke-seed formed previously. In this study, we choose C and CH as candidates for coke growth monomers. Reactions in which they are involved will be referred to as *coke-growth* reactions.

#### *5.3.3.1 Coke-growth with C through C/CH coupling*

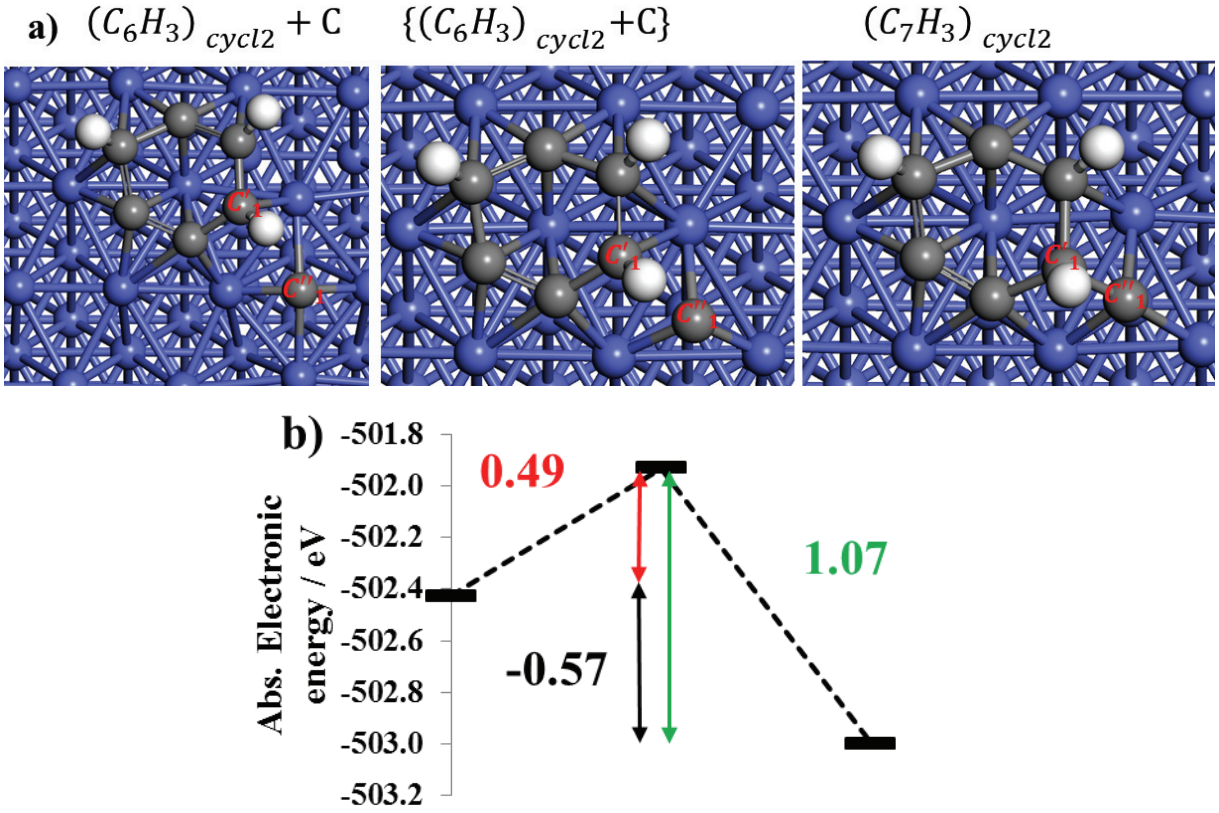


**Figure** 62**.** a) Structural and b) energetic properties of a coke-growth with C as a monomer specie.

Atomic C found in the *four-fold hollow* site[4] near initially formed coke-seed, cyclic surface species $(C_6H_3)_{cycl2}$ (d(C$_1$'C$_1$")=2.65) approaches its C$_1$' end of the cycle through a Co bridge position (d(C$_1$'C$_1$")=2.05) and sits on another hollow site, where CH/C coupling reaction occurs, resulting in a cyclic $(C_7H_3)_{cycl}$ surface species. The energy barrier for this reaction is 0.49 suggesting that growing coke-seed is kinetically favored if C is considered as a coke-growth monomer and if the hydrogenated C$_1$' end of a cycle is involved. In addition, this coke-growth reaction is exothermic. Note that we aim for coupling C and CH unit of the cycle due to higher barriers for C/C coupling reactions reported in the litterature[108].

### *5.3.3.2 Coke-growth with C through CH/CH coupling*

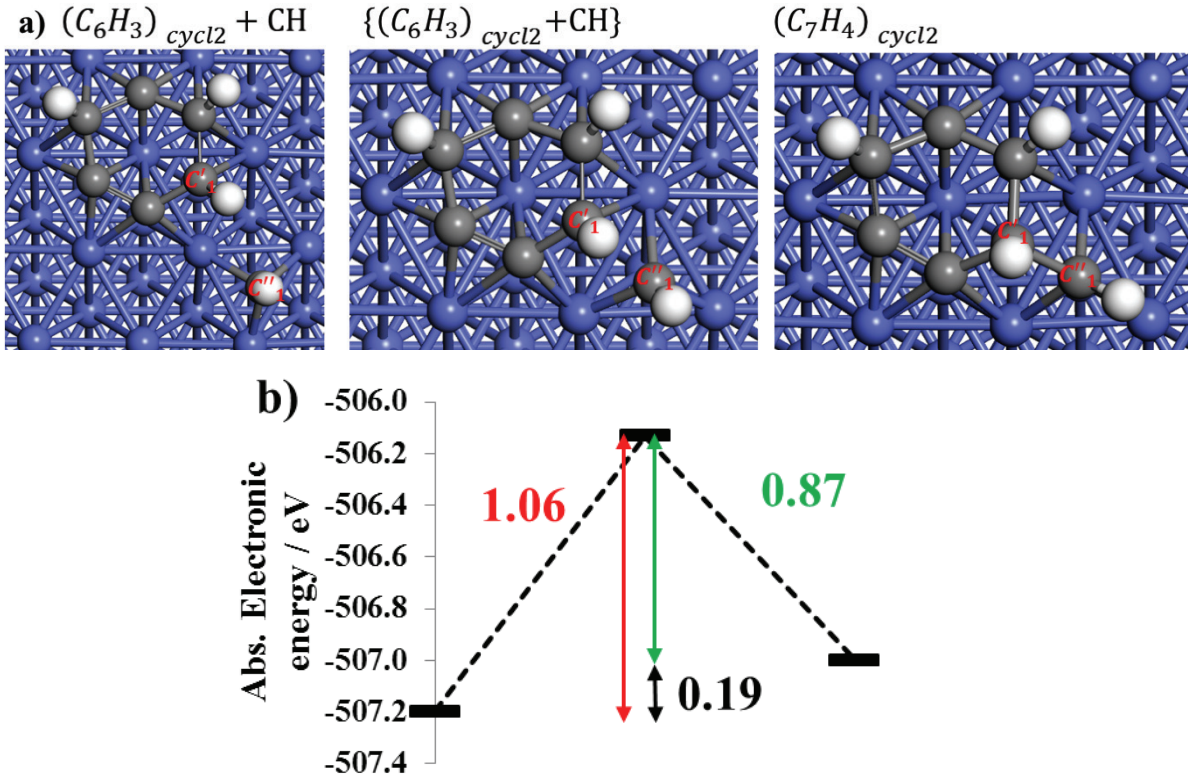


**Figure** 63**.** a) Structural and b) energetic properties a coke-growth with CH as a monomer specie.

[4] Note the surface rearrangement of Co atoms where a four-fold hollow site, previously non-existing, formed.

CH surface species in the three-fold hollow site near initially formed coke-seed, cyclic surface species $(C_6H_3)_{cycl2}$ (d($C_1$'$C_1$")=2.94), migrate through a bridge Co site to another Co hollow site where CH/CH coupling reaction occur (d($C_1$'$C_1$")=1.94). The energy barrier of CH/CH is significantly higher than the coupling reaction of C/CH in disagreement with previous results for C/C coupling reactions (for flat Co surface, barriers of 2.63 and 2.27 eV have been reported for C/CH and CH/CH, repsectively) [108].

Coke-growth reactions studied in this section represent some of the possibilities for coke to grow among many others. For instance, several coupling reactions can be proposed for coke-growth such as $C_{ring}/CH_\beta$ (carbon ring unit coupling with $CH_\beta$) and $C_{ring}H_\beta/CH_\beta$ (hydrocarbon ring unit $C_{ring}H_\beta$ coupling with $CH_\beta$) depending on the structure of cyclic intermediates but also the nature of deactivation growth intermediate.

## 5.4 Conclusions from kinetic calculations

In the present work, we presented some pathways for the formation of cyclic species considered as deleterious in the FTS, assuming that the *deactivation initiator* species (**Section 5.2**) has the same structure as ethylene decomposition product at T=500K. To our knowledge, our study is the first DFT study that proposes a mechanism for cyclic intermediate formation, its structure and offers some explanations on how cyclic intermediates grow.

In **Section 5.2**, we analyzed using combined DFT and microkinetic modeling experimental studies on graphene formation from ethene in surface science study conditions. From those findings, we obtained some new insights and ideas related to the unknown nature of underlying bond scission and formation reactions that lead to the experimentally proven formation of graphene. Our study shows that surface ethynyl species CCH may be regarded as the most plausible deactivation initiator. This is the outcome of our study on the decomposition of ethylene (**Section 5.2**). Moreover, we hypothesize that the formation of

those species under FT conditions is possible considering the reaction mechanisms described in **Section 2.3.** Thus, in our opinion, our conclusion is not restricted to the ethylene readsorption concept since the deactivation initiator found, surface ethynyl may also be formed during in $C_1/C_1$ coupling reactions.

We presented in **Section 5.3** some DFT results on the nature of the CC coupling reactions of deactivation initiators assuming evoked 2+2+2 cycloaddition reactions in the litterature[211]. More specifically, we proposed both thermodynamic and kinetic results of a stepwise mechanism for coke formation. First, we presented results on the condensation of deactivation initiators CCH to obtain polymeric $C_4$ species (found in the transition of **Zone** 1 to **Zone 2** in **Chapter 4**). Then we assumed that polymeric species can further grow to $C_6$ and cyclize on the surface yielding structures we found at the beginning of **Zone** 3 in **Chapter 4** and considered them detrimental coke seed (precursor) by the site-blocking effect. To account for progressive deactivation as observed in **Figure** 21, we assumed that coke seed can continue to grow and for that purpose, we proposed atomic C and CH species as monomers to obtain cyclic $C_7$ species found in **Zone** 3. We did not study further growth of such species but considering other theoretical works [108] further CC coupling reactions seem kinetically and thermodynamically favorable. Hence, we postulate that such CC coupling reactions give essentially graphene-like covered surface resulting in a long-term deactivation.

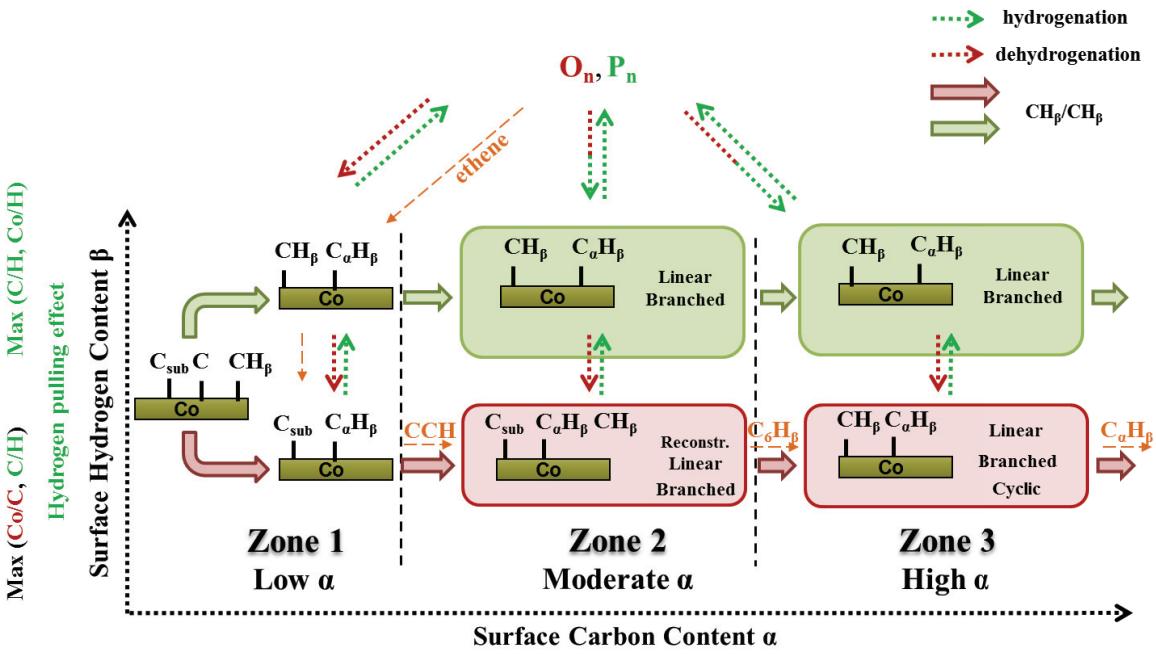


**Figure** 64. Schematic representation of reactions that could result in deactivation by carbon. The pathway studied in this work is shown in orange.

In **Figure** 64, we present schematically the summary of results acquired in **Chapter** 4 and 5. It is not difficult to imagine some other pathways that would lead from **Zone** 1 to **Zone** 2 other than that we studied in this chapter (presented in orange in **Figure** 64). More precisely, we have shown that in **Zone** 1 characterized with low carbon surface coverage α, hydrocarbon monomers, chains and subsurface carbon may be found. Surface species $CH_\beta$ in **Zone** 1 are found thermodynamically very favorable in accordance with commonly proposed FT reaction mechanisms. Also, we have shown that hydrogen has a profound impact on the overall geometry of the hydrocarbon structure considering that it detaches carbon atoms from the surface, i.e., Co/C bond breaking at the expense of C/H bonds (hydrogen pulling effect). Note that low surface coverages of hydrogen in **Figure** 64 favor the presence of subsurface carbon atoms. Hence, **Zone** 1 in **Figure** 64 is divided into two distinct groups of hydrocarbon units, on the one hand, hydrocarbon monomers and chains where CH bonds are maximized and consequently the latter is considered as some FT product precursor. On the other hand, hydrocarbon units $C_\alpha H_\beta$ with low H content that are “stuck” to the surface acting as coke

precursors. We believe that in this zone, coke precursors can still be hydrogenated to give some FT product if the condition of local surface hydrogen concentration is fulfilled. In this chapter, we have proposed that in **Zone 1**, CCH species can be considered as the most plausible coke precursors. More specifically, we suggested that such deactivation initiator may be obtained in ethylene dehydrogenation reactions. However, C/CH coupling reactions may represent a second possible formation pathway. Moreover, it should be noted that this pathway would compete with chain growth towards FTS products. In this chapter, we have also proposed species such as acetylene CHCH and dicarbide CC as possible coke precursors. Further investigation needs to be conducted to examine the thermodynamics and the kinetics of their transformations to **Zone 2** and **3**.

**Zone 2**, characterized by moderate carbon coverages, is also composed of two types of hydrocarbons. For hydrogen-poor conditions (represented by low β in our study), on the one hand, polymeric carbon species (linear and branched) and for hydrogen-rich conditions, on the other hand, precursors of linear and branched hydrocarbons. In this zone, however, the surface concentration of carbon in the subsurface positions may be sufficient to induce surface reconstruction phenomenon if hydrogen surface concentration is low. In addition, the conditions for the formation of branched ternary carbon atoms are met in this zone. Considering the hydrogen resistance of branched C we have presented in **Chapter 4**, the accumulation of linear and in particularly branched C species (referred to as polymeric carbon) is considered harmful for the activity of FT catalysts. In this chapter, we presented the dimerization and trimerization reactions of CCH as the possible reaction pathways of transition from **Zone 1** to **Zone 2** where polymeric linear chains are formed. We believe that in **Zone 2**, regeneration of surface may still be possible under typical FT conditions unless if branched C chains are formed (ternary C is sterically hindered from surface hydrogens by other carbon atoms). Further work is needed to clarify the role of ternary-branched C on the

deactivation phenomenon such as the reaction mechanism of their transformation to cyclic structures.

In **Zone 3**, the surface presents a high concentration of branched C chains and cyclic compounds. Surface active sites are shielded with those carbon-containing structures and thus the deactivation phenomenon is expected to be pronounced. Based on some experimental findings, we studied the growth of the cyclic compound using $C_1$ monomer species. As a perspective, other pathways may be considered. Considering that **Zone 3** is covered in inaccessible (to hydrogen) branched C atoms, at this point, we do not see how this surface may be regenerated under typical FTS conditions. Hence, the key in the long-lasting catalysts seems to be the control of the quantity of *surface* hydrocarbon quantity in **Zones 1** and **2** in order to avoid reaching **Zone 3**.

In **Chapter 6**, we will add those elementary steps into a micro-kinetic model, aiming to describe a long-term activity and selectivity losses phenomena based on the results we obtained in this chapter. Our interest is hence to see whether the introduction of the reaction mechanisms described here in the micro-kinetic model can account for experimental observations and in particular the deactivation profile.

# 6 Micro-kinetic modeling of deactivation of Co-based FT catalysts

The present thesis has an objective to supply the micro-kinetic model with elementary steps essential to describe the deactivation phenomena based on DFT results and to facilitate the optimization of industrial FT process. In **Chapter 4**, a DFT study was used to evaluate the structure and the energy of surface intermediates of the FT reaction and deactivation phenomenon related to it. In that thermodynamic study, it has been established that carbon has a preponderating role in the catalyst deactivation phenomenon. Thus, based on those findings, we propose thermodynamically and kinetically relevant carbon-induced deactivation mechanism in **Chapter 5**. Our study shows that surface ethynyl species CCH, ethylene dehydrogenation product, may be regarded as deactivation initiators. We then presented in **Section 5.3** some DFT results on the nature of the CC coupling reactions of those deactivation initiators assuming 2+2+2 cycloaddition reactions evoked in the literature. Thus, we presented arguments for condensation of deactivation initiators CCH to obtain polymeric $C_4$ species that can further grow to $C_6$ and cyclize on the surface yielding detrimental coke seed (precursor) by the site-blocking effect. To account for progressive deactivation as observed in **Figure 21**, we assumed that coke seed can proceed to further growing reactions and for that purpose, we proposed atomic C and CH species as monomers. In this chapter, we undertake the addition of proposed deactivation mechanism in the micro-kinetic model described in **Section 2.4** and we evaluate the impact of deactivation steps on some FT observables that we further compare with the literature. Hence, in current work, we contribute to the current understanding of the deactivation phenomenon related to the FT reaction. Firstly, we optimize the deactivation-free model of Tronconi et al. described in **Section 2.4** using experimental data described in **Section 8.8** in order to estimate values of unknown micro-kinetic model parameters (rate constants and activation energies). Secondly, we incorporate the deactivation model from

**Chapter 5** into the micro-kinetic model scheme in **Section 2.4** and we re-optimize this deactivation-containing micro-kinetic model. Thirdly, we present some perspectives for improving our deactivation model.

## 6.1 Experimental measurements

Experimental measurements are not part of this thesis but are the subject of an ongoing thesis at IFPEN[148]. However, it is convenient to present the basis of experimental set-up, as well as operating conditions under which those measurements are carried out, considering that this data will be used for the optimization of the deactivation-free model of Tronconi et al.

The evaluation of performances of the non-commercial catalyst (see [148]) is conducted in the high throughput experimentation (HTE) unit. This unit consists of 16 parallelized fixed-bed reactors (internal diameter of 2 mm, height 56cm) that operate simultaneously. The HTE unit is equipped with the system for collecting liquid fractions of the reaction effluent as well as the Gas Chromatograph (GC) that allows online analysis. This experimental setup allows quantifying low-weight hydrocarbons up to $C_{14}$, as well as typical gas-phase FTS reactants and products every 4h for all 16 fixed-bed reactors. On the contrary, this experimental setup lacks the possibility of performing material balance on C, H and O considering that the analysis of the gas-phase products $>C_{14}$ is impossible and that of $>C_7$ is prone to errors. Experimental conditions were varied in the following ranges: $H_2$/CO feed ratio = 1.85-2.4, GHSW= 3.93-25.86, T=210-230°C and P=10-30 bar. The central point is defined at 220°C, 2.12 and 20 bar in order to check for the absence of deactivation phenomenon. In all experimental plans, Pt-doped Co/$Al_2O_3$ catalysts of the average size of 18 nm are employed. As discussed by Diehl et Khodakov, promotion with platinum considerably increases FT reaction rate, increases methane selectivity and reduces a selectivity compared to monometallic counterparts [314]. Thus, results discussed in this work should be carefully

compared with other data in the literature discussing deactivation phenomena. The summary of the experimental plans considered in our work is given in **Table 12**. Considering the absence of thorough product analysis in all experimental plans, paraffin and olefins chain growth probabilities α in this work is deterimined based on $C_5/C_4$ products distribution rather than on the $C_{15+}$ basis, assuming that the former and the latter yield identical result.

**Table 12**. Operating conditions for experimental plans.

| Description | No. | T / °C | P / bar | $H_2$/CO inlet | GHSV / NL/h/g | Catalyst Mass / mg |
|---|---|---|---|---|---|---|
| Central Point | 1 | 220 | 20 | 2.12 | 11.10 | 215 |
| | 2 | 220 | 20 | 2.12 | 14.46 | 165 |
| | 3 | 220 | 20 | 2.12 | 18.36 | 130 |
| | 4 | 220 | 20 | 2.12 | 23.87 | 100 |
| Reevaluated Central Point | **5** | **220** | **20** | **2.12** | **6.98** | **215** |
| | 6 | 220 | 20 | 2.12 | 9.09 | 165 |
| | 7 | 220 | 20 | 2.12 | 11.54 | 130 |
| | 8 | 220 | 20 | 2.12 | 15.00 | 100 |
| Low $H_2$/CO | 9 | 220 | 20 | 1.85 | 5.80 | 215 |
| | 10 | 220 | 20 | 1.85 | 7.56 | 165 |
| | 11 | 220 | 20 | 1.85 | 9.59 | 130 |
| | 12 | 220 | 20 | 1.85 | 12.47 | 100 |
| High $H_2$/CO | 13 | 220 | 20 | 2.4 | 8.73 | 215 |
| | 14 | 220 | 20 | 2.4 | 10.30 | 165 |
| | 15 | 220 | 20 | 2.4 | 12.45 | 130 |
| | 16 | 220 | 10 | 2.4 | 11.06 | 100 |
| Low P | 17 | 220 | 10 | 2.12 | 4.97 | 215 |
| | 18 | 220 | 10 | 2.12 | 6.47 | 165 |
| | 19 | 220 | 10 | 2.12 | 8.22 | 130 |
| | 20 | 220 | 10 | 2.12 | 10.69 | 100 |
| High P | 21 | 220 | 30 | 2.12 | 8.09 | 214 |
| | 22 | 220 | 30 | 2.12 | 10.93 | 158 |
| | 23 | 220 | 30 | 2.12 | 13.43 | 129 |
| | 24 | 220 | 30 | 2.12 | 17.67 | 98 |
| Low T | 25 | 210 | 20 | 2.12 | 3.93 | 214 |
| | 26 | 210 | 20 | 2.12 | 5.32 | 158 |
| | 27 | 210 | 20 | 2.12 | 6.53 | 129 |
| | 28 | 210 | 20 | 2.12 | 8.59 | 98 |
| High T | 29 | 230 | 20 | 2.12 | 11.84 | 214 |
| | 30 | 230 | 20 | 2.12 | 16.00 | 158 |
| | 31 | 230 | 20 | 2.12 | 19.65 | 129 |
| | 32 | 230 | 20 | 2.12 | 25.86 | 98 |

## 6.2 Reaction scheme

In **Table 13** adsorption steps of both CO and $H_2$ are assumed to approach thermodynamic equilibrium under working conditions of FTS[147,96] (which allows writing equilibrium expressions for elementary steps (1) and (2) as discussed by Visconti et al. [73]). In their model, elementary step (3) is also at thermodynamic equilibrium whereas the second hydrogenation step (4) is a rate-determining step (**RDS**) in the series of steps (4) – (7). Rate constants that describe elementary steps for the chain growth of the adsorbed species (9), (11), and (13) are assumed independent of the carbon atom number of the involved intermediates $R_n - \sigma$. This reaction scheme is integrated in the fixed-bed model reactor (described in **Section 3.2**) and then solved and optimized using the procedure described in **Section 3.2.5**. All kinetic rate constants are expressed according to **Eq.** 72 and allowed to vary in [0,$10^5$] interval.

**Table 13**. Initial model parameters used in this study.

| El. Step number | El. Step Name | Elementary Step reaction [a)] | $k_{forward}$ | $k_{backward}$ [a)] | $E_{a,forward}$ kJ/mol | $E_{a,backward}$ kJ/mol |
|---|---|---|---|---|---|---|
| **1** | Initiation | $H_2 + 2\sigma^* \leftrightarrow 2H - \sigma$ | 3.980E-03 | 1.126E-02 | 210 | 120 |
| **2** | | $CO + \sigma^* \leftrightarrow CO - \sigma$ | 4.075E-02 | 4.115E-01 | 205 | 120 |
| **3** | | $CO - \sigma + H - \sigma \leftrightarrow HCO - \sigma + \sigma^*$ | 3.116E-02 | 9.903E-01 | 0 | 0 |
| **4-6** [b)] | Methylene species formation | $HCO - \sigma + H - \sigma \leftrightarrow HCOH - \sigma + \sigma^*$<br>$HCOH - \sigma + \sigma^* \leftrightarrow CH - \sigma + OH - \sigma$<br>$CH - \sigma + H - \sigma \leftrightarrow CH_2 - \sigma + \sigma^*$ | 5.353E+00 | 0 | 120 | 0 |
| **7** | Water formation | $OH - \sigma + H - \sigma \leftrightarrow H_2O + 2\sigma^*$ | | | | |
| **8** | Initiator formation | $CH_2 - \sigma + H - \sigma \leftrightarrow CH_3 - \sigma + \sigma^*$ | 7.519E-01 | 0 | 0 | 0 |
| **9** | Propagation | $R_n - \sigma + CH_2 - \sigma \leftrightarrow R_{n+1} - \sigma + \sigma^*$ | 4.591E+02 | 0 | 0 | 0 |
| **10** | Termination to paraffin for $n = 1$ | $CH_3 - \sigma + H - \sigma \leftrightarrow CH_4 + 2\sigma^*$ | 5.443E+00 | 0 | 0 | 0 |
| **11** | Termination to paraffin $\forall n \in \{2,50\}$ | $R_n - \sigma + H - \sigma \leftrightarrow P_n + 2\sigma^*$ | 6.774E-01 | 0 | 0 | 0 |

| | | | | | | |
|---|---|---|---|---|---|---|
| **12** | Termination to olefin for $n = 2$ | $C_2H_5 - \sigma \leftrightarrow C_2H_4 + H - \sigma$ | 8.511E-01 | 1.574E-03 | 0 | 120 |
| **13** | Termination to olefin $\forall n \in \{3,50\}$ | $R_n - \sigma \leftrightarrow O_n + H - \sigma$ | 5.174E-03 | 1.056E-07 | 0 | 0 |

a) If no $k_{backward}$ is given, the reaction is assumed irreversible.
b) Sum of 4-7: $HCO - \sigma + 3H - \sigma \leftrightarrow CH_2 - \sigma + H_2O + 3\sigma^*$

## 6.3 Results and Discussion

### 6.3.1 Optimization of deactivation-free micro-kinetic model

The initial parameter set is presented in **Table 13** and is evaluated using micro-kinetic scheme of Tronconi et al. [147,96] in order to test the adequacy of FT observables with experimental run 5 in **Table 12**. The results of those calculations are presented in **Table 14**.

**Table 14**. Comparison of experimental and simulated results of experimental run 5.

| Observable | Model | Experimental[a)] |
|---|---|---|
| $X(H_2)$ % | 1.85% | / |
| $X(CO)$ % | 2.44% | 70.25 |
| $\alpha_{P_n}$ | 0.0008 | 0.9294 |
| $\alpha_{O_n}$ | 0.0005 | 0.6329 |
| $S(CH_4)$ %$wt$ | 99.99% | 10.34% |
| $S(O_n)$ %$wt$ | 0.00% | / |
| $\frac{H_2}{CO}$ $inlet$ | 2.120 | 2.120 |
| $\frac{H_2}{CO}$ $outlet$ | 2.107 | 2.142 |

[a)]With "/" we denote experimental observations that are not evaluated.

Inspection of results presented in **Table 14** suggests that the initial set of parameters in **Table 13** is far from the optimal one, seeing that this model does not reproduce well any of the typical FT observables. This comes from the catalyst used but also the initial set of kinetic parameters that were determined on a partially deactivated catalyst with a different formulation and over a different set of operating conditions. Thus, there is a need to re-optimize rate constants given in **Table 13**. For that purpose, all kinetic rate constants are re-optimized using Levenberg-Marquardt technique described in **Section 3.2.5** and experimental runs 1-24 (T=const.) where typical FT observables such as CO conversion $X(CO)$, paraffin

chain growth coefficient $\alpha_{P_n}$, olefin chain growth coefficient $\alpha_{O_n}$ and methane selectivity $S(CH_4)$ have been used to construct the objective function defined by **Eq.** 65. **Table 15**, **Table 16** and parity plots depicted in **Figure 65** summarize the result of such optimization technique.

**Table 15.** Micro kinetic model parameters obtained after fitting to experimental runs 1-24.

| El. Step number | El. Step Name | Elementary Step reaction [a] | $k_{forward}$ [b] | $k_{backward}$ [a),b] | $E_{a,forward}$ kJ/mol | $E_{a,backward}$ kJ/mol |
|---|---|---|---|---|---|---|
| **1** | Initiation | $H_2 + 2\sigma^* \leftrightarrow 2H - \sigma$ | $1.96*10^{-2}$ | $6.20*10^{-4}$ | 210 | 120 |
| **2** | | $CO + \sigma^* \leftrightarrow CO - \sigma$ | $1.47*10^{-2}$ | $7.99*10^{-2}$ | 205 | 120 |
| **3** | | $CO - \sigma + H - \sigma \leftrightarrow HCO - \sigma + \sigma^*$ | $1.7*10^{-2}$ | $1.36*10^{-4}$ | 0 | 0 |
| **4-6** | Methylene species formation | $HCO - \sigma + H - \sigma \leftrightarrow HCOH - \sigma + \sigma^*$<br>$HCOH - \sigma + \sigma^* \leftrightarrow CH - \sigma + OH - \sigma$<br>$CH - \sigma + H - \sigma \leftrightarrow CH_2 - \sigma + \sigma^*$ | 1.18 | 0 | 120 | 0 |
| **7** | Water formation | $OH - \sigma + H - \sigma \leftrightarrow H_2O + 2\sigma^*$ | | | | |
| **8** | Initiator formation | $CH_2 - \sigma + H - \sigma \leftrightarrow CH_3 - \sigma + \sigma^*$ | $4.31*10^{-1}$ | 0 | 0 | 0 |
| **9** | Propagation | $R_n - \sigma + CH_2 - \sigma \leftrightarrow R_{n+1} - \sigma + \sigma^*$ | $3.59*10^{2}$ | 0 | 0 | 0 |
| **10** | Termination to paraffin for $n = 1$ | $CH_3 - \sigma + H - \sigma \leftrightarrow CH_4 + 2\sigma^*$ | 2.39 | 0 | 0 | 0 |
| **11** | Termination to paraffin $\forall n \in \{2,50\}$ | $R_n - \sigma + H - \sigma \leftrightarrow P_n + 2\sigma^*$ | $1.32*10^{-1}$ | 0 | 0 | 0 |
| **12** | Termination to olefin for $n = 2$ | $C_2H_5 - \sigma \leftrightarrow C_2H_4 + H - \sigma$ | $3.32*10^{-2}$ | $8.46*10^{-5}$ | 0 | 120 |
| **13** | Termination to olefin $\forall n \in \{3,50\}$ | $R_n - \sigma \leftrightarrow O_n + H - \sigma$ | $2.63*10^{-2}$ | $3.18*10^{-6}$ | 0 | 0 |

a) If no $k_{backward}$ is given, the reaction is assumed irreversible.
b) Kinetic rate constants at $T_{ref}$.

**Table 16**. Comparison of FT observables obtained in experimental and simulated runs 1-24

| Run | $X(CO)$ % | | | $S(CH_4)$ %$wt$ | | | $\alpha_{P_n}$ | | | $\alpha_{O_n}$ | | |
|---|---|---|---|---|---|---|---|---|---|---|---|---|
| | Sim. | Exp. | Err. [a] | Sim. | Exp. | Err. [a] | Sim. | Exp. | Err. [a] | Sim. | Exp. | Err. [a] |
| 1 | 48.5 | 45.4 | 6.3 | 11.4 | 10.9 | 4.4 | 0.93 | 0.89 | 4.44 | 0.65 | 0.79 | 21.56 |
| 2 | 32.9 | 33.8 | 2.6 | 12.1 | 10.8 | 10.9 | 0.92 | 0.89 | 3.18 | 0.66 | 0.81 | 22.69 |
| 3 | 27.2 | 26.2 | 3.5 | 13.0 | 10.7 | 17.6 | 0.92 | 0.89 | 2.82 | 0.68 | 0.83 | 22.18 |
| 4 | 20.4 | 20.7 | 1.5 | 13.7 | 10.6 | 22.1 | 0.90 | 0.89 | 1.43 | 0.69 | 0.84 | 21.54 |
| **5** | 70.2 | 71.5 | 1.7 | 10.3 | 11.6 | 11.8 | 0.93 | 0.88 | 4.96 | 0.63 | 0.75 | 18.52 |
| 6 | 51.1 | 53.7 | 5.1 | 11.0 | 11.1 | 0.6 | 0.93 | 0.89 | 4.44 | 0.65 | 0.78 | 20.84 |
| 7 | 44.2 | 41.7 | 5.6 | 11.7 | 10.9 | 7.4 | 0.93 | 0.89 | 4.75 | 0.65 | 0.80 | 22.74 |
| 8 | 33.3 | 33.0 | 0.8 | 12.5 | 10.8 | 14.3 | 0.93 | 0.89 | 4.52 | 0.66 | 0.82 | 23.31 |
| 9 | 62.2 | 65.3 | 5.0 | 9.2 | 10.4 | 13.0 | 0.96 | 0.89 | 7.06 | 0.67 | 0.76 | 13.42 |
| 10 | 47.9 | 50.3 | 5.1 | 9.8 | 10.1 | 3.4 | 0.93 | 0.89 | 4.57 | 0.67 | 0.79 | 17.19 |
| 11 | 40.4 | 39.6 | 1.9 | 10.6 | 10.1 | 5.6 | 0.93 | 0.89 | 4.15 | 0.67 | 0.80 | 20.37 |
| 12 | 30.7 | 31.6 | 2.7 | 11.7 | 10.0 | 14.4 | 0.93 | 0.89 | 4.17 | 0.68 | 0.82 | 20.97 |
| 13 | 70.8 | 77.0 | 8.7 | 12.0 | 13.4 | 11.5 | 0.92 | 0.87 | 4.46 | 0.60 | 0.73 | 22.27 |
| 14 | 50.2 | 57.6 | 14.8 | 12.6 | 12.3 | 2.3 | 0.92 | 0.88 | 3.99 | 0.62 | 0.77 | 24.44 |
| 15 | 42.4 | 44.6 | 5.1 | 13.4 | 11.9 | 11.2 | 0.93 | 0.88 | 5.28 | 0.63 | 0.79 | 26.63 |
| 16 | 32.0 | 35.1 | 9.8 | 14.3 | 11.7 | 18.0 | 0.93 | 0.88 | 4.69 | 0.64 | 0.81 | 26.38 |
| 17 | 60.7 | 57.6 | 5.0 | 11.6 | 16.1 | 38.1 | 1.02 | 0.86 | 15.23 | 0.63 | 0.77 | 21.61 |
| 18 | 47.6 | 43.9 | 7.8 | 12.0 | 15.7 | 31.2 | 1.02 | 0.86 | 15.68 | 0.65 | 0.79 | 22.56 |
| 19 | 40.7 | 34.5 | 15.3 | 12.3 | 15.5 | 26.6 | 1.03 | 0.86 | 15.86 | 0.65 | 0.81 | 23.88 |
| 20 | 31.9 | 27.5 | 13.8 | 12.8 | 15.4 | 20.7 | 1.04 | 0.87 | 16.41 | 0.67 | 0.82 | 21.77 |
| 21 | 55.8 | 60.0 | 7.5 | 10.7 | 9.2 | 14.1 | 0.84 | 0.90 | 6.38 | 0.64 | 0.77 | 19.42 |
| 22 | 49.5 | 43.4 | 12.4 | 11.3 | 9.0 | 20.9 | 0.86 | 0.90 | 4.76 | 0.65 | 0.80 | 23.26 |
| 23 | 37.2 | 32.6 | 12.4 | 12.3 | 8.9 | 28.0 | 0.85 | 0.90 | 6.43 | 0.64 | 0.81 | 26.28 |
| 24 | 32.1 | 29.0 | 9.7 | 12.9 | 8.8 | 31.3 | 0.84 | 0.90 | 7.66 | 0.63 | 0.82 | 29.90 |

[a] Error is given by $\left(\left|\frac{(sim-exp)}{exp} * 100\right|\right)$.

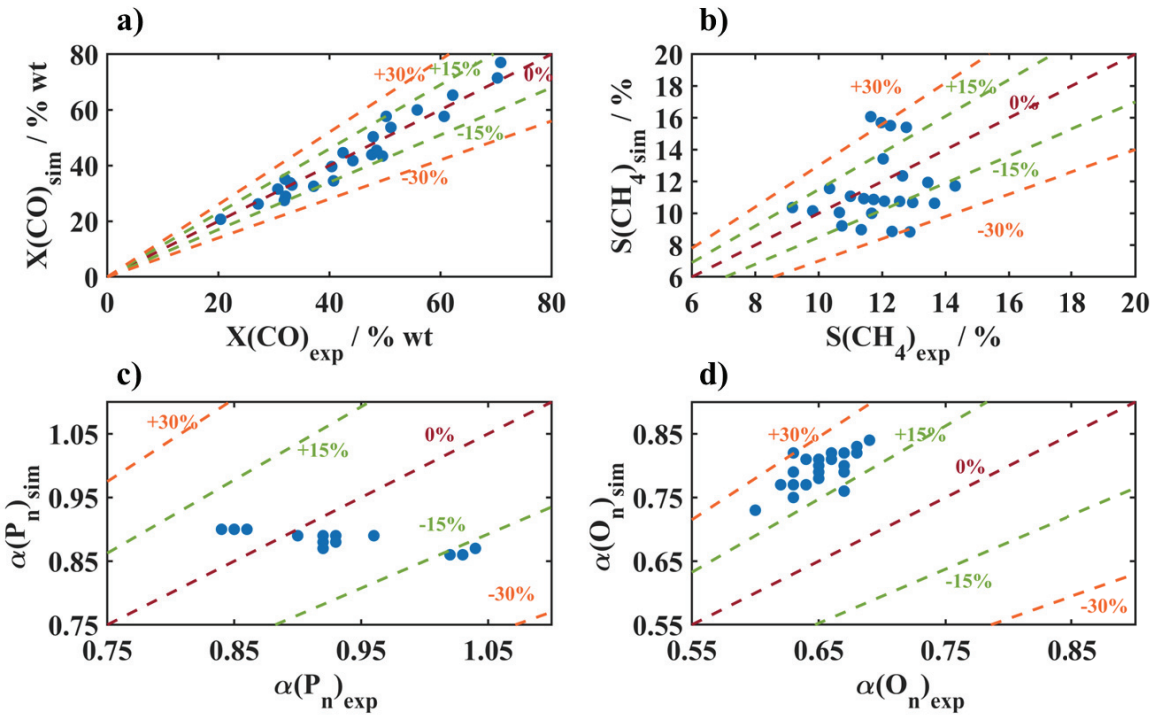


**Figure 65**. Parity plots of FT observables obtained after fitting. Red Line y=x, Green and orange line 15 and 30% error interval, respectively. a) CO conversion b) Methane Selectivity c) chain growth probability of olefins d) chain growth probability of olefins.

Regarding results presented in **Table 16** and **Figure 65**, we see that our optimized micro-kinetic model predicts most of the experimental results (runs 1-24) with a satisfactory agreement. Results presented in **Figure 65** suggest an average relative error of 13% on CO conversion, which is higher than the error reported in some other FT micro-kinetic models reported in the literature[154,75,315,316,84]. Results in **Table 16** infer that the individual relative error increases in the following order $\alpha(P_n)<X(CO)<S(CH_4)<\alpha(O_n)$ with individual values of around 7, 7, 16 and 22% respectively. Thus, for the most crucial FT observables such as X(CO) we obtain to a certain extent, accurate results, whereas methane, $\alpha(P_n)$ and olefin selectivities are less accurate. We note that in our model, calculated $\alpha(P_n)$ appears to be insensitive with respect to measured ones.

Results presented in **Table 16** and **Figure 65** also infer that our model has severe issues in describing products selectivities such as paraffin and olefins, whereas CO conversion

seems well predicted. As presented in **Figure 66** and **Figure 67**, most of the trends are qualitatively well-reproduced; however, quantitative comparison demonstrates some deviations. This is particularly the case for selectivities of FTS products and chain-growth probabilities. This discrepancy may be related to the precision of calculated selectivities in experiments used or our ability to escape local minima during the minimization process.

Comparison of results presented in **Figure 66** shows that the syngas composition has a strong influence on FTS observables since its increase reduces chain growth probabilities of products (**Figure 66** c) and d)) and increases CO conversion level and methane selectivity (**Figure 66** a) and b)) in accordance with the experimental work used in this thesis[148] as well as some other literature work[317–319]. For instance, Todić et al.[319] analyzed the effect of $H_2$/CO ratio on the product distribution and confirmed that lowering of $H_2$/CO ratios reduces methane selectivity and increases $C_{5+}$ selectivities. Although our model underestimates the chain-growth probability of paraffins and overestimates one of olefins, qualitative trends reported in **Figure 66** a) remain correct. The discrepancy between model predictions and experimental work can be understood from the procedure for determinating chain-growth probabilities, i.e. the procedure in which chain-growth probability is estimated based on $C_5$/$C_4$ selectivities and not high-weight hydrocarbons $C_{15+}$. As for conversion, our model shows good agreement with experimental data[74,148,320] as it increases with $H_2$/CO ratios. The non-monotonic trend of conversion with the syngas composition is currently discussed.

In **Figure 67**, we present the impact of CO conversion on some FT observables. Compared to experimental data used in this work [148] we obtain good qualitative agreement for chain growth probability of olefins whereas chain growth probability of paraffin and methane selectivity are not well reproduced. A possible disagreement for chain-growth probabilities and methane selectivity can be found in the nature of experiments performed. Experimental study used for a fitting in our work has been performed on the fresh catalyst and therefore

observables have been measured based on intrisic kinetics corresponding to the catalyst that is not stabilized. It is well-known fact that selectivity of parrafins corresponding to the catalyst initial kinetics is very different from that corresponding to stabilized one as it can be seen from the time-profile of selectivity reported in the literature [280,190,3]. Besides, our optimized micro-kinetic model shows a slight increase (+2 weight %) whereas experiments present a substantial decrease (-4 weight %) in methane selectivity from low to moderately high conversion levels CO conversion (up to 70% see **Figure 67** a)). We highlight the fact that literature data seems to be equally divided on this subject as both phenomena have been observed on Co-based catalysts. For instance, in [321,319] a slight decrease has been observed whereas in [322] a decrease and rapid increase above around 65% conversion has been observed. Marion et al. [323] observed almost constant methane selectivity up to 65% conversion level and a rapid increase above it in line with Yang et al. [3] and Ma et al. [175]. Todić et al.[319] and Kwack et al. [320] found that increase in CO conversion levels leads to decrease and increase in light and heavy hydrocarbon fractions respectively, which is in agreement with experimental data used in this work but not with the optimized micro-kinetic model (**Figure 67** b)). Those observations are in complete disagreement with Marion et al. [323] who performed catalytic tests on the stabilized catalyst and who observed an increase in methane selectivity and a significant decrease of hydrocarbon selectivity with CO conversion increase in agreement with our model. Hence, we conclude that experimental observations used for our model fitting are the consequence of the measurement performed on non-stabilized catalysts during the initial phase of its intrinsic kinetics. Considering that our interest lies in studying performances of industrial Co-based catalysts we rely on experimental observations reported by Marion et al. [323] which are in complete agreement with our micro-kinetic model. Results presented in **Figure 67** c) shows a decrease in olefin selectivity with CO conversion levels

which is reported in many experimental works[148,319,318,3] and related to increased activity of secondary reactions of olefin as described in **Section 2.3.8**.

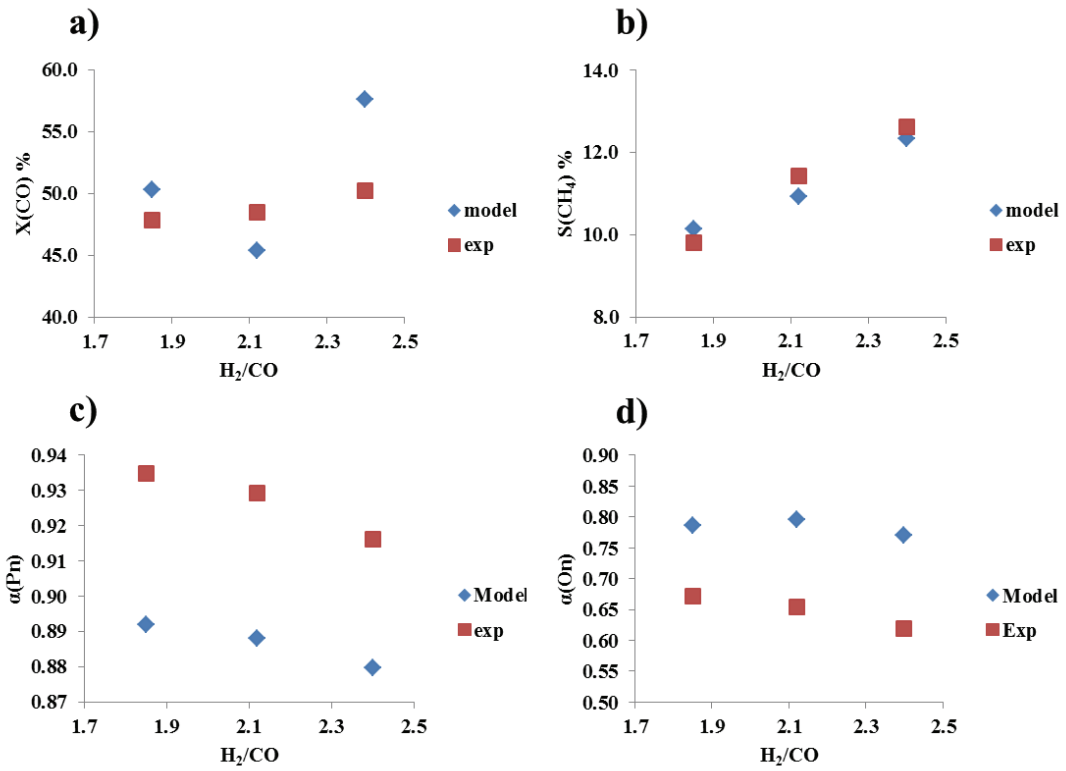


**Figure 66**. The influence of syngas composition on some FT process observables a) CO conversion, b) methane selectivity, c) chain-growth of paraffin and d) chain-growth coefficient of olefins at isothermal and isobaric conditions (experimental runs 1, 10 and 14[148]).

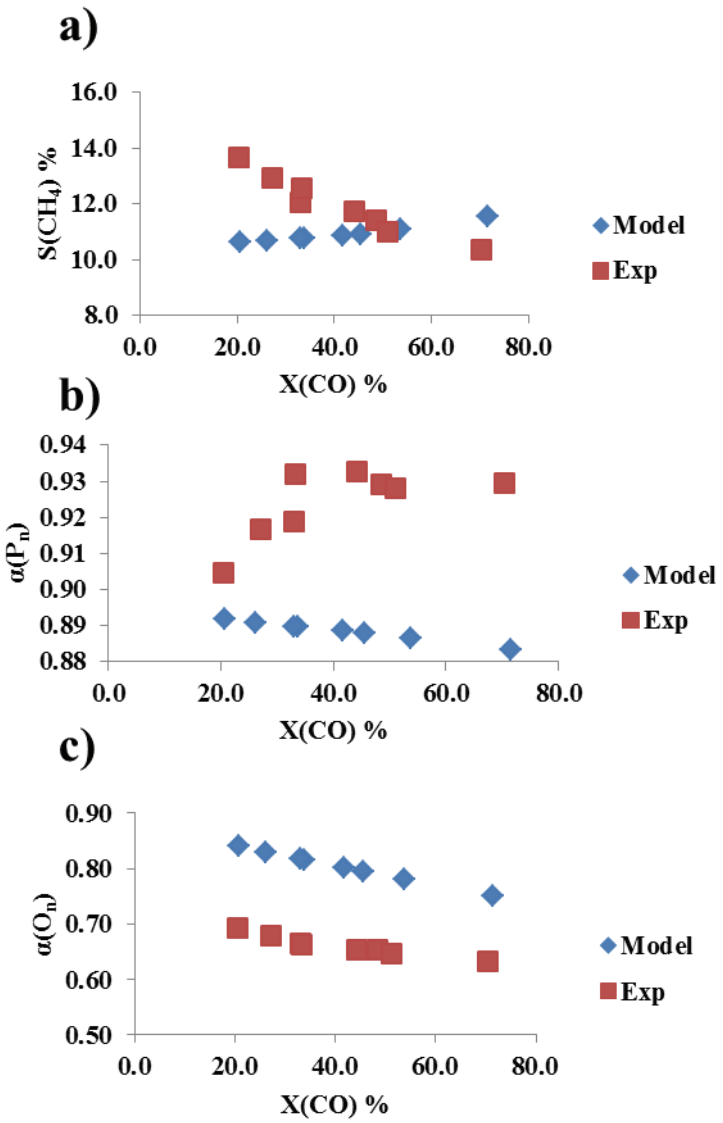


**Figure 67**. The influence of CO conversion on some FT process observables a) methane selectivity, b) chain-growth of paraffin and c) chain-growth coefficient of olefins at isothermal, isobaric and iso-$H_2$/CO conditions (experimental runs 1-8[148]).

To address some of the issues reported above we are also interested in investigating the extent to which the optimized model can describe the effect of the single process conditions on CO conversion and compare it with some literature data such as in [73,74,3].

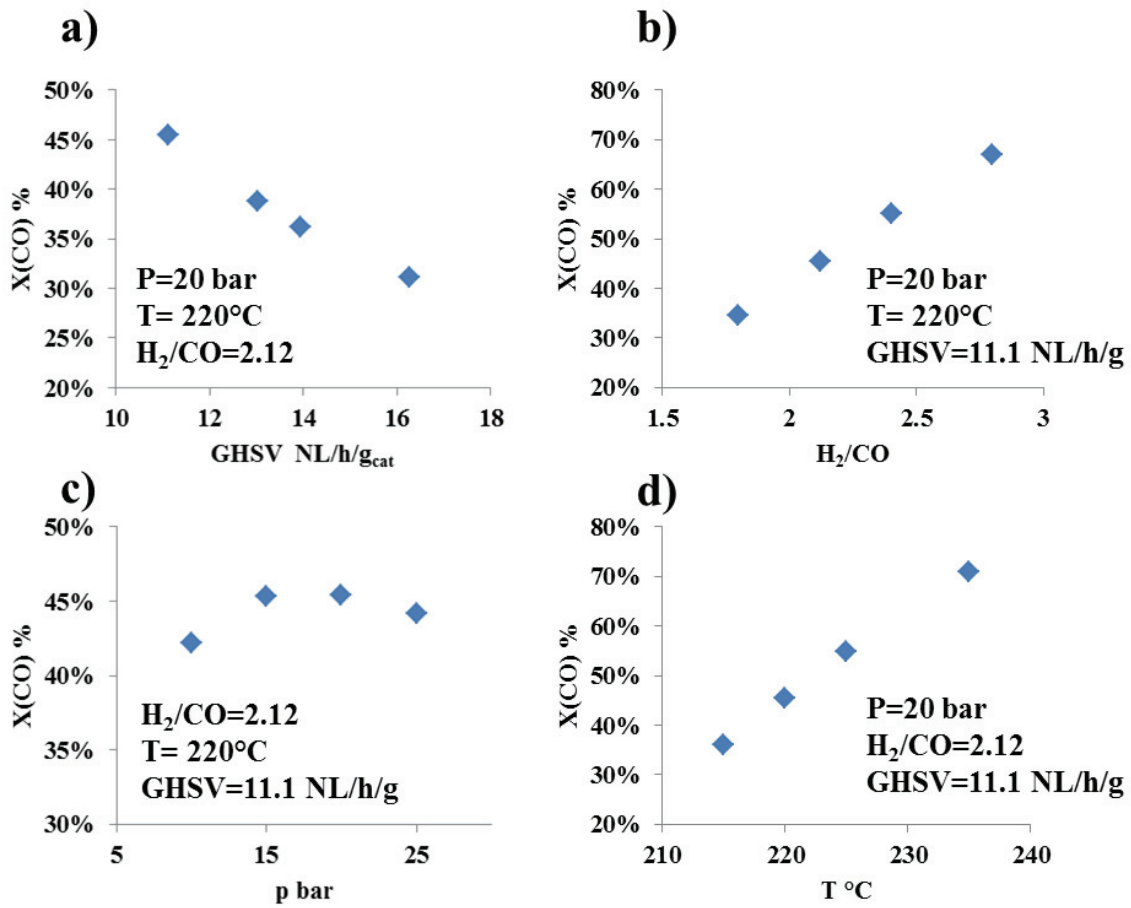


**Figure 68**. Optimized micro-kinetic model predictions of some single parameter on CO conversion levels. a) GHSV b) $H_2$/CO ratio c) Pressure d) Temperature.

Results presented in **Figure 68** shows an excellent qualitative agreement with the experimental work of Visconti et al. [73] considering a simulated increase in catalyst activity with temperature, $H_2$/CO ratio increase and GHSV decrease. According to our model, a low impact of pressure on the activity (<5%) can be reported similarly to Visconti et al. [73] and Kwack et al. [320]. It should be noted, however, that the quality of our optimized micro-kinetic model is governed by the quality of experimental points used for fitting but also our ability to obtain global minima. Experimental data acquisition has not been the object of the present thesis. Hence, considering the fact that experimental data used in this work are obtained for a very short time on stream (TOS), but also the lack of possibility to perform a full FT products analysis, as well as a material balance, we infer that this experimental data and results of the

micro-kinetic model obtained from it should be interpreted with caution. Nevertheless, those set of experimental findings allowed to optimize the catalyst activity as a function of operating conditions as we have seen above.As for other FTS observables, we rely on experimental studies in the literature performed on stabilized catalysts that compare well with our optimized model predictions.

#### *6.3.1.1 Impact of operating conditions on product selectivities*

In this section, we discuss briefly calculated influence of some process parameters on product selectivities such as temperature, pressure, GHSV and syngas composition and we compare those predictions with some literature findings. In summary, the micro-kinetic model we optimized predicts an increase in $C_{5+}$ product selectivity when decreasing $H_2$/CO ratio, increasing GHSV, T and P. Methane selectivity, in contrast, presents inversed trends. Simultaneously, the high-weight olefinic part of FT hydrocarbon mixture generally decreases with $H_2$/CO increase, GHSV increase and pressure decrease. The low-weight olefinic products selectivity increases when $H_2$/CO and T decrease and pressure increases.

**Figure 69** presents the calculated impact of syngas ratio on some FT product selectivities. Our optimized model predictions agree very well with [73] for both low- and high-weight paraffin selectivity with an inversion point around $C_{14}$. Interestingly, a similar inversion point has been simulated and experimentally measured in the work of [84]. As for low-weight olefin product mixture, our results are not in agreement with neither Visconti et al. [73] nor Kwack et al. [84]. Moreover, our olefin distribution does not follow the typical ASF distribution law as ethene selectivity is rather high compared to other olefin molecules. This further supports our doubt that selectivities and consequently chain-growth probabilities of products should have been optimized separately instead of in an averaged manner through $\alpha(O_n)$ as we have done, considering that low- and high-chain FT products behave differently.

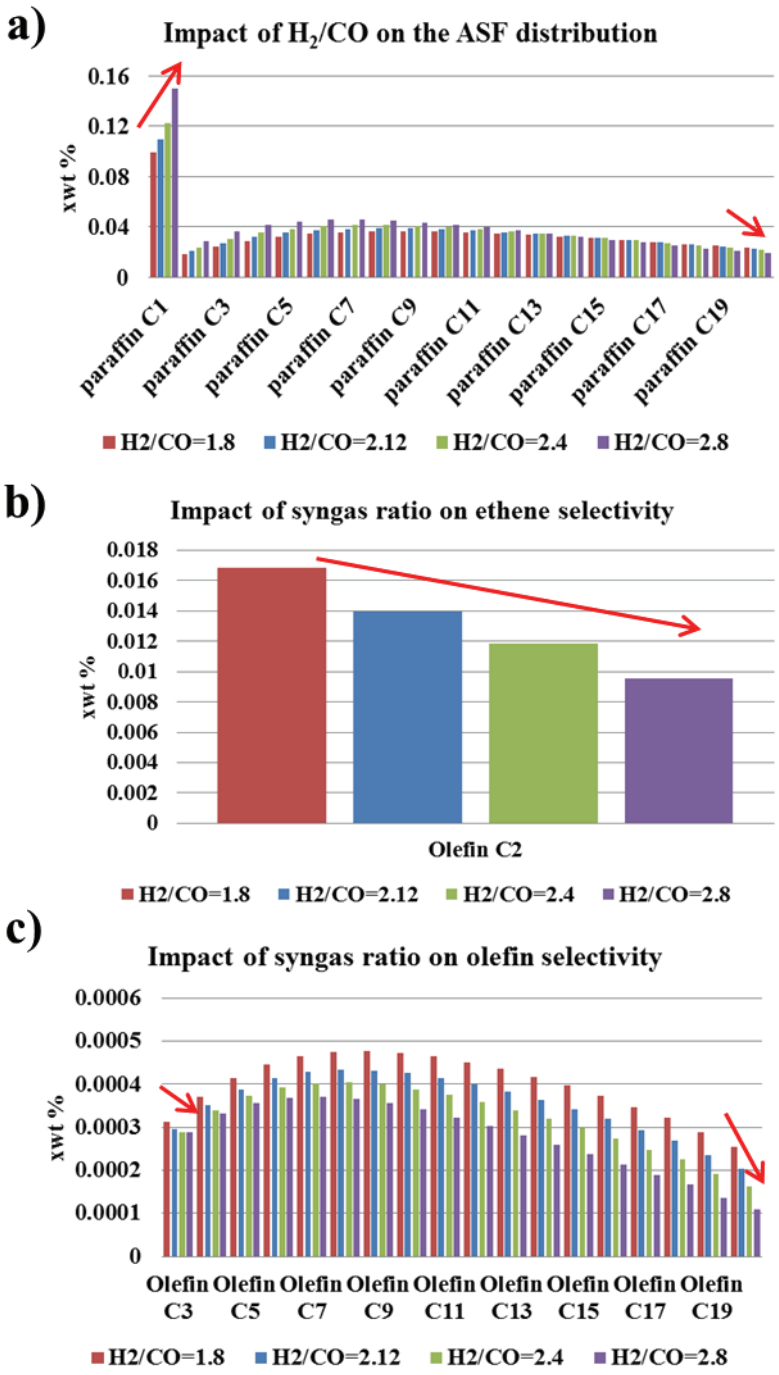


**Figure 69**. Calculated influence of inlet $H_2/CO$ ratio on a) paraffin $P_n$ b) ethylene $O_2$ and c) olefin $O_n$ selectivities for T=220°C, P=20 bar and GHSV=11.14 NL/g/h.

**Figure 70** presents the calculated impact of GHSV on the selectivities of the essential FT products. Results presented in **Figure 70** infer that low-weight paraffin selectivities (methane included) is little impacted with GHSV. More particularly, lower GHSV seems to favor the formation of low-chained paraffin, whereas the opposite trend is calculated for high-chain paraffin in agreement with experimental and theoretical work of Visconti et al. [73]. This

calculated behavior is not in agreement with the experimental and theoretical work of Kwack et al. [84], where a decrease of low-chain paraffin is observed with GHSV increase. However, in this work[84], the effect of GHSV has been determined for the catalytic test in which the inlet ratio $H_2/CO=2$ has been used i.e. below the stoichometric ratio of 2.12. Hence, in those tests, an increase in GHSV (decrease in CO conversion) leads to a decrease of the outlet ratio $H_2/CO$ which consequently reduces the selectivity of paraffins as reported by Kwack et al. [84]. In our test, the inlet syngas ratio is set to the stoichometric value and therefore the impact of GHSV is negligable. Also, Kwack et al. [84] measured methane increase with GHSV increase which can be also attributed to the inlet syngas ratio below the stoichometric value.

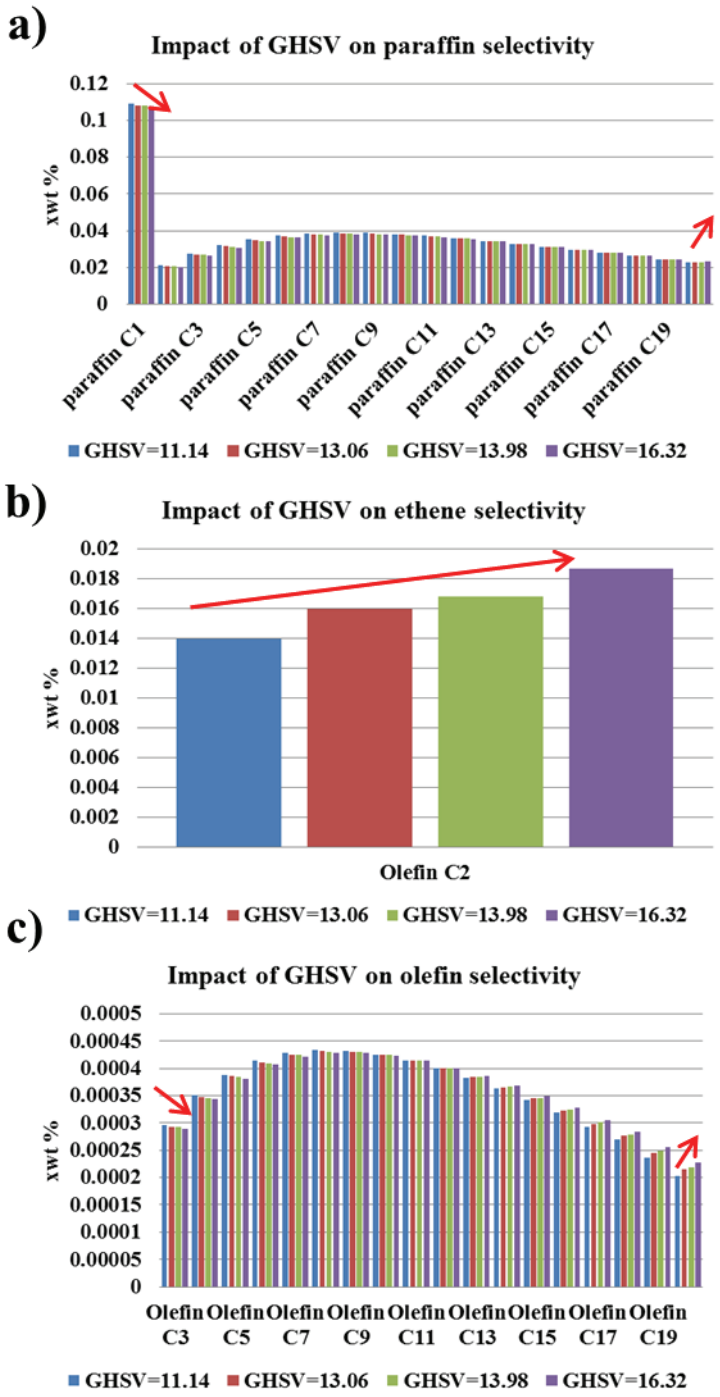


**Figure 70**. Calculated influence of the GHSV in NL/h/g on a) paraffin $P_n$ b) ethylene $O_2$ and c) olefin $O_n$ selectivities for T=220°C, P=20 bar and $H_2/CO$=2.12.

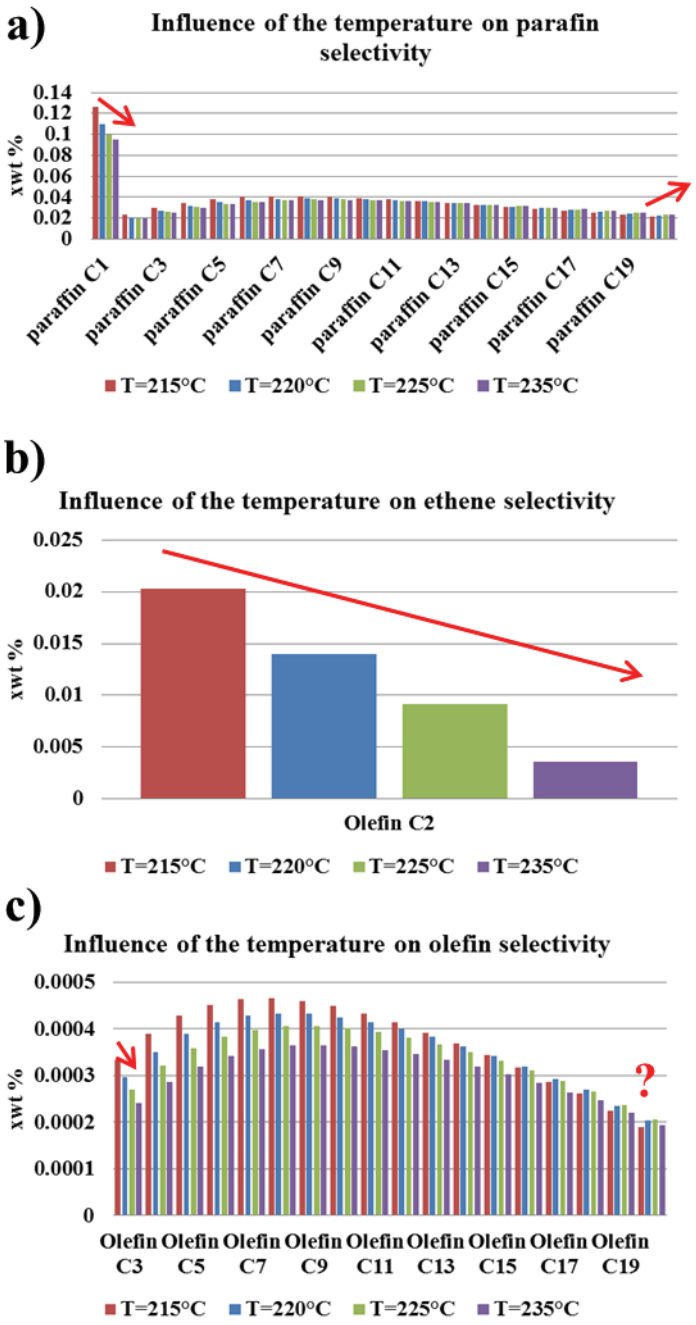


**Figure 71**. Calculated influence of the temperature in °C on a) paraffin $P_n$ b) ethylene $O_2$ and c) olefin $O_n$ selectivities for T=220°C, P=20 bar and $H_2/CO$=2.12.

**Figure 71** reveals the calculated impact of temperature on some typical FT product selectivities based on our optimized micro-kinetic model. Our model does not seem to produce well the temperature impact on methane and other low-weight as well as high-weight paraffin selectivities if compared to the literature work [84,73]. The reason for this discrepancy can be found once again in the $H_2/CO$ feed molar ratio employed in that work that is below

the stoichiometric value[84,73]. As for [73,154] in which the feed molar ratio is 2.1, the temperature increase, increases the paraffin selectivity which is in agreement with our model predictions. In that work[73], $C_2$ olefin selectivity decreases with the temperature increase as predicted with our model.

**Figure 71** presents the calculated impact of pressure on the selectivities of the essential FT products. The optimized micro-kinetic model shows a decrease in selectivities of low-chain paraffinic products, whereas an increase is observed for high-weight products. Pressure effect on paraffin selectivities is entirely in line with experimental works of Kwack et al. [84] and Visconti et al. [73]. As for olefins, Visconti et al. [73] measured an increase and decrease of ethene, and both low- and high-weight olefins, respectively, with pressure. Thus, our results are not in line when compared to the calculated pressure dependency of ethene selectivity. In contrast, our results for all olefins are in full agreement with experimental and theoretical work reported by Kwack et al. [84] since low-weight olefin decrease and high-weight olefin increase is observed with pressure increase.

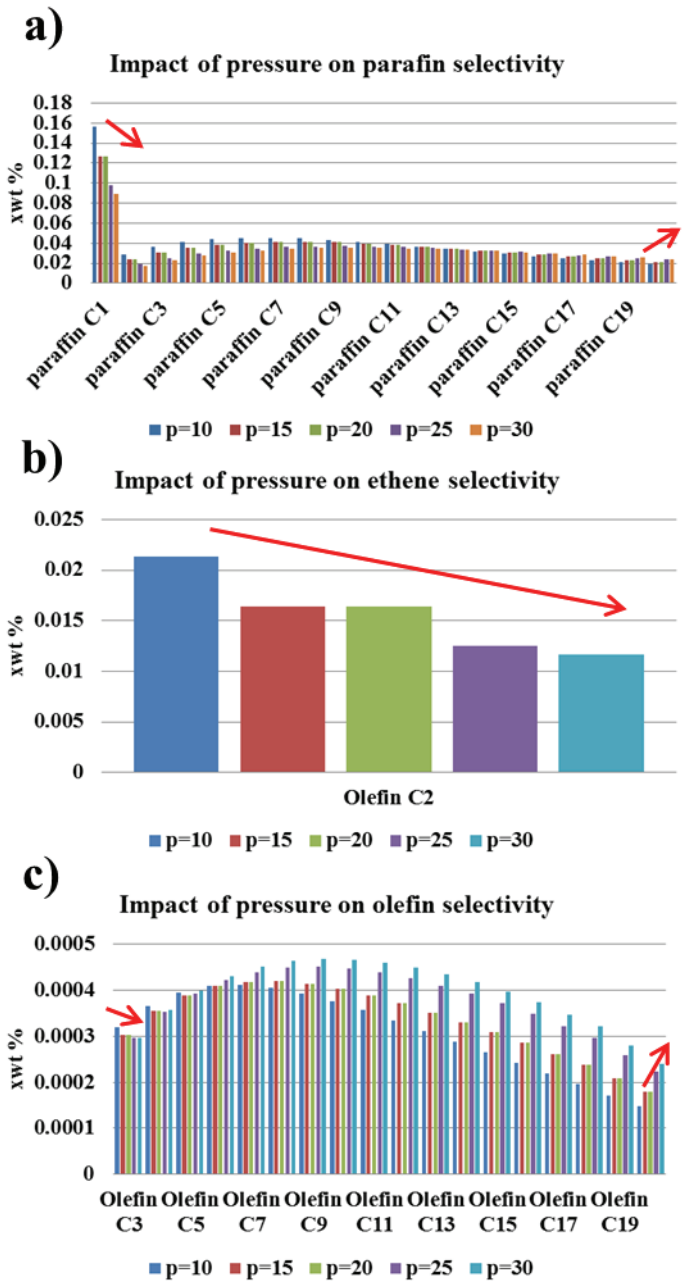


**Figure 72**. Calculated influence of the pressure in bars on a) paraffin $P_n$ b) ethylene $O_2$ and c) olefin $O_n$ selectivities for T=220°C, P=20 bar and $H_2$/CO=2.12.

### 6.3.1.2 *Catalyst surface state*

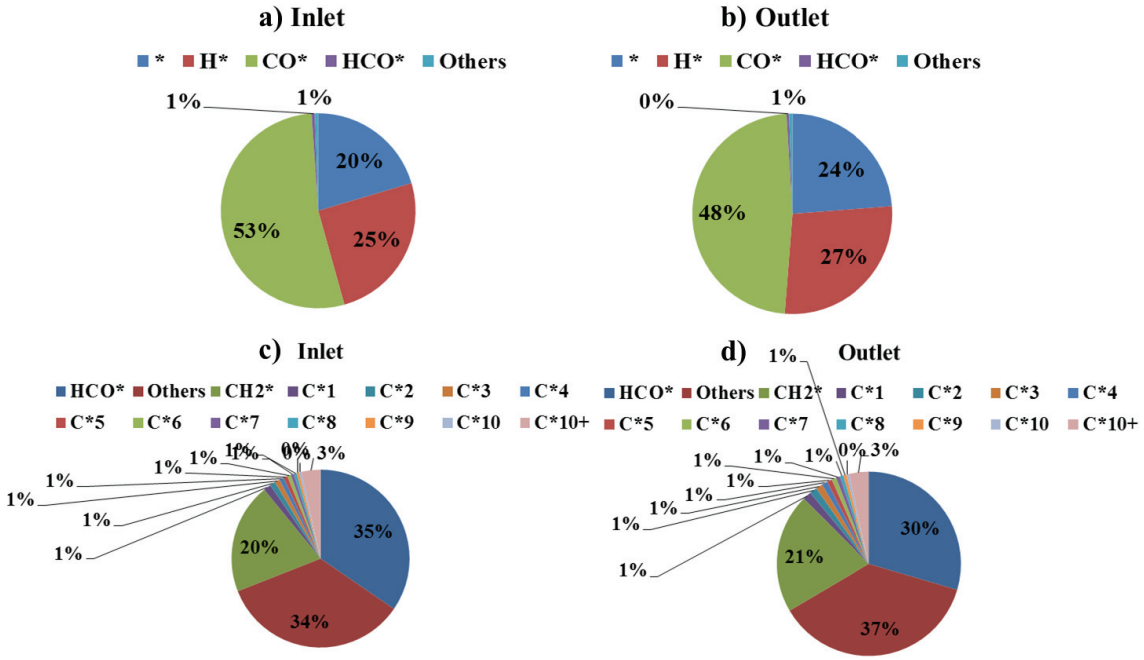


**Figure 73**. The relative abundance of surface species used in the micro-kinetic modeling scheme for experimental run 1. Surface coverages of the most abundant surface species in the reactor inlet (a) and outlet (b). Surface coverages of minor surface species ("Others" in a) and b)) in the reactor inlet (c) and outlet (d).

**Figure 73** shows the distribution of adsorbed species on the catalyst at both reactor inlet and outlet for experimental run 5 for which T=220, p=20 bar, GHSV=11.14 NL/h/g and H2/CO=2.12. Our results for the catalyst surface composition are comparable with some results found by Boyer et al. in the slurry bubble reactor [36] but also Visconti et al. [73] and Storsæter et al. [91] in the fixed-bed configuration. More precisely, micro-kinetic modeling shows that the most abundant surface species are chemisorbed CO* and H* species with the surface concentrations reaching levels of around 53 and 25%, respectively. This is in line with surface coverages measured using the SSITKA by den Breejen [297] for CO* , $CH_\beta$* and H* that are around 45 , 10 and 10%, respectively. Besides, Yang et al. [92] reported surface concentrations of CO*, H*, $CH_\beta$* and * using SSITKA in the following intervals, respectively, 50-55%, 10-30% and around 10%. depending on the operating conditions. Our calculations infer that the surface concentration of free surface sites is around 20% for those

experimental conditions in line with the micro-kinetic model of Storsæter et al. [91]. Visconti et al. [73] found significantly lower values for surface concentrations of both H* and free sites *. Low concentrations of surface radicals Rn* can be explained in relatively high desorption probability of chain-growth intermediates yielding paraffinic and olefinic products. The computational study of van Helden et al. [296] also shows around 60% in CO surface concentrations in agreement with our work.

### 6.3.2 Single-site micro-kinetic model of deactivation

Having evaluated the performances of the deactivation-free micro-kinetic model, we proceed to the integration of the elementary steps presented in **Chapter 5** in order to obtain deactivation containing micro-kinetic model. In this section, we are going to present briefly the example of the single-site deactivation-containing micro-kinetic model scheme we developed based on our DFT findings. Our goal is to produce a micro-kinetic model scheme able to predict the activity and selectivity losses in time (CO conversion and chain-growth probability of paraffin) as well as an increase in methane selectivity phenomena that are typically observed for Co-based catalyst for the long time-on-stream.

The complete manually optimized model is presented in **Table 17**. Note that this model contains several reactions that have been modified with respect to the original micro-kinetic model scheme of Visconti et al. [73]. The new set of initiation reaction is composed of molecular adsorption of hydrogen and subsequent dissociation, reaction 1 and 2, respectively. Steps 3-4 remain unchanged with respect to the original scheme. Steps 5-6 are some new steps we introduced to account for surface oxidation phenomenon and formation of CH* surface species (step 5) and another possible route for $CH_2$* formation (step 6). Reaction (5) has been already studied in the literature using DFT[86,96]. This data represents the starting point in the estimation of energy barriers presented in **Table 17**. Note that the surface oxidation step is in complete agreement with our previous work presented in **Chapter** 4 where we have

proved that CO derived oxygen represents thermodynamically the most favorable oxidizing agent for Co surface. Steps 7-9 remain intact compared to the original micro-kinetic scheme. Note, however, that in steps 7-9 and in step 6 we introduced represent two possible routes for the formation of FT monomer specie $CH_2$*. Steps 10 and 12-17 are the same as in the model of Visconti et al. [73]. However, we introduced the reversibility of this reaction step compared to the model of Visconti et al. [73] in order to account for methane increase with simultaneous site-blocking effect i.e. shifting equilibrium towards methane formation with surface sites concentration decrease. We do not have any experimental nor theoretical argument for introducing the reversibility of methane formation reaction. However, to our experience, the microkinetic model scheme presented in **Table 17** would not produce the envisaged time evolution of methane selectivity without this step. Further inspection is required to confirm this hypothesis. Step 11 is introduced to evacuate the excess of surface oxygen in the form of $CO_2$. Based on the literature data, although Co-based catalysts are rather non-selective towards $CO_2$, it appears that the selectivity of $CO_2$ is a good descriptor of surface oxidation phenomenon considering its increase with CO conversion attributed to high water partial pressures[130,321,323,317,319]. Reactions (18)-(22) represent the set of reactions we studied in **Chapter 5** in which we have shown that ethylene readsorption and decomposition is thermodynamically and kinetically favorable reaction in which coke-initiator specie is formed (18)-(19). Deactivation initiator may engage tripolymerization reaction in which coke seed is formed (20)-(21) and which can grow with the subsequent attachment of $C_1$ monomer species as shown in the set of reactions (22). In this micro-kinetic model, we considered the formation up to tri-aromatic hydrocarbon, i.e. $C_{16}H_{13}$ considered as coke in our micro-kinetic model scheme. As discussed in **Chapters 4** and **5**, this structure blocks active cobalt sites inducing coke built-up and consequently deactivation and selectivity losses phenomena.

Comparison of data in and **Table 15**, **Table 16** and **Table 17** shows that a great readjusting is required to obtain the initial activity observed with the deactivation-free micro-kinetic model scheme. For instance, if we take the experimental run 5 as an example, time-dependent CO conversion, methane selectivity and chain-growth coefficient of paraffin obtained within the model presented in **Table 17** can be investigated. Those results are presented in **Figure 74**.

**Table 17**. Deactivation containing model parameters used in this study.

| El. Step number | El. Step Name | Elementary Step reaction [a)] | $k_{forward}$ | $k_{backward}$ [a)] | $E_{a,forward}$ kJ/mol | $E_{a,backward}$ kJ/mol |
|---|---|---|---|---|---|---|
| **1** | Initiation | $H_2 + \sigma^* \leftrightarrow H_2 - \sigma$ | 5.874E-03 | 1.126E-02 | 0 | 0 |
| **2** | | $H_2 - \sigma + \sigma^* \leftrightarrow 2H - \sigma$ | 5.000E+02 | 0 | 0 | 0 |
| **3** | | $CO + \sigma^* \leftrightarrow CO - \sigma$ | 2.351E-02 | 6.390E-02 | 205 | 120 |
| **4** | Oxide formation | $CO - \sigma + H - \sigma \leftrightarrow HCO - \sigma + \sigma^*$ | 1.699E-02 | 1.360E-04 | 0 | 0 |
| **5** | | $HCO - \sigma + \sigma^* \leftrightarrow CH - \sigma + O - \sigma$ | 1.184E-05 | 1.184E-05 | 92 | 82 |
| **6** | Methylene Formation 1 | $CH - \sigma + H - \sigma \leftrightarrow CH_2 - \sigma + \sigma^*$ | 1.184 | 0 | 0 | 0 |
| **7-9** [b)] | Methylene Formation 2 | $HCO - \sigma + H - \sigma \leftrightarrow HCOH - \sigma + \sigma^*$<br>$HCOH - \sigma + \sigma^* \leftrightarrow CH - \sigma + OH - \sigma$<br>$CH - \sigma + H - \sigma \leftrightarrow CH_2 - \sigma + \sigma^*$ | 1.184 | 0 | 0 | 0 |
| **10** | Water formation | $OH - \sigma + H - \sigma \leftrightarrow H_2O + 2\sigma^*$ | | | | |
| **11** | $CO_2$ formation | $CO - \sigma + O - \sigma \leftrightarrow CO_2 + 2\sigma^*$ | 2.390E-02 | 0 | 0 | 0 |
| **12** | Initiator formation | $CH_2 - \sigma + H - \sigma \leftrightarrow CH_3 - \sigma + \sigma^*$ | 4.310E-01 | 0 | 0 | 0 |
| **13** | Propagation | $R_n - \sigma + CH_2 - \sigma \leftrightarrow R_{n+1} - \sigma + \sigma^*$ | 1.796E+02 | 0 | 0 | 0 |
| **14** | Termination to paraffin for $n = 1$ | $CH_3 - \sigma + H - \sigma \leftrightarrow CH_4 + 2\sigma^*$ | 1.195 | 3.399E-04 | 0 | 0 |
| **15** | Termination to paraffin $\forall n \in \{2,50\}$ | $R_n - \sigma + H - \sigma \leftrightarrow P_n + 2\sigma^*$ | 1.320E-01 | 0 | 0 | 0 |
| **16** | Termination to olefin for $n = 2$ | $C_2H_5 - \sigma \leftrightarrow C_2H_4 + H - \sigma$ | 3.324E-02 | 8.455E-05 | 0 | 120 |
| **17** | Termination to olefin $\forall n \in \{3,50\}$ | $R_n - \sigma \leftrightarrow O_n + H - \sigma$ | 2.633E-02 | 3.182E-06 | 0 | 0 |

| | | | | | | |
|---|---|---|---|---|---|---|
| **18** | Ethylene readsorption | $C_2H_4 + 2\sigma^* \leftrightarrow C_2H_4 - 2\sigma$ | 3.324E-04 | 0 | 0 | 0 |
| **19** | Ethylene dehydrogenation | $C_2H_4 - 2\sigma + 3\sigma^* \leftrightarrow C_2H_1 - 2\sigma + 3H - \sigma$ | 1.699E-02 | 0 | 0 | 0 |
| **20** | $C_4$ metallacycle formation | $2C_2H_1 - 2\sigma \leftrightarrow C_4H_2 - 4\sigma$ | 1.699E-04 | 0 | 0 | 0 |
| **21** | Coke-seed cyclic $C_6$ formation | $C_4H_2 - 4\sigma + C_2H_1 - 2\sigma \leftrightarrow C_6H_3 - 6\sigma$ | 1.699E-04 | 0 | 0 | 0 |
| **22** | Coke-growth | $C_nH_{n-3} - n\sigma + CH - \sigma \leftrightarrow C_{n+1}H_{n-2} - (n+1)\sigma$ | 3.399E-04 | 0 | 0 | 0 |

a) If no $k_{backward}$ is given, the reaction is assumed irreversible.
b) Sum of 7-9: $HCO - \sigma + 3H - \sigma \leftrightarrow CH_2 - \sigma + H_2O + 3\sigma^*$

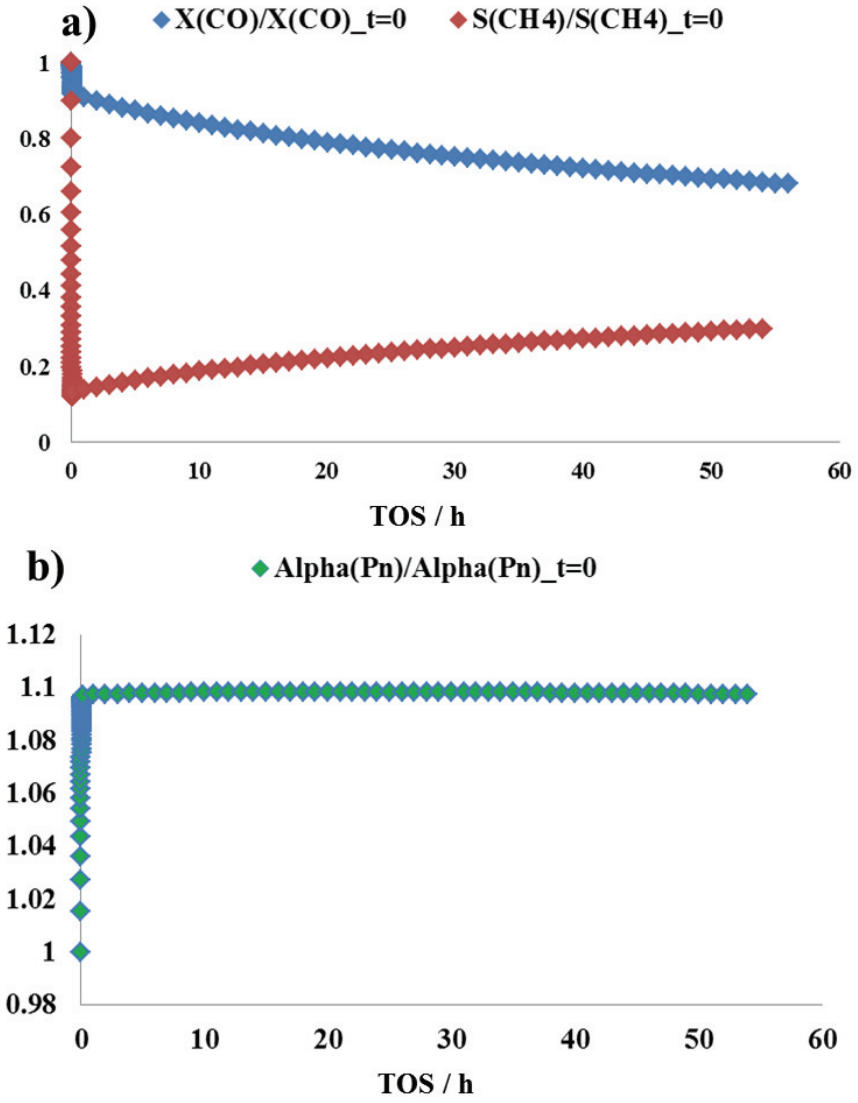


**Figure 74**. Time evolution of a) X(CO), S($CH_4$) and b) α($P_n$) according to single-site deactivation micro-kinetic model after 500h of time-on-stream for experimental run 5. Initial

X(CO), S(CH4) and $\alpha(P_n)$ are 81%, 20 wt % and 0.83, respectively.

Inspection of results presented in **Figure** 74 reveals that the single-site microkinetic model we presented can reproduce a time evolution of X(CO), S(CH4) and α(Pn) related to realistic Co-based catalyst qualitatively for long TOS. However, compared to performances of deactivation-free catalysts studied in **Section 6.3.1** we see that the initial CO conversion, methane selectivity and paraffin chain-growth probabilities are inaccurate. It should be noted that in the manual readjustment of kinetic rate constants from **Table 17**, we did not succeed in obtaining the experimentally measured observables. Moreover, the time-evolution of $\alpha(P_n)$ presented in **Figure** 74 b exhibits first an increase compared to initial chain growth probability and then remains constant. Note also that TOS simulated in this study is around 50h, hence, simulated dynamics of X(CO), $S(CH_4)$ and $\alpha(P_n)$, although in qualitative agreement (for long TOS) are too rapid for realistic Co-based catalyst. For instance, Peña et al. [294] observed a decrease of around 5% in CO conversion after TOS=400h. Moreover, they observed around 3 wt% increase and 5 wt % decrease in $S(CH_4)$ and $S(C_{5+})$, respectively after TOS=700h which is far longer than in this study.

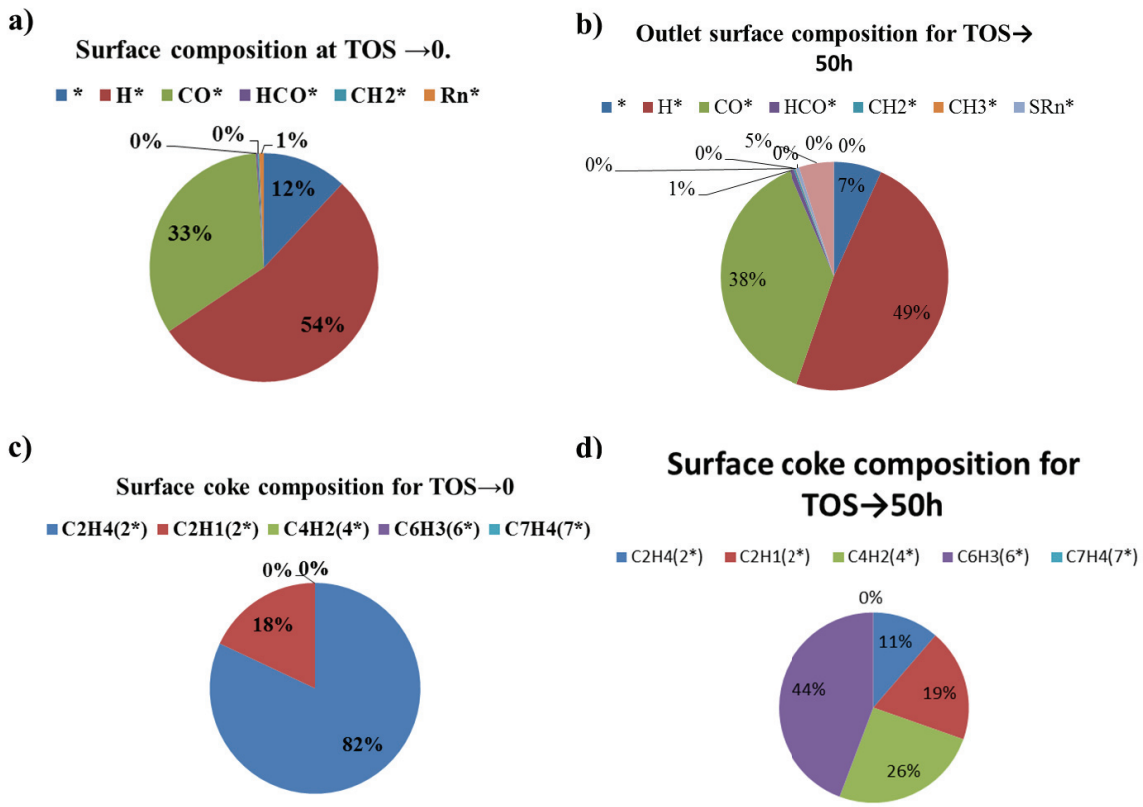


**Figure 75**. Surface composition of fresh a), c) and b), d) deactivated Co catalyst.

Inspection of results presented in **Figure** 75 depicts differences in surface composition of entirely fresh and deactivated catalyst. Although time-evolution of typical FT observables is not accurately determined, our results in **Figure** 75 suggest that we succeeded in our initial idea, i.e., we successfully produced coke species deleterious for catalyst activity and product selectivities by integrating elementary steps for coke formation in the deactivation-free model proposed by Visconti et al.

Since we cannot entirely exclude the existence of some other set of kinetic parameters in **Table 17** that would produce qualitative and quantitative desired evolution of typical FT observables, we cannot neglect the fact that the micro-kinetic model scheme presented in **Table 17** is somewhat artificial, considering that it contains an elementary step for reversible methane formation, i.e. methane decomposition on Co that, to the best of our knowledge is not observed for Co-based catalysts. Besides, without this reversible step, we can not simulate

an increase in methane selectivity and decrease in long-chain paraffin selectivity simultaneously. Nevertheless, this model proves that it is possible in principle to simulate the time-evolution of FT observables using a micro-kinetic model. Hence, our next objective is substituting non-physical methane decomposition reaction step with a new chemically sound reaction set while producing similar trends on X(CO), S($CH_4$) and α($P_n$).

### 6.3.3 Double-site micro-kinetic model of deactivation

Methane selectivity exhibits deviation from typical ASF distribution of the product as we discussed in **Section 2.2**. Besides, there are a few studies [324–326], and very recently Chen et al. [281] where two-site (double-site) models are discussed to explain a deviation of methane (and ethane) from the ASF products distribution. As discussed by Chen et al. [281] a current DFT view is that a hydrogenation reaction of growing chain ($CH_\beta$ included) is site-insensitive whereas CO dissociation and chain-growth reactions are site-sensitive[106]. Chen et al. [281] speculated that a large part of methane is produced on terrace sites whereas CO dissociation is taking place on step-edge sites leading to hydrocarbons and a small amount of methane. In addition, SSITKA experiments suggest two different carbon pools for methane formation as discussed in the literature [327,325,92]. This site-sensitivity phenomenon of surface reactions briefly described in **Section 2.3** allows some flexibility concerning the issue we encountered with methane.

Due to the time limitations, a thorough investigation of site-sensitivity phenomena is out of the scope of this work. Hence, in the mechanism below, we assume the presence of surface-sensitivity phenomena and we speculate that there exist particular sites for methane formation reaction in addition to the one reported in **Table 17**. We will call those sites methanation sites or μ-sites. More particularly, considering that opposite trends are expected on methane and paraffin selectivities during the deactivation phenomena, it seems

numerically convenient and physically reasonable to separate elementary steps 13 (propagation) and 14 (methane formation) by introducing a second active site μ in the micro-kinetic model scheme.

Based on experimental results by Chen et al.[281], there is a strong correlation between cobalt surface area and $CH_4$ formation rate. In their opinion, the one-site model and H-assisted mechanism cannot explain experimentally obtained pattern of $S(CH_4)$, $C_{2+}$ formation rates and chain-growth probability on carbon deposits. Nevertheless, they do not exclude two parallel reaction pathways for methane formation, one taking on place on terraces and another on steps. In this study, we consider an exclusive methane formation on μ-sites, i.e. we assume that the latter pathway produces negligible amounts of methane. Chen et al.[281] also provide the mechanism scheme taking into consideration surface diffusion of adsorbates between step-edge and terrace sites with a final goal to explain their experimental observations in which $S(CH_4)$ decreases with deactivation in contrast to some other experimental work[196,285]. In this deactivation model, we propose a similar adsorbate migration mechanism towards methane formation. Considering low diffusion barriers for some adsorbates such as hydrogen[79], carbon[209] and CO[93] and some $CH_\beta$ species [106] we introduced reactions 3 (H* diffusion) and 14 ($CH_3$* diffusion) given in **Table 18**. Methanation reaction (16) is assumed dominant on methanation site μ in a similar manner as in [281]. Other elementary steps remain intact compared to the micro-kinetic model of deactivation we developed in 6.3.2. Elementary step 14 is the crucial one for calculating the time-evolution of methane since in this step, decrease in the concentration of σ* sites, i.e. active sites we wish to block in reactions 20-24, leads to an increase in $CH_3\mu$ surface concentrations leading to methane formation. Thus, a decrease in active sites σ* indirectly increases methane selectivity in line with the literature data on deactivation phenomenon. Hence, previous non-physical elementary step is substituted with physically acceptable surface migration given by reaction 14 and the introduction of a new

type of active sites. In this work, the initial concentration of surface methanation sites μ is set to 10% of the overall initial concentration of surface active sites σ* and μ .This in line with experimental and theoretical data in the literature where it is demonstrated that two active sites may co-exist during the FTS reaction. Moreover, it is well known from morphological considerations that the ratio between the terrace and step sites of for a large Co nanoparticle [101] is of the same order of magnitude as the ratio between σ*/ μ sites considered in our current model. However, we have not enough data to stablish a direct link between, on the one hand, our σ* and μ sites and, on the other hand, step and terraces sites in nanoparticles.

In order to obtain initial CO conversions and product selectivities, we first adjusted manually kinetic constants of reactions 1-19 given in **Table 18** i.e. without using the the Levenberg-Marquardt (LM) algorithm[260]. Comparison of results in **Table 18** with those in **Table 15** shows that kinetic rate constants for steps 3, 14 and 16 (with steps 20-24 equal to zero) have to be estimated in order to produce a quantitative agreement with a deactivation-free model presented in **Section 6.3.1**. Kinetic rate constants of elementary steps we conserved from a deactivation-free model presented in **Section 6.3.1** are slightly modified to approach the limiting case for TOS=0. After readjustment of the limiting case with no deactivation, we manually modified kinetic rate constants to reproduce well-known deactivation behavior i.e. methane selectivity increase, $\alpha(P_n)$ and X(CO) decrease with the TOS. The result of this manual readjustment is presented in **Figure 76**.

**Table 18**. Deactivation containing model parameters used in this study.

| El. Step number | El. Step Name | Elementary Step reaction [a)] | $k_{forward}$ | $k_{backward}$ [a)] | $E_{a,forward}$ kJ/mol | $E_{a,backward}$ kJ/mol |
|---|---|---|---|---|---|---|
| 1 | Initiation | $H_2 + \sigma^* \leftrightarrow H_2 - \sigma$ | 2.096E-03 | 0 | 0 | 0 |
| 2 | | $H_2 - \sigma + \sigma^* \leftrightarrow 2H - \sigma$ | 4.000E+02 | 0 | 0 | 0 |
| 3 | | $H - \sigma + \mu * \leftrightarrow H - \mu + \sigma *$ | 1.000E-01 | 0 | 0 | 0 |
| 4 | | $CO + \sigma^* \leftrightarrow CO - \sigma$ | 4.075E-02 | 4.115E-01 | 205 | 120 |

| | | | | | | |
|---|---|---|---|---|---|---|
| **5** | | $CO-\sigma+H-\sigma \leftrightarrow HCO-\sigma+\sigma^*$ | 3.116E-02 | 9.903E-01 | 0 | 0 |
| **6** | Oxide formation | $HCO-\sigma+\sigma^* \leftrightarrow CH-\sigma+O-\sigma$ | 4.735E-03 | 0 | 92 | 0 |
| **7** | Methylene Formation 1 | $CH-\sigma+H-\sigma \leftrightarrow CH_2-\sigma+\sigma^*$ | 1.126E-01 | 0 | 0 | 0 |
| **8-10**[b] | Methylene Formation 2 | $HCO-\sigma+H-\sigma \leftrightarrow HCOH-\sigma+\sigma^*$<br>$HCOH-\sigma+\sigma^* \leftrightarrow CH-\sigma+OH-\sigma$<br>$CH-\sigma+H-\sigma \leftrightarrow CH_2-\sigma+\sigma^*$ | 5.353 | 0 | 0 | 0 |
| **11** | Water formation | $OH-\sigma+H-\sigma \leftrightarrow H_2O+2\sigma^*$ | | | | |
| **12** | $CO_2$ formation | $CO-\sigma+O-\sigma \leftrightarrow CO_2+2\sigma^*$ | 3.670E-03 | 0 | 0 | 0 |
| **13** | Initiator formation | $CH_2-\sigma+H-\sigma \leftrightarrow CH_3-\sigma+\sigma^*$ | 7.519E-01 | 0 | 0 | 0 |
| **14** | $CH_3$ Diffusion | $CH_3-\sigma+\mu \leftrightarrow CH_3-\mu+\sigma$ | 2.355E+01 | 0 | 0 | 0 |
| **15** | Propagation | $R_n-\sigma+CH_2-\sigma \leftrightarrow R_{n+1}-\sigma+\sigma^*$ | 4.591E+02 | 0 | 0 | 0 |
| **16** | Termination to paraffin for $n=1$ | $CH_3-\mu+H-\mu \leftrightarrow CH_4+2\mu^*$ | 5.443 | 0 | 0 | 0 |
| **17** | Termination to paraffin $\forall n \in \{2,50\}$ | $R_n-\sigma+H-\sigma \leftrightarrow P_n+2\sigma^*$ | 6.774E-01 | 0 | 0 | 0 |
| **18** | Termination to olefin for $n=2$ | $C_2H_5-\sigma \leftrightarrow C_2H_4+H-\sigma$ | 8.511E-01 | 1.574E-03 | 0 | 120 |
| **19** | Termination to olefin $\forall n \in \{3,50\}$ | $R_n-\sigma \leftrightarrow O_n+H-\sigma$ | 5.174E-03 | 1.056E-07 | 0 | 0 |
| **20** | Ethylene readsorption | $C_2H_4+2\sigma^* \leftrightarrow C_2H_4-2\sigma$ | 8.511E-07 | 0 | 0 | 0 |
| **21** | Ethylene dehydrogenation | $C_2H_4-2\sigma+3\sigma^* \leftrightarrow C_2H_1-2\sigma+3H-\sigma$ | 1.699E-02 | 0 | 0 | 0 |
| **22** | $C_4$ metallacycle formation | $2C_2H_1-2\sigma \leftrightarrow C_4H_2-4\sigma$ | 1.699E-03 | 0 | 0 | 0 |
| **23** | Coke-seed cyclic $C_6$ formation | $C_4H_2-4\sigma+C_2H_1-2\sigma \leftrightarrow C_6H_3-6\sigma$ | 1.699E-03 | 0 | 0 | 0 |
| **24** | Coke-growth | $C_nH_{n-3}-n\sigma+CH-\sigma \leftrightarrow C_{n+1}H_{n-2}-(n+1)\sigma$ | 3.399E-01 | 0 | 0 | 0 |

a) If no $k_{backward}$ is given, the reaction is assumed irreversible.
b) Sum of 8-10: $HCO-\sigma+3H-\sigma \leftrightarrow CH_2-\sigma+H_2O+3\sigma^*$

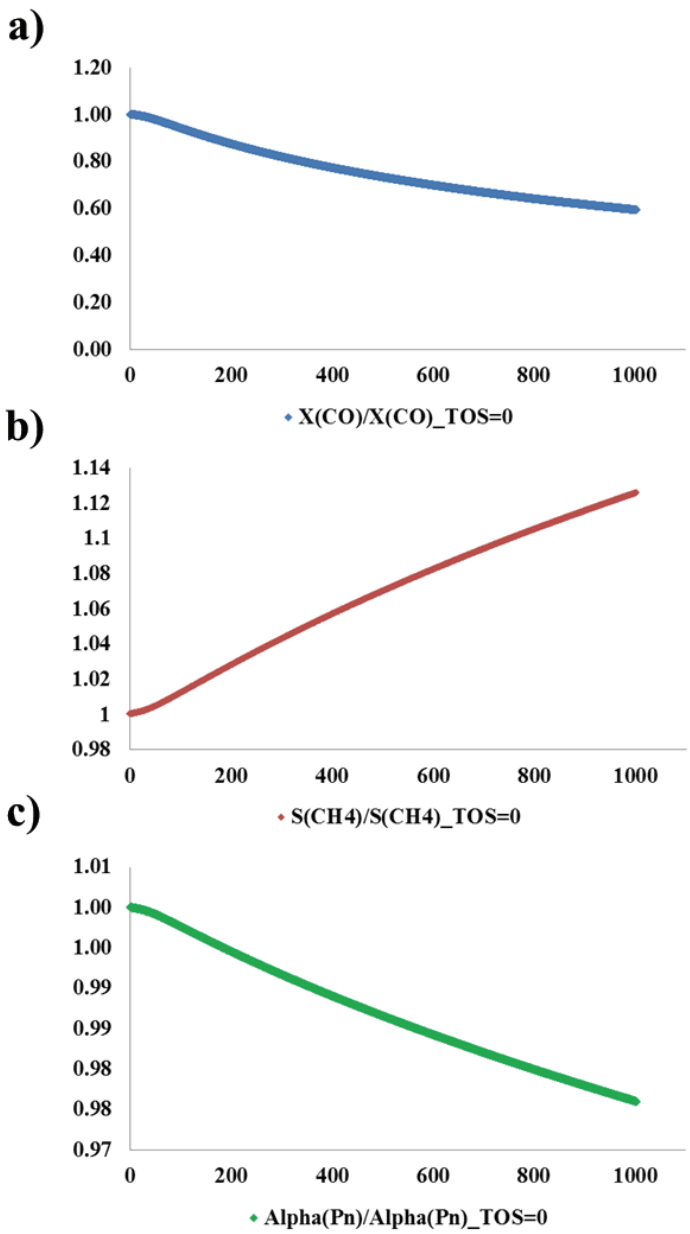


**Figure 76.** Time-evolution of FT observables calculated based on a double-site micro-kinetic model for Experimental Run 5. a) CO conversion b) Methane Selectivity c) Chain-growth probability of paraffin. For limiting case initial values of 70.18, 10.56% and 0.878 respectively.

**Figure 76** presents the time-on-stream evolution of some typical FT observables. Our micro-kinetic model prediction is in good qualitative but also quantitative agreement with observed deactivation rates in some experimental works[285,199,3,195,130,3]. As for surface concentrations of radical species, those are presented in **Figure 77**, the comparaison of **Figure 77** and **Figure 76** leads to the conclusion that deactivation mechanism is the consequence of, on one hand, a reduction in the number of active sites occupied by coke precursors as shown

in **Figure 77** e) and, on the other hand, a decrease in surface concentrations of FT reagents as shown in **Figure 77** d). For instance, Carvalho et al. [327] found in SSITKA experiments a decrease in CO* surface overages during a deactivation phenomenon. Based on the results in **Figure 77** and **Figure 76**, it seems that there is a correlation between the amount of coke on the surface and the time evolution of FT observables. In order to verify this hypothesis, we evaluate the amount of surface occupied by coke ($>C_4$) versus time-dependent FT observables. Those correlations are presented in **Figure 78**. Based on the results in **Figure 78**, we conclude that the catalyst activity and methane selectivity are directly correlated to the amount of coke-covered surface coverages. A similar trend has been observed for CO conversion in another experimental work [199]. As for the chain-growth probability of paraffins, except at low coke coverages, it seems that the same linear correlation holds. It should be noted that the quality of this prediction depends on the quality of the initial fitting procedure.

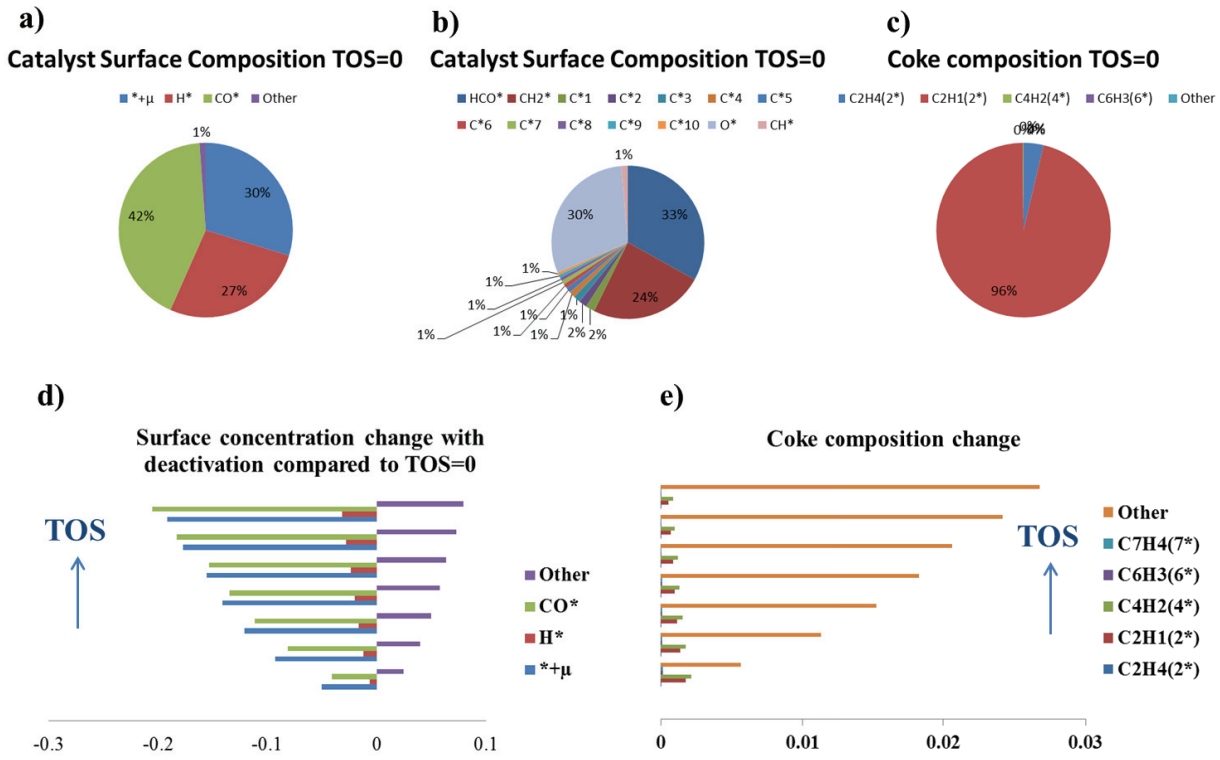


**Figure** 77. a,b and c) Surface composition before deactivation. e) and e) Evolution of surface composition with TOS and deactivation phenomena.

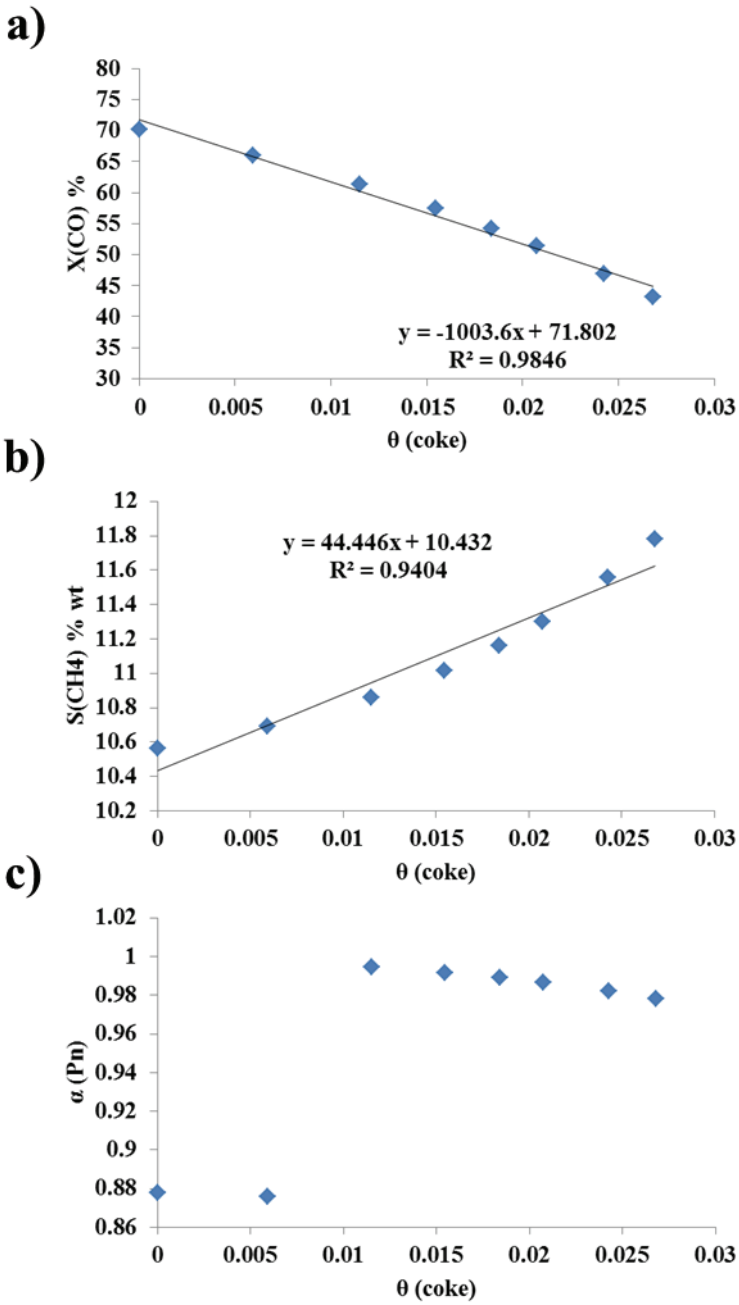


**Figure 78**. Correlation of the FT observables to the amount of surface covered with coke. a) CO conversion b) Methane Selectivity c) Chain-growth probability of paraffin.

## 6.4 Conclusion and Perspectives from the micro-kinetic model study

In this chapter we presented, to the best of our knowledge, the first micro-kinetic model scheme that takes into consideration the deactivation phenomenon inspired by H-assisted CO dissociation scheme previously proposed for the deactivation-free model by

Visconti et al. Firstly, we optimized deactivation-free model of Tronconi based on the in-house data and we showed a satisfactory agreement with experiments can be achieved. However, our model predicts some inconsistency in term of product selectivities, which may be related to the quality of experimental data obtained from HTE. We can not exclude entirely the possibility that a local minimum has been obtained during the optimization procedure and that we fail to reach the global one. Besides, literature data [328] on the micro-kinetic model optimization recognized the necessity to employ global optimizers along with the Levenberg-Marquardt technique as, for example, Genetic-based Algorithms, in order to obtain better parameter estimation. An implementation of such global optimizers in our current reactor and optimizer code may represent a rewarding perspective for future work.

Besides, we have presented two micro-kinetic modeling schemes that contain carbon induced deactivation phenomena based on our previous DFT work. The former one, regarded as non-physical as it contains some elementary steps challenging to justify, and the latter being more physically sound, as it completely lies on principles discovered in our previous work during this thesis, or found in the literature. However, because we do not possess any data on long-term, deactivation relevant, performances of Co-based FT catalyst, no formal fitting of this model is performed. Instead, a manual adjustment has been achieved based on the deactivation-free micro-kinetic scheme. This so-called μ-deactivation model assumes the separation of the active sites responsible for methanation from other reactions and allows predicting both qualitatively and quantitatively the evolution of some typical FT observables.

# 7 General Conclusions and Outlook

The present work aimed to shed some light on the deactivation and selectivity losses phenomena of cobalt-based Fischer-Tropsch catalysts, one of the main issues in the industrialization of this process. More precisely, considering the lack of agreement in the literature on the preferential long-term deactivation pathway of Co-based catalysts, our task was to assess some of the hypothesis evoked in the literature and to find, among them, the most likely ones. We first searched for the most likely deactivation pathway with thermodynamic and kinetic calculations and we then aimed at confronting our findings with up-to-date experimental observations. Lastly, we updated a microkinetic model in order to model and predict the deactivation process with the final aim of optimizing the industrial catalysts in the future.

**Chapter** 1 and 2 present a critical overview of historical and current literature data on the fundamentals of the FT reaction, its thermodynamic and kinetic properties (such as current views on the reaction mechanism and the structure-sensibility of active sites) and the causes evoked for the catalyst activity and selectivity loss. In this chapter, we aimed at presenting the different theoretical and experimental approaches in the field and the limitation of different methods. Particular focus was given to the FT mechanism scheme proposed by Tronconi et al. and to three deactivation pathways related to the active phase: surface oxidation, carbon deposition and surface reconstruction.

In **Chapter** 3, we presented the computational tools and the fixed-bed reactor model employed in our work. Based on these methods, we obtained the results we presented in **Chapters** 4 to 6.

In **Chapter** 4, we presented a comprehensive thermodynamic DFT investigation of the Co surface state under FT reaction conditions. For that purpose, we developed a full thermodynamic model (see Section 8.4), combining consistently DFT and experimental data.

Gibbs free energy calculations were conducted on the different chemical reactions leading to a specific Co catalyst surface state. We selected some of these surface states as representatives of the active phase deactivation phenomenon based on their reaction energies. Information about surface speciation was summarized in several diagrams representing the different surface states and their associated free energy of formation as a function of C, H and O coverages. Among the latter three, the surface coverage in carbon has the most substantial impact on the free energy for the deposition of $C_\alpha H_\beta O_\gamma$ species on Co. In those diagrams, we found three zones of chemical surface speciation with different chemical intermediates from the fresh to the deactivated Co catalyst. In Zone 1 ($\theta(C) \leq 0.75$ ML and $0 \leq \theta(H) \leq 1$ ML), surface species $CH_\beta$ required for FT synthesis have been identified. In this Zone, CO-derived oxygen is identified as having a strong oxidizing potential for Co sites in contrast to water-derived oxygen. In Zone 2, ($1 \leq \theta(C) \leq 1.25$ ML and $0 \leq \theta(H) \leq 1$ ML), some key $C_\alpha H_\beta$ surface species have been identified. Among them, linear and branched polymeric hydrocarbon species that can act as precursors of deleterious carbon species found in the literature leading to activity loss. Also, in this Zone, the reconstruction of the cobalt surface occurs through the migration of C in metal subsurface sites. It has been underlined that in Zone 2, O atoms are only expected to have a weak effect on activity due to the higher carbon surface coverages. In this region of the speciation diagram, O atoms do not interact directly with Co sites as they preferably bind with the C overlayer. In Zone 3 ($1.5 \leq \theta(C) \leq 2$ ML) the Co surface is predominantly covered by C atoms forming either multiple branched chains or a graphitic overlayer. The latter surface state has been defined as representative of the deactivated catalyst since Co supported graphite is very stable and it is usually found in coke deactivated catalysts. The branched hydrocarbons (found in Zone 2 and 3) may also be considered as precursors of this graphitic over layer. Hence, according to our results, the preferential deactivation pathway for the active phase Co-based FT catalysts is the one in which

deposition of carbon species occurs. Finally, regarding H atoms, it has been found that they may be located either on C atoms, O or Co sites if available. The weak effect of the H position in the structure and formation energies of $C_\alpha H_\beta O_\gamma$ species implies that these atoms are free to move in the surface and able to participate in different reactions.

In **Chapter** 5 we investigated the mechanism and kinetics of reaction pathways leading to the formation of graphitic-like species. A simple three-step mechanism has been examined based on findings in **Chapter** 4 and the literature: deactivation initiator, coke-seed formation, and coke-seed growth. Among the several $C_2H_\beta$ deactivation initiator structures we found in our results, ethynyl surface species $C_2H$ seems to be kinetically and thermodynamically the most favorable one. Coke seed, a cyclic $C_6H_\beta$ intermediate, is formed in the cyclotrimerization reaction of ethynyl surface species. Finally, a mechanism of coke-seed growth by coupling with some $C_1H_\beta$ fragments is presented.

In **Chapter** 6, firstly, we adjusted the single-site microkinetic model of Tronconi et al. (that does not account for deactivation phenomenon) with in-house catalytic tests. The model accounts satisfactory for experimental observations such as CO conversion, selectivity of paraffins, methane and olefins. Secondly, the initial micro-kinetic model was upgraded with the deactivation mechanism described in **Chapter** 5. Given the absence of in-house experimental data acquired in long-term, deactivation relevant runs, we adjusted "manually" kinetic rate constants to reproduce trends in deactivation such as CO conversion decrease, methane selectivity increase and paraffin selectivity decrease. Our deactivation model performed accurately compared to some literature data in terms of CO conversion and paraffin selectivity but not methane selectivity. This discrepancy was attributed to the model and was circumvented by introducing a second active site involved in methane production. The resulting two-site deactivation model is in agreement with the most common deactivation-dependent experimental observations. Moreover, the two-site deactivation model

was examined in terms of the surface composition of the spent catalyst and compared to literature data.

The present thesis provides several valuable insights into the fundamental understanding of the cobalt-based FT catalysts deactivation mechanism.

For instance, our work highlights that the deactivation of the active phase in Co-based FT catalysts comes from the formation of coke, rather than the oxidation of the active sites. Moreover, we provide evidence that CO is a stronger oxidizing agent than it is water under these reactions conditions. Besides, we also found that O would rather interact with C than with Co or leave in the form of water molecules once formed during the FT reaction. Based on this first set of results, we identified several surface states that are precursors of deleterious carbon species and showed that, from our kinetical calculations, several reaction mechanisms that can lead to such species. According to our results, the elementary steps leading to those surface species have reaction barriers that can be easily overcome under FT reaction as they are in the same range of values as those involved in the FT polymerization mechanism. Hence, our results demonstrate that the deactivation by the formation of coke is favorable both from a thermodynamic and a kinetic point of view. Lastly, we showed how this information can be used to upgrade an existing microkinetic model of the FT reaction in order to account for the observed deactivation phenomena and optimize the process.

This work also provides guidelines and ideas for future research. More thorough work needs to be done in the identification of the kinetically and thermodynamically most favorable coke formation mechanisms. The basis of those ideas has been highlighted in **Chapter** 5. Briefly, at this point, we cannot exclude other $C_\alpha H_\beta$ species as deactivation initiators. One fundamental question related to the deactivation initiator is their exact origin. Although we assumed ethylene molecule as the most plausible precursor of deleterious carbon species, is it also possible that $C_1H_\beta$ species form by hydrogenation of CO molecules. What are the

consequences of these different reaction pathways with the mechanism of the FT polymerization reaction, considering that they all co-exist and are in competition? What is the role of oxygen in those reactions? What is the exact nature of $C_\alpha H_\beta/C_\alpha H_\beta$ coupling reactions that lead to detrimental carbon species? Is the cyclotrimerization reaction we presented in **Chapter** 5 the most favorable pathway to the formation of cyclic species? At the point where no agreement exists on the mechanism of the FT reaction itself, it is very challenging to provide an answer to these questions. In this regard, we believe that the mechanism of the FT reaction should be studied along with the deactivation phenomena and not separately since the underlying nature of the reactions involved in both of them appears to be the same ($C_\alpha H_\beta/C_\alpha H_\beta$ coupling reactions). Hence, future works in this area could include an extension of our microkinetic calculations to the full FT reaction in order to have more atomistic insights on the deactivation phenomena and a more quantitative agreement between theory and experiments. As for experimental studies in this area, in our opinion, surface science, isotope labeling, operando and co-feeding experiments may have a preponderant role in the context of providing guidance in future mechanistic investigations.

Future results in the field will surely elucidate the negative effects of water in the FT process. Indeed, according to our results this molecule does not seem have a negative impact on the active phase. Nevertheless, there is evidence that water is involved in the sintering of metal particles and the chemical weathering of the support. These deactivation mechanisms involve solid-state reactions that are difficult to investigate by both theoretical and experimental approaches and represent interesting topics of future work. Experimental studies related to the deactivation phenomenon are another critical challenge to be overcome in reactor modeling. This is the reason why publications linking reaction parameters to deactivation phenomena are scant and contradictory.

Also, more research is needed in order to find a relationship between the catalyst properties (morphology, crystallite size, the nature of support …) and possible implications and performances in long deactivating runs. More studies in this area will, in our view facilitate the task of theoretical scientists working on models of the FTS reaction as they provide the relevant parameters of the reaction as well as the relevant reaction intermediates for mechanistic studies. Hopefully, all this work will help to unravel the 100-year old “FT puzzle”.

# 8 Appendix

## 8.1 Total Energy Convergence Tests

The success in interpreting the results of calculations based on the theory described in **Chapters 4** and **5,** largely depends on the convergence of the properties of interest regarding input parameters used in those calculations. Besides, maximal calculation accuracy is envisaged while maintaining a minimal amount of time required for those calculations to be performed. In this project, we are primarily interested in thermodynamical properties, such as the Gibbs free energy and its components (see **Section 8.2**). Thus, to ensure the quality of our results, the convergence of total (electronic) energy tests is performed, with respect to different calculation parameters. In this section, we show and discuss our choices for model structure and different calculations parameters such as k-point number, smearing parameter $\sigma$, energy cut-off, the dimension of unit cell and number of slab layers described in **Chapter** 3.

### 8.1.1 k-point grid optimization

**Figure** 79 and **Figure** 80 present the results of single-point energy calculations performed on the bulk Co structure at constant volume for a different choice of k-point meshes. Inspection of both **Figure** 79 and **Figure** 80 shows that the single-point energy obtained for a 9x9x9 k-point mesh should be a reference value since all energy values beyond this k-point mesh oscillate negligibly in a range of $\sim 10^{-4} eV$/cell or less. However, in order to determinate the optimal k-point mesh, we also need to take into consideration the time required to perform calculations, and those results are presented in **Figure** 81. The analysis of the results presented in **Figure** 81 reveals that the computational time required to perform single-energy calculations increases exponentially with the number of k-points. Thus, the computational efficiency of our calculations requires a careful selection of the k-point mesh.

As a rule of thumb, we consider that absolute energies are converged with respect to k-meshes when the energy difference between two adjacent k-meshes is of the order of 1 meV/atom. This is a reasonable choice considering the accuracy of other parameters discussed below. In **Figure** 80 we can see that the energy differences are too big ($> 0.01\,eV$) in the case of 5x5x5 and 6x6x6 meshes; however, the ones for 7x7x7 and 8x8x8 are attractive choices, taking into consideration the computational cost (see **Figure** 81) but also the convergence of those calculations that is of order $\sim 10^{-4} eV/atom$ and $\sim 10^{-3} eV/atom$, respectively. Thus, from results in **Figure** 80, we deduce that for meshes bigger than 9x9x9, absolute energies change is negligible. Hence, the absolute energy obtained with 9x9x9 grid is used as the *reference energy* for every fuure considerations.

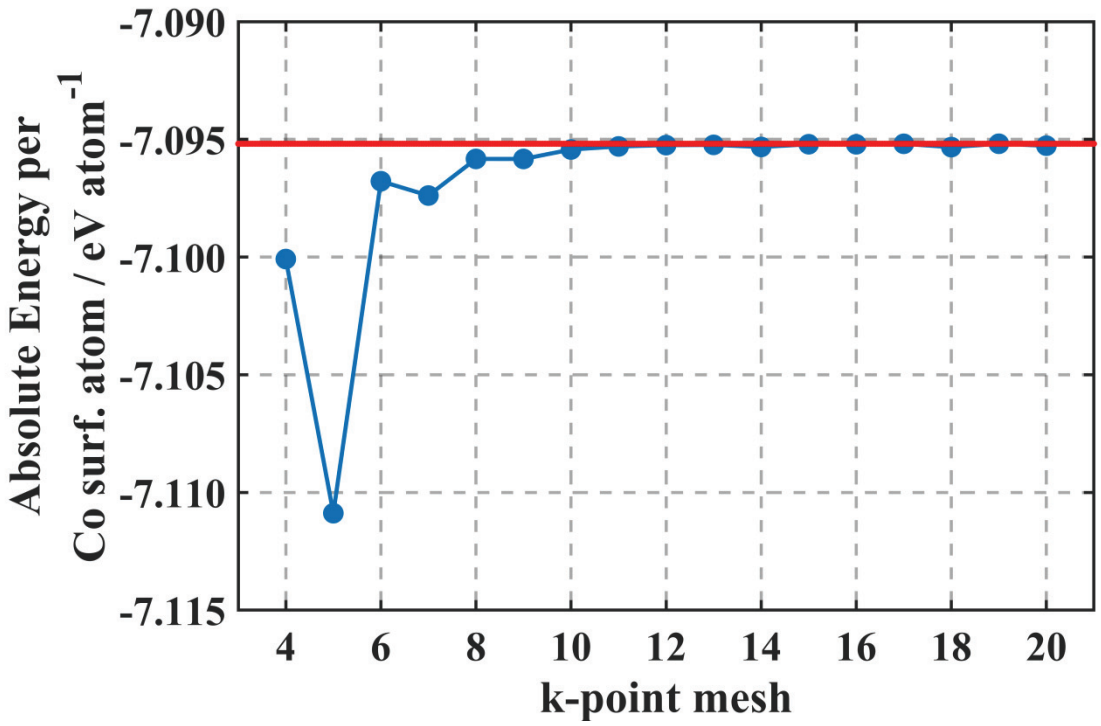


**Figure** 79. Single-point absolute energy as a function of the k-points mesh. Energies are per number of Co atoms in the face-centered cubic unit cell. Convergence line extrapolated to converged energy (Red dashed curve).

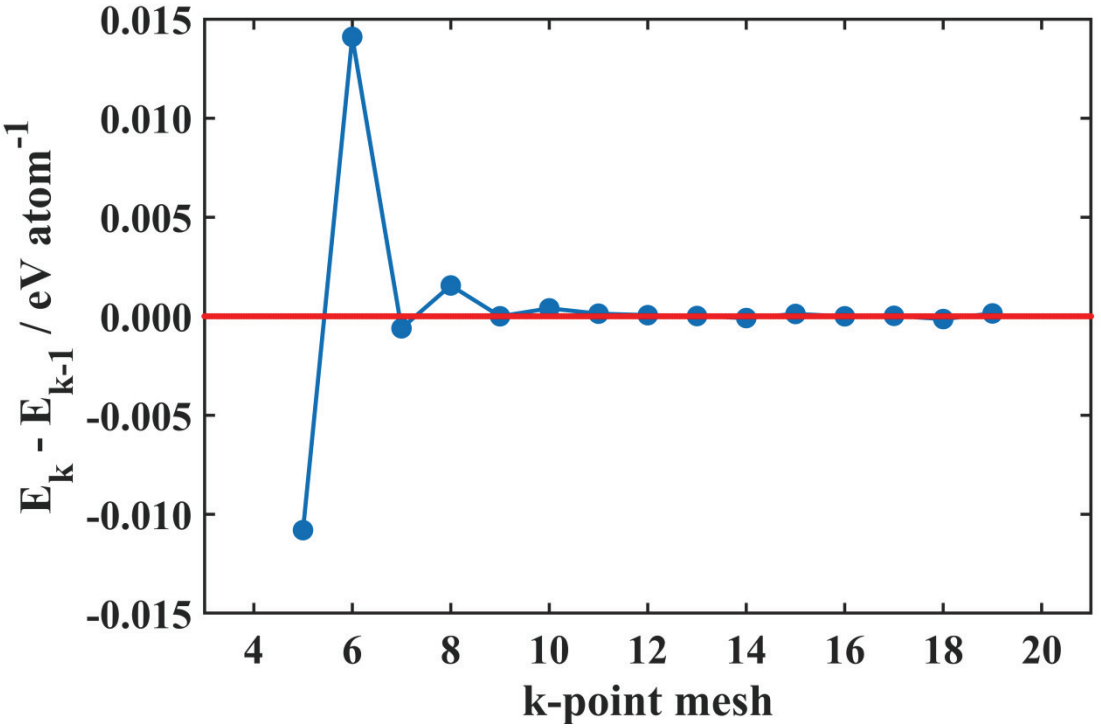


**Figure** 80. Single-point energy differences between calculations of successive k-point mesh (Blue line). Convergence line (Red dashed curve).

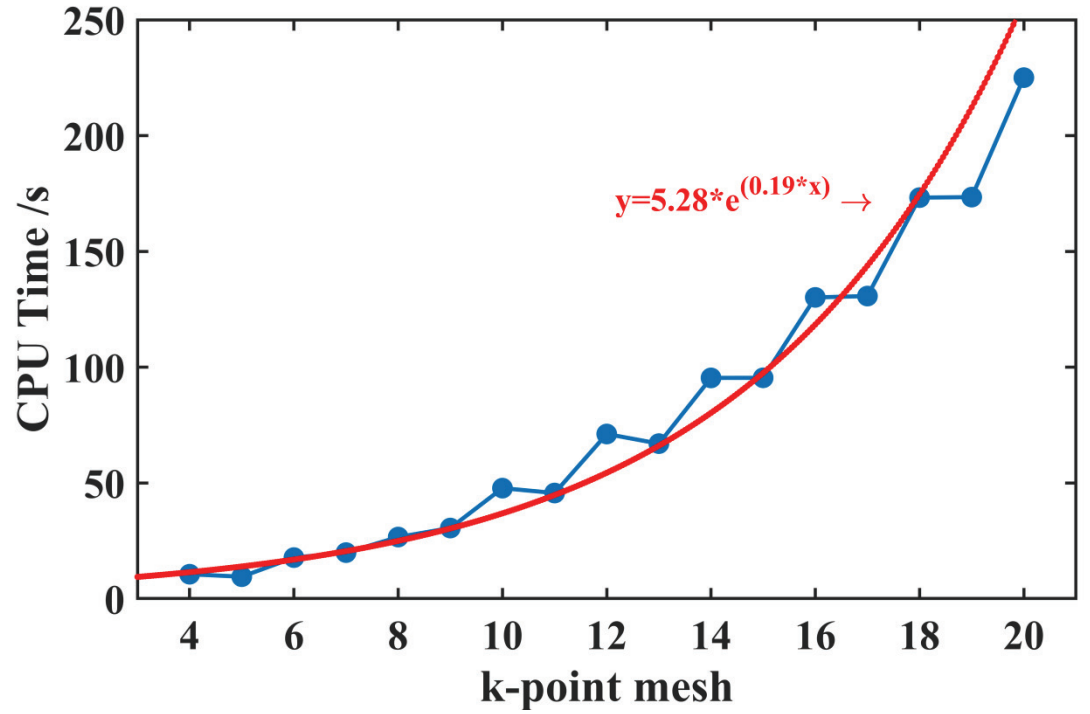


**Figure** 81. Computational time increase with a density of k-points chosen to sample the Brillouin zone (Blue line). Exponential function fit (Red line).

### 8.1.2 Smearing-width optimization

Although the method of Methfessel-Paxton (MP) gives a very accurate description of the total energy, the width of smearing, defined by σ parameter in our calculations, should be carefully chosen. The criteria usually employed for choosing an appropriate σ parameter is the difference between the free energy term and the total energy (entropic term T*S in the output file) that should be negligible as much as possible ($< 1meV$ per atom is usually a good choice). When optimizing the smearing width, we tested five different k-point meshes along with three typical values for smearing width: 6x6x6, 7x7x7, 8x8x8, 9x9x9 and 10x10x10 and 0.05, 0.1 and 0.2 eV, respectively. The results of those calculations are presented in **Figure** 82 and **Figure** 83.

The analysis of results presented in **Figure** 82 suggests that $\sigma = 0.1\ eV$ and $\sigma = 0.2\ eV$ are not good smearing width choices for 7x7x7 and 8x8x8 meshes respectively. However, all other combinations of k-points number and smearing width are inside the acceptation criteria ($|T * S| < 1\ meV$ per atom). Concerning the evolution of the entropy term with respect to smearing width, no particular trends can be observed. In **Figure** 83 we presented the differences of calculated energies with respect to the reference energy obtained for a 9x9x9 mesh and we found a negligible ($\sim 10^{-3} eV$/atom) dependence with respect to smearing widths studied. Inspection of **Figure** 83 implies also that 6x6x6 mesh performs well for the smearing widths we used here although energy fluctuations are of the same order of magnitude ($\sim 10^{-3} eV$/atom) are achieved with 7x7x7 and 8x8x8 meshes too. Denser grids (9x9x9 and 10x10x10) give the best convergences at the expense of computational time (see **Figure** 81). Although it is clear that the best convergences are achieved with denser grids such as 9x9x9 and 10x10x10, the computational time necessary to perform those calculations

are significantly higher.. Therefore, we decided to refine the results in a search for ideal σ for less dense k-mesh grids such as 6x6x6, 7x7x7 and 8x8x8. The results of those refinements are presented in **Figure** 84 and **Figure** 85 for σ's between 0.050 and 0.100 and the increments of 0.005.

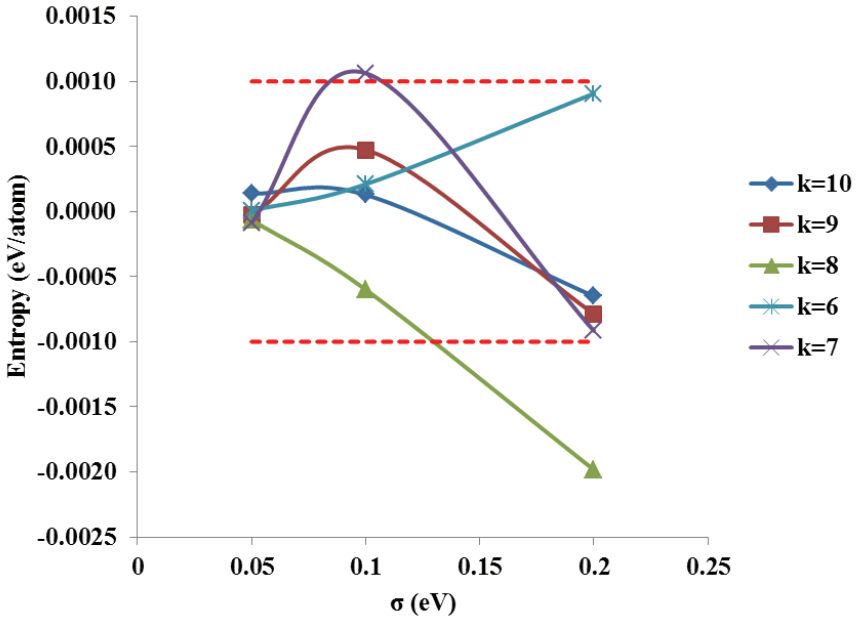


**Figure** 82. Residual entropy per atom in Co face-centered cubic unit cell for different k-point meshes to smearing width. Thresholds are represented by red dashed lines.

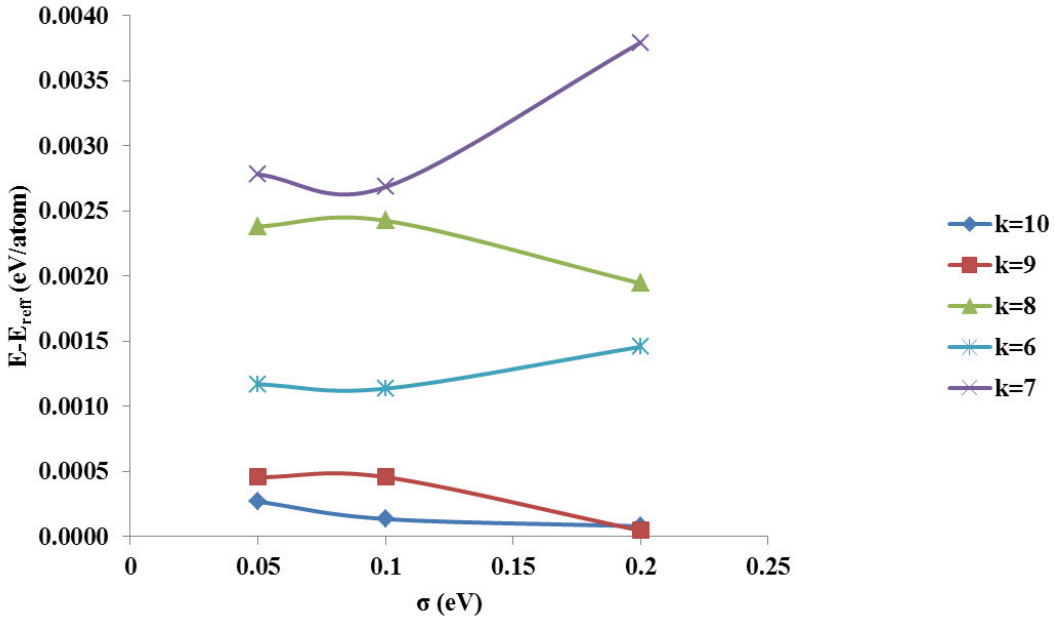


**Figure** 83. Difference between calculated and reference energy for different k-point meshes

to smearing width.

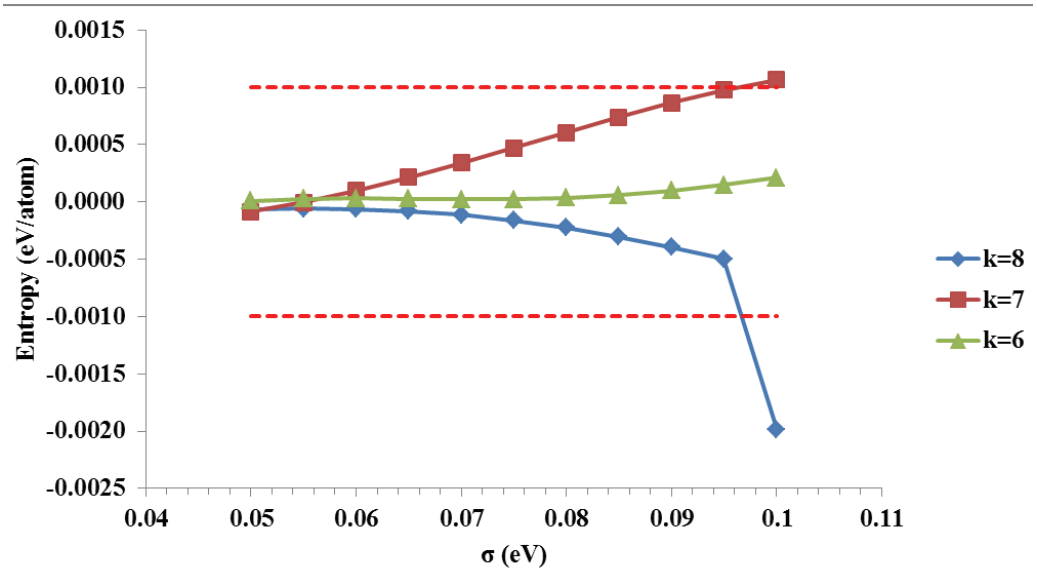


**Figure** 84. Entropy term per atom in Co face-centered cubic unit cell for the least dense k-point grids to different smearing widths. Thresholds are represented by red dashed lines.

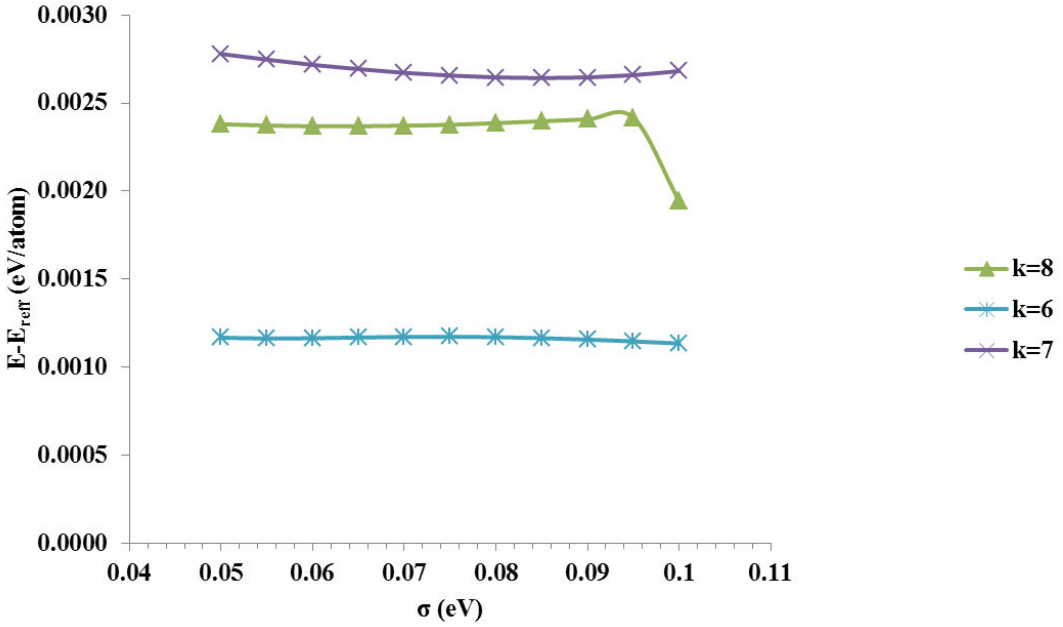


**Figure** 85. Difference between calculated and reference energy for the least dense k-point grids to smearing widths.

Inspection of results in **Figure** 84 suggests that a few combinations of k-point grids and smearing width are unacceptable such as 8x8x8 7x7x7 grids combined with the widest

smearing used here, σ=0.1 eV. All the other combinations satisfy the convergence criteria commonly used in the literature. Interestingly, the 6x6x6 grid seems insensitive to the σ used. On the other hand, the 7x7x7 grid yields results with the highest entropy while in the 8x8x8 grid, the entropy diminishes when increasing smearing widths. Analysis of results in **Figure** 85 suggests that the three grids mentioned here give approximately the same deviations with respect to the reference energy $\sim 10^{-3} eV$/atom. Hence, taking into account all these facts, we decided to use 7x7x7 grid with a width of σ=0.085 eV for which there is the better trade-off between computational cost and accuracy.

### 8.1.3 Cut-off energy optimization

We tested several possibilities for cut-off energy between 300 and 500 eV with an increment of 50 eV as these are usually employed in the literature when studying metallic systems. The only difference regarding previous calculations is that here we are performing an optimization rather than performing single-point calculations as it was the case when we tried to find the optimal size of k-point grid and smearing width. The results of those calculations are presented in **Figure** 86 where we plotted successive the total energy evolution (normalized per Co atom in the unit FCC cell at constant volume) with respect to different cut-off energies we used. Analysis of results presented in **Figure** 86 indicates that energy deviations are of order $\sim 10^{-3} eV$ per atom, which is considered as good taking into account the accuracy of all other parameters. In accordance with previous calculations performed on FCC Co, we think that the best option is to take cut-off of 500eV.

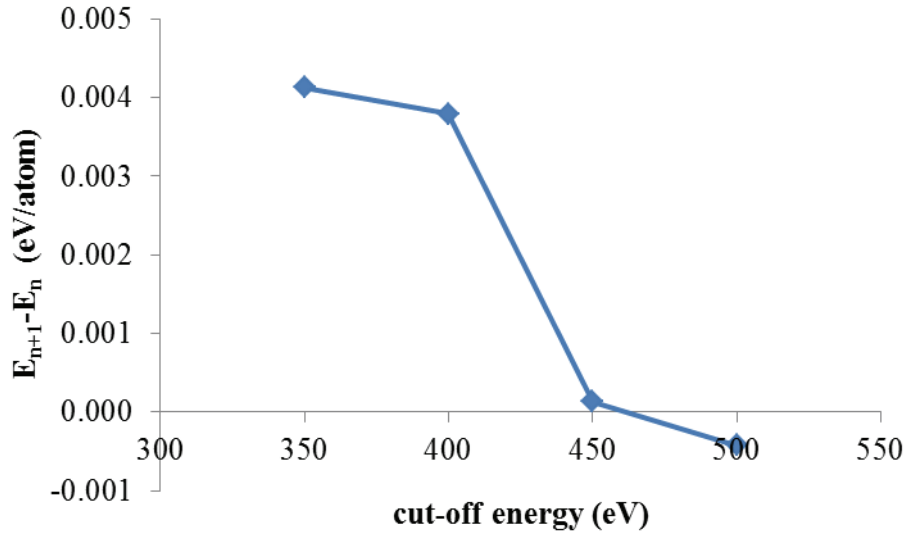


**Figure** 86. Calculated differences in successive energies to chosen cut-off energy.

### 8.1.4 Unit-cell constant optimization

To determine the equilibrium lattice constant of bulk FCC Co, $a$, we need to allow volume relaxation in our calculations. Equilibrium lattice constants can be obtained using different approaches. In this thesis, we use the Birch-Murnaghan equation of state, and Pulay stress minimization approaches. Pulay stress is the consequence of the incompleteness of the plane wave basis set with respect to volume changes. First, we vary moderately the experimental lattice constant $a_0$ [254], and we minimize the energy with respect to the varied lattice constants. Then, we refine those results by calculating the Pulay stress for those volumes, and we find the volume where the Pulay stress is close to zero. The volume for which these conditions are satisfied and the corresponding lattice constant are the equilibrium volume and lattice constant, respectively. The results of those calculations are presented in **Figure** 87 and **Figure** 88. Inspection of results in **Figure** 87 clearly shows a broad minimum for scaling factors $\frac{a}{a_0}$ between 0.995 and 1 (the equilibrium volume is in the interval $0.995V_0 < V_{eq} < V_0$). Instead of calculating a derivative of obtained curve and setting it to

zero in order to trace a minimum, we choose plotting of the Pulay stress (read from output data in the VASP package) with respect to scaling factor, since this plot is already linear which evites possible errors of data fitting and finding the position of very broad minimum. This plot is presented in **Figure** 88. From the results presented in **Figure** 88 along with the slope $k$ and the intercept $n$ therein, is can be concluded that the Pulay pressure is equal to zero for $a = a_0 * \frac{n}{k} = 3.52773 * 0.99892 \approx 3.5239\text{Å}$. Throughout this project, the equilibrium lattice constant used is thus $a = 3.5239\text{Å}$.

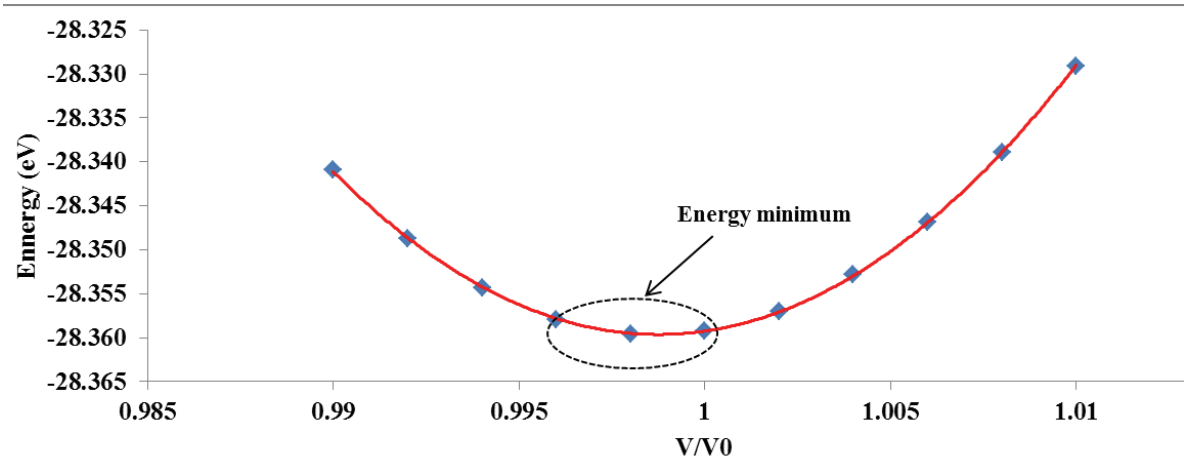


**Figure** 87. The energy of bulk FCC Co with respect to volume (lattice constant) change. Volume changes are expressed as multiples (scaling factor) of the experimental volume for which we took the value from the reference. [254]

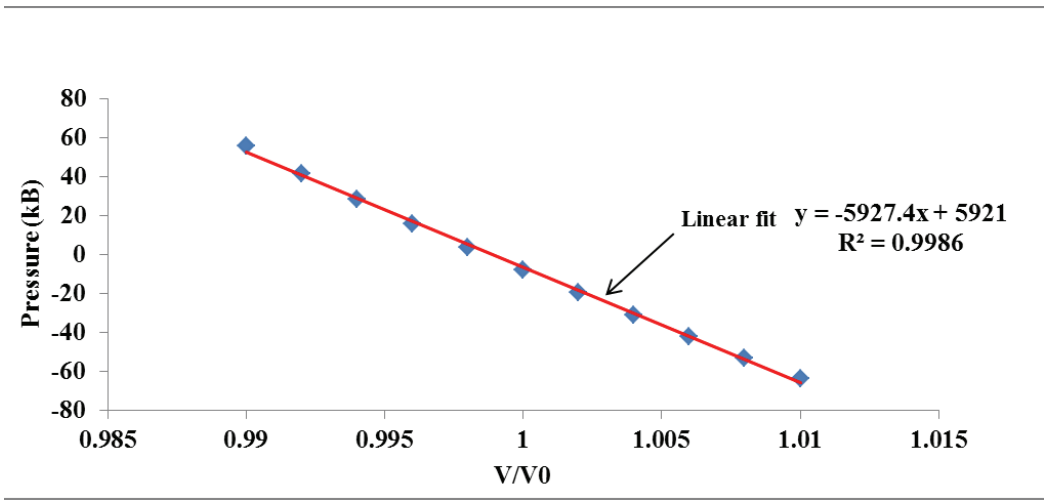


**Figure** 88. The Pulay pressure dependence on the volume change. Red line represents linear fit.

### 8.1.5 Slab thickness optimization

A surface model consists of a slice of material that is infinite in two dimensions, parallel to the surface plane, but finite along the surface normal as represented in **Figure** 89. The crystal slab must be thick enough so that two exposed surfaces of the slab with each other. Also, the vacuum region in **Figure** 89 must be wide enough to prevent interactions between adjacent slabs across the vacuum so that electron density tails to zero in the vacuum region. In general terms, the thicker slabs and the larger the vacuum regions, the better the calculation is. However, this is done at the expense of computational time, since during the calculations plane waves expansions are also used in the vacuum region when using the PW basis sets approach. Therefore, a compromise must be made between the computational cost and the desired physical accuracy. In the case of the Co(111) slab, a vacuum thickness of $\sim 15$ Å and a supercell p(2x2) is the most typically used setting. Here, we don't test the convergence of those two properties. We did, however, examined the convergence on slab thickness. The optimization of slabs with a different number of layers was performed using the calculation parameters described in **Section 8.1.5**. We computed the surface energy as a function of the slab thickness according to **Eq.** 73. We allowed all the atoms in the supercell p(2x2) to move during the optimization except for those in the bottom two layers that mimic the bulk part of the material.

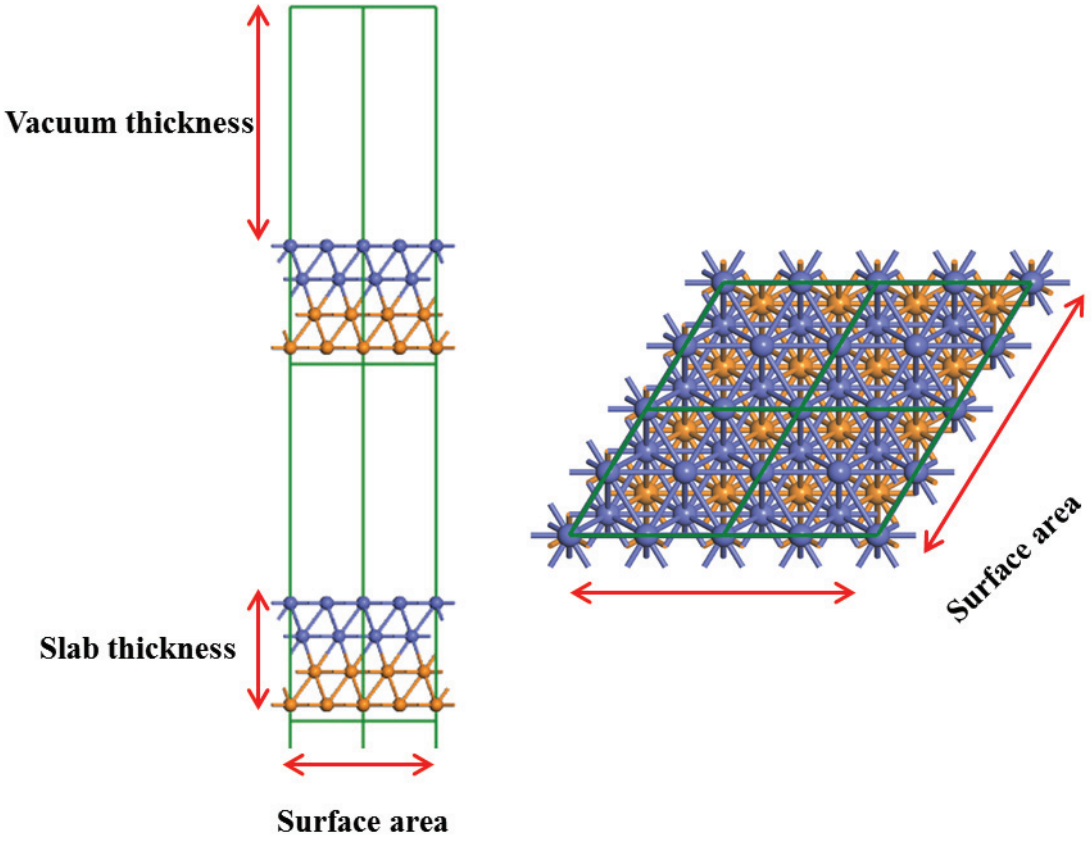


**Figure** 89. Side (left) and on-top view (right) of slab model.

$$\Delta E_{surf}^{0K} = (E_{slab} - n_{atoms} * E_{bulk}^{n})/2 \qquad \textbf{Eq.}\ 73$$

In equation **Eq.** 73 $E_{slab}$ is slab energy, $n_{atoms}$ is the number of Co atoms in the slab of a given number of layers, $E_{bulk}^{n}$ is the energy of a bulk FCC Co. Division by 2 ensures accounting for the two surfaces that are created (see **Figure** 89). Surface energies calculated by means of equation **Eq.** 73 are presented in **Figure** 90**.** Examination of results presented in **Figure** 90 implies that small variations in surface energy take place when successively increasing slab thickness. Those variations are the most important ($\sim 0.1\ eV$) for the least number of layers studied here (3 layers) and become less important ($\sim 0.01\ eV$) when increasing slab thickness. As far as the literature is concerned, slab models for Co vary from 3-layer to around 7-layer slab models. During this project, we decided to use a 4-layer slab model since the energy is sufficiently well converged (see **Figure** 90) for a reasonable cost in

computational time. Therefore, all the calculations performed in **Chapter 4** use a 4-layer slab model for the Co(111) surface.

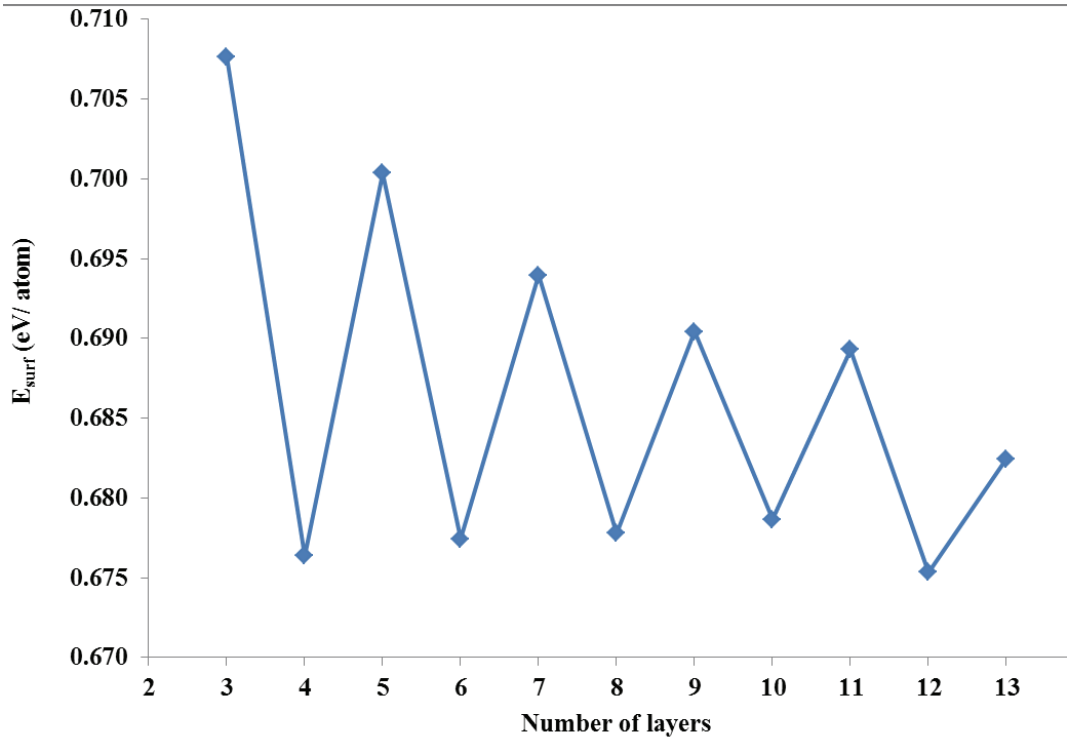


**Figure** 90. Surface energy variations to a number of layers (slab thickness) used in our calculations.

## 8.2 Thermochemical predictions based on DFT results

### 8.2.1 Introduction

One of the most crucial assets of ab initio methods is its use with statistical mechanics theory, to predict accurately thermodynamic quantities of different materials (molecules, solids …). Here, our primary goal in this section is to show how using Density Functional Theory we calculated in this work some thermodynamic quantities such as the enthalpy of a reaction ($\Delta_r H$), its entropy ($\Delta_r S$) and its free energy change ($\Delta_r G$).

The Gibbs free energy change for a given temperature can be decomposed according to the Gibbs-Helmholtz equation as follows:

$$\Delta_r G(T) = \Delta_r H(T) - T\Delta_r S_{tot}(T)$$
$$= \Delta_r(U(T) + pV(T)) - T\Delta_r S_{tot}(T). \qquad \textbf{Eq.}\ 74$$

In equation **Eq.** 74, $\Delta_r H(T)$ is the reaction enthalpy change that is decomposed to internal energy change, pressure-volume work and $\Delta_r S_{tot}(T)$ is the total entropy change by the chemical reaction. The internal energy change can be further decomposed into electronic, translational, rotational and vibrational contributions, which allows rewriting the enthalpy change as follows: [5]

$$\Delta_r(U + pV) = \Delta_r(U_{el} + U_{transl} + U_{rot} + U_{vib}) + \Delta_r(pV). \qquad \textbf{Eq.}\ 75$$

Due to computational cost, the zero-point energy (ZPE), that is, the energy that the system has in its ground vibrational state, is excluded from the total vibrational contribution to enthalpy. Hence, the first term in equation **Eq.** 75 on the right can be further decomposed as follows:

[5] We are omitting explicit temperature dependences in a further elaboration of formula due to space limitations.

$$\Delta_r(U_{el} + U_{transl} + U_{rot} + U_{vib}) =$$

$$= \Delta_r\big(U_{el} + U_{transl} + U_{rot} + U_{vib,without\ ZPE} + ZPE\big). \quad \textbf{Eq.}\ 76$$

Below the define the sum of $U_{transl}$ , $U_{rot}$ , and $U_{vib,without\ ZPE}$ as the thermal correction to the enthalpy change:

$$\Delta_r H^{corr} = \Delta_r\big(U_{transl} + U_{rot} + U_{vib,without\ ZPE}\big). \quad \textbf{Eq.}\ 77$$

Also, assuming ideal-gas behaviour, pressure-volume work term in **Eq.** 75 can be written as $\Delta_r(pV) = \Delta_r(nRT) = \Delta_r n * RT$. Hence, equation **Eq.** 74 becomes**:**

$$\Delta_r G = (\Delta_r U_{el} + \Delta_r H^{corr} + \Delta_r ZPE + \Delta_r n * RT) - T\Delta_r S_{tot}. \quad \textbf{Eq.}\ 78$$

$\Delta_r U_{el}$ , $\Delta_r H^{corr}$ , $\Delta_r ZPE$ , $\Delta_r n * RT$ and $\Delta_r S_{tot}$ are, respectively, the differences between products' and reactants' **(a)** electronic energies (we calculate with some ab-initio software package), **(b)** thermal corrections to enthalpy without ZPE emerged from translational, rotational and vibrational degrees of freedom, **(c)** zero-point vibrational energies (explicitly excluded from vibrational contributions), **(d)** compression/expansion work done by/on the system and **(e)** total entropies composed of translational, rotational and vibrational contributions. These terms are multiplied with appropriate stoichiometric coefficients (indicated by $\Delta_r$ symbol).

In the case of surfaces, we tend to neglect vibrational contributions both to enthalpy and entropy. In other words, we suppose that those two contributions are similar before and after adsorption and therefore cancel out. That means that in the case of surface reactions, equation **Eq.** 78 can be approximated to:

$$\Delta_r G \approx (\Delta_r U_{el} + \Delta_r H^{corr} + \Delta_r n * RT) - T\Delta_r(S_{transl} + S_{rot}) \quad \textbf{Eq.}\ 79$$

In equation **Eq.** 79 no vibrational contributions (including ZPE) are included in $\Delta_r H^{corr}$ (see **Eq.** 76).

### 8.2.2 Electronic contributions

The electronic energy term $U_{el}$ contributes to Gibbs free energy and it is calculated using ab-initio packages. As we will show later, this term contributes the most to Gibbs free energies. Therefore, to ensure comparability of results, special care must be taken when choosing calculation parameters.

As for the electronic contribution to entropy, our calculations are at the electronic ground state, and we assume a large energy gap between the ground and excited states. Therefore, the electronic partition function $Q_{elec}(T) = 1$. Thus, using the Boltzmann definition of entropy $S_{elec} = \ln Q_{elec}(T) = 0$. However, this is not always the case. Chemical transformations that involve excited electronic states (such as those found in photochemistry, for example) and quantum chemical calculations involving those electronic states are extremely complex.

### 8.2.3 Translational contributions

The translational partition function is a measure of the accessible translational microstates to a molecule and is given by:

$$Q_{transl}(T) = \left(\sqrt{\frac{2\pi MkT}{N_a h^2}}\right)^3 * \frac{1}{V}. \qquad \textbf{Eq.}\ 80$$

where $M$ is the molecule molecular mass, $k$ is Boltzmann's constant, $T$ is the absolute temperature, $N_a$ is the Avogadro's number, $h$ is Planck's constant and $V$ is the molar volume. According to the equipartition theorem, the translation contribution to the total internal energy

of a molecule is equal[6] to $DOF * \frac{1}{2}RT$. Since molecules can move into all directions of space, $x$, $y$, and $z$, this contribution will always be the same and is equal to $\frac{3}{2}RT$. Hence, translational contribution to the overall[7] entropy can be calculated explicitly from the partition function in **Eq.** 80**.** It can be shown (see [329,330]) that for one mole of substance, this contribution is given by:

$$S_{transl}(T) = R\ ln\left[\left(\frac{2\pi MkT}{h^2}\right)^{3/2}\left(\frac{e}{N_a}\right)^{5/2}V\right] \qquad \textbf{Eq.}\ 81$$

Where $R$ is the universal gas constant and $e$ is Euler's number.

### 8.2.4 Rotational contributions

The rotational partition function is a measure of accessible rotational microstates available to a given molecule at given conditions. Its form depends on the geometrical characteristics of molecules such as the moment of inertia $I$ and the symmetry number $\sigma$. In general terms, it depends on the characteristic rotational temperature, $\Theta_i$ ($i = A, B,$ and $C$and each one corresponds to one of the three principal moments of inertia $\mathrm{I}_i$ of the molecule)[8]:

$$\Theta_i = \frac{h^2}{8\pi^2 k \mathrm{I}_i}, \forall i \qquad \textbf{Eq.}\ 82$$

The exact form of the partition function will depend on the geometry of the molecule and relative magnitudes of the three principal moments of inertia. The last property is usually exploited to classify molecules into linear molecules ($\mathrm{I}_A \ll \mathrm{I}_B = \mathrm{I}_c$), spherical tops ($\mathrm{I}_A =$

[6] DOF= Number of **D**egrees **o**f **F**reedom.
[7] That is, the sum of translational, rotational and vibrational entropy contributions.
[8] The definition of these and other moments can be found elsewhere[329,330].

$I_B = I_c$), symmetric tops ($I_A = I_B \neq I_c$) and asymmetric tops ($I_A \neq I_B \neq I_c$), which is an outcome of the rigid-body approximation implicitly used in these computations. Due to large number of formula available for each case, we will omit them here but we will stress to which class our molecules of interest belong: $H_2$ (homo-nuclear diatomic; linear molecule), $CO$ (hetero-nuclear diatomic; linear molecule), $CH_4$ (spherical top) and $H_2O$ (asymmetric top). Rotor groups and corresponding expressions for partition functions are available in [329].

The rotational contribution to the internal energy is, similar to translational contributions, given by the theorem of equipartitioning of energy: $DOF * \frac{1}{2}RT$, and does not require knowledge of the exact form of the partition function. Care must be taken however, in order to account correctly for indistinguishable rotations (for example, rotation around the inter-nuclear axis of linear molecules such as $CO$, $H_2$ …). Nevertheless, the determination of the rotational entropy for a given molecule requires knowledge of the exact form of its partition function. For 1 $mol$ of the asymmetric top, spherical top (which can also be treated as linear molecules) respectively, the rotational contribution to the overall entropy is given by the following expressions:

$$S_{rot}(T) = R\ ln\left[\frac{\pi^{1/2}e^{3/2}}{\sigma}\left(\frac{T^3}{\Theta_A\Theta_B\Theta_C}\right)^{1/2}\right] \text{ asymmetric top} \qquad \textbf{Eq.}\ 83$$

$$S_{rot} = R\ ln\left(\frac{Te}{\sigma\Theta}\right) \text{ spherical top or linear} \qquad \textbf{Eq.}\ 84$$

The moments of inertia around the three axes in **Eq.** 83-**Eq.** 84 can be calculated using appropriate formulas.

### 8.2.5 Vibrational contributions

The vibrational partition function is a measure of the number of accessible vibrational microstates to a given molecule at given conditions. Assuming that vibrations are harmonic,

we have calculated the vibrational partition function using the values of the Hessian matrix obtained from frequency calculations and the formula below:

$$Q_{vib}(T) = \prod_{i=1}^{DOF} \frac{e^{-\frac{100hc\tilde{\nu}_i}{2kT}}}{1 - e^{-\frac{100hc\tilde{\nu}_i}{kT}}} \qquad \textbf{Eq. } 85$$

Note that in **Eq.** 85, we have already included all the conversion factors so that the typical output of most quantum chemical packages, where frequencies are reported in spectroscopic wavenumbers $\tilde{\nu}$ (in $cm^{-1}$), can be direcly used. The multiplication is done over all degrees of freedom: $3N - 5$ for linear and $3N - 6$ for nonlinear molecules. From **Eq.** 85 and using $U_{vib} = -\left(\frac{\partial \ln Q_{vib}}{\partial\left(\frac{1}{kT}\right)}\right)$, the vibrational contribution to internal energy (under the harmonic approximation for 1 $mol$ of the molecule) is given by:

$$U_{vib}(T) = R\sum_{i=1}^{DOF}\left(\frac{100hc\tilde{\nu}_i}{2} + \frac{100hc\tilde{\nu}_i * e^{-\frac{100hc\tilde{\nu}_i}{2kT}}}{e^{\frac{100hc\tilde{\nu}_i}{kT}}}\right) \qquad \textbf{Eq. } 86$$

After introduction of the vibrational temperature, defined as $\Theta_{v,i} = \frac{h\nu}{k} = \frac{100hc\tilde{\nu}_i}{k}$, **Eq.** 86 becomes:

$$U_{vib}(T) = R\sum_{i=1}^{DOF}\left(\frac{\Theta_{v,i}}{2} + \frac{\Theta_{v,i}}{e^{\frac{\Theta_{v,i}}{T}} - 1}\right) =$$

$$= R\sum_{i=1}^{DOF}\left(\frac{\Theta_{v,i}}{2}\right) + R\sum_{i=1}^{DOF}\left(\frac{\Theta_{v,i}}{e^{\frac{\Theta_{v,i}}{T}} - 1}\right) = ZPE + U_{vib}^{corr}(T). \qquad \textbf{Eq. } 87$$

The first term on the right in **Eq.** 87 is the so-called zero-point energy of the molecule and it accounts for the molecules' energy at the ground vibrational state ($\upsilon = 0$). Note that there are quantum chemical packages (such as $D_3$Mol) that exclude explicitly this contribution

and report vibrational energies as $U_{vib}^{corr}$. Strictly speaking, the vibrational contribution to the internal thermodynamic energy is given by **Eq.** 87. Thus, it includes both the zero-point energy and the vibrational temperature correction to energy. The last term on the right in **Eq.** 87 represents the energy of thermally excited vibrational states ($\upsilon > 0$) of a molecule at a given temperature. Note that the ZPE does not depend on temperature. Lastly, vibrational entropy is given by the following expression:

$$S_{vib}(T) = R\sum_{i=1}^{DOF}\left(\left(\frac{\Theta_{v,i}/T}{e^{\frac{\Theta_{v,i}}{T}}-1}\right) - ln\left[1-e^{-\frac{\Theta_{v,i}}{T}}\right]\right). \qquad \textbf{Eq.}\ 88$$

## 8.3 Comparison of DFT data with the literature

### 8.3.1 Hydrogen stability on Co(111) surface in Fischer-Tropsch reaction conditions

In this section, we will present some studies we performed in the initial stages of our calculations shown in **Chapter 4**. Although the results of those calculations have been already reported in the literature [276,275,79], we insisted on repeating them here since they represent the basis of our future work and can also serve as some sort of validation of previous results that have been published. Hydrogen adsorption energies at $0K$ calculated by the means of **Eq.** 89 altogether with some geometry characteristic are presented in **Table** 19-**Table** 21 for on-top, fcc and hcp hollow sites respectively. We didn't succeed in optimizing hydrogen on the Co(111) surface in the bridge position.

$$\Delta E_{ads}^{0K} = E_{Co(111)-H_y} - E_{Co(111)} + mCH4 + (x + m - z)H2O - (x + 3m - z + y/2)H2 - (x + m)CO \qquad \textbf{Eq.}\ 89$$

**Table** 19. Hydrogen adsorption energy in OT site and its geometry with respect to Co(111) surface along with values reported elsewhere.

| OT site | Adsorption energy | | Geometry[a)] | |
|---|---|---|---|---|
| θ [b)] (ML) | $\Delta E_{ads}$ (eV) | $\Delta\Delta E_{ads}$ [c)] (eV) | Z [a)] (Å) | $\Delta Z$ [c)] (Å) |
| 0.25 | -3.11 | -0.04 | 1.51 | +0.01 |
| 0.50 | / | / | / | / |
| 0.75 | -2.35 | -0.02 | 1.50 | -0.05 |
| 1.00 | -1.79 | -0.01 | 1.50 | 0.00 |

[a)] average distance between hydrogen atoms and surface in Å
[b)] surface coverage
[c)] difference from reference[276]

**Table** 20. Hydrogen adsorption energy in FH site and its geometry with respect to Co(111) surface along with values reported elsewhere.

| **FH site** | **Adsorption energy** | | **Geometry[a)]** | |
|---|---|---|---|---|
| θ [b)] (ML) | $\Delta E_{ads}$ (eV) | $\Delta\Delta E_{ads}$ [c)] (eV) | Z [a)] (Å) | $\Delta Z$ [c)] (Å) |
| 0.25 | -3.76 | +0.04 | 0.95 | +0.02 |
| 0.50 | -4.22 | +0.03 | 0.93 | 0.00 |
| 0.75 | -4.63 | +0.03 | 0.90 | 0.00 |
| 1.00 | -4.99 | +0.02 | 0.91 | 0.00 |

[a)] the average distance between hydrogen atoms and surface in Å
[b)] surface coverage
[c)] difference from reference [276]

**Table** 21. Hydrogen adsorption energy in HH site and its geometry with respect to Co(111) surface along with values reported elsewhere.

| HH site | Adsorption energy | | Geometry[a)] | |
|---|---|---|---|---|
| θ [b)] (ML) | $\Delta E_{ads}$ (eV) | $\Delta\Delta E_{ads}$ [c)] (eV) | Z [a)] (Å) | $\Delta Z$ [c)] (Å) |
| 0.25 | -3.74 | +0.03 | 0.99 | -0.02 |
| 0.50 | -4.18 | +0.03 | 0.94 | 0.00 |
| 0.75 | -4.57 | +0.01 | 0.95 | -0.04 |
| 1.00 | -4.92 | +0.01 | 0.91 | 0.00 |

[a)] The average distance between hydrogen atoms and surface in Å
[b)] surface coverage
[c)] difference from reference [276]

From the results presented in the ensemble of **Table 19-Table 21**, we see that regardless the surface coverage of hydrogen $\theta$ and adsorption sites, calculated adsorption energies and geometrical characteristics are very close to referenced data (when recalculated with the formula therein). It should be stressed that results in reference [276] are obtained using somewhat different calculation parameters (PW91 instead of PBE), k-points mesh (9x9x1 instead of 7x7x1), different number of surface layers (5 vs 4), vacuum height (10Å instead of

15 Å) and electron distribution at Fermi level ($\sigma = 0.2$ eV instead of $\sigma = 0.08$ eV). Nonetheless, our results are in almost perfect accordance with the literature.

Inspection of adsorption energies also suggests that adsorption of hydrogen is thermodynamically favored. Besides, hollow sites are seemingly more favored compared to OT sites for every $\theta(H)$ studied here. Geometry differences between those two categories of sites are also present; hydrogen is farther away from the Co (111) surface in OT than in HH and FCC sites. Comparison of data in **Table** 20 and **Table** 21 suggests that FH sites are slightly ($\sim 0.05eV$) more favorable than HH sites for the same surface coverage in accordance with the literature [79]. Since those differences correspond to the average error from DFT energies, we cannot claim that FH sites are more stable than HH. Geometry characteristics of hydrogen on both FH and HH sites are very similar.

Inspired by previously published results for the stability of carbon, [205] not only we considered hydrogen on the surface, but we also studied the adsorption energies at 0 $K$ for hydrogens in the first sublayer. That is to say, we studied the adsorption of hydrogen on the surface, subsurface and mixed surface/subsurface sites. The results of those calculations are presented in **Table** 22 and **Figure** 91.

**Table** 22**.** Hydrogen adsorption energy in different configurations (a-on the surface, b-in the first subsurface).

| System | θ[a)] (ML) | $\Delta E_{ads}$ (eV) | Description |
|---|---|---|---|
| **a**1 | 0.25 | -3.76 | FH |
| **a**2 | 0.50 | -4.27 | FH+HH |
| **a**3 | 0.75 | -4.63 | 3 FH |
| **a**4 | 1.00 | -5.00 | 4 FH |
| **b**1 | 0.25 | -3.00 | FH |
| **b**2 | 0.50 | -2.75 | 2 FH |
| **b**3 | 0.75 | -2.55 | 3 FH |
| **b**4 | 1.00 | -2.38 | 4 FH |
| **a**1**b**1 | 0.50 | -3.53 | **a** -FH; **b**-FH |
| **a**1**b**2 | 0.75 | -3.34 | **a** -FH; **b**-2 FH |
| **a**1**b**3 | 1.00 | -3.18 | **a** -FH; **b**-3 FH |
| **a**2**b**1 | 0.75 | -4.02 | **a** -2 FH; **b**-FH |
| **a**2**b**2 | 1.00 | -3.86 | **a** -2 FH; **b**-2 FH |
| **a**3**b**1 | 1.00 | -4.46 | **a** -3 FH; **b**-FH |

[a)] surface coverage

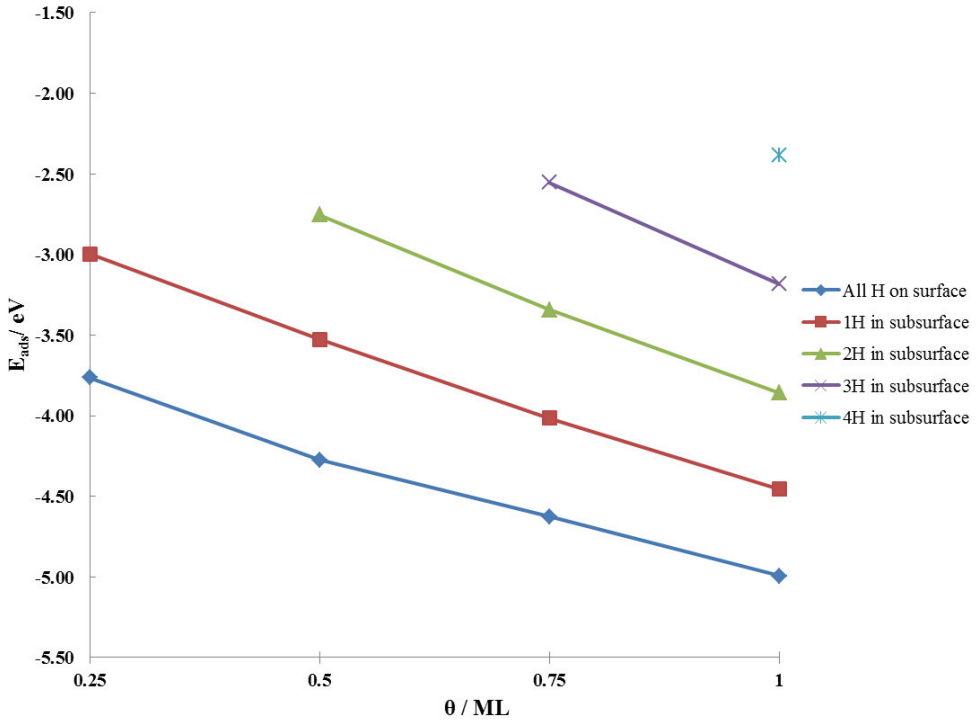


**Figure** 91. Stability of hydrogen in different configurations on the Co(111) surface.

Inspection of numerical data in **Table** 22 and **Figure** 91 leads to the conclusion that all configurations (hydrogen on the surface, in the subsurface and mixed on the surface and in the subsurface) of hydrogen are thermodynamically stable although their relative stabilities vary greatly. According to our results, hydrogen is the most stable when adsorbed on the surface of Co(111) surface and no hydrogen in the subsurface is to be expected. Regardless of the number of hydrogens in the subsurface (0, 1, 2 and 3 per unit cell) we see that its stability rises when increasing the overall surface coverage of hydrogen which can be related to high surface coverages of hydrogen reported in the literature. Increasing the number of hydrogens in the subsurface destabilizes hydrogen. No surface reconstruction phenomenon is induced for any of the structures presented in this study.

In conclusion, hydrogen adsorption energies on Co (111) surface and its geometry agree with data in the literature. Hydrogen has a strong tendency to adsorb on the Co (111)

surface during Fischer-Tropsch reaction conditions as manifested by elevated adsorption energies. In general, hydrogen tends to rest on the surface at FH adsorption sites, although can migrate into a subsurface. Introducing hydrogen in subsurface leads to structures that are visibly less stable, and therefore we do not expect to find it adsorbed on those sites although they are thermodynamically possible. To the best of our knowledge, there is no stability analysis of hydrogen in the subsurface layer of Co (111). The trends obtained from this stability analysis facilitated us to a great extent, future calculations, as we show below.

### 8.3.2 Adsorption of CO on the Co(111) surface

Carbon monoxide adsorption energies at 0 $K$ are calculated based on (variation of) **Eq.** 89 in 8.3.1 when substitution of appropriate coefficients $x$ and $z$ takes place. Since there are no hydrogens on the surface and since we are studying molecular adsorption of carbon monoxide on the surface according to reference [271], this modified equation obtains the following form:

$$\Delta E_{ads}^{0K} = E_{Co(111)-C_xO_z} - E_{Co(111)} - xCO \qquad \textbf{Eq.}\ 90$$

The calculations concerning adsorption of carbon monoxide on other Co surfaces and in particular for higher surface coverages were also performed. [271,273,331] The results concerning energetics and some geometry characteristics along with a comparison with reference [271] for 0.25 $ML$ in CO adsorption are presented in **Table** 23 for on-top, fcc hollow, hcp hollow and bridge site. In the initial stages of our calculations of the Gibbs free energy of $C_xH_yO_z$ deposition, we considered the possibility of the eventual dipole interactions (the work function jump when going through the slab) in our periodic calculations and here, on the example of $CO$ adsorption, we testes the importance of those interactions. Hence, along with

the results where energies are not corrected to dipole interactions (**Table** 23), we report the same characteristics corrected to dipole interactions in **Table** 24.

**Table** 23. Adsorption energies of 1ML of $CO$ on different surface-specific sites along with differences with respect to reference [271]. Optimizations are performed without using dipole corrections.

| | **Adsorption energy** | | **Geometry**[a)] | |
|---|---|---|---|---|
| Site | $\Delta E_{ads}$ (eV) | $\Delta\Delta E_{ads}$ (eV)[b)] | Z (Å)[a)] | $\Delta$Z (Å)[b)] |
| **BR** | -1.61 | -0.03 | 1.42 | 0.03 |
| **FCC** | -1.65 | -0.05 | 1.37 | 0.00 |
| **HCP** | -1.66 | -0.04 | 1.34 | 0.03 |
| **OT** | -1.65 | -0.05 | 1.75 | -0.01 |

[a)] average distance between carbon atoms and surface in Å

[b)] difference from reference

**Table** 24**.** Adsorption energies of 1ML of $CO$ on different surface-specific sites along with differences with respect to reference [271] Optimizations are performed using dipole corrections.

| | **Adsorption energy** | | **Geometry**[a)] | |
|---|---|---|---|---|
| Site | $\Delta E_{ads}$ (eV) | $\Delta\Delta E_{ads}$ (eV)[b)] | Z (Å)[a)] | $\Delta$Z (Å)[b)] |
| **BR** | -1.60 | -0.04 | 1.46 | -0.01 |
| **FCC** | -1.64 | -0.06 | 1.37 | 0.00 |
| **HCP** | -1.64 | -0.06 | 1.34 | 0.03 |
| **OT** | -1.65 | -0.05 | 1.75 | -0.01 |

[a)] average distance between carbon atoms and surface in Å

[b)] difference from reference

Inspection of results in **Table** 23 suggests that both thermochemical and geometrical characteristics are well reproduced. Pick [271] used somewhat different calculations parameters such as cut-off energy, k-points grid, and included dipole corrections. Hence, differences can be already anticipated. Indeed, deviation concerning adsorption energies at $T = 0\ K$

calculated without dipole corrections are $\sim 0.04\ eV$. Taking into account the relative error of DFT methods, those differences are negligible and, we may say that our calculations are not accurate enough so that we could state with a certainty which surface state is most probably occupied. As far as the literature is concerned, for low surface coverages in $CO$, the on-top site seems to be the most favorable for $Co$ [273]. In addition to the adsorption energies, geometrical characteristic are equally well reproduced with deviations from reference of $\sim 0.02$Å [271]. Analysis of results presented in **Table** 24 implies trivial differences with respect to results where no dipole corrections were considered (**Table** 23). In contrast to reference [271], our results with dipole corrections are slightly worse since deviations in energies and geometries are $\sim 0.05\ eV$ and $\sim 0.02$Å, respectively. Nevertheless, we showed that applying of dipole corrections has a minor influence on the quality of the results obtained for both energies and geometric characteristics. This is the reason why, we do not include dipole corrections when reporting our results in **Chapter 4**. However, those corrections might be more influential especially for the structures (see **Chapter 4**) where C-chains are significantly spread out from the surface and where neighbor images might interact between themselves. To this moment, we did not perform those tests.

## 8.4 Development of the thermodynamic model

The overall chemical equation for the deposition of $C_\alpha H_\beta O_\gamma$ species on Cobalt from a mixture of Fischer-Tropsch typical species (CO, $H_2$, $H_2O$ and mixture of hydrocarbons) is given by this general equation:

$$Co + xCO + yH_2 + zH_2O + \sum_{i=1}^{n} \delta_i * C_iH_{2i+2} \rightarrow Co^* - C_\alpha H_\beta O_\gamma \qquad \textbf{Eq.}\ 91$$

where $x$, $y$, $z$ and $\delta_i$ are the stoichiometric positive or negative coefficients of the corresponding molecular species that can either appear as reactants or products, respectively.

In this section, we present how we calculate the Gibbs free energy change of this equation from first-principles calculations. We first address the problem of the material balance in equation **Eq.** 91 and how to define the stoichiometric coefficients uniquely by using the Anderson-Schulz-Flory (ASF) distribution of products. We then present our methodology to compute the Gibbs free energy change of this reaction.

Theoretical thermochemistry calculations rely on some general assumptions and approximations. Since in equation **Eq.** 91 many chemical species intervene, thermochemical reference states must be carefully chosen and approximations checked for validity in order to ensure the preservation of the energy balance between the consumption of reactants and the formation of products in the overall chemical equation. Following our discussion on the material balance, we firstly present the standard equation for the calculation of $\Delta_r G^{p,T}$. We then present how we compute the absolute chemical potentials involved and how they refer to tabulated data in thermochemistry databases. At this point, we show that, in order to use tabulated experimental data and preserve the energy balance between reactants and products in our model, DFT reference states need to be readjusted; we also show that, despite this

readjustment, our model in consistent with previous calculations in the literature since $\Delta_r G^{p=0\ bar,T=0K} = \Delta_r E_{DFT}^{0K}$.

### 8.4.1 General Equation and Material Balance

If we specify the composition of surface state, we are able in principle to find the set of stoichiometries $(x, y, z, \{\delta_i\})$ (i.e., chemical reactions), that will produce a surface state as specified by $(\alpha, \beta, \gamma)$. Note that there are only 3 known variables in our model (ordered set $(\alpha, \beta, \gamma)$) and that there are $(3 + i)$ unknown variables we wish to determine.

In order to simplify the model reaction given by **Eq.** 91, we will first assume that the paraffin mixture (whose composition in **Eq.** 91 is defined by stoichiometric coefficient $\delta_i$ for each molecule of paraffin $P_i$ ($P_i \equiv C_i H_{2(i+1)}$)) obeys the ASF distribution, i.e. $x_i^{ASF} = \alpha_{ASF}^{(i-1)}(1 - \alpha_{ASF})$. For the mole fraction we can also write $x_i = \frac{\delta_i}{\sum_{i=1}^{n} \delta_i} = \frac{\delta_i}{n_{tot}} \Rightarrow \delta_i = x_i n_{tot}$ where $n_{tot}$ is the total amount of hydrocarbons formed and $x_i$ the mole fraction of hydrocarbon $i$. Thus, we reduced the number of unknown variables to four $(x, y, z, n_{tot})$. If we perform now the material balance in terms of carbon, oxygen and hydrogen in the **Eq.** 91 we can obtain the following relations between the surface state as specified by $(\alpha, \beta, \gamma)$ and the set of stoichiometries $(x, y, z, \{\delta_i\})$:

$$\begin{cases} \alpha = x + \sum_{i=1}^{n} \delta_i i \\ \beta = 2\left(y + z + \sum_{i=1}^{n} \delta_i * (i+1)\right) \\ \gamma = x + z \end{cases} \quad \textbf{Eq. 92}$$

From the definition of the mole fractions given above, the following equivalencies can be obtained:

$$\begin{cases} \alpha = x + \sum_{i=1}^{n} \delta_i i \\ \beta = 2\left(y + z + \sum_{i=1}^{n} \delta_i * (i+1)\right) \\ \gamma = x + z \end{cases} \Leftrightarrow \begin{cases} \alpha = x + n_{tot} \sum_{i=1}^{n} x_i^{ASF} i \\ \beta = 2\left(y + z + n_{tot}\left(\sum_{i=1}^{n} x_i^{ASF} i + 1\right)\right) \\ \gamma = x + z \end{cases} \quad \textbf{Eq.}\ 93$$

If we now exploit the fact that $\sum_i \left(x_i^{ASF} * i\right) = (1 - \alpha_{ASF})^{-1}$ for $|\alpha| < 1$, **Eq.** 93 can be simplified:

$$\begin{cases} \alpha = x + \dfrac{n_{tot}}{(1 - \alpha_{ASF})} \\ \beta = 2\left(y + z + n_{tot}\left(\dfrac{2 - \alpha_{ASF}}{1 - \alpha_{ASF}}\right)\right) \\ \gamma = x + z \end{cases} \quad \textbf{Eq.}\ 94$$

Note that in **Eq.** 94, the composition of the surface state is given by the carbon that may come from a CO molecule or a paraffin, hydrogen that comes from a hydrogen molecule, water or a paraffin and oxygen that can be deposed from CO or water molecules. Note also that we reduced the problem of finding $(i + 3)$ unknown variables, to the problem of finding four variables (stoichiometric coefficients $(x, y, z, n_{tot})$[9]) by imposing the ASF distribution of hydrocarbons. Still, the system of equations is mathematically undetermined considering that the number of know variables (3) is smaller than the number of unknown variables (4). Moreover, the fact that the system is undetermined is exactly what allows us to study different chemical pathways for the deposition of carbon, hydrogen and oxygen on the surface. In other words, by defining $n_{tot}$ we determine the chemical transformations that take place on the surface (see example below). Thus, **Eq.** 91 is transformed to:

$$Co + xCO + yH_2 + zH_2O + n_{tot} \sum_{i=1}^{n} x_i^{ASF} * C_i H_{2i+2} \rightarrow Co^* - C_\alpha H_\beta O_\gamma \quad \textbf{Eq.}\ 95$$

[9] We consider $\alpha_{ASF}$ as a known variable (i.e. a fixed parameter).

and the solutions of our material balance equations are given by:

$$(x, y, z, n_{tot}) = \left( \left( \alpha - \frac{n_{tot}}{(1 - \alpha_{ASF})} \right), \left( \frac{\beta}{2} - \gamma + \alpha - n_{tot} \left( \frac{3 - \alpha_{ASF}}{1 - \alpha_{ASF}} \right) \right), \left( \gamma - \alpha + \frac{n_{tot}}{(1 - \alpha_{ASF})} \right), n_{tot} \right) \quad \textbf{Eq. 96}$$

**Example:** Formation of the surface state $\{Co^* - C_1O_2H_1 + 3Co^* - H\}$ at methanazing conditions $\alpha_{ASF} \to 0$.

The composition of the surface state is:

$$\alpha = 1, \beta = 4, \gamma = 2$$

However, to specify the chemical reaction, we need to specify $n_{tot}$ as discussed previously. Thus, we could choose not to decompose hydrocarbons at all, in that case $n_{tot} = 0$ and the stoichiometric equation is:

$$(x, y, z, n_{tot}) = \big((1 - 0), (2 - 2 + 1 - 3 * 0), (2 - 1 + 0), 0\big) \Leftrightarrow (x, y, z, n_{tot}) = (1,1,1,0)$$

$$4 * + CO + H_2 + H_2O \to \{Co^* - C_1O_2H_1 + 3Co^* - H\} \quad \textbf{Eq. 97}$$

We could also choose to deposit both carbon and oxygen from a CO molecule in the presence of gas-phase hydrocarbon molecules, $n_{tot} = \alpha - \gamma = -1$:

$$(x, y, z, n_{tot}) = (2,4,0, -1)$$

$$4 * + 2CO + 4H_2 \to \{Co^* - C_1O_2H_1 + 3Co^* - H\} + CH_4 \quad \textbf{Eq. 98}$$

Note also that reaction **Eq.** 98 is both mathematically and chemically related to **Eq.** 97. By subtracting **Eq.** 97 from **Eq.** 98 we obtain the FTS reaction in the gas phase:

$$CO + 3H_2 \to CH_4 + H_2O \quad \textbf{Eq. 99}$$

Thus, the equations of our material balance allow us to study the adsorption and desorption processes on the surface of a catalyst involved the FTS reaction. Moreover, from the chemical point of view, reactions given by **Eq.** 97 and **Eq.** 98 are different and, as discussed in the main text, we are interested in those chemical pathways that lead to minimal Gibbs free energy of reaction for a given surface state. In our previous works[191,205], this mathematical equivalency was achieved by breaking the overall FTS reaction into a two steps Born-Haber cycle. In this work, we chose to use an equivalent approach by computing the general **Eq.** 91 in order to systematically sample all possible surface states and chemical pathways.

### 8.4.2 Gibbs free energy change of deposition step

The Gibbs free energy of species involved in **Eq.** 95 is computed as follows:

$$\Delta_r G^{p,T} = \frac{1}{N_{Co}^{Co(111)}}\left( G_{Co-C_\alpha H_\beta O_\gamma} - G_{Co_{(111)}} - xG_{CO_{(g)}} - yG_{H_{2(g)}} - zG_{H_2O_{(g)}} - n_{tot}\sum_{i=1}^{n} x_i^{ASF} G_{P_{i(g)}} \right) \quad \textbf{Eq. 100}$$

where $G_i$ are the Gibbs free energy of gas and solid-phases.

The Gibbs free energy of gas-phase species is defined as:

$$\begin{aligned} G_i(p,T) &= H_i^{0K} + \Delta_{0K\to T} h_i(T,p_i) - TS_i^{\circ}(T) \\ &= H_i^{0K} + \Delta_{0K\to T} h_i^{\circ}(T,p^{\circ}) - TS_i^{\circ}(T) + RT\ \ln\frac{p_i}{p^{\circ}} \end{aligned} \quad \textbf{Eq. 101}$$

where $H_i^{0K}$ represents total ZPE-corrected electronic energy in the framework of DFT, $\Delta_{0K\to T} h_i^{\circ}$ is thermal correction to the enthalpy at given temperature $T$ relatively to 0 K and obtained from experimental data bases at $p^{\circ}$[263,264], $p_i$ is the partial pressure of the gas-phase specie $i$ whereas $p^{\circ}$ represents the standard pressure which is taken to be 1 bar, $R$ is the

universal gas constant, and $S_i^{\circ}(T)$ represents the standard entropy of the species $i$ at the given temperature also obtained from experimental databases[264,263].

The Gibbs free energy of surface and surface/adsorbate species is defined as:

$$G_i(p,T) = H_i^{0K} + \Delta_{0K\to T} g_i \qquad \textbf{Eq.}\ 102$$

where $H_i^{0K}$ represents total ZPE-corrected electronic energy in the framework of DFT at 0K, $\Delta_{0K\to T} g_i$ is the change of the free energy from 0K to T which corresponds to finite temperature and pressure effects in solids which are sometimes neglected in DFT calculations at T<1500K and p<100 atm [332–335]. In reference[332] authors studied the validity of this approximation with reactions involving face-centered cubic Ni. Hence, in this work we consider that the same approximations are valid to face-centered cubic Co.

So equation **Eq.** 100 becomes:

$$\begin{aligned}\Delta_r G^{p,T} = \frac{1}{N_{Co}^{Co(111)}}\Bigg( & H_{Co-C_\alpha H_\beta O_\gamma} - H_{Co_{(111)}} - xH_{CO_{(g)}} - yH_{H_{2(g)}} \\ & - zH_{H_2O_{(g)}} - n_{tot}\sum_{i=1}^{n} x_i^{ASF} H_{P_{i(g)}} \\ & - T\Bigg( S^{\circ}_{Co-C_\alpha H_\beta O_\gamma}(T) - S^{\circ}_{Co}(T) - xS^{\circ}_{CO_{(g)}}(T) \\ & - yS^{\circ}_{H_{2(g)}}(T) - zS^{\circ}_{H_2O_{(g)}}(T) - n_{tot}\sum_{i=1}^{n} x_i^{ASF} S^{\circ}_{P_{i(g)}}(T)\Bigg) \\ & - RT\ \ln\left(p_{CO}^{x} p_{H_2}^{y} p_{H_2O}^{z} \prod_{i=1}^{n} p_{P_i}^{n_{tot}x_i^{ASF}}\right)\Bigg)\end{aligned} \qquad \textbf{Eq.}\ 103$$

For the sake of clarity, we assume that the pressure reference state is 1 bar. Moreover, assuming for the solid phase that

$$\Delta_{0K\to T} g_{Co-C_\alpha H_\beta O_\gamma} - \Delta_{0K\to T} g_{Co(111)}$$
$$= \Delta_{0K\to T} h_{Co-C_\alpha H_\beta O_\gamma} - \Delta_{0K\to T} h_{Co(111)}$$
$$- T\left(S^{\circ}_{Co-C_\alpha H_\beta O_\gamma}(T) - S^{\circ}_{Co(111)}(T)\right) \sim 0 \qquad \textbf{Eq.}\ 104$$

we deduce that

$$\Delta_r G^{p,T} = \frac{1}{N_{Co}^{Co(111)}}\Bigg[\Delta_r H^{0K} - x\Delta_{0K\to T} h^{\circ}_{CO_{(g)}} - y\Delta_{0K\to T} h^{\circ}_{H_{2(g)}}$$
$$- z\Delta_{0K\to T} h^{\circ}_{H_2O_{(g)}} - n_{tot}\sum_{i=1}^{n} x_i^{ASF}\Delta_{0K\to T} h^{\circ}_{P_{i(g)}}$$
$$+ T\Bigg(xS^{\circ}_{CO_{(g)}}(T) + yS^{\circ}_{H_{2(g)}}(T) + zS^{\circ}_{H_2O_{(g)}}(T) \qquad \textbf{Eq.}\ 105$$
$$+ n_{tot}\sum_{i=1}^{n} x_i^{ASF} S^{\circ}_{P_{i(g)}}(T)$$
$$- R\ \ln\left(p_{CO}^{x} p_{H_2}^{y} p_{H_2O}^{z}\prod_{i=1}^{n} p_{P_i}^{n_{tot}x_i^{ASF}}\right)\Bigg)\Bigg]$$

where

$$\Delta_r H_{th}^{0K} = \frac{1}{N_{Co}^{Co(111)}}\Bigg(H_{Co-C_\alpha H_\beta O_\gamma}^{0K,th} - H_{Co_{(111)}}^{0K,th} - xH_{CO}^{0K,th} - yH_{H_2}^{0K,th}$$
$$- zH_{H_2O}^{0K,th} - n_{tot}\sum_{i=1}^{n} x_i^{ASF} H_{P_i}^{0K,th}\Bigg) \qquad \textbf{Eq.}\ 106$$

In **Eq.** 106 $H_i^{0K,th}$ are the enthalpies of the various components of the system: gas phase molecules and solid-phases, calculated in the framework of DFT at 0K. The application

of this equation would require the computation of the absolute enthalpy of a large series of $P_i$=$C_iH_{2i+2}$ molecules (with i as large as 50 in our numerical applications), which is both unpractical and inaccurate at the DFT level. Experimental thermodynamic databases can be used to circumvent this problem provided that a careful choice is made of the reference states so that energy consistency is preserved between experimental and theoretical calculations.

### 8.4.3 Reference states definition and use of experimental databases

Since absolute energies are not experimentally available, the enthalpy change of a chemical reaction can be computed from tabulated data using formation enthalpy of the involved species. By definition, the heat released (or adsorbed) in the chemical transformation is defined as:

$$\Delta_r H = \sum_i^n \nu_i \Delta_f H_i(ref.j) \qquad \textbf{Eq.}\ 107$$

where $\nu_i$ are the stoichiometric coefficients in the reaction of interest and $\Delta_f H_i(ref.j)$ are the formation enthalpies calculated relatively to chosen references $j$'s. Applied to chemical reaction given by **Eq.** 95, **Eq.** 107 at $T = 0K$ becomes:

$$\Delta_r H^{0K} = \frac{1}{N_{Co}^{Co(111)}}\left(\Delta_f H_{Co-C_\alpha H_\beta O_\gamma}^{0K} - \Delta_f H_{Co_{(111)}}^{0K} - x\Delta_f H_{CO}^{0K} - y\Delta_f H_{H_2}^{0K} - z\Delta_f H_{H_2O}^{0K} - n_{tot}\sum_{i=1}^{n} x_i^{ASF}\Delta_f H_{P_i}^{0K}\right) \qquad \textbf{Eq.}\ 108$$

**Eq.** 108 is equivalent to equation **Eq.** 103 if all formation enthalpies in the former equation are computed with standard reference states consistent with absolute enthalpies in

the latter equation. In experimental databases, for the species considered in this work, that is $C_{(s)}, H_{2_{(g)}}, O_{2_{(g)}}$ and $Co_{(s)}$. Moreover, in our previous publications we showed that, in order to ensure the compatibility between DFT and experimental thermodynamic values, the reference energy of $O_{2_{(g)}}$ at the theoretical level needs to be readjusted [1] and the reference state for C be that of $C_{(g)}$ [2]. Therefore, equations **Eq.** 107 and **Eq.** 108 become (note that the reference state for bulk Co cancels out):

$$\begin{aligned}\Delta_r H^{0K} &= \frac{1}{N_{Co}^{Co(111)}} \sum_i^n \nu_i \Delta_f H_i^{0K}{}_i(ref.j) \\ &= \frac{1}{N_{Co}^{Co(111)}} \Bigg( H_{Co-C_\alpha H_\beta O_\gamma}^{0K} - H_{Co_{(111)}}^{0K} - \alpha H_{C_{(g)}}^{0K} - \frac{\beta}{2} H_{H_2}^{0K} \\ &\quad - \frac{\gamma}{2} H_{O_2}^{0K} - x\Delta_f H_{CO}^{0K}(refC_{(g)}) - y\Delta_f H_{H_2}^{0K} - z\Delta_f H_{H_2O}^{0K} \\ &\quad - n_{tot} \sum_{i=1}^n x_i^{ASF} \Delta_f H_{P_i}^{0K}(refC_{(g)}) \Bigg)\end{aligned} \qquad \textbf{Eq.}\ 109$$

In what follows, we assume that all formation enthalpies of C containing species are referenced to $C_{(g)}$ and that all enthalpies are calculated at 0K to alleviate the text.

### 8.4.4 Computation of $\Delta_r H^{0K}$ by using both experimental and theoretical data

Below we demonstrate that we can compute equation **Eq.** 106 with experimental tabulated formation enthalpies for CO, $H_2$, $H_2O$ and the paraffins and still approximate $\Delta_r E_{DFT}^{0K}$ to $\Delta_r H^{0K}$ (as it is currently done in most theoretical publications) if $H_{C_{(g)}}^{0K}, H_{H_2}^{0K}$ and $H_{O_2}^{0K}$ are carefully chosen to ensure compatibility between experimental and DFT calculations.

Firstly, we consider that $H_{Co-C_\alpha H_\beta O_\gamma}^{0K} - H_{Co_{(111)}}^{0K} - \alpha H_{C_{(g)}}^{0K} - \frac{\beta}{2} H_{H_2}^{0K} - \frac{\gamma}{2} H_{O_2}^{0K}$ in **Eq.** 109 will be calculated by DFT: $H_{Co-C_\alpha H_\beta O_\gamma}^{th} - H_{Co_{(111)}}^{0K,th} - \alpha H_C^{0K,th} - \frac{\beta}{2} H_{H_2}^{0K,th} - \frac{\gamma}{2} H_{O_2}^{0K,th}$ .

Secondly, we use the experimental formation enthalpies for CO, $H_2$, $H_2O$ and the paraffins. Thirdly, we add and subtract theoretical absolute enthalpies of gas-phase species $\pm xH_{CO}^{th}$, $\pm yH_{H_2}^{th}$, $\pm zH_{H_2O}^{th}$, $\pm n_{tot}\sum_{i=1}^{n} x_i^{ASF} H_{P_i}^{th}$ to **Eq.** 109 so that the expression remains intact:

$$\begin{aligned}\Delta_r H^{0K} = \frac{1}{N_{Co}^{Co(111)}}\Bigg( & H_{Co-C_\alpha H_\beta O_\gamma}^{th} - H_{Co_{(111)}}^{th} - \alpha H_C^{th} - \frac{\beta}{2} H_{H_2}^{th} - \frac{\gamma}{2} H_{O_2}^{th} \\ & - xH_{CO}^{th} - yH_{H_2}^{th} - zH_{H_2O}^{th} - n_{tot}\sum_{i=1}^{n} x_i^{ASF} H_{P_i}^{th}\Bigg) \\ & - x\left(H_{CO}^{exp} - H_C^{exp} - \frac{1}{2} H_{O_2}^{exp} - H_{CO}^{th}\right) \\ & - y\left(H_{H_2}^{exp} - H_{H_2}^{exp} - H_{H_2}^{th}\right) \\ & - z\left(H_{H_2O}^{exp} - H_{H_2}^{exp} - \frac{1}{2} H_{O_2}^{exp} - H_{H_2O}^{th}\right) \\ & - n_{tot}\sum_{i=1}^{n} x_i^{ASF}\left(H_{P_i}^{exp} - iH_C^{exp} - (i+1)H_{H_2}^{exp} - H_{P_i}^{th}\right)\end{aligned} \qquad \textbf{Eq.}\ 110$$

In **Eq.** 110 we exploit **Eq.** 94 in order to replace $\alpha$, $\beta$ and $\gamma$ and we obtain:

$$\Delta_r H^{0K} = \frac{1}{N_{Co}^{Co(111)}}\Bigg(H_{Co-C_\alpha H_\beta O_\gamma}^{th} - H_{Co_{(111)}}^{th} - xH_{CO}^{th} - yH_{H_2}^{th} - zH_{H_2O}^{th} - n_{tot}\sum_{i=1}^{n} x_i^{ASF} H_{P_i}^{th}\Bigg) - x\left(H_{CO}^{exp} - H_{CO}^{th} + H_C^{th} - H_C^{exp} + \frac{1}{2}H_{O_2}^{th} - \frac{1}{2}H_{O_2}^{exp}\right) - y\left(H_{H_2}^{exp} - H_{H_2}^{exp}\right) - z\left(H_{H_2O}^{exp} - H_{H_2O}^{th} - H_{H_2}^{exp} + H_{H_2}^{th} - \frac{1}{2}H_{O_2}^{exp} + \frac{1}{2}H_{O_2}^{th}\right) - n_{tot}\sum_{i=1}^{n} x_i^{ASF}\left(H_{P_i}^{exp} - H_{P_i}^{th} - iH_C^{exp} + iH_C^{th} - (i+1)H_{H_2}^{exp} + (i+1)H_{H_2}^{th}\right)$$

**Eq.** 111

$$\Delta_r H^{0K} = \frac{1}{N_{Co}^{Co(111)}}\Bigg(\Delta_r H_{th}^{0K} - x\left(\Delta_f H_{CO}^{exp} - \Delta_f H_{CO}^{th}\right) - y\left(\Delta_f H_{H_2}^{exp}\right) - z\left(\Delta_f H_{H_2O}^{exp} - \Delta_f H_{H_2O}^{th}\right) - n_{tot}\sum_{i=1}^{n} x_i^{ASF}\left(\Delta_f H_{P_i}^{exp} - \Delta_f H_{P_i}^{th}\right)\Bigg)$$

**Eq.** 112

Where

$$\Delta_r H_{th}^{0K} = H_{Co-C_\alpha H_\beta O_\gamma}^{th} - H_{Co_{(111)}}^{th} - xH_{CO}^{th} - yH_{H_2}^{th} - zH_{H_2O}^{th} - n_{tot}\sum_{i=1}^{n} x_i^{ASF} H_{P_i}^{th} = \Delta_r E_{DFT}^{0K} + \Delta ZPE_i^{th}$$

**Eq.** 113

Where

$$\Delta_r E_{DFT}^{0K} = E_{Co-C_\alpha H_\beta O_\gamma}^{th} - E_{Co_{(111)}}^{th} - xE_{CO}^{th} - yE_{H_2}^{th} - zE_{H_2O}^{th} - n_{tot}\sum_{i=1}^{n} x_i^{ASF} E_{P_i}^{th}$$

**Eq.** 114

And

$$\Delta ZPE_i^{th} = ZPE_{Co-C_\alpha H_\beta O_\gamma}^{th} - ZPE_{Co_{(111)}}^{th} - xZPE_{CO}^{th} - yZPE_{H_2}^{th} - zZPE_{H_2O}^{th} - n_{tot}\sum_{i=1}^{n} x_i^{ASF} ZPE_{P_i}^{th} \quad \textbf{Eq.}\ 115$$

Thus, **Eq.** 112 specifies correction terms to be applied to the theoretical reaction enthalpy $\Delta_r H^{0K}$ so that there is compatibility between DFT and experimental energies.

In this work, we chose to readjust the theoretical energies for the reference states of C, $H_2$ and $O_2$ so that the experimental and theoretical formation enthalpies in **Eq.** 112 cancel out. Thus, we have the following system of linearly independent equations:

$$\begin{cases} \Delta_f H_{CO}^{exp} = H_{CO}^{th} - H_C^{th*} - \frac{1}{2}H_{O_2}^{th*} \\ \Delta_f H_{H_2O}^{exp} = H_{H_2O}^{th} - H_{H_2}^{th*} - \frac{1}{2}H_{O_2}^{th*} \\ \Delta_f H_{CH_4}^{exp} = H_{CH_4}^{th} - H_C^{th*} - 2H_{H_2}^{th*} \end{cases} \quad \textbf{Eq.}\ 116$$

Moreover, we also assume that the difference between DFT and experimental values for, on the one hand, zero-point energies and, on the other hand, absolute enthalpies for CO, $H_2$ and $O_2$ molecules to be negligible (mind that the $ZPE_C$ of gas-phase C is 0). Thus, we have 3 equations and 3 unknowns (marked in red): $H_C^{th*}$, $H_{H_2}^{th*}$ and $H_{O_2}^{th*}$ which can be determined. The numerical results are reported in **Table** 25.

**Table** 25**.** Thermodynamic properties of selected species determined with DFT, from experiments and after correction of the theoretical reference values (th*) to be compatible with experiments.

| **Species** | $E_i$/ eV | $ZPE_i^{th}$/ eV | $H_i^{0K,th}$/ eV | $\Delta_f H_i^{0K,th}$/ eV | $\Delta_f H_{i,}^{0K,exp}$/ eV | $H_i^{0K,th*}$ **/ eV** | $\Delta_f H_{i,th}^{0K,th*}$ / eV |
|---|---|---|---|---|---|---|---|
| $CO_{(g)}$ | -14.79 | 0.13 | -14.66 | -8.46 | -8.55 | -14.66 | -8.55 |
| $H_{2(g)}$ | -6.76 | 0.27 | -6.49 | 0 | 0 | -6.61 | 0 |
| $O_{2(g)}$ | -9.84 | 0.09 | -9.75 | 0 | 0 | -9.13 | 0 |
| $H_2O_{(g)}$ | -14.22 | 0.57 | -13.65 | -2.29 | -2.48 | -13.65 | -2.48 |
| $CH_{4(g)}$ | -24.03 | 1.20 | -22.83 | -8.54 | -8.06 | -22.83 | -8.06 |
| $C_{(g)}$ | -1.32 | 0 | -1.32 | 0 | 0 | -1.54 | 0 |

Coming back to equation **Eq.** 109, and assuming that $\Delta ZPE_i^{th} \sim 0$,

$$\Delta_r H^{0K} = \frac{1}{N_{Co}^{Co(111)}}\left(E_{Co-C_\alpha H_\beta O_\gamma} - E_{Co_{(111)}} - \alpha H_{C_{(g)}}^{0K,th*} - \frac{\beta}{2} H_{H_2}^{0K,th*} - \frac{\gamma}{2} H_{O_2}^{0K,th*} - x\left[\Delta_f H_{CO}^{exp} - ZPE_{CO}\right] - y\left[\Delta_f H_{H_2}^{exp} - ZPE_{H_2}\right] - z\left[\Delta_f H_{H_2O}^{exp} - ZPE_{H_2O}\right] - n_{tot}\sum_{i=1}^{n} x_i^{ASF}\left[\Delta_f H_{P_i}^{exp} - ZPE_{Pi}\right]\right) \quad \textbf{Eq.}\ 117$$

Note that $H_{i_{(g)}}^{0K,th*}$ correspond to the corrected reference values resulting from the resolution of **Eq.** 116, and reported in **Table 26**.

Finally, we use theoretical enthalpy of reaction given by **Eq.** 117 in equation **Eq.** 105 to determine the Gibbs free energy of the deposition of C, H, and O species on the surface.

### 8.4.5 Formation enthalpies of paraffins

The goal of this section is to show how we determine the formation energies of paraffins in equation **Eq.** 117.

The application of our thermodynamic model needs thermochemistry data for a large number of paraffins, most of whom are either unfeasible at the DFT level or unavailable from experimental data. We found data[264] up to $C_{10}$. Thus, we decided to determine formation

enthalpies by a linear interpolation based on the first 7 members of a homologous series of alkanes (methane to heptane). Linearly interpolated $C_8$-$C_{10}$ hydrocarbons (**Table** 26) formation enthalpies based on values of $C_1$-$C_7$ are given by

$$\Delta_f H^{0K}_{P_{i(g),DFT}}\left(ref.C_{(g)}\right) = -7.9221 * i - 0.5957,$$

$$\Delta_f H^{0K}_{P_{i(g),exp}}\left(ref.C_{(g)}\right) = -7.5164 * i - 0.4643,$$

and $\Delta_f H^{0K}_{P_{i(g),corr.}}\left(ref.C_{(g)}\right) = -7.5766 * i - 0.4664$

for theoretical, experimental and corrected using the approach in the previous section, respectively. In all approaches, the linear model (formation enthalpies versus carbon number) explains all the variability of the response data around its mean ($R^2 \approx 1$) which is rather good but still not a very surprising result since the molecules belong to the same homologous series (of alkanes) with $CH_2$ group additivity as expected. The enthalpies of formation obtained (up to decane) are presented in **Table** 26**.**

**Table** 26**.** Theoretical (DFT), experimental and corrected DFT enthalpies of formation of hydrocarbons (eV) for first ten members of the homologous series of alkanes.

| $i$/ $C_iH_{2i+2(g)}$ | $\Delta_f H_i^{0K,th}$ a,b | $\Delta_f H_i^{0K,exp}$ a | $\Delta_f H_i^{0K,th*}$ a,b |
|---|---|---|---|
| 1 | -8.54 | -8.06 | -8.06 |
| 2 | -16.41 | -15.45 | -15.59 |
| 3 | -24.36 | -22.97 | -23.20 |
| 4 | -32.29 | -30.51 | -30.78 |
| 5 | -40.21 | -38.04 | -38.35 |
| 6 | -48.13 | -45.57 | -45.93 |
| 7 | -56.05 | -53.11 | -53.50 |
| 8 | -63.97[c)] | -60.64 (-60.63) [c] | -61.08 |
| 9 | -71.89 [c] | -68.17 (-68.16) [c] | -68.66 |
| 10 | -79.82 [c] | -75.71 (-75.68) [c] | -76.23 |

a) In eV; carbon reference is C(g).

b) ZPE corrected.

c) Obtained based on the linear interpolation.

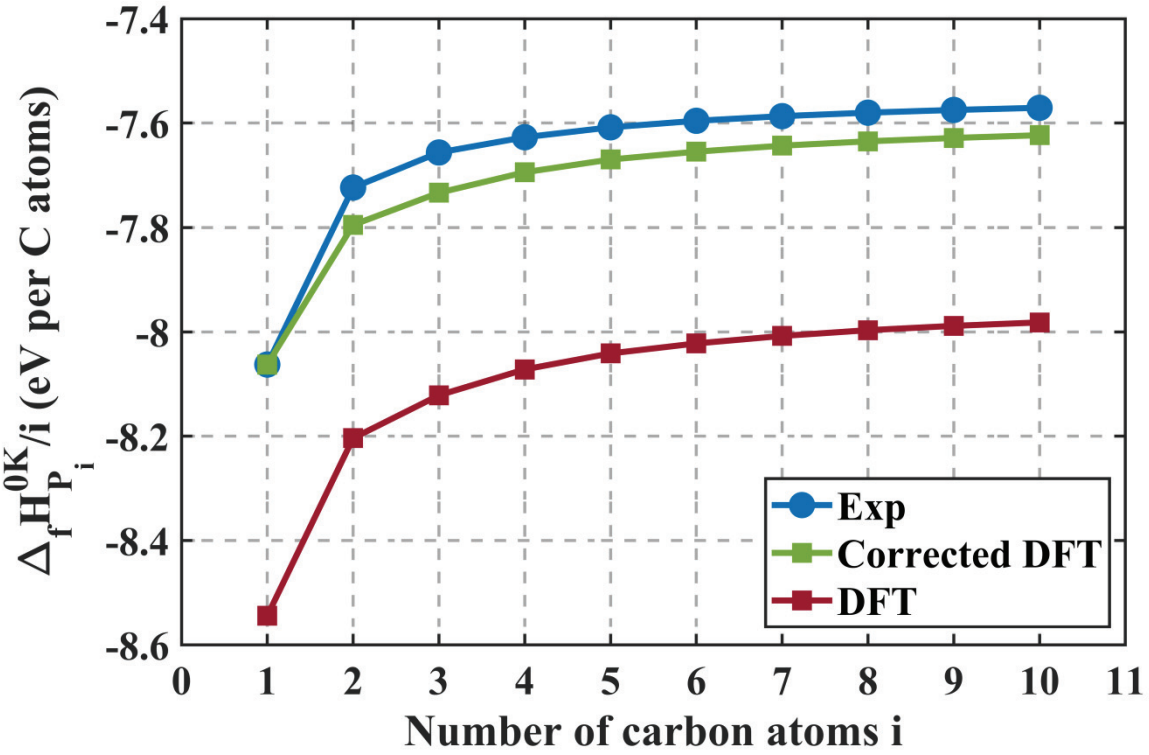


**Figure** 92. Formation enthalpies (per number of C atoms) at $\boldsymbol{T = 0K}$ of various hydrocarbons up to decane based on ZPE-corrected DFT electronic energies (red squares), experimental data bases (blue circles) and corrected DFT approach (green squares).

From formation enthalpies presented in **Table** 26 and **Figure** 92, it is clear that DFT calculations at the PBE level overestimate the $\Delta_f H^{0K}$ of hydrocarbons (The error is $> 0.1$ eV per Co surface atom). The theoretical origins of this discrepancy (PBE functional performance, dispersion corrections…) are beyond the scope of this work. Considering this, we argue that the safest approach is to exploit experimental databases in order to obtain corrected formation energies of all species at $T = 0K$ as described in **Section** 8.4.4**.** More importantly, this approach will allow us to use experimental formation enthalpies of longer paraffins (as large as $C_{50}$) in a consistent manner with DFT calculations of C, H, O surface deposition.

### 8.4.6 Evaluation of the Fischer-Tropsch reaction enthalpy

The advantage related to the accuracy of this corrected DFT/experimental approach over purely DFT approach can also be seen if we now calculate the enthalpy of the FT reaction (i.e., **Eq.** 91 for $\alpha = \beta = \gamma = 0 \ \wedge \ n_{tot} < 0$ in **Eq.** 96):

$$(x, y, z, n_{tot}) = \left( \left( \alpha - \frac{n_{tot}}{(1 - \alpha_{ASF})} \right), \left( \frac{\beta}{2} - \gamma + \alpha - n_{tot} \left( \frac{3 - \alpha_{ASF}}{1 - \alpha_{ASF}} \right) \right), \left( \gamma - \alpha + \frac{n_{tot}}{(1 - \alpha_{ASF})} \right), n_{tot} \right) = \quad \textbf{Eq.} \ 118$$
$$= \left( -\frac{n_{tot}}{1 - \alpha_{ASF}}, -n_{tot} \frac{3 - \alpha_{ASF}}{1 - \alpha_{ASF}}, \frac{n_{tot}}{1 - \alpha_{ASF}}, n_{tot} \right) =$$
$$= \left( 1, (3 - \alpha_{ASF}), 1, (1 - \alpha_{ASF}) \right)$$

Note that division with $-\frac{n_{tot}}{1-\alpha_{ASF}}$ we performed in **Eq.** 118 means that the calculated Gibbs free energies of reaction are *per mole* of hydrocarbon mixture produced. The Fischer-Tropsch synthesis reaction given by **Eq.** 118 is the reaction we presented in **Chapter** 4 (**Eq.** 66).

Hence, **Eq.** 91 becomes the Fischer-Tropsch synthesis reaction:

$$CO + (3 - \alpha_{ASF}) H_2 \rightarrow H_2O + (1 - \alpha_{ASF}) \sum_{i=1}^{n} x_i^{ASF} P_i \qquad \textbf{Eq.} \ 119$$

If DFT formation enthalpies are used, $\Delta_f H_{i,DFT}^{0K}$, the enthalpy of reaction **Eq.** 119 at $T = 0K$ is calculated as:

$$\Delta_r H_{DFT}^{0K} = H_{H_2O}^{th} + (1 - \alpha^{ASF}) \sum_{i=1}^{n} x_i^{ASF} H_{P_i}^{th} - H_{CO}^{th} - (3 - \alpha^{ASF}) H_{H_2}^{th} \qquad \textbf{Eq.} \ 120$$

where $H_i^{th}$ are ZPE-corrected electronic energies of gas-phase species involved. However, if experimental formation (and corrected theoretical $\Delta_f H_i^{0K,th*}$ ) enthalpies are used, $\Delta_f H_i^{0K,exp}$, the enthalpy of reaction **Eq.** 119 at $T = 0K$ is calculated as:

$$\Delta_r H^{0K} = \Delta_f H^{0K}_{H_2O} + (1 - \alpha^{ASF}) \sum_{i=1}^{n} x_i^{ASF} \Delta_f H^{0K}_{P_i} - \Delta_f H^{0K}_{CO} - (3 - \alpha^{ASF}) \Delta_f H^{0K}_{H_2} \quad \textbf{Eq. 121}$$

where $\Delta_f H_i^{0K}$ are experimental (or corrected theoretical) formation enthalpies at $T = 0K$.

The combined result of those calculations is given in **Figure** 93 and as shown by Masuku [265], the Gibbs free energies of reaction are minimized for $\alpha_{ASF} \longrightarrow 0$.

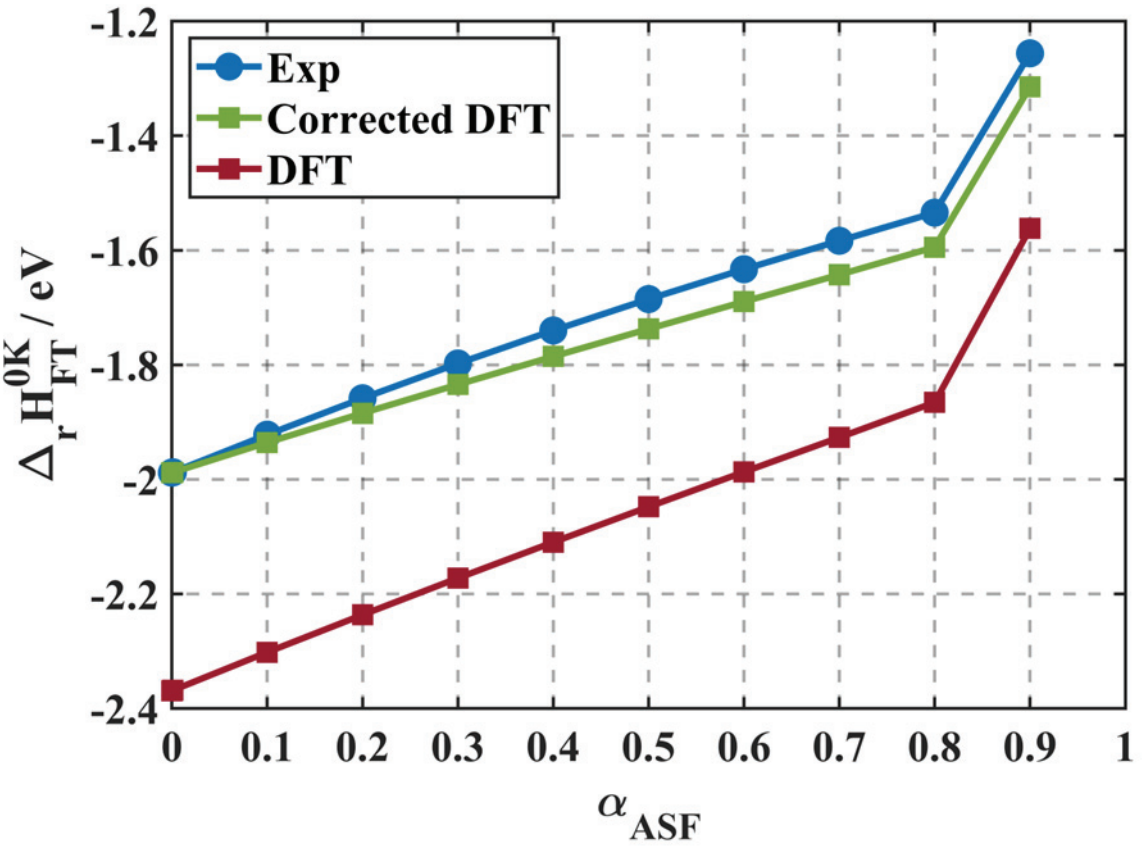


**Figure** 93. The enthalpy of the FTS reaction **Eq.** 119 for $\boldsymbol{T = 0K}$ for different chain-growth coefficients $\boldsymbol{\alpha_{ASF}}$ based on purely DFT **Eq.** 120 (red squares), experimental (blue circles). and corrected theoretical (green squares) approach **Eq.** 121.

Calculations presented in **Figure** 92 and **Figure** 93 clearly show the interest in using experimental formation energies rather than purely theoretical ones. Although the deviations

of purely DFT calculations over experimental are somewhat systematic and around 0.40 eV, the inability to calculate all hydrocarbon molecules in the framework of DFT and the greater error of this approach is the reason why we exploit experimental formation enthalpies of all gas-phase species over purely DFT ones. Moreover, for both approaches in **Figure** 93 there is a deviation from linearity as $\alpha_{ASF} \to 1$. This is the consequence of using a limited number of hydrocarbons (here we used $n = 50$ hydrocarbon molecules in **Eq.** 119 and **Eq.** 120 for calculating $\Delta_r H_{FT}^{0K}$ which further implies the small amount of hydrocarbons that is "missing" from the material balance and thus calculated $\Delta_r H_{FT}^{0K}$ is more positive than the real one[10]. This error is less than -0.05 eV/ Co surface atoms for $\alpha_{ASF} = 0.9$ and is thus negligible. However, we should keep in mind that this numerical error underestimates ($\Delta_r H_{FT}^{0K}$ are more positive) the reaction energies when hydrocarbons are produced and overestimates ($\Delta_r H_{FT}^{0K}$ are more negative) the reaction energies when hydrocarbons are reactants.

In conclusion, the advantage of this combined theoretical/experimental approach is two-fold, on the one hand, it avoids the computation of a large number of hydrocarbon molecules involved in the framework of DFT, and on the other hand, it allows improvements in the accuracy of calculated $\Delta_r H^{0K}$ while enssuring that both theoretical and experimental sources are consistent. Hence, in this work, all deposition energies are described using experimental databases leading to approximated $\Delta_r G^{p,T}$ and $\Delta_r H^{0K}$ respectivly, as described in **Section 8.4.3**

[10] i.e. It is mathematically impossible to impose: the approximate ASF distribution $x_i^{ASF}$ , the condition $\sum_i x_i = 1$ and to work on limited set of hydrocarbons at the same time. Thus, in our mathematical model, we sacrificed the condition $\sum_i x_i = 1$ at the expense of respecting the ASF distribution with a limited set of hydrocarbons.

## 8.5 Complementary results regarding the structures of some carbonaceous species

### 8.5.1 Effect of co-adsorbed hydrogen on carbon deposition and surface reconstruction

We investigate here the impact of co-adsorbed hydrogen on the stability of carbon species (particularly carbide species) as previously reported to be formed in the Co(111) subsurface [205]. Calculated deposition Gibbs free energies of $C_\alpha H_\beta$ species for FT conditions refer to the most stable ways of deposition (see below) and are presented in **Figure** 94 for surface coverages of carbon up to 2 ML and of hydrogen up to 1 ML. As in the previous work[205], we investigate the possible migration of C surface atoms into subsurface positions in **Figure** 94-**Figure** 95 and **Table** 27.

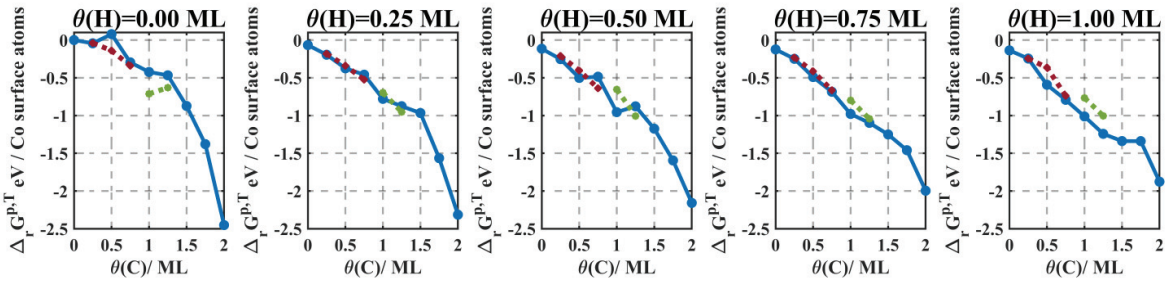


**Figure** 94. Gibbs free energy of deposition reaction at T=500 K and $\alpha_{ASF} = 0.90$ of $C_\alpha$ species (see reference[205]) and $C_\alpha H_\beta$ species for increasing surface coverages of hydrogen. Blue line: all C ontop of the Co(111); for red and green lines 0.25 ML and 0.5 ML C are in subsurface positions, respectively.

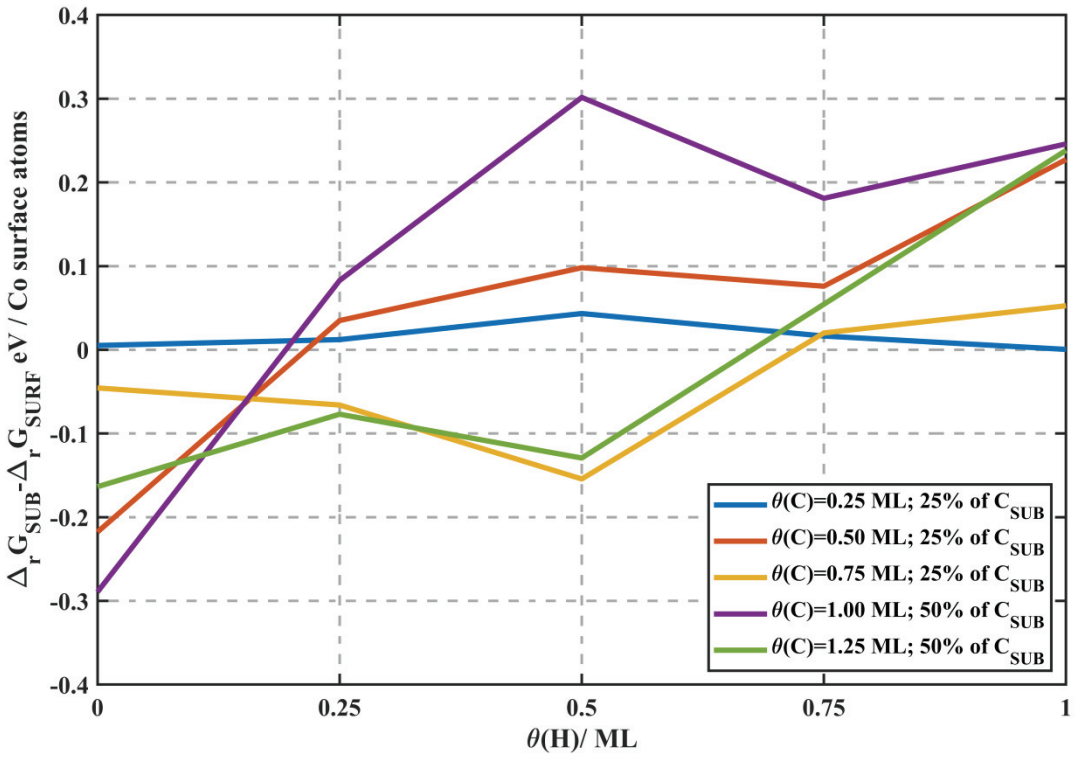


**Figure** 95. Carbon migration $\Delta_{surf \rightarrow sub}(\Delta_r G)$ energy as a function of hydrogen coverage for 0.25 ML ≤ θ(C) ≤ 1.25 ML.

**Figure** 94 reveals a general monotonic decrease in the deposition energy when increasing carbon surface content at constant $\theta(H)$. In addition, Gibbs free deposition energies lie approximately in the same range (between approximately 0 and -2.5 eV) for all surface coverages of hydrogen studied here.

**Figure** 95 shows that hydrogen co-adsorption, stabilizes carbon species for $\theta(C) \leq 1.25\, ML$, but to a lesser extent when some carbon atoms are in subsurface positions. However, for high H coverages, co-adsorption of hydrogen substantially decreases the stability of subsurface carbon atoms (**Table** 27).

As a consequence, the gap between the energy curve for carbon atoms on the surface and the energy curve where some carbon atoms are in subsurface narrows and eventually structures with all carbon atoms on the surface become the most stable ones (**Figure** 94). Apparently, for low surface coverages of hydrogen ($\theta(H) \leq 0.50\, ML$) and intermediate

coverages of carbon ( $0.50 \leq \theta(C) \leq 1.25\ ML$ ), the effect of Co-C bond strength maximization prevails. In this C coverage range, up to 50 % of C atoms can be found in subsurface giving rise to Co-C bond maximization and surface reconstruction phenomena with a nonplanar arrangement of surface Co atoms (**Table** 27 and **Figure** 97**-Figure** 98. In order to attain the surface reconstruction phenomenon reported previously[223,87], the diffusion of carbon from the surface towards sub-the surface layer is necessary. According to previous DFT calculations on Co(111)[279], the activation barrier of this migration step is around 0.74 eV and thus facile. Irrespectively of the location of C adsorption sites, hydrogen atoms are mainly co-adsorbed on the C surface atoms (**Figure** 96).

**Table** 27. Percentage of subsurface C for different surface coverages of carbon and hydrogen.

| θ(H) / ML \ θ(C) / ML | 0.00 | 0.25 | 0.50 | 0.75 | 1.00 | 1.25 | 1.50 | 1.75 | 2.00 |
|---|---|---|---|---|---|---|---|---|---|
| 0.00 | 0 | 0 | 25 | 25 | 50* | 40* | 0 | 0 | 0 |
| 0.25 | 0 | 0 | 0 | 25 | 0 | 40* | 0 | 0 | 0 |
| 0.50 | 0 | 0 | 0 | 25 | 0 | 40* | 0 | 0 | 0 |
| 0.75 | 0 | 0 | 0 | 0 | 0 | 0 | 0 | 0 | 0 |
| 1.00 | 0 | 0 | 0 | 0 | 0 | 0 | 0 | 0 | 0 |

*) Surface reconstruction observed

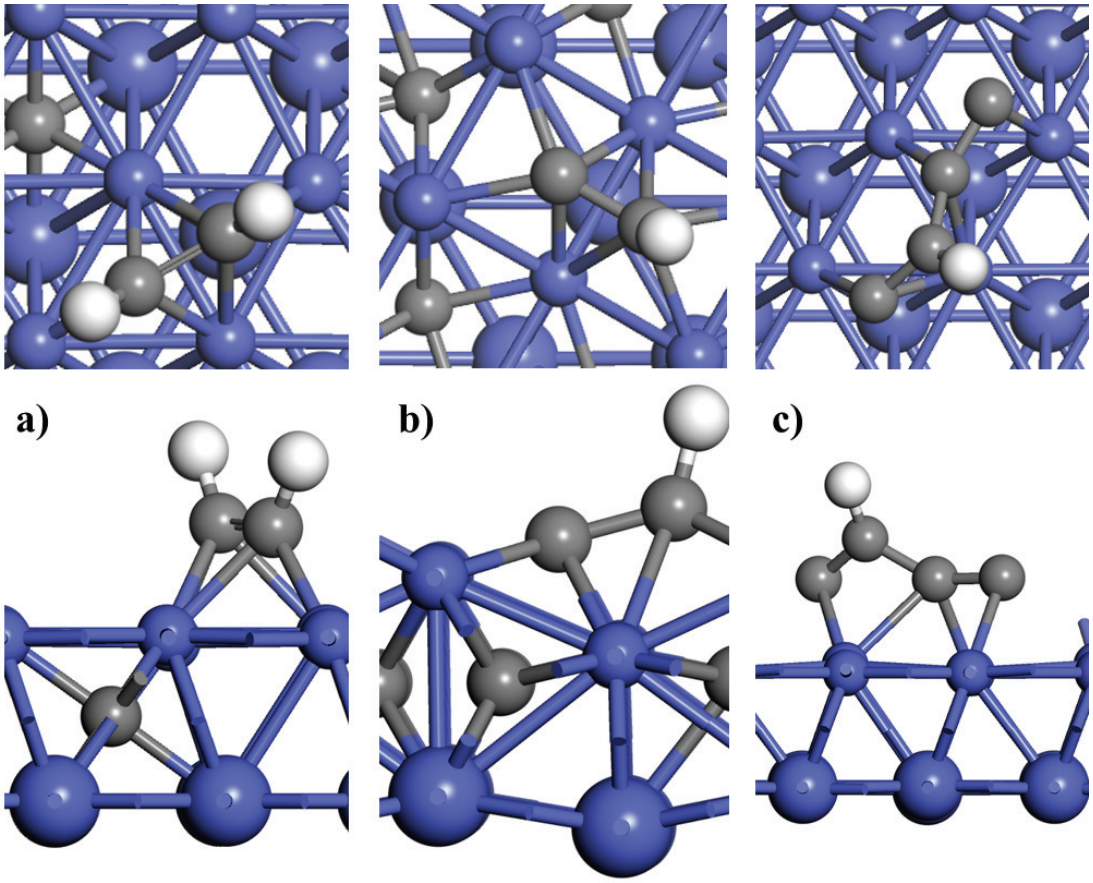


**Figure** 96. On top (top) and side (bottom) view of some $C_\alpha H_\beta$ systems a) $\theta(C) = 0.75, \theta(H) = 0.5\ ML$ b),c) $\theta(C) = 1.00, \theta(H) = 0.25\ ML$ with (b) and without (a and c) surface reconstruction.

High hydrogen coverages ($\theta(H) \geq 0.75$ ML) thermodynamically inhibit subsurface migration and therefore circumvent the surface reconstruction phenomena (**Figure** 98 and **Table** 27). In this case, C-C and C-H bonds are formed preferentially. In this domain, co-adsorption of hydrogen leads to the formation of $CH_\beta$ species as presented in the main text. As a consequence, the surface reconstruction with formation of less active Co-carbide occurs mainly at low surface hydrogen coverages and for intermediate carbon coverages, which could therefore be related to one type of deactivation phenomenon reported for hydrogen deficient conditions[195,155].

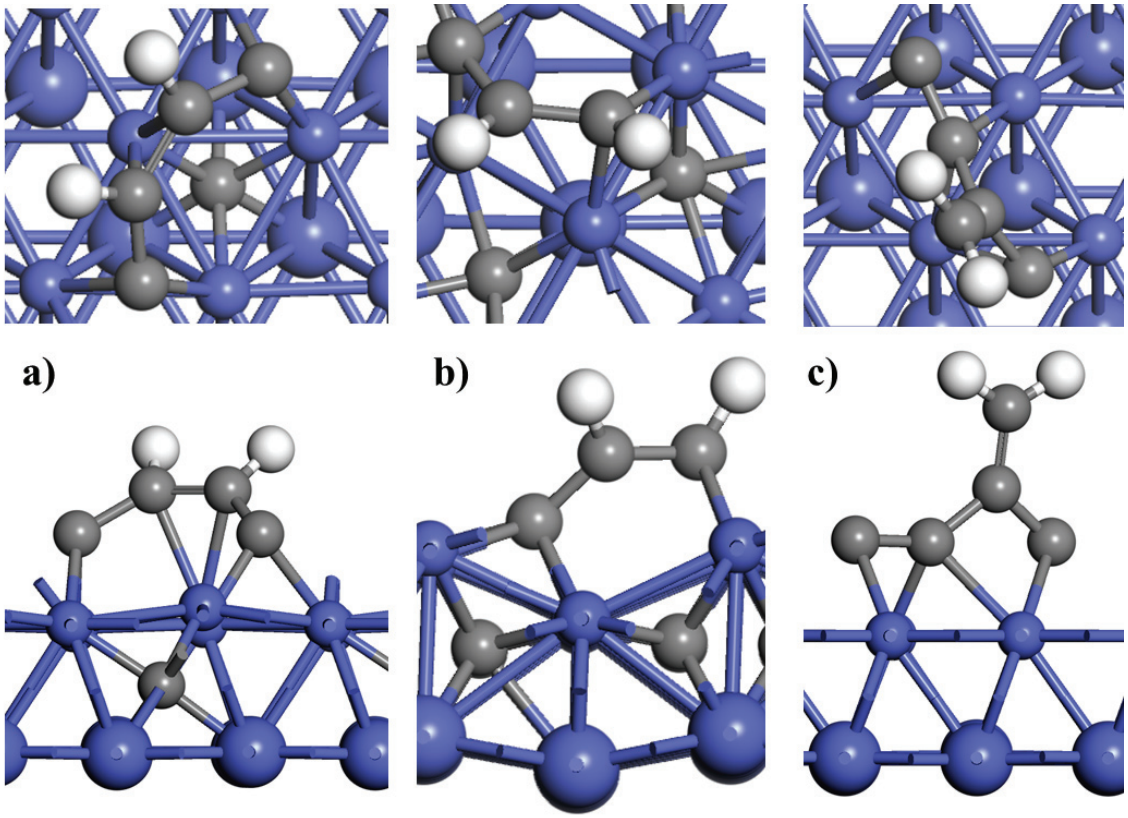


**Figure** 97. On top (top) and side (bottom) view of some $C_\alpha H_\beta$ systems for $\theta(H) = 0.5\ ML$, $\theta(C) = 1.25$ ML of which a) 0.25 ML and b) 0.50 ML C atoms are in subsurface giving rise to severe surface reconstruction and c) 0.00 ML $C_{SUB}$. Stability increases in the order c) (-0.87 eV/Co) a) (-0.94 eV/Co) b) (-1.01eV/Co).

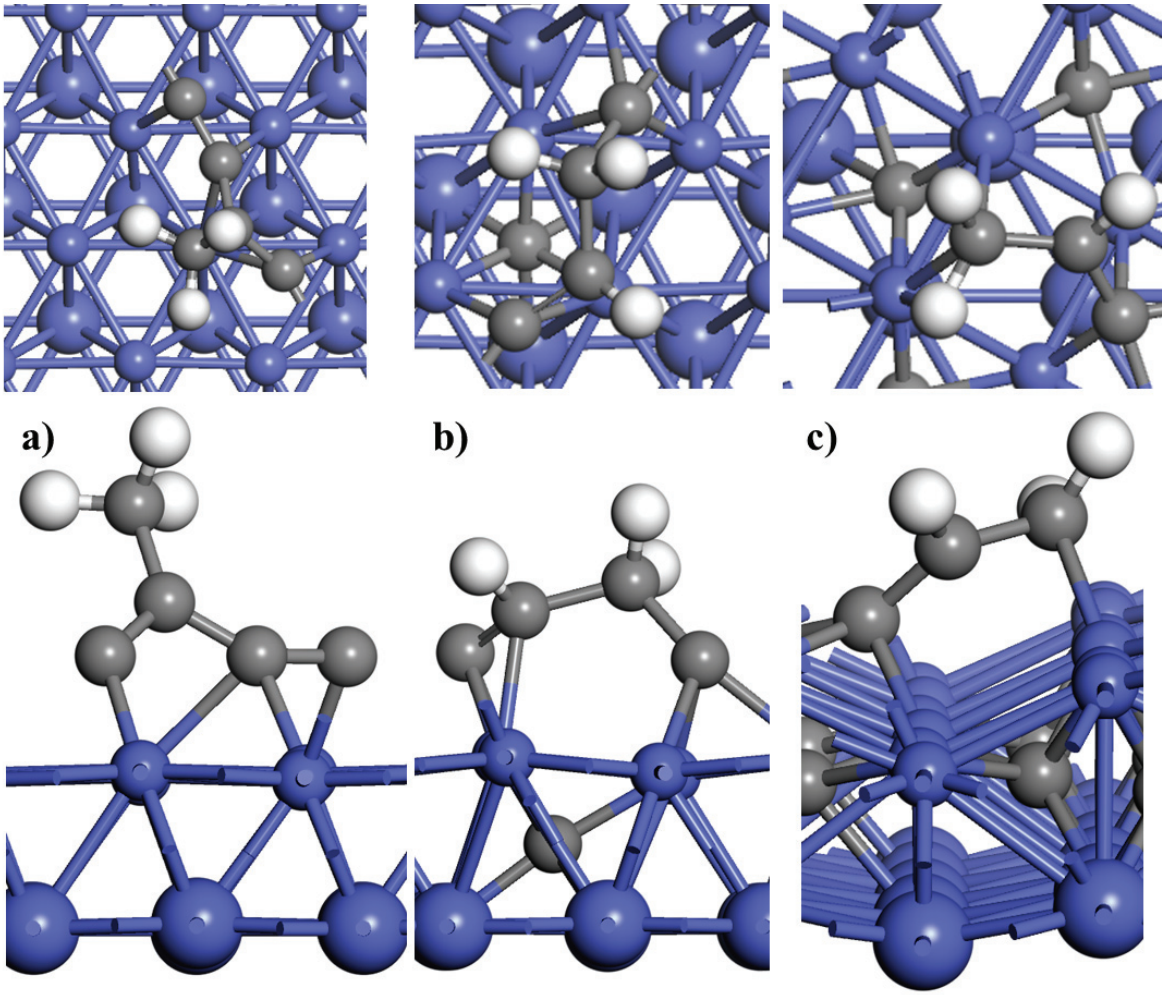


**Figure** 98. On top (top) and side (bottom) view of some $C_\alpha H_\beta$ systems for $\theta(H) = 0.75\ ML$, $\theta(C) = 1.25$ ML of which a) 0.00 b) 0.25 and c) 0.50 ML are in $C_{SUB}$ positions giving rise to severe surface reconstruction. Stability increases in the order b) (-0.96 eV/Co) c) (-1.01 eV/Co) a) (-1.24 eV/Co).

### 8.5.2 Stability of aromatic C species at θ(C)=2.00 ML in the presence of hydrogen

As illustrated in **Figure** 99, carbon rings present on the surface of Co at $\theta(C) = 2.00$ and $\theta(H) = 0\ ML$ exhibit mean C-C distances of 1.44 Å corresponding to highly stable aromatic $C = C$ bonds ($\Delta_r G^{p,T} = -2.45$ eV/Co surface atoms). Hence, hydrogen addition to $\theta(H) = 0.25\ ML$ elongates $C - C$ bonds (to approximately 1.51 Å) around the carbon atom to which hydrogen is attached, breaks the aromatic structure of carbon ring and destabilizes the system ($\Delta_r G^{p,T} = -2.31$ eV/Co surface atoms). Further deposition in hydrogen towards $\theta(H) = 0.50, 0.75$ and $1\ ML$ results in destabilization of carbon ring $-2.16, -2.00$ and

$-1.88$ eV/Co surface atoms, respectively ($\alpha = 0.90$, $T = 500\ K$, $P = 20$ bar, $H_2$/CO=2). For comparison, the Gibbs free energy of carbon ring-like structure with one hydrogen molecule in the gas phase is $\Delta_r G^{p,T} = -2.30$ eV/Co surface atoms (compared to $-2.16$ when two hydrogen atoms are on the surface). Therefore, we can consider those carbon structures as hydrogen-resistant ones.

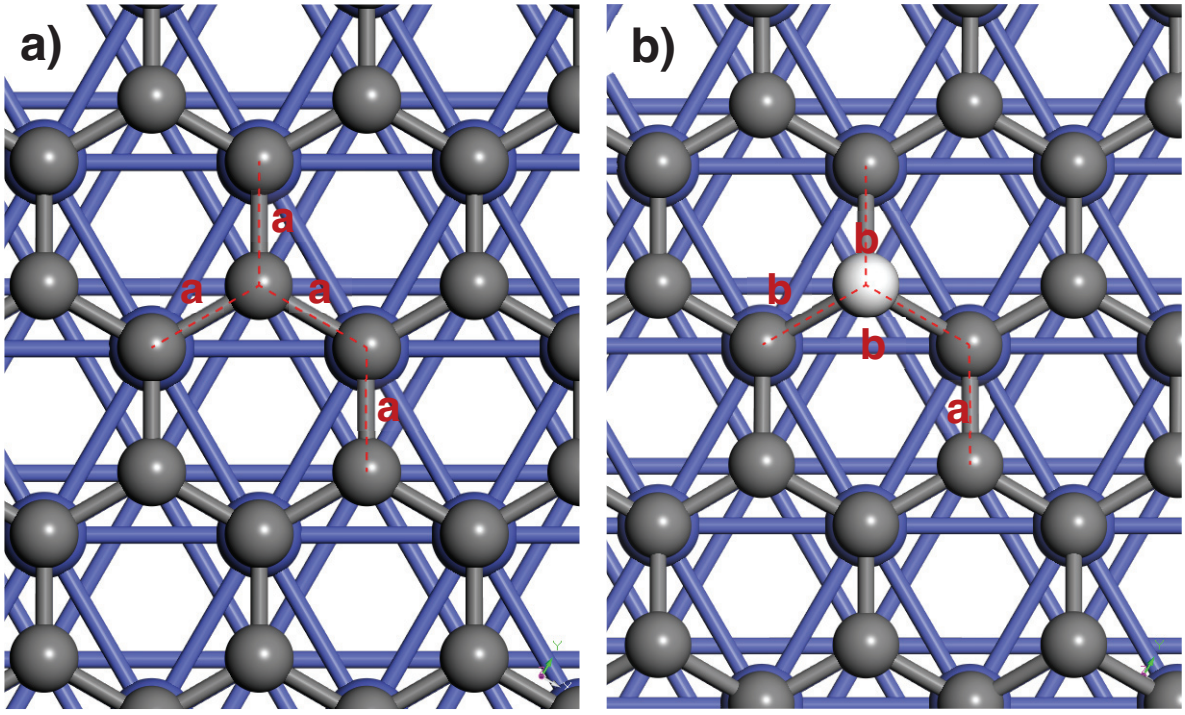


**Figure** 99. Influence of hydrogen b) on the geometry of carbonaceous structures for $\theta(C) = 2.00\ ML$ presented in a). Hydrogen addition of $\theta(H) = 0.25\ ML$ ($\Delta_r G^{p,T} = -2.31$ eV/Co surface atoms) destabilizes the structure at $\theta(C) = 2.00\ ML$ ($\Delta_r G^{p,T} = -2.45$ eV/Co surface atoms), by breaking the aromatic structure of the ring presented in a) as seen from $C - C$ distances (distance a-$d_{C-C} \approx 1.44$ Å; distance b-$d_{C-C} \approx 1.51$ Å). The carbon atom (not seen in **Figure**) below hydrogen in b) is above the plane defined by three other carbon atoms. ($\boldsymbol{\alpha = 0.90, T = 500\ K}$, $P = 20$ bar, $H_2$/CO=2).

## 8.6 Complementary oxygenated hydrocarbons

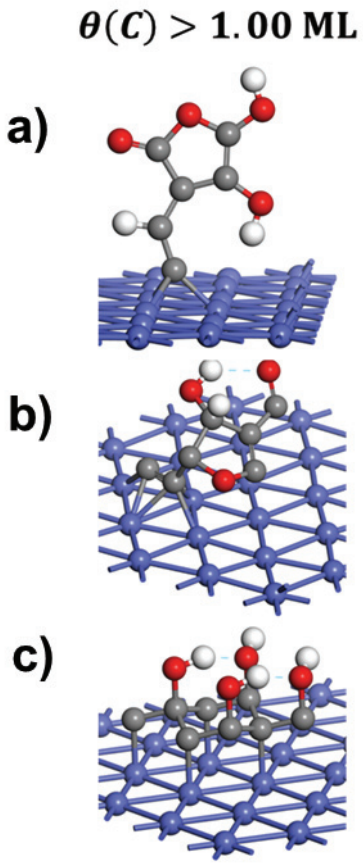


**Figure** 100. Structure of some oxygenated hydrocarbon structures for high surface coverages of carbon presented in **Figure** 35 of the manuscript a) $\theta(C) = 1.25$, $\theta(O) = 1\ ML$, $\theta(H) = 0.75$ ML b) $\theta(C) = 1.50$, $\theta(O) = 0.75\ ML$, $\theta(H) = 0.50$ ML c) $\theta(C) = 2.00$, $\theta(O) = 1$ , $\theta(H) = 1$ ML.

## 8.7 Key chemical reactions leading to $C_\alpha H_\beta O_\gamma$ deposition

| α | β | γ | Reaction (x,y,z,$n_{tot}$) | $\alpha_{ASF} = 0.9$ $\Delta_r G^{p,T}$ | $\Delta_r H^{1bar,0K}$ |
|---|---|---|---|---|---|
| 0 | 0 | 1 | $\mathbf{1} * + \mathbf{1}CO + \mathbf{1.1}H_2 \rightarrow \{O_1\}^* + \mathbf{0.1}P_i$ | -0.23 | -0.53 |
| 0 | 1 | 2 | $\mathbf{2} * + \mathbf{2}CO + \mathbf{2.7}H_2 \rightarrow \{O_1\}^* + \{O_1H_1\}^* + \mathbf{0.2}P_i$ | -0.19 | -0.86 |
| 0 | 2 | 3 | $\mathbf{3} * + \mathbf{3}CO + \mathbf{4.3}H_2 \rightarrow \mathbf{2}\{O_1\}^* + \{H_2O\}^* + \mathbf{0.3}P_i$ | -0.39 | -1.42 |
| 0 | 3 | 3 | $\mathbf{3} * + \mathbf{3}CO + \mathbf{4.8}H_2 \rightarrow \{O_1\}^* + \{O_1H_1\}^* + \{H_2O\}^* + \mathbf{0.3}P_i$ | -0.39 | -1.48 |
| 0 | 4 | 4 | $\mathbf{4} * + \mathbf{4}CO + \mathbf{6.4}H_2 \rightarrow \mathbf{2}\{O_1\}^* + \mathbf{2}\{H_2O\}^* + \mathbf{0.4}P_i$ | -0.54 | -2.00 |
| 1 | 0 | 2 | $\mathbf{2} * + \mathbf{2}CO + \mathbf{1.1}H_2 \rightarrow \{C_1O_1\}^* + \{O_1\}^* + \mathbf{0.1}P_i$ | -0.29 | -0.81 |
| 1 | 1 | 3 | $\mathbf{2} * + \mathbf{3}CO + \mathbf{2.7}H_2 \rightarrow \{H_1C_1O_3\}^* + \mathbf{0.2}P_i$ | -0.34 | -1.23 |
| 1 | 2 | 3 | $\mathbf{2} * + \mathbf{3}CO + \mathbf{3.2}H_2 \rightarrow \{CO\}^* + \{O_1\}^* + \{H_2O\}^* + \mathbf{0.2}P_i$ | -0.46 | -1.41 |
| 1 | 3 | 3 | $\mathbf{3} * + \mathbf{3}CO + \mathbf{3.7}H_2 \rightarrow \{C_1O_1\}^* + \{O_1H_1\}^* + \{H_2O\}^* + \mathbf{0.2}P_i$ | -0.46 | -1.47 |
| 1 | 4 | 3 | $\mathbf{4} * + \mathbf{3}CO + \mathbf{4.2}H_2 \rightarrow \{C_1O_1\}^* + \{H_1\}^* + \{O_1H_1\}^* + \{H_2O\}^* + \mathbf{0.2}P_i$ | -0.37 | -1.44 |
| 2 | 0 | 2 | $\mathbf{2}* + \mathbf{2}CO \rightarrow \mathbf{2}\{C_1O_1\}^*$ | -0.35 | -0.79 |
| 2 | 1 | 1 | $\mathbf{3} * + \mathbf{2}CO + \mathbf{1.5}H_2 \rightarrow \{C_1O_1\}^* + \{H_1\}^* + \{C_1\}_* + \mathbf{0.2}P_i$ | -0.40 | -0.83 |
| 2 | 2 | 0 | $\mathbf{1} * + \mathbf{2}CO + \mathbf{3}H_2 \rightarrow \{C\,CH2\}^* + + \mathbf{2}H_2O$ | -0.50 | -0.91 |
| 2 | 3 | 0 | $\mathbf{2} * + \mathbf{2}CO + \mathbf{3.5}H_2 \rightarrow \{H_3C - C\}^* + + \mathbf{2}H_2O$ | -0.49 | -0.96 |
| 2 | 4 | 0 | $\mathbf{2} * + \mathbf{2}CO + \mathbf{4}H_2 \rightarrow \{H_3C - C\}^* + \{H_1\}^* + \mathbf{2}H_2O$ | -0.59 | -1.13 |

| | | | | | |
|---|---|---|---|---|---|
| 3 | 0 | 2 | $\mathbf{3*+3CO+1H_2 \rightarrow 2\{C_1O_1\}^* + \{C_1\}_* + 1H_2O}$ | -0.51 | -1.09 |
| 3 | 1 | 0 | $\mathbf{2*+3CO+3.5H_2 \rightarrow \{C_2H_1\}^* + \{C_1\}_* + 3H_2O}$ | -0.52 | -1.01 |
| 3 | 2 | 0 | $\mathbf{2*+3CO+4H_2 \rightarrow \{C_2H_2\}^* + \{C_1\}_* + 3H_2O}$ | -0.64 | -1.19 |
| 3 | 3 | 0 | $\mathbf{2*+3CO+4H_2 \rightarrow \{C_2CH_3\}^* + 3H_2O}$ | -0.69 | -1.30 |
| 3 | 4 | 0 | $\mathbf{2*+3CO+4H_2 \rightarrow \{CHCCH_3\}^* + 3H_2O}$ | -0.79 | -1.47 |
| 4 | 0 | 0 | $\mathbf{2*+4CO+4H_2 \rightarrow \{C_2\}^* + \{C_2\}_* + 4H_2O}$ | -0.71 | -1.27 |
| 4 | 1 | 0 | $\mathbf{2*+4CO+4.5H_2 \rightarrow \{C_4H_1\}^* + 4H_2O}$ | -0.78 | -1.40 |
| 4 | 2 | 0 | $\mathbf{2*+4CO+5H_2 \rightarrow \{C_4H_2\}^* + 4H_2O}$ | -0.96 | -1.64 |
| 4 | 3 | 0 | $\mathbf{2*+4CO+5.5H_2 \rightarrow \{C_4H_3\}^* + 4H_2O}$ | -0.98 | -1.73 |
| 4 | 4 | 0 | $\mathbf{2*+4CO+6H_2 \rightarrow \{C_4H_4\}^* + 4H_2O}$ | -1.01 | -1.83 |
| 5 | 0 | 2 | $\mathbf{4*+5CO+3H_2 \rightarrow \{C_1O_1\}^* + \{C_2O_1\}^* + 2\{C_1\}_* + 3H_2O}$ | -0.71 | -1.57 |
| 5 | 1 | 0 | $\mathbf{3*+5CO+5.5H_2 \rightarrow \{C_3H_1\}^* + 2\{C_1\}_* + 5H_2O}$ | -0.95 | -1.72 |
| 5 | 2 | 0 | $\mathbf{3*+5CO+6H_2 \rightarrow \{C_3H_2\}^* + 2\{C_1\}_* + 5H_2O}$ | -1.01 | -1.83 |
| 5 | 3 | 0 | $\mathbf{*+5CO+6.5H_2 \rightarrow \{C_5H_3\}^* + 5H_2O}$ | -1.10 | -1.99 |
| 5 | 4 | 0 | $\mathbf{*+5CO+7H_2 \rightarrow \{C_5H_4\}^* + 5H_2O}$ | -1.24 | -2.20 |
| 6 | 0 | 0 | $\mathbf{*+6CO+6H_2 \rightarrow \{C_6\}^* + 6H_2O}$ | -0.87 | -1.71 |
| 6 | 1 | 0 | $\mathbf{*+6CO+6.5H_2 \rightarrow \{C_6H_1\}^* + 6H_2O}$ | -0.97 | -1.87 |
| 6 | 2 | 0 | $\mathbf{*+6CO+7H_2 \rightarrow \{C_6H_2\}^* + 6H_2O}$ | -1.17 | -2.14 |
| 6 | 3 | 0 | $\mathbf{*+6CO+7.5H_2 \rightarrow \{C_6H_3\}^* + 6H_2O}$ | -1.25 | -2.28 |

| | | | | | |
|---|---|---|---|---|---|
| 6 | 4 | 0 | $*+\mathbf{6}CO+\mathbf{7.5}H_2\rightarrow\{C_6H_4\}^*+\mathbf{6}H_2O$ | -1.34 | -2.43 |
| 7 | 0 | 0 | $*+\mathbf{7}CO+\mathbf{7}H_2\rightarrow\{C_7\}^*+\mathbf{7}H_2O$ | -1.38 | -2.36 |
| 7 | 1 | 0 | $*+\mathbf{7}CO+\mathbf{7}H_2\rightarrow\{C_7H_1\}^*+\mathbf{7}H_2O$ | -1.56 | -2.61 |
| 7 | 2 | 0 | $*+\mathbf{7}CO+\mathbf{7.5}H_2\rightarrow\{C_7H_2\}^*+\mathbf{7}H_2O$ | -1.59 | -2.70 |
| 7 | 3 | 0 | $*+\mathbf{7}CO+\mathbf{8}H_2\rightarrow\{C_7H_3\}^*+\mathbf{7}H_2O$ | -1.46 | -2.63 |
| 7 | 4 | 0 | $*+\mathbf{7}CO+\mathbf{8.5}H_2\rightarrow\{C_7H_4\}^*+\mathbf{7}H_2O$ | -1.34 | -2.57 |
| 8 | 0 | 0 | $*+\mathbf{8}CO+\mathbf{8}H_2\rightarrow\{C_8\}^*+\mathbf{8}H_2O$ | -2.45 | -3.57 |
| 8 | 1 | 0 | $*+\mathbf{8}CO+\mathbf{8.5}H_2\rightarrow\{C_8H_1\}^*+\mathbf{8}H_2O$ | -2.31 | -3.50 |
| 8 | 2 | 0 | $*+\mathbf{8}CO+\mathbf{9}H_2\rightarrow\{C_8H_2\}^*+\mathbf{8}H_2O$ | -2.16 | -3.40 |
| 8 | 3 | 0 | $*+\mathbf{8}CO+\mathbf{9.5}H_2\rightarrow\{C_8H_3\}^*+\mathbf{8}H_2O$ | -2.00 | -3.31 |
| 8 | 4 | 0 | $*+\mathbf{8}CO+\mathbf{10}H_2\rightarrow\{C_8H_4\}^*+\mathbf{8}H_2O$ | -1.88 | -3.25 |

## 8.8 Catalytic tests

In parallel with this thesis, another research is conducted at IFPEN, whose objective is to identify the deactivation and the loss of selectivity mechanisms experimentally [148]. This experimental study elaborates pretreatment and experimental procedures that can be used to simulate the deactivation phenomena, thus provoking the catalyst aging artificially. More specifically, the treatment of the catalyst in the CO, ethylene and hydrothermal atmospheres independently have been used to mimic the formation of Co-carbide, carburization and oxidation phenomenon, respectively, all three of them described in **Chapter 2**. The goal of this study is to study quantitatively the effect of deactivation on the performance of differently deactivated Co-based catalysts as well as a characterization of the catalyst surface.

The evaluation of the catalysts (fresh and pretreated in the potentially deleterious atmospheres) performances was conducted on a commercial High-throughput screening (HTS) unit [336] composed of 16 parallel fixed-bed reactors that allow the acquisition of experimental data in a short time. The complete description of this unit can be found in [148]. For the purpose of the fitting, we have chosen Pt promoted Co-based catalyst used in that work. The performance of this catalyst under various operating conditions is given below and is used to fit the micro-kinetic model described in **Section 2.4**.

| Operating Conditions | | | # Exp | Catalyst Mass (mg) | Catalytic Bed Height (mm) | GHSV (NL/h/g) | Conv. CO (%) | Sel. $CH_4$ (%) | Sel. $C_{5+}$ (%) | Sel. $CO_2$ (%) | $O/P_{C2}$ | $O/P_{C5}$ | $H_2$/CO out |
|---|---|---|---|---|---|---|---|---|---|---|---|---|---|
| **Initial Point** | T (°C) | 220 | 1 | 215 | 66 | 11.10 | 48.49 | 11.42 | 78.7 | 0.18 | 0.08 | 0.70 | 2.12 |
| | P (barg) | 20 | 2 | 165 | 49 | 14.46 | 32.94 | 12.07 | 77.5 | 0.16 | 0.11 | 0.96 | 2.12 |
| | $H_2$/CO in | 2.12 | 3 | 130 | 38 | 18.36 | 27.16 | 12.96 | 76.0 | 0.17 | 0.12 | 1.04 | 2.12 |
| | | | 4 | 100 | 30 | 23.87 | 20.40 | 13.65 | 74.4 | 0.18 | 0.15 | 1.25 | 2.11 |
| **Revaluated Initial Point** | T (°C) | 220 | 5 | 215 | 66 | 6.98 | 70.25 | 10.34 | 80.5 | 0.25 | 0.06 | 0.51 | 2.14 |
| | P (barg) | 20 | 6 | 165 | 49 | 9.09 | 51.07 | 11.00 | 79.3 | 0.18 | 0.07 | 0.69 | 2.11 |
| | $H_2$/CO in | 2.12 | 7 | 130 | 38 | 11.54 | 44.22 | 11.73 | 78.2 | 0.18 | 0.07 | 0.72 | 2.12 |
| | | | 8 | 100 | 30 | 15.00 | 33.25 | 12.55 | 76.7 | 0.18 | 0.09 | 0.88 | 2.12 |
| **High $H_2$/CO** | T (°C) | 220 | 9 | 215 | 66 | 5.80 | 62.20 | 9.17 | 81.9 | 0.26 | 0.08 | 0.77 | 1.39 |
| | P (barg) | 20 | 10 | 165 | 49 | 7.56 | 47.88 | 9.81 | 80.9 | 0.19 | 0.09 | 0.92 | 1.57 |
| | $H_2$/CO in | 1.85 | 11 | 130 | 38 | 9.59 | 40.41 | 10.65 | 79.5 | 0.19 | 0.10 | 0.94 | 1.63 |
| | | | 12 | 100 | 30 | 12.47 | 30.71 | 11.67 | 77.6 | 0.19 | 0.12 | 1.08 | 1.68 |
| **Low $H_2$/CO** | T (°C) | 220 | 13 | 215 | 66 | 8.73 | 70.84 | 12.03 | 78.1 | 0.23 | 0.04 | 0.35 | 3.05 |
| | P (barg) | 20 | 14 | 165 | 49 | 10.30 | 50.22 | 12.64 | 77.0 | 0.16 | 0.06 | 0.54 | 2.66 |
| | $H_2$/CO in | 2.4 | 15 | 130 | 38 | 12.45 | 42.45 | 13.44 | 75.7 | 0.17 | 0.06 | 0.58 | 2.59 |
| | | | 16 | 100 | 30 | 11.06 | 32.01 | 14.30 | 74.1 | 0.17 | 0.08 | 0.74 | 2.52 |
| **High P** | T (°C) | 220 | 17 | 215 | 66 | 4.97 | 60.66 | 11.64 | 78.6 | 0.33 | 0.04 | 0.36 | 2.12 |
| | P (barg) | 10 | 18 | 165 | 49 | 6.47 | 47.63 | 11.97 | 78.0 | 0.28 | 0.05 | 0.46 | 2.10 |
| | $H_2$/CO in | 2.12 | 19 | 130 | 38 | 8.22 | 40.74 | 12.26 | 77.6 | 0.25 | 0.06 | 0.52 | 2.12 |
| | | | 20 | 100 | 30 | 10.69 | 31.88 | 12.76 | 76.5 | 0.25 | 0.07 | 0.68 | 2.11 |
| **Low P** | T (°C) | 220 | 21 | 214 | 67 | 8.09 | 55.81 | 10.73 | 78.4 | 0.11 | 0.11 | 0.92 | 2.11 |
| | P (barg) | 30 | 22 | 158 | 49 | 10.93 | 49.55 | 11.34 | 77.5 | 0.11 | 0.11 | 0.88 | 2.11 |
| | $H_2$/CO in | 2.12 | 23 | 129 | 37 | 13.43 | 37.17 | 12.31 | 76.0 | 0.10 | 0.12 | 1.01 | 2.12 |
| | | | 24 | 98 | 33 | 17.67 | 32.10 | 12.87 | 75.0 | 0.10 | 0.13 | 1.04 | 2.12 |
| **High T** | T (°C) | 210 | 25 | 214 | 67 | 3.93 | 64.08 | 8.61 | 82.7 | 0.13 | 0.10 | 0.89 | 2.15 |
| | P (barg) | 20 | 26 | 158 | 49 | 5.32 | 54.62 | 9.39 | 81.3 | 0.12 | 0.10 | 0.91 | 2.15 |
| | $H_2$/CO in | 2.12 | 27 | 129 | 37 | 6.53 | 40.29 | 10.44 | 79.5 | 0.12 | 0.12 | 1.06 | 2.13 |
| | | | 28 | 98 | 33 | 8.59 | 34.38 | 10.80 | 79.0 | 0.13 | 0.13 | 1.11 | 2.12 |
| **Low T** | T (°C) | 230 | 29 | 214 | 67 | 11.84 | 62.91 | 11.92 | 78.2 | 0.23 | 0.05 | 0.44 | 2.07 |
| | P (barg) | 20 | 30 | 158 | 49 | 16.00 | 60.24 | 12.64 | 77.2 | 0.24 | 0.04 | 0.40 | 2.07 |
| | $H_2$/CO in | 2.12 | 31 | 129 | 37 | 19.65 | 47.22 | 13.13 | 76.4 | 0.19 | 0.05 | 0.51 | 2.10 |
| | | | 32 | 98 | 33 | 25.86 | 44.80 | 13.83 | 75.3 | 0.21 | 0.05 | 0.49 | 2.09 |

**Figure** 101. Co catalyst performance under various conditions.

# 9 References


(1) Davis, B. H.; Occelli, M. L. *Fischer-Tropsch synthesis, catalysts and catalysis*, 1st ed.; Studies in Surface Science and Catalysis 163; Elsevier: Amsterdam, Boston, 2007.
(2) Botes, F. G.; Niemantsverdriet, J. W.; van de Loosdrecht, J. A comparison of cobalt and iron based slurry phase Fischer–Tropsch synthesis. *Catal. Today* **2013**, *215*, 112–120.
(3) Yang, J.; Ma, W.; Chen, D.; Holmen, A.; Davis, B. H. Fischer–Tropsch synthesis. *Appl. Catal., A* **2014**, *470*, 250–260.
(4) Dry, M. E. The Fischer–Tropsch Process. *Catal. Today* **2002**, *71*, 227–241.
(5) Klerk, A. d. *Fischer-Tropsch refining*, 1st. ed.; Wiley-VCH: Weinheim Germany, 2011.
(6) Schulz, H. Short history and present trends of Fischer–Tropsch synthesis. *Appl. Catal., A* **1999**, *186*, 3–12.
(7) Ail, S. S.; Dasappa, S. Biomass to liquid transportation fuel via Fischer Tropsch synthesis – Technology review and current scenario. *Renew. Sustain. Energy Rev.* **2016**, *58*, 267–286.
(8) Dancuart, L. P.; Steynberg, A. P. Fischer-Tropsch Based GTL Technology: A New Process? *Steynberg, Dry (Ed.) 2004 – Stud. Surf. Sci. Catal.*; pp 379–399.
(9) Dry, M. E. Practical and Theoretical Aspects of the Catalytic Fischer-Tropsch Process. *Appl. Catal., A* **1996**, *138*, 319–344.
(10) Leckel, D. Diesel Production from Fischer−Tropsch. *Energy Fuels* **2009**, *23*, 2342–2358.
(11) Basu, P. *Biomass gasification, pyrolysis and torrefaction*. *Practical design and theory;* Academic Press, 2018.
(12) Wang, P.; Massoudi, M. Slag Behavior in Gasifiers. Part I. *Energies* **2013**, *6*, 784–806.
(13) Liu, K.; Song, C.; Subramani, V. *Hydrogen and syngas production and purification technologies;* John Wiley & Sons, 2009.
(14) Rostrup-Nielsen, J. R. Syngas in perspective. *Catal. Today* **2002**, *71*, 243–247.
(15) Aasberg-Petersen, K.; Dybkjær, I.; Ovesen, C. V.; Schjødt, N. C.; Sehested, J.; Thomsen, S. G. Natural gas to synthesis gas – Catalysts and catalytic processes. *J. Nat. Gas. Sci. Eng.* **2011**, *3*, 423–459.
(16) Rostrup-Nielsen, J. R. New aspects of syngas production and use. *Catal. Today* **2000**, *63*, 159–164.
(17) Curry-Hyde, H. E.; Howe, R. F. *Natural gas conversion II* 81; Elsevier, 1994.
(18) *Fischer-Tropsch technology;* Steynberg, A., Dry, M., Eds., 1. ed.; Studies in Surface Science and Catalysis 152; Elsevier: Amsterdam, 2004.
(19) Maitlis, P. M.; Klerk, A. d. *Greener Fischer-Tropsch processes for fuels and feedstocks;* Wiley-VCH: Weinheim, 2013.
(20) Tijmensen, M. J. A.; Faaij, A. P. C.; Hamelinck, C. N.; van Hardeveld, M. R. M. Exploration of the possibilities for production of Fischer Tropsch liquids and power via biomass gasification. *Biomass Bioenergy* **2002**, *23*, 129–152.
(21) Takeshita, T.; Yamaji, K. Important roles of Fischer‐Tropsch synfuels in the global energy future. *Energy Policy* **2008**, *36*, 2773–2784.
(22) Sie, S. T.; Krishna, R. Fundamentals and selection of advanced Fischer–Tropsch reactors. *Appl. Catal., A* **1999**, *186*, 55–70.
(23) Khodakov, A. Y.; Chu, W.; Fongarland, P. Advances in the development of novel cobalt Fischer-Tropsch catalysts for synthesis of long-chain hydrocarbons and clean fuels. *Chem. Rev.* **2007**, *107*, 1692–1744.
(24) Bukur, D. B.; Patel, S. A.; Lang, X. Fixed bed and slurry reactor studies of Fischer-Tropsch synthesis on precipitated iron catalyst. *Appl. Catal.* **1990**, *61*, 329–349.

(25) Majid Sadeqzadeh. Deactivation Modeling of Cobalt Fischer-Tropsch Catalysts in Different Reactor Configurationts; Université Lille 1 - Sciences et Technologies, 2012.
(26) Chambrey, S.; Fongarland, P.; Karaca, H.; Piché, S.; Griboval-Constant, A.; Schweich, D.; Luck, F.; Savin, S.; Khodakov, A. Y. Fischer–Tropsch synthesis in milli-fixed bed reactor. *Catal. Today* **2011**, *171*, 201–206.
(27) Klerk, A. d.; Furimsky, E. *Catalysis in the refining of Fischer-Tropsch syncrude*; RSC catalysis series no. 4; RSC Publishing: Cambridge, 2010.
(28) Davis, B. H. Overview of reactors for liquid phase Fischer–Tropsch synthesis. *Catal. Today* **2002**, *71*, 249–300.
(29) Guettel, R.; Turek, T. Comparison of different reactor types for low temperature Fischer–Tropsch synthesis. *Chem. Eng. Sci.* **2009**, *64*, 955–964.
(30) *Catalysis in C1 Chemistry;* Springer, 1983.
(31) Visconti, C. G.; Tronconi, E.; Lietti, L.; Groppi, G.; Forzatti, P.; Cristiani, C.; Zennaro, R.; Rossini, S. An experimental investigation of Fischer–Tropsch synthesis over washcoated metallic structured supports. *Appl. Catal., A* **2009**, *370*, 93–101.
(32) Lerou, J. J.; Tonkovich, A. L.; Silva, L.; Perry, S.; McDaniel, J. Microchannel reactor architecture enables greener processes. *Chem. Eng. Sci.* **2010**, *65*, 380–385.
(33) Perego, C.; Bortolo, R.; Zennaro, R. Gas to liquids technologies for natural gas reserves valorization. *Catal. Today* **2009**, *142*, 9–16.
(34) VANNICE, M. The catalytic synthesis of hydrocarbons from H2/CO mixtures over the group VIII metals I. The specific activities and product distributions of supported metals. *J. Catal.* **1975**, *37*, 449–461.
(35) van Santen, R. A. *Computational methods in catalysis and materials science*. *An introduction for scientists and engineers;* Wiley-VCH: Weinheim, 2009.
(36) Boyer, C.; Gazarian, J.; Lecocq, V.; Maury, S.; Forret, A.; Schweitzer, J. M.; Souchon, V. Development of the Fischer-Tropsch Process. *Oil Gas Sci. Technol. – Rev. IFP Energies nouvelles* **2016**, *71*, 44.
(37) Ernst, B.; Libs, S.; Chaumette, P.; Kiennemann, A. Preparation and characterization of Fischer–Tropsch active Co/SiO2 catalysts. *Appl. Catal., A* **1999**, *186*, 145–168.
(38) Ernst, B.; Bensaddik, A.; Hilaire, L.; Chaumette, P.; Kiennemann, A. Study on a cobalt silica catalyst during reduction and Fischer–Tropsch reaction. *Catal. Today* **1998**, *39*, 329–341.
(39) Huffman, G. P.; Shah, N.; Zhao, J. M.; Huggins, F. E.; Hoost, T. E.; Halvorsen, S.; Goodwin, J. G. In-Situ XAFS Investigation of K-Promoted Co Catalysts. *J. Catal.* **1995**, *151*, 17–25.
(40) Klugmann, E.; Blythe, H. J.; Walz, F. Investigation of thermomagnetic effects in monocrystalline cobalt near the martensitic phase transition. *Phys. Stat. Sol. (a)* **1994**, *146*, 803–813.
(41) Dehghan, R.; Hansen, T. W.; Wagner, J. B.; Holmen, A.; Rytter, E.; Borg, Ø.; Walmsley, J. C. In-Situ Reduction of Promoted Cobalt Oxide Supported on Alumina by Environmental Transmission Electron Microscopy. *Catal. Lett.* **2011**, *141*, 754.
(42) Liu, J.-X.; Su, H.-Y.; Sun, D.-P.; Zhang, B.-Y.; Li, W.-X. Crystallographic dependence of CO activation on cobalt catalysts. *J. Am. Chem. Soc.* **2013**, *135*, 16284–16287.
(43) Kitakami, O.; Sato, H.; Shimada, Y.; Sato, F.; Tanaka, M. Size effect on the crystal phase of cobalt fine particles. *Phys. Rev. B* **1997**, *56*, 13849–13854.
(44) Bartholomew, C. H. Mechanisms of Catalyst Deactivation. *Appl. Catal., A* **2001**, *212*, 17–60.
(45) Tsakoumis, N. E.; Rønning, M.; Borg, Ø.; Rytter, E.; Holmen, A. Deactivation of Cobalt Based Fischer-Tropsch Catalysts. *Catal. Today* **2010**, *154*, 162–182.

(46) Chaumette, P.; Verdon, C.; Boucot, P. Influence of the hydrocarbons distribution on the heat produced during Fischer-Tropsch synthesis. *Top. Catal.* **1995**, *2*, 301–311.
(47) Adesoji A. Adesina. Hydrocarbon synthesis via Fischer-Tropsch reaction: travails and triumphs. *Appl. Catal., A* **1996**, *138*, 345–367.
(48) Anderson, R. B.; Lee, C. B.; Machiels, J. C. The thermodynamics of the hydrogenation of oxides of carbon. *Can. J. Chem. Eng.* **1976**, *54*, 590–594.
(49) Frohning, C. D.; Kölbel, H.; Ralek, M.; Rottig, W.; Schnur, F.; Schulz, H. Fischer-Tropsch Synthese. *Chemierohstoffe aus kohle (Falbe J., ed.) [Online]* **1977**.
(50) Röper, M. Fischer-Tropsch synthesis. *Catalysis in C1 Chemistry*; Springer, 1983; pp 41–88.
(51) Anderson, R. B.; Kölbel, H.; Rálek, M. *The Fischer-Tropsch synthesis;* Academic Press: Orlando, 1984.
(52) Pichler, H.; Schulz, H. Neuere Erkenntnisse auf dem Gebiet der Synthese von Kohlenwasserstoffen aus CO und H2. *Chemie Ing. Techn.* **1970**, *42*, 1162–1174.
(53) Storch, H. H. *The Fischer-Tropsch and related syntheses*. *Including a summary of theoretical and applied contact catalysis;* Wiley: New York, 1951.
(54) Herington, E.F.G. Fischer-Tropsch synthesis considered as a polymerization reaction. *Chem. Ind. (London) [Online]* **1946**.
(55) Anderson, R. B.; Friedel, R. A.; Storch, H. H. Fischer? *J. Chem. Phys.* **1951**, *19*, 313–319.
(56) Flory, P. J. Molecular Size Distribution in Linear Condensation Polymers 1. *J. Am. Chem. Soc.* **1936**, *58*, 1877–1885.
(57) Bertoncini, F.; Marion, M. C.; Brodusch, N.; Esnault, S. Unravelling Molecular Composition of Products from Cobalt Catalysed Fischer-Tropsch Reaction by Comprehensive Gas Chromatography. *Oil Gas Sci. Technol. – Rev. IFP Energies nouvelles* **2009**, *64*, 79–90.
(58) Puskas, I.; Hurlbut, R.S. Comments about the causes of deviations from the Anderson–Schulz–Flory distribution of the Fischer–Tropsch reaction products. *Catal. Today* **2003**, *84*, 99–109.
(59) Pichler, H.; Schulz, H.; Elstner, M. Generalizations in the synthesis of hydrocarbons from carbon monoxide and hydrogen. *Brennst.-Chem* **1967**, *48*, 78–87.
(60) Schulz H; Beck K; Erich E. Mechanism of the Fischer Tropsch Process **1988**, *36*, 457–471.
(61) Huff, G. A.; Satterfield, C. N. Intrinsic kinetics of the Fischer-Tropsch synthesis on a reduced fused-magnetite catalyst. *Ind. Eng. Chem. Proc. Des. Dev.* **1984**, *23*, 696–705.
(62) van der Laan, Gegard P.; Beenackers, A. A. C. M. Kinetics and Selectivity of the Fischer–Tropsch Synthesis. *Cat. Rev. - Sci. Eng.* **1999**, *41*, 255–318.
(63) Madon, R. J.; Reyes, S. C.; Iglesia, E. Primary and secondary reaction pathways in ruthenium-catalyzed hydrocarbon synthesis. *J. Phys. Chem.* **1991**, *95*, 7795–7804.
(64) Madon, R. J.; Iglesia, E.; Reyes, S. C. Non-Flory Product Distributions in Fischer-Tropsch Synthesis Catalyzed by Ruthenium, Cobalt, and Iron. In *Selectivity in catalysis*; Davis, M. E., Suib, S. L., Eds.; ACS Symposium Series 517; American Chemical Society: Washington DC, 1993; pp 383–396.
(65) Madon, R. J.; Iglesia, E. The importance of olefin readsorption and H2/CO reactant ratio for hydrocarbon chain growth on ruthenium catalysts. *J. Catal.* **1993**, *139*, 576–590.
(66) *Fischer-Tropsch CO-hydrogenation as a means for linear olefins production;* Schulz, H., Gokcebay, H., Eds.; Marcel Dekker: New York, 1984.
(67) Schulz, H.; Rao, B. R.; Elstner, M. *Erdöl u Kohle-Erdgas-Petrochemie* **1970**, *23*.
(68) Iglesia, E. Transport-enhanced alpha;-olefin readsorption pathways in Ru-catalyzed hydrocarbon synthesis. *J. Catal.* **1991**, *129*, 238–256.

(69) Schulz, H. Major and Minor Reactions in Fischer‐Tropsch Synthesis on Cobalt Catalysts. *Top. Catal.* **2003**, *26*, 73–85.
(70) *Advances in Fischer-Tropsch Synthesis, Catalysts, and Catalysis;* Davis, B. H., Occelli, M. L., Eds.; CRC Press Taylor & Francis Group, 2009.
(71) Nijs, H. Metal particle size distributions and Fischer-Tropsch selectivity. An extended Schulz-Flory model. *J. Catal.* **1980**, *65*, 328–334.
(72) Schulz, H. Trends in research and development of coal conversion to liquid fuels and basic chemicals in Europe. *Pure Appl. Chem.* **1979**, *51*, 283.
(73) Visconti, C. G.; Tronconi, E.; Lietti, L.; Forzatti, P.; Rossini, S.; Zennaro, R. Detailed Kinetics of the Fischer–Tropsch Synthesis on Cobalt Catalysts Based on H-Assisted CO Activation. *Top. Catal.* **2011**, *54*, 786–800.
(74) Visconti, C. G.; Tronconi, E.; Lietti, L.; Zennaro, R.; Forzatti, P. Development of a Complete Kinetic Model for the Fischer–Tropsch Synthesis over Co/Al2O3 Catalysts. *Chem. Eng. Sci.* **2007**, *62*, 5338–5343.
(75) Yang, J.; Liu, Y.; Chang, J.; Wang, Y.-N.; Bai, L.; Xu, Y.-Y.; Xiang, H.-W.; Li, Y.-W.; Zhong, B. Detailed Kinetics of Fischer−Tropsch Synthesis on an Industrial Fe−Mn Catalyst. *Ind. Eng. Chem. Res.* **2003**, *42*, 5066–5090.
(76) Mousavi, S.; Zamaniyan, A.; Irani, M.; Rashidzadeh, M. Generalized kinetic model for iron and cobalt based Fischer–Tropsch synthesis catalysts. *Appl. Catal., A* **2015**, *506*, 57–66.
(77) van Santen, R. A.; Ciobîcă, I. M.; van Steen, E.; Ghouri, M. M. Chapter 3 - Mechanistic Issues in Fischer–Tropsch Catalysis. In *Advances in Catalysis*; Gates, B. C., Knözinger, H., Eds.; Academic Press, 2011; pp 127–187.
(78) Cheng, J.; Gong, X.-Q.; Hu, P.; Lok, C.; Ellis, P.; French, S. A quantitative determination of reaction mechanisms from density functional theory calculations. *J. Catal.* **2008**, *254*, 285–295.
(79) Ferrin, P.; Kandoi, S.; Nilekar, A. U.; Mavrikakis, M. Hydrogen Adsorption, Absorption and Diffusion on and in Transition Metal Surfaces. *Surf. Sci.* **2012**, *606*, 679–689.
(80) Christmann, K. Interaction of hydrogen with solid surfaces. *Surf. Sci. Rep.* **1988**, *9*, 1–163.
(81) Robert C.Reuel; Calvin H.Bartholomew. The stoichiometries of H2 and CO adsorptions on cobalt. *J. Catal.* **1984**, *85*, 63–77.
(82) Ciobîcă, I. M.; Kramer, G. J.; Ge, Q.; Neurock, M.; van Santen, R. A. Mechanisms for Chain Growth in Fischer–Tropsch Synthesis over Ru(0001). *J. Catal.* **2002**, *212*, 136–144.
(83) Bell, A. T. Catalytic Synthesis of Hydrocarbons over Group VIII Metals. A Discussion of the Reaction Mechanism. *Cat. Rev. - Sci. Eng.* **2006**, *23*, 203–232.
(84) Kwack, S.-H.; Park, M.-J.; Bae, J. W.; Ha, K.-S.; Jun, K.-W. Development of a kinetic model of the Fischer–Tropsch synthesis reaction with a cobalt-based catalyst. *React. Kinet. Mech. Cat.* **2011**, *104*, 483–502.
(85) Shetty, S.; van Santen, R. A. CO dissociation on Ru and Co surfaces: the initial step in the Fischer‐Tropsch synthesis. *Catal. Today* **2011**, *171*, 168–173.
(86) Inderwildi, O. R.; Jenkins, S. J.; King, D. A. Fischer- Tropsch Mechanism Revisited: Alternative Pathways for the Production of Higher Hydrocarbons from Synthesis Gas. *J. Phys. Chem. C* **2008**, *112*, 1305–1307.
(87) Ciobica, I. M.; van Santen, R. A. Carbon Monoxide Dissociation on Planar and Stepped Ru(0001) Surfaces. *J. Phys. Chem. B* **2003**, *107*, 3808–3812.
(88) Shetty, S.; Jansen, A. P. J.; van Santen, R. A. Direct versus hydrogen-assisted CO dissociation. *J. Am. Chem. Soc.* **2009**, *131*, 12874–12875.
(89) Morgan, G. A.; Sorescu, D. C.; Zubkov, T.; Yates, J. T. The Formation and Stability of Adsorbed Formyl as a Possible Intermediate in Fischer-Tropsch Chemistry on Ruthenium. *The journal of physical chemistry. B* **2004**, *108*, 3614–3624.

(90) Andersson, M. P.; Abild-Pedersen, F.; Remediakis, I. N.; Bligaard, T.; Jones, G.; Engbæk, J.; Lytken, O.; Horch, S.; Nielsen, J. H.; Sehested, J. Structure sensitivity of the methanation reaction. *J. Catal.* **2008**, *255*, 6–19.
(91) Storsæter, S.; Chen, D.; Holmen, A. Microkinetic modelling of the formation of C1 and C2 products in the Fischer–Tropsch synthesis over cobalt catalysts. *Surf. Sci.* **2006**, *600*, 2051–2063.
(92) Yang, J.; Qi, Y.; Zhu, J.; Zhu, Y.-A.; Chen, D.; Holmen, A. Reaction mechanism of CO activation and methane formation on Co Fischer–Tropsch catalyst. *J. Catal.* **2013**, *308*, 37–49.
(93) Huo, C.-F.; Li, Y.-W.; Wang, J.; Jiao, H. Formation of CH x Species from CO Dissociation on Double-Stepped Co(0001). *J. Phys. Chem. C* **2008**, *112*, 14108–14116.
(94) Zhuo, M.; Tan, K. F.; Borgna, A.; Saeys, M. Density Functional Theory Study of the CO Insertion Mechanism for Fischer−Tropsch Synthesis over Co Catalysts. *J. Phys. Chem. C* **2009**, *113*, 8357–8365.
(95) Mitchell, W. J.; Xie, J.; Jachimowski, T. A.; Weinberg, W. H. Carbon monoxide hydrogenation on the Ru (001) surface at low temperature using gas-phase atomic hydrogen: spectroscopic evidence for the carbonyl insertion mechanism on a transition metal surface. *J. Am. Chem. Soc.* **1995**, *117*, 2606–2617.
(96) Ojeda, M.; Nabar, R.; Nilekar, A. U.; Ishikawa, A.; Mavrikakis, M.; Iglesia, E. CO Activation Pathways and the Mechanism of Fischer–Tropsch Synthesis. *J. Catal.* **2010**, *272*, 287–297.
(97) Claeys, M.; van Steen, E. Basic studies; pp 601–680.
(98) Gaube, J.; Klein, H.-F. Further support for the two-mechanisms hypothesis of Fischer–Tropsch synthesis. *Appl. Catal., A* **2010**, *374*, 120–125.
(99) van Santen, R. A.; J. Markvoort, A.; W. Filot, I. A.; M. Ghouri, M.; M. Hensen, E. J. Mechanism and microkinetics of the Fischer–Tropsch reaction. *Phys. Chem. Chem. Phys.* **2013**, *15*, 17038–17063.
(100) van Steen, E.; Claeys, M.; Dry, M. E.; van de Loosdrecht, J.; Viljoen, E. L.; Visagie, J. L. Stability of Nanocrystals: Thermodynamic Analysis of Oxidation and Re-reduction of Cobalt in Water/Hydrogen Mixtures. *J. Phys. Chem. B* **2005**, *109*, 3575–3577.
(101) Agrawal, R.; Phatak, P.; Spanu, L. Effect of phase and size on surface sites in cobalt nanoparticles. *Catal. Today* **2018**, *312*, 174–180.
(102) van Santen, R. A. Complementary structure sensitive and insensitive catalytic relationships. *Accounts of chemical research* **2009**, *42*, 57–66.
(103) van Santen, R. A.; Ghouri, M. M.; Shetty, S.; Hensen, E. M. H. Structure sensitivity of the Fischer–Tropsch reaction; molecular kinetics simulations. *Catal. Sci. Technol.* **2011**, *1*, 891.
(104) Liu, Z.-P.; Hu, P. General rules for predicting where a catalytic reaction should occur on metal surfaces. *J. Am. Chem. Soc.* **2003**, *125*, 1958–1967.
(105) Fischer, N.; van Steen, E.; Claeys, M. Structure sensitivity of the Fischer–Tropsch activity and selectivity on alumina supported cobalt catalysts. *J. Catal.* **2013**, *299*, 67–80.
(106) van Santen, R. A.; Ghouri, M. M.; Shetty, S.; Hensen, E. M. H. Structure sensitivity of the Fischer‐Tropsch reaction; molecular kinetics simulations. *Catal. Sci. Technol.* **2011**, *1*, 891–911.
(107) Loveless, B. T.; Buda, C.; Neurock, M.; Iglesia, E. CO Chemisorption and Dissociation at High Coverages During CO Hydrogenation on Ru Catalysts. *J. Am. Chem. Soc.* **2013**, *135*, 6107–6121.
(108) Cheng, J.; Hu, P.; Ellis, P.; French, S.; Kelly, G.; Lok, C. M. Chain Growth Mechanism in Fischer- Tropsch Synthesis: A DFT Study of C- C Coupling over Ru, Fe, Rh, and Re Surfaces. *J. Phys. Chem. C* **2008**, *112*, 6082–6086.

(109) Shetty, S. G.; Ciobîcă, I. M.; Hensen, E. J. M.; van Santen, R. A. Site regeneration in the Fischer-Tropsch synthesis reaction. *Chemical communications (Cambridge, England)* **2011**, *47*, 9822–9824.
(110) Fischer, F._; Tropsch, H. The synthesis of petroleum at atmospheric pressures from gasification products of coal. *Brennstoff-Chemie* **1926**, *7*, 97–104.
(111) Brady III, R. C.; Pettit, R. Mechanism of the Fischer-Tropsch reaction. The chain propagation step. *J. Am. Chem. Soc.* **1981**, *103*, 1287–1289.
(112) Cheng, J.; Hu, P.; Ellis, P.; French, S.; Kelly, G.; Lok, C. M. An Energy Descriptor To Quantify Methane Selectivity in Fischer−Tropsch Synthesis. *J. Phys. Chem. C* **2009**, *113*, 8858–8863.
(113) Zuo, Z.; Huang, W.; Han, P.; Li, Z. A density functional theory study of CH4 dehydrogenation on Co(111). *Appl. Surf. Sci.* **2010**, *256*, 5929–5934.
(114) Michaelides, A.; Hu, P. Insight into Microscopic Reaction Pathways in Heterogeneous Catalysis. *J. Am. Chem. Soc.* **2000**, *122*, 9866–9867.
(115) Zhao, Z.-J.; Chiu, C.-C.; Gong, J. Molecular understandings on the activation of light hydrocarbons over heterogeneous catalysts. *Chemical science* **2015**, *6*, 4403–4425.
(116) Liu, Z.-P.; Hu, P. A New Insight into Fischer−Tropsch Synthesis. *J. Am. Chem. Soc.* **2002**, *124*, 11568–11569.
(117) Huo, C.-F.; Li, Y.-W.; Wang, J.; Jiao, H. Adsorption and Dissociation of CO as Well as CHx Coupling and Hydrogenation on the Clean and Oxygen Pre-covered Co(0001) Surfaces. *J. Phys. Chem. C* **2008**, *112*, 3840–3848.
(118) Maitlis, P. M.; Zanotti, V. The role of electrophilic species in the Fischer-Tropsch reaction. *Chemical communications (Cambridge, England) [Online]* **2009,** No. 13, 1619–1634.
(119) Rofer-DePoorter, C. K. A comprehensive mechanism for the Fischer-Tropsch synthesis. *Chem. Rev.* **1981**, *81*, 447–474.
(120) Schulz, H.; Beck, K.; Erich, E. Kinetics of Fischer-Tropsch selectivity. *Fuel Process. Technol.* **1988**, *18*, 293–304.
(121) Schulz, H.; Erich, E.; Gorre, H.; van Steen, E. Regularities of selectivity as a key for discriminating FT-surface reactions and formation of the dynamic system. *Catal. Lett.* **1990**, *7*, 157–167.
(122) Schulz, H.; vein Steen, E.; Claeys, M. Selectivity and mechanism of Fischer-Tropsch synthesis with iron and cobalt catalysts. *Natural Gas Conversion II - Proceedings of the Third Natural Gas Conversion Symposium*; Studies in Surface Science and Catalysis; Elsevier, 1994; pp 455–460.
(123) Maitlis, P. M.; Long, H. C.; Quyoum, R.; Turner, M. L.; Wang, Z.-Q. Heterogeneous catalysis of C–C bond formation. *Chem. Commun.* **1996**, *35*, 1–8.
(124) Storch, H. H.; Anderson, R. A.; Golumbic, N. *The Fischer-Tropsch and related syntheses* 6; Wiley New York, 1951.
(125) Storch, H. H. *Sintez uglevodorodov iz okisi ugleroda i vodoroda*, 1954.
(126) GUPTA, R. Interaction of hydrogen and carbon monoxide on cobalt catalysts. Part I. *J. Catal.* **1972**, *26*, 212–217.
(127) Kokes, R. J.; Hall, W. K.; Emmett, P. H. Fischer-Tropsch synthesis mechanism studies. The addition of radioactive ethanol to the synthesis gas. *J. Am. Chem. Soc.* **1957**, *79*, 2989–2996.
(128) Tau, L.-M.; Dabbagh, H. A.; Halasz, J.; Davis, B. H. Fischer—Tropsch synthesis. *J. Mol. Catal.* **1992**, *71*, 37–55.
(129) Weststrate, C. J.; Gericke, H. J.; Verhoeven, Martinus W. G. M.; Ciobîcă, I. M.; Saib, A. M.; Niemantsverdriet, J. W. Ethanol Decomposition on Co(0001). *J. Phys. Chem. Lett.* **2010**, *1*, 1767–1770.

(130) Todic, B.; Bhatelia, T.; Froment, G. F.; Ma, W.; Jacobs, G.; Davis, B. H.; Bukur, D. B. Kinetic Model of Fischer–Tropsch Synthesis in a Slurry Reactor on Co–Re/Al 2 O 3 Catalyst. *Ind. Eng. Chem. Res.* **2013**, *52*, 669–679.
(131) Bhatelia, T.; Li, C.'e.; Sun, Y.; Hazewinkel, P.; Burke, N.; Sage, V. Chain length dependent olefin re-adsorption model for Fischer–Tropsch synthesis over Co-Al2O3 catalyst. *Fuel Processing Technology* **2014**, *125*, 277–289.
(132) Shi, B.; Wu, L.; Liao, Y.; Jin, C.; Montavon, A. Explanations of the Formation of Branched Hydrocarbons During Fischer–Tropsch Synthesis by Alkylidene Mechanism. *Top. Catal.* **2014**, *57*, 451–459.
(133) Shi, B.; Jin, C. Inverse kinetic isotope effects and deuterium enrichment as a function of carbon number during formation of C–C bonds in cobalt catalyzed Fischer–Tropsch synthesis. *Appl. Catal., A* **2011**, *393*, 178–183.
(134) Shi, B.; Jin, C. Deuterium tracer studies on cobalt catalyzed Fischer–Tropsch synthesis. *Appl. Catal., A* **2011**, *398*, 54–58.
(135) Gaube, J.; Klein, H.-F. Studies on the reaction mechanism of the Fischer–Tropsch synthesis on iron and cobalt. *J. Mol. Catal. Chem.* **2008**, *283*, 60–68.
(136) Riguang Zhang; Fu Liu; Qiang Wang; Baojun Wang; Debao Li. Insight into CHx formation in Fischer–Tropsch synthesis on the hexahedron Co catalyst: Effect of surface structure on the preferential mechanism and existence form [Online].
(137) Zhang, R.; Kang, L.; Liu, H.; He, L.; Wang, B. Insight into the C C chain growth in Fischer-Tropsch synthesis on HCP Co(10-10) surface. *Comput. Mater. Sci* **2018**, *145*, 263–279.
(138) Buchang Shi. Alkylidene Mechanism for the Fischer-Tropsch Synthesis. *J. Thermodyn. Catal.* **2014**, *5*, 1–2.
(139) Novak, S.; Madon, R. J.; Suhl, H. Secondary effects in the Fischer-Tropsch synthesis. *J. Catal.* **1982**, *77*, 141–151.
(140) Schulz, H.; Claeys, M. Reactions of α-olefins of different chain length added during Fischer–Tropsch synthesis on a cobalt catalyst in a slurry reactor. *Appl. Catal., A* **1999**, *186*, 71–90.
(141) Cheng, J.; Hu, P.; Ellis, P.; French, S.; Kelly, G.; Lok, C. M. Some Understanding of Fischer‐Tropsch Synthesis from Density Functional Theory Calculations. *Top. Catal.* **2010**, *53*, 326–337.
(142) Xu, L.; Ma, Y.; Zhang, Y.; Chen, B.; Wu, Z.; Jiang, Z.; Huang, W. Surface Chemistry of C 2 H 4 , CO, and H 2 on Clean and Graphite Carbon-Modified Co(0001) Surfaces. *J. Phys. Chem. C* **2011**, *115*, 3416–3424.
(143) Wintterlin, J.; Bocquet, M.-L. Graphene on metal surfaces. *Surf. Sci.* **2009**, *603*, 1841–1852.
(144) Tetlow, H.; Posthuma de Boer, J.; Ford, I. J.; Vvedensky, D. D.; Curcio, D.; Omiciuolo, L.; Lizzit, S.; Baraldi, A.; Kantorovich, L. Ethylene decomposition on Ir(111). *Phys. Chem. Chem. Phys.* **2016**, *18*, 27897–27909.
(145) Shi, B.; Keogh, R. A.; Davis, B. H. Fischer–Tropsch synthesis. *J. Mol. Catal. Chem.* **2005**, *234*, 85–97.
(146) Iglesia, E.; Reyes, S. C.; Madon, R. J. dxfbcvb [Online] **1999**.
(147) Wang, Y.-N.; Ma, W.-P.; Lu, Y.-J.; Yang, J.; Xu, Y.-Y.; Xiang, H.-W.; Li, Y.-W.; Zhao, Y.-L.; Zhang, B.-J. Kinetics modelling of Fischer‐Tropsch synthesis over an industrial Fe‐Cu‐K catalyst. *Fuel* **2003**, *82*, 195–213.
(148) Paul, H. *Rapport de thèse à mi-parcours : «Désélectivation en synthèse Fischer-Tropsch : vers une identification des mécanismes »*.
(149) Moulijn, J.A.; van Diepen, A.E.; Kapteijn, F. Catalyst deactivation. *Appl. Catal., A* **2001**, *212*, 3–16.

(150) van Berge, P. J.; Everson, R. C. Cobalt as an alternative Fischer-Tropsch catalyst to iron for the production of middle distillates. *Natural Gas Conversion IV*; Studies in Surface Science and Catalysis; Elsevier, 1997; pp 207–212.
(151) Saib, A. M.; Borgna, A.; Vandeloosdrecht, J.; Vanberge, P.; Neiemantsverdriet, J. XANES study of the susceptibility of nano-sized cobalt crystallites to oxidation during realistic Fischer–Tropsch synthesis. *Appl. Catal., A* **2006**, *312*, 12–19.
(152) Nikolaos E. Tsakoumis; Magnus Rønning; Øyvind Borg; Erling Rytter; Anders Holmen. Deactivation of cobalt based Fischerâ€“Tropsch catalysts: A review [Online].
(153) Bartholomew, C. H.; Agrawal, P. K.; Katzer, J. R. Sulfur Poisoning of Metals. In *Advances in catalysis*; Eley, D. D., Ed.; Advances in Catalysis; Academic Press: New York, 1982; pp 135–242.
(154) Visconti, C. G.; Lietti, L.; Forzatti, P.; Zennaro, R. Fischer–Tropsch synthesis on sulphur poisoned Co/Al2O3 catalyst. *Appl. Catal., A* **2007**, *330*, 49–56.
(155) Saib, A. M.; Moodley, D. J.; Ciobîcă, I. M.; Hauman, M. M.; Sigwebela, B. H.; Weststrate, C. J.; Niemantsverdriet, J. W.; van de Loosdrecht, J. Fundamental Understanding of Deactivation and Regeneration of Cobalt Fischer–Tropsch Synthesis Catalysts. *Catal. Today* **2010**, *154*, 271–282.
(156) Ma, S. H.; Jiao, Z. Y.; Yang, Z. X. Coverage effects on the adsorption of sulfur on Co(0001). *Surf. Sci.* **2010**, *604*, 817–823.
(157) McCarty, J. G.; Wise, H. Thermodynamics of sulfur chemisorption on metals. I. Alumina ‐ supported nickel. *J. Chem. Phys.* **1980**, *72*, 6332–6337.
(158) McCarty, J. G.; Wise, H. Thermodynamics of sulfur chemisorption on metals. II. Alumina ‐ supported ruthenium. *J. Chem. Phys.* **1981**, *74*, 5877–5880.
(159) McCarty, J. G.; Wise, H. Thermodynamics of sulfur chemisorption on metals. III. Iron and cobalt. *J. Chem. Phys.* **1982**, *76*, 1162–1167.
(160) McCarty, J. Thermodynamics of sulfur chemisorption on metals IV. Alumina-supported platinum. *J. Catal.* **1983**, *82*, 92–97.
(161) McCarty, J. Thermodynamics of sulfur chemisorption on metals V. Alumina-supported iridium. *J. Catal.* **1985**, *94*, 543–546.
(162) Dry, M. E. *The Fischer-Tropsch synthesis;* Springer-Verlag, Berlin, 1981.
(163) Huber, G. W.; Guymon, C. G.; Conrad, T. L.; Stephenson, B. C.; Bartholomew, C. H. Hydrothermal Stability of Co/SiO2 Fischer-Tropsch Synthesis Catalysts. In *Catalyst deactivation 2001*: *Proceedings of the 9th international symposium, Lexington, KY, USA, 7-10 October 2001*; Spivey, J. J., Roberts, G. W., Davis, B. H., Eds.; Studies in Surface Science and Catalysis vol. 139; Elsevier: Amsterdam, New York, 2001; pp 423–430.
(164) Schanke, D.; Hilmen, A. M.; Bergene, E.; Kinnari, K.; Rytter, E.; Ådnanes, E.; Holmen, A. Reoxidation and Deactivation of Supported Cobalt Fischer−Tropsch Catalysts. *Energy Fuels* **1996**, *10*, 867–872.
(165) Hilmen, A. M.; Schanke, D.; Hanssen, K. F.; Holmen, A. Study of The Effect of Water on Alumina Supported Cobalt Fischer–Tropsch Catalysts. *Appl. Catal., A* **1999**, *186*, 169–188.
(166) Abi Aad, J.; Casale, S.; Michau, M.; Courty, P.; Diehl, F.; Marceau, E.; Carrier, X. Chemical Weathering of Alumina in Aqueous Suspension at Ambient Pressure. *ChemCatChem* **2017**, *9*, 2186–2194.
(167) Iglesia, E. Design, Synthesis and Use of Cobalt-Based Fischer-Tropsch Synthesis Catalysts. *Appl. Catal., A* **1997**, *161*, 59–78.
(168) van Berge, P.J.; van de Loosdrecht, J.; Barradas, S.; van der Kraan, A.M. Oxidation of Cobalt Based Fischer–Tropsch Catalysts as a Deactivation Mechanism. *Catal. Today* **2000**, *58*, 321–334.

(169) Rothaemel, M.; Hanssen, K. F.; Blekkan, E. A.; Schanke, D.; Holmen, A. The Effect of Water on Cobalt Fischer-Tropsch Catalysts Studied by Steady-State Isotopic Transient Kinetic Analysis (SSITKA). *Catal. Today* **1997**, *38*, 79–84.
(170) Crajé, M.W.J.; van der Kraan, A. M.; van de Loosdrecht, J.; van Berge, P. J. The Application of Mössbauer Emission Spectroscopy to Industrial Cobalt Based Fischer–Tropsch Catalysts. *Catal. Today* **2002**, *71*, 369–379.
(171) Dalai, A. K.; Davis, B. H. Fischer–Tropsch Synthesis. *Appl. Catal., A* **2008**, *348*, 1–15.
(172) van de Loosdrecht, J.; Balzhinimaev, B.; Dalmon, J.-A.; Niemantsverdriet, J. W.; Tsybulya, S. V.; Saib, A. M.; van Berge, P. J.; Visagie, J. L. Cobalt Fischer-Tropsch Synthesis. *Catal. Today* **2007**, *123*, 293–302.
(173) Blekkan, E. A.; Borg, Ø.; Frøseth, V.; Holmen, A. Fischer-Tropsch Synthesis on Cobalt Catalysts: The Effect of Water. *Catal.* **2007**, *20*, 13–32.
(174) Schulz, H.; Claeys, M.; Harms, S. Effect of Water Partial Pressure on Steady State Fischer-Tropsch Activity and Selectivity of a Promoted Cobalt Catalyst. *Stud. Surf. Sci. Catal.* **1997**, *107*, 193–200.
(175) Ma, W.; Jacobs, G.; Ji, Y.; Bhatelia, T.; Bukur, D. B.; Khalid, S.; Davis, B. H. Fischer ‐ Tropsch Synthesis: Influence of CO Conversion on Selectivities, H2/CO Usage Ratios, and Catalyst Stability for a Ru Promoted Co/Al2O3 Catalyst Using a Slurry Phase Reactor. *Top. Catal.* **2011**, *54*, 757.
(176) Zhang, Y.; Wei, D.; Hammache, S.; Goodwin, J. G. Effect of Water Vapor on the Reduction of Ru-Promoted Co/Al2O3. *J. Catal.* **1999**, *188*, 281–290.
(177) Chaopeng, H.; Guofu, X.; Xia, S.; Yu, W.; Chao, J.; Zhennan, Y.; Mingfeng, L.; Zhihai, H.; Hong, N.; Dadong, L. Thermodynamics of Oxidation of an Alumina-Supported Cobalt Catalyst by Water in F-T Synthesis. *Catal. Today* **2016**, *264*, 91–97.
(178) Moodley, D. J.; Saib, A. M.; van de Loosdrecht, J.; Welker-Nieuwoudt, C. A.; Sigwebela, B. H.; Niemantsverdriet, J. W. The impact of cobalt aluminate formation on the deactivation of cobalt-based Fischer–Tropsch synthesis catalysts. *Catal. Today* **2011**, *171*, 192–200.
(179) Sadeqzadeh, M.; Hong, J.; Fongarland, P.; Curulla-Ferré, D.; Luck, F.; Bousquet, J.; Schweich, D.; Khodakov, A. Y. Mechanistic Modeling of Cobalt Based Catalyst Sintering in a Fixed Bed Reactor Under Different Conditions of Fischer–Tropsch Synthesis. *Ind. Eng. Chem. Res.* **2012**, *51*, 11955–11964.
(180) Sadeqzadeh, M.; Chambrey, S.; Hong, J.; Fongarland, P.; Luck, F.; Curulla-Ferré, D.; Schweich, D.; Bousquet, J.; Khodakov, A. Y. Effect of Different Reaction Conditions on the Deactivation of Alumina-Supported Cobalt Fischer–Tropsch Catalysts in a Milli-Fixed-Bed Reactor. *Ind. Eng. Chem. Res.* **2014**, *53*, 6913–6922.
(181) Sadeqzadeh, M.; Chambrey, S.; Piché, S.; Fongarland, P.; Luck, F.; Curulla-Ferré, D.; Schweich, D.; Bousquet, J.; Khodakov, A. Y. Deactivation of a Co/Al2O3 Fischer–Tropsch Catalyst by Water-Induced Sintering in Slurry Reactor. *Catal. Today* **2013**, *215*, 52–59.
(182) Karaca, H.; Hong, J.; Fongarland, P.; Roussel, P.; Griboval-Constant, A.; Lacroix, M.; Hortmann, K.; Safonova, O. V.; Khodakov, A. Y. In situ XRD Investigation of The Evolution of Alumina-Supported Cobalt Catalysts Under Realistic Conditions of Fischer-Tropsch Synthesis. *Chem. Commun.* **2010**, *46*, 788–790.
(183) Karaca, H.; Safonova, O. V.; Chambrey, S.; Fongarland, P.; Roussel, P.; Griboval-Constant, A.; Lacroix, M.; Khodakov, A. Y. Structure and Catalytic Performance of Pt-Promoted Alumina-Supported Cobalt Catalysts Under Realistic Conditions of Fischer–Tropsch Synthesis. *J. Catal.* **2011**, *277*, 14–26.
(184) Moyes, R.; Roberts, M. W. Interaction of Cobalt with Oxygen, Water Vapor, and Carbon Monoxide. *J. Catal.* **1977**, *49*, 216–224.

(185) Heras, J. M.; Papp, H.; Spiess, W. Face Specificity of The H2O Adsorption and Decomposition on Co Surfaces. *Surf. Sci.* **1982**, *117*, 590–604.
(186) Xu, L.; Ma, Y.; Zhang, Y.; Chen, B.; Wu, Z.; Jiang, Z.; Huang, W. Water Adsorption on a Co(0001) Surface. *J. Phys. Chem. C* **2010**, *114*, 17023–17029.
(187) Ma, F. F.; Ma, S. H.; Jiao, Z. Y.; Dai, X. Q. Adsorption and Decomposition of H2O on Cobalt Surfaces. *Appl. Surf. Sci.* **2016**, *384*, 10–17.
(188) Yang, J.; Ma, J. J.; Ma, S. H.; Dai, X. Q. Theoretical Study of Direct versus Oxygen-Assisted Water Dissociation on Co(0001) Surface. *Chem. Phys. Lett.* **2017**, *681*, 29–35.
(189) Ma, J.-J.; Wang, L.-F.; Ma, S.-H.; Yang, J. Interaction of Water with Stepped Co(0001). *Eur. Phys. J. B* **2018**, *91*, 185.
(190) Lancelot, C.; Ordomsky, V. V.; Stéphan, O.; Sadeqzadeh, M.; Karaca, H.; Lacroix, M.; Curulla-Ferré, D.; Luck, F.; Fongarland, P.; Griboval-Constant, A.; Khodakov, A. Y. Direct Evidence of Surface Oxidation of Cobalt Nanoparticles in Alumina-Supported Catalysts for Fischer–Tropsch Synthesis. *ACS Catal.* **2014**, *4*, 4510–4515.
(191) Corral Valero, M.; Raybaud, P. Competitive Deposition of C and O Species on Cobalt Surface in Fischer–Tropsch Synthesis Conditions. *J. Phys. Chem. C* **2015**, *119*, 23515–23526.
(192) Anders Blekkan, E.; Borg, Ø.; Frøseth, V.; Holmen, A. Fischer-Tropsch synthesis on cobalt catalysts: the effect of water. In *Catalysis*: *Volume 20*; Spivey, J. J., Margitfalvi, J. L., Blekkan, E. E., Eds.; Catalysis; Royal Society of Chemistry: [Place of publication not identified], 2007; pp 13–32.
(193) Saib, A. M.; D.J. Moodley; I.M. Ciobîcă; M.M. Hauman; B.H. Sigwebela; C.J. Weststrate; J.W. Niemantsverdriet; J. van de Loosdrecht. Fundamental understanding of deactivation and regeneration of cobalt Fischer-Tropsch synthesis catalysts [Online].
(194) Lee, D.-K.; Lee, J.-H.; Ihm, S.-K. Effect of Carbon Deposits on Carbon Monoxide Hydrogenation over Alumina-Supported Cobalt Catalyst. *Appl. Catal.* **1988**, *36*, 199–207.
(195) Moodley, D. J.; van de Loosdrecht, J.; Saib, A. M.; Overett, M. J.; Datye, A. K.; Niemantsverdriet, J. W. Carbon Deposition as a Deactivation Mechanism of Cobalt-Based Fischer-Tropsch Synthesis Catalysts Under Realistic Conditions. *Appl. Catal., A* **2009**, *354*, 102–110.
(196) D. Peña; A. Griboval-Constant; C. Lancelot; M. Quijada; N. Visez; O. Stéphan; V. Lecocq; F. Diehl; A.Y. Khodakov. Molecular structure and localization of carbon species in alumina supported cobalt Fischer–Tropsch catalysts in a slurry reactor [Online].
(197) Ducreux, O.; Lynch, J.; Rebours, B.; Roy, M.; Chaumette, P. In Situ Characterisation of Cobalt Based Fischer-Tropsch Catalysts: A New Approach to the Active Phase. In *Natural gas conversion V*: *Proceedings of the Fifth International Natural Gas Conversion Symposium, Giardini Naxos-Taormina, Italy, September 20-25, 1998*; Parmaliana, A., Ed.; Studies in Surface Science and Catalysis vol. 119; Elsevier: Amsterdam, New York, 1998; pp 125–130.
(198) Weststrate, C. J.; Kızılkaya, A. C.; Rossen, E. T. R.; Verhoeven, Martinus W. G. M.; Ciobîcă, I. M.; Saib, A. M.; Niemantsverdriet, J. W. Atomic and Polymeric Carbon on Co(0001): Surface Reconstruction, Graphene Formation, and Catalyst Poisoning. *J. Phys. Chem. C* **2012**, *116*, 11575–11583.
(199) Keyvanloo, K.; Fisher, M. J.; Hecker, W. C.; Lancee, R. J.; Jacobs, G.; Bartholomew, C. H. Kinetics of Deactivation by Carbon of a Cobalt Fischer-Tropsch Catalyst: Effects of CO and H2 Partial Pressures. *J. Catal.* **2015**, *327*, 33–47.
(200) Shatynski, S. R. The Thermochemistry of Transition Metal Carbides. *Oxid. Met.* **1979**, *13*, 105–118.
(201) Xiong, J.; Ding, Y.; Wang, T.; Yan, L.; Chen, W.; Zhu, H.; Lu, Y. The Formation of Co2C Species in Activated Carbon Supported Cobalt-Based Catalysts and its Impact on Fischer–Tropsch Reaction. *Catal. Lett.* **2005**, *102*, 265–269.

(202) Gruver, V.; Zhan, X.; Engman, J.; Robota, H. J.; Suib, S. L.; Polverejan, M. Deactivation of a Fischer-Tropsch Catalyst through the Formation of Cobalt Carbide Under Laboratory Slurry Reactor Conditions. *Prepr. - Am. Chem. Soc., Div. Pet. Chem.* **2004**, *49*, 192–194.
(203) Ducreux, O.; Rebours, B.; Lynch, J.; Roy-Auberger, M.; Bazin, D. Microstructure of Supported Cobalt Fischer-Tropsch Catalysts. *Oil Gas Sci. Technol. – Rev. IFP Energies nouvelles* **2009**, *64*, 49–62.
(204) Fei Tan, K.; Xu, J.; Chang, J.; Borgna, A.; Saeys, M. Carbon Deposition on Co Catalysts During Fischer–Tropsch Synthesis. *J. Catal.* **2010**, *274*, 121–129.
(205) Corral Valero, M.; Raybaud, P. Stability of Carbon on Cobalt Surfaces in Fischer‐Tropsch Reaction Conditions: A DFT Study. *J. Phys. Chem. C* **2014**, *118*, 22479–22490.
(206) Valero, M. C.; Raybaud, P. Cobalt Catalyzed Fischer‐Tropsch Synthesis: Perspectives Opened by First Principles Calculations. *Catal. Lett.* **2013**, *143*, 1–17.
(207) Zonnevylle, M. C.; Geerlings, J. J.C.; van Santen, R. A. Conversion of Surface Carbidic to Subsurface Carbon on Cobalt (0001): a Theoretical Study. *Surf. Sci.* **1990**, *240*, 253–262.
(208) Swart, J. C. W.; van Steen, E.; Ciobícă, I. M.; van Santen, R. A. Interaction of Graphene with FCC-Co(111). *Phys. Chem. Chem. Phys.* **2009**, *11*, 803–807.
(209) Swart, J. C. W.; Ciobîcă, I. M.; van Santen, R. A.; van Steen, E. Intermediates in the Formation of Graphitic Carbon on a Flat FCC-Co (111) Surface. *J. Phys. Chem. C* **2008**, *112*, 12899–12904.
(210) Zhai, P.; Chen, P.-P.; Xie, J.; Liu, J.-X.; Zhao, H.; Lin, L.; Zhao, B.; Su, H.-Y.; Zhu, Q.; Li, W.-X.; Ma, D. Carbon induced selective regulation of cobalt-based Fischer–Tropsch catalysts by ethylene treatment. *Faraday Discuss. [Online]* **2017**, *197*, 207–224. https://pubs.rsc.org/en/content/articlepdf/2017/fd/c6fd00194g.
(211) Weststrate, C. J.; Ciobîcă, I. M.; van de Loosdrecht, J.; Niemantsverdriet, J. W. Adsorption and Decomposition of Ethene and Propene on Co(0001). *J. Phys. Chem. C* **2016**, *120*, 29210–29224.
(212) Weststrate, C. J.; Ciobîcă, I. M.; Saib, A. M.; Moodley, D. J.; Niemantsverdriet, J. W. Fundamental issues on practical Fischer–Tropsch catalysts. *Catal. Today* **2014**, *228*, 106–112.
(213) Vang, R. T.; Honkala, K.; Dahl, S.; Vestergaard, E. K.; Schnadt, J.; Lægsgaard, E.; Clausen, B. S.; Nørskov, J. K.; Besenbacher, F. Ethylene dissociation on flat and stepped Ni(111). *Surf. Sci.* **2006**, *600*, 66–77.
(214) Zhu, X.-Y.; White, J. M. Evidence for ethylidyne formation on Ni(111). *Catal. Lett.* **1988**, *1*, 247–254.
(215) Ramsvik, T.; Borg, A.; Venvik, H.J.; Hansteen, F.; Kildemo, M.; Worren, T. Acetylene chemisorption and decomposition on the Co(11$\bar{2}$0) single crystal surface. *Surf. Sci.* **2002**, *499*, 183–192.
(216) Vaari, J.; Lahtinen, J.; Hautojärvi, P. The adsorption and decomposition of acetylene on clean and K-covered Co(0001). *Catal. Lett.* **1997**, *44*, 43–49.
(217) Xu, L.; Ma, Y.; Wu, Z.; Chen, B.; Yuan, Q.; Huang, W. A Photoemission Study of Ethylene Decomposition on a Co(0001) Surface. *J. Phys. Chem. C* **2012**, *116*, 4167–4174.
(218) Wang, B.; König, M.; Bromley, C. J.; Yoon, B.; Treanor, M.-J.; Garrido Torres, J. A.; Caffio, M.; Grillo, F.; Früchtl, H.; Richardson, N. V.; Esch, F.; Heiz, U.; Landman, U.; Schaub, R. Ethene to Graphene. *J. Phys. Chem. C* **2017**, *121*, 9413–9423.
(219) Zhang, M.; Huang, H.; Yu, Y. Insight into the Mechanism of Ethylene Decomposition Over Co(0001) Surface. *Catal. Lett.* **2019**, *149*, 744–752.
(220) Kyriakou, G.; Kim, J.; Tikhov, M. S.; Macleod, N.; Lambert, R. M. Acetylene coupling on Cu(111). *J. Phys. Chem. B* **2005**, *109*, 10952–10956.
(221) Lee, A. F.; Wilson, K.; Lambert, R. M. In situ observation of a surface catalysed chemical reaction by fast X-ray photoelectron spectroscopy. In *Studies in Surface Science and*

*Catalysis : Fischer-Tropsch Technology*; Steynberg, A., Dry, M., Eds.; Elsevier, 2004; pp 3095–3100.
(222) Nikolaos E. Tsakoumis; Magnus Rønning; Øyvind Borg; Erling Rytter; Anders Holmen. Deactivation of cobalt based Fischer-Tropsch catalysts: A review [Online].
(223) Ciobîcă, I. M.; van Santen, R. A.; van Berge, P. J.; van de Loosdrecht, J. Adsorbate Induced Reconstruction of Cobalt Surfaces. *Surf. Sci.* **2008**, *602*, 17–27.
(224) Somorjai, G. A.; van Hove, M. A. Adsorbate-induced restructuring of surfaces. *Prog. Surf. Sci.* **1989**, *30*, 201–231.
(225) Wilson, J.; Groot, C. de. Atomic-Scale Restructuring in High-Pressure Catalysis. *J. Phys. Chem.* **1995**, *99*, 7860–7866.
(226) Sautet, P.; Cinquini, F. Surface of Metallic Catalysts under a Pressure of Hydrocarbon Molecules. *ChemCatChem* **2010**, *2*, 636–639.
(227) Beitel, G. A.; Laskov, A.; Oosterbeek, H.; Kuipers, E. W. Polarization modulation infrared reflection absorption spectroscopy of CO adsorption on Co (0001) under a high-pressure regime. *J. Phys. Chem.* **1996**, *100*, 12494–12502.
(228) Beitel, G. A.; Groot, C. P. M. de; Oosterbeek, H.; Wilson, J. H. A combined in-situ PM-RAIRS and kinetic study of single-crystal cobalt catalysts under synthesis gas at pressures up to 300 mbar. *J. Phys. Chem. B* **1997**, *101*, 4035–4043.
(229) Banerjee, A.; van Bavel, A. P.; Kuipers, H. P.C.E.; Saeys, M. Origin of the Formation of Nanoislands on Cobalt Catalysts during Fischer–Tropsch Synthesis. *ACS Catal.* **2015**, *5*, 4756–4760.
(230) Giustino, F. *Materials modelling using density functional theory*. *Properties and predictions / Feliciano Giustino;* Oxford University Press: Oxford, 2014.
(231) Szabo, A.; Ostlund, N. S. *Modern quantum chemistry*. *Introduction to advanced electronic structure theory / Attila Szabo, Neil S. Ostlund*, 1st ed., rev; Dover; London : Constable: Mineola, N.Y, 1996, 1989.
(232) Atkins, P. W.; Friedman, R. *Molecular quantum mechanics*, 5th ed.; Oxford University Press: Oxford, 2011.
(233) Koch, W.; Holthausen, M. C. *A Chemist's Guide to Density Functional Theory*, Second edition; Wiley-VCH: Weinheim, 2015.
(234) Perdew; Burke; Ernzerhof. Generalized Gradient Approximation Made Simple. *Physical review letters* **1996**, *77*, 3865–3868.
(235) Bloch, F. Über die Quantenmechanik der Elektronen in Kristallgittern. *Zeitschrift für Physik* **1929**, *52*, 555–600.
(236) Monkhorst, H. J.; Pack, J. D. Special Points for Brillouin-Zone Integrations. *Phys. Rev. B* **1976**, *13*, 5188–5192.
(237) Pseudopotential. https://en.wikipedia.org/wiki/Pseudopotential (accessed January 9, 2018).
(238) Martin, R. M. *Electronic structure*. *Basic theory and practical methods;* Cambridge University Press: Cambridge, New York, 2004.
(239) Blöchl, P. E. Projector augmented-wave method. *Phys. Rev. B* **1994**, *50*, 17953–17979.
(240) S. Cottenier. *Density Functional Theory and the family of (L)APW-methods: a step-by-stepintroduction, 2002-2013 (2ndedition)*.
(241) Henkelman, G.; Uberuaga, B. P.; Jónsson, H. A climbing image nudged elastic band method for finding saddle points and minimum energy paths. *J. Chem. Phys.* **2000**, *113*, 9901–9904.
(242) Sheppard, D.; Terrell, R.; Henkelman, G. Optimization methods for finding minimum energy paths. *J. Chem. Phys.* **2008**, *128*, 134106.
(243) Jónsson, H.; MILLS, G.; JACOBSEN, K. W. Nudged elastic band method for finding minimum energy paths of transitions. In *Classical and quantum dynamics in condensed phase*

*simulations*, Proceedings of th International School of Physics "Computer Simulation of are Events and the Dynamics of Classical and Quantum Condensed-Phase Systems", Lerici, Villa Marigola, 7 July- 18 July 1997; Berne, B. J., Ciccotti, G., Coker, D. F., Eds.; WORLD SCIENTIFIC: Singapore, op. 1998; pp 385–404.
(244) Henkelman, G.; Jónsson, H. A dimer method for finding saddle points on high dimensional potential surfaces using only first derivatives. *J. Chem. Phys.* **1999**, *111*, 7010–7022.
(245) Fleurat-Lessard, P. Opt'n Path. http://pfleurat.free.fr/ReactionPath.php.
(246) Henkelman, G.; Jónsson, H. Improved tangent estimate in the nudged elastic band method for finding minimum energy paths and saddle points. *J. Chem. Phys.* **2000**, *113*, 9978–9985.
(247) Kresse, G.; Furthmüller, J. Efficiency of Ab-initio Total Energy Calculations for Metals and Semiconductors using a Plane-Wave Basis Set. *Comput. Mater. Sci* **1996**, *6*, 15–50.
(248) Kresse, G.; Furthmüller, J. Efficient Iterative Schemes for Ab Initio Total-Energy Calculations using a Plane-Wave Basis Set. *Phys. Rev. B* **1996**, *54*, 11169–11186.
(249) Kresse, G.; Joubert, D. From Ultrasoft Pseudopotentials to the Projector Augmented-Wave Method. *Phys. Rev. B* **1999**, *59*, 1758–1775.
(250) Blöchl, P. E.; Jepsen, O.; Andersen, O. K. Improved tetrahedron method for Brillouin-zone integrations. *Phys. Rev. B* **1994**, *49*, 16223–16233.
(251) Methfessel, M.; Paxton, A. T. High-Precision Sampling for Brillouin-Zone Integration in Metals. *Phys. Rev. B* **1989**, *40*, 3616–3621.
(252) Enache; D. I.; et al. In Situ XRD Study of the Influence of Thermal Treatment on the Characteristics and the Catalytic Properties of Cobalt-Based Fischer–Tropsch Catalysts [Online].
(253) ENACHE, D. Differences in the characteristics and catalytic properties of cobalt-based Fischer? *Appl. Catal., A* **2004**, *268*, 51–60.
(254) Corral Valero, M.; Raybaud, P. Stability of Carbon on Cobalt Surfaces in Fischer–Tropsch Reaction Conditions. *J. Phys. Chem. C* **2014**, *118*, 22479–22490.
(255) Jakobsen, H. A. *Chemical reactor modeling*. *Multiphase reactive flows;* Springer: Berlin, 2008.
(256) Méndez, C. I.; Ancheyta, J.; Trejo, F. Modeling of Catalytic Fixed-Bed Reactors for Fuels Production by Fischer–Tropsch Synthesis. *Energy Fuels* **2017**, *31*, 13011–13042.
(257) Boyer C., Gazarian J., Lecocq V., Maury S., Forret A., Schweitzer J.M., Souchon V. Development of the Fischer-Tropsch Process: From the Reaction Concept to the Process Book [Online].
(258) Schweitzer, J. M.; Viguié, J. C. Reactor Modeling of a Slurry Bubble Column for Fischer-Tropsch Synthesis. *Oil Gas Sci. Technol. – Rev. IFP Energies nouvelles* **2009**, *64*, 63–77.
(259) Schwaab, M.; Pinto, J. C. Optimum reference temperature for reparameterization of the Arrhenius equation. Part 1. *Chem. Eng. Sci.* **2007**, *62*, 2750–2764.
(260) Press, W. H.; Flannery, B. P.; Teukolsky, S. A.; Vetterling, W. T. Numerical Recipes in Pascal, The Art of Scientific Computing. *New York: Cambridge University [Online]* **1989**.
(261) Ashcroft, N. W.; Mermin, N. D. *Solid State Physics;* Brooks / Cole Cengage Learning: Belmont (Calif.), 1976.
(262) West, A. R. *Basic Solid State Chemistry;* John Wiley & Sons Inc, 1999.
(263) Chase Jr, M. W. NIST-JANAF Thermochemical Tables. *J. Phys. Chem. Ref. Data* **1998**, *9*.
(264) Scott, D. W. *Chemical Thermodynamic Properties of Hydrocarbons and Related Substances*. *Properties of the Alkane Hydrocarbons, C1 through C10, in the Ideal Gas State From 0 to 1500 K* 666; US Department of the Interior, Bureau of Mines, 1974.

(265) Masuku, C. M.; Hildebrandt, D.; Glasser, D. Olefin Pseudo-Equilibrium in the Fischer–Tropsch Reaction. *Chem. Eng. J.* **2012**, *181-182*, 667–676.
(266) Effect of Pt and Ru Promoters on Deactivation of Co Catalysts by C Deposition During Fischer–Tropsch Synthesis. *Appl. Catal., A* **2013**, *462-463*, 107–115.
(267) J. Jansen, A. P.; Ravi Agrawal; Leonardo Spanu. Thermodynamics and Kinetics of Carbon Deposits on Cobalt. *Phys. Chem. Chem. Phys.* **2016**, *18*, 28515–28523.
(268) Gong, X.-Q.; Raval, R.; Hu, P. CHx Hydrogenation on Co(0001): a Density Functional Theory Study. *J. Chem. Phys.* **2005**, *122*, 24711.
(269) Gong, X.-Q.; Raval, R.; Hu, P. A Density Functional Theory Study on the Water Formation at High Coverages and the Water Effect in the Fischer–Tropsch Synthesis. *Mol. Phys.* **2004**, *102*, 993–1000.
(270) Wolf, M.; Mutuma, B. K.; Coville, N. J.; Fischer, N.; Claeys, M. Role of CO in the Water-Induced Formation of Cobalt Oxide in a High Conversion Fischer–Tropsch Environment. *ACS Catal.* **2018**, *8*, 3985–3989.
(271) Pick, Š. Density-Functional Study of the CO Adsorption on Ferromagnetic Co(0001) and Co(111) Surfaces. *Surf. Sci.* **2007**, *601*, 5571–5575.
(272) Chen, C.; Wang, Q.; Zhang, R.; Hou, B.; Li, D.; Jia, L.; Wang, B. High Coverage CO Adsorption and Dissociation on the Co(0001) and Co(100) Surfaces from DFT and Thermodynamics. *Appl. Catal., A* **2016**, *523*, 209–220.
(273) Gunasooriya, G. K. K.; van Bavel, A. P.; Kuipers, H. P.C.E.; Saeys, M. CO Adsorption on Cobalt. *Surf. Sci.* **2015**, *642*, L6-L10.
(274) Ge, Q.; Neurock, M. Adsorption and Activation of CO over Flat and Stepped Co Surfaces. *J. Phys. Chem. B* **2006**, *110*, 15368–15380.
(275) Nakhaei Pour, A.; Keyvanloo, Z.; Izadyar, M.; Modaresi, S. M. Dissociative Hydrogen Adsorption on the Cubic Cobalt Surfaces. *Int. J. Hydrog. Energy (International Journal of Hydrogen Energy)* **2015**, *40*, 7064–7071.
(276) van Helden, P.; van den Berg, J.-A.; Weststrate, C. J. Hydrogen Adsorption on Co Surfaces. *ACS Catal.* **2012**, *2*, 1097–1107.
(277) Cheng, J.; Hu, P.; Ellis, P.; French, S.; Kelly, G.; Lok, C. M. Density Functional Theory Study of Iron and Cobalt Carbides for Fischer−Tropsch Synthesis. *J. Phys. Chem. C* **2010**, *114*, 1085–1093.
(278) Cheng, J.; Hu, P. Utilization of the Three-Dimensional Volcano Surface to Understand the Chemistry of Multiphase Systems in Heterogeneous Catalysis. *J. Am. Chem. Soc.* **2008**, *130*, 10868–10869.
(279) Li, B.; Zhang, Q.; Chen, L.; Cui, P.; Pan, X. Vacancy-Mediated Diffusion of Carbon in Cobalt and its Influence on CO Activation. *Phys. Chem. Chem. Phys.* **2010**, *12*, 7848–7855.
(280) Peña, D.; Griboval-Constant, A.; Lancelot, C.; Quijada, M.; Visez, N.; Stéphan, O.; Lecocq, V.; Diehl, F.; Khodakov, A. Y. Molecular Structure and Localization of Carbon species in Alumina Supported Cobalt Fischer‐Tropsch Catalysts in a Slurry Reactor. *Catal. Today* **2014**, *228*, 65–76.
(281) Chen, W.; Kimpel, T. F.; Song, Y.; Chiang, F.-K.; Zijlstra, B.; Pestman, R.; Wang, P.; Hensen, E. J. M. Influence of Carbon Deposits on the Cobalt-Catalyzed Fischer–Tropsch Reaction. *ACS Catal.* **2018**, *8*, 1580–1590.
(282) Nakamura, J.; Tanaka, K.-i.; Toyoshima, I. Reactivity of deposited carbon on Co □ Al2O3 catalyst. *J. Catal.* **1987**, *108*, 55–62.
(283) Cheng, J.; Hu, P.; Ellis, P.; French, S.; Kelly, G.; Lok, C. M. A First-Principles Study of Oxygenates on Co Surfaces in Fischer−Tropsch Synthesis. *J. Phys. Chem. C* **2008**, *112*, 9464–9473.

(284) Peña, D. PhD Thesis: Identification of Deactivation Mechanisms of Cobalt Fischer-Tropsch Catalysts in Slurry Reactor; Université Lille 1 - Sciences et Technologies, Villeurbanne, 2013.
(285) Peña, D.; Griboval-Constant, A.; Lecocq, V.; Diehl, F.; Khodakov, A. Y. Influence of Operating Conditions in a Continuously Stirred Tank Reactor on the Formation of Carbon Species on Alumina Supported Cobalt Fischer-Tropsch Catalysts. *Catal. Today* **2013**, *215*, 43–51.
(286) Gruver, V.; Young, R.; Engman, J.; Robota, H. J. The Role of Accumulated Carbon in Deactivating Cobalt Catalysts During FT Synthesis in a Slurry-Bubble-Column Reactor. *Prepr. - Am. Chem. Soc., Div. Pet. Chem.* **2005**, *50*, 164–166.
(287) Pinard, L.; Bichon, P.; Popov, A.; Lemberton, J. L.; Canaff, C.; Maugé, F.; Bazin, P.; S.-Aguiar, E. F.; Magnoux, P. Identification of the Carbonaceous Compounds Present on a Deactivated Cobalt-Based Fischer–Trospch Catalyst Resistant to "Rejuvenation Treatment". *Appl. Catal., A* **2011**, *406*, 73–80.
(288) Duncan, T. M.; Winslow, P.; Bell, A. T. The Characterization of Carbonaceous Species on Ruthenium Catalysts with 13C Nuclear Magnetic Resonance Spectroscopy. *J. Catal.* **1985**, *93*, 1–22.
(289) Winslow, P. Studies of the Surface Coverage of Unsupported Ruthenium by Carbon- and Hydrogen-Containing Adspecies during CO Hydrogenation. *J. Catal.* **1985**, *91*, 142–154.
(290) Banerjee, A.; Navarro, V.; Frenken, J. W. M.; van Bavel, A. P.; Kuipers, H. P. C. E.; Saeys, M. Shape and Size of Cobalt Nanoislands Formed Spontaneously on Cobalt Terraces During Fischer-Tropsch Synthesis. *J. Phys. Chem. Lett.* **2016**, *7*, 1996–2001.
(291) Luo, W.; Asthagiri, A. Density Functional Theory Study of Methanol Steam Reforming on Co(0001) and Co(111) Surfaces. *J. Phys. Chem. C* **2014**, *118*, 15274–15285.
(292) Balakrishnan, N.; Joseph, B.; Bhethanabotla, V. R. Effect of Platinum Promoters on the Removal of O from the Surface of Cobalt Catalysts. *Surf. Sci.* **2012**, *606*, 634–643.
(293) Zhuo, M.; Borgna, A.; Saeys, M. Effect of the CO Coverage on the Fischer–Tropsch Synthesis Mechanism on Cobalt Catalysts. *J. Catal.* **2013**, *297*, 217–226.
(294) Peña, D.; Griboval-Constant, A.; Diehl, F.; Lecocq, V.; Khodakov, A. Y. Agglomeration at the Micrometer Length Scale of Cobalt Nanoparticles in Alumina-Supported Fischer-Tropsch Catalysts in a Slurry Reactor. *ChemCatChem* **2013**, *5*, 728–731.
(295) Asiaee, A.; Benjamin, K. M. A Density Functional Theory Based Elementary Reaction Mechanism for Early Steps of Fischer-Tropsch Synthesis over Cobalt Catalyst. 2. Microkinetic Modeling of Liquid-Phase vs. Gaseous-Phase Process. *Mol. Catal.* **2017**, *436*, 210–217.
(296) van Helden, P.; van den Berg, J.-A.; Petersen, M. A.; van Janse Rensburg, W.; Ciobîcă, I. M.; van de Loosdrecht, J. Computational Investigation of the Kinetics and Mechanism of the Initial Steps of the Fischer-Tropsch Synthesis on Cobalt. *Faraday Discuss.* **2017**, *197*, 117–151.
(297) den Breejen, J. P.; Radstake, P. B.; Bezemer, G. L.; Bitter, J. H.; Frøseth, V.; Holmen, A.; Jong, K. P. de. On the Origin of the Cobalt Particle Size Effects in Fischer−Tropsch Catalysis. *J. Am. Chem. Soc.* **2009**, *131*, 7197–7203.
(298) Li, M.; Guo, W.; Jiang, R.; Zhao, L.; Lu, X.; Zhu, H.; Fu, D.; Shan, H. Mechanism of the Ethylene Conversion to Ethylidyne on Rh(111). *J. Phys. Chem. C* **2010**, *114*, 8440–8448.
(299) Filot, I. A.W., Zijlstra, B., Hensen, E. J.M. *MKMCXX, a C++ program for constructing microkinetic models*. https://www.mkmcxx.nl/.
(300) Filot, I. A.W. *Introduction to microkinetic modeling;* Eindhoven, 2017.
(301) Albert, M. R.; Sneddon, L. G.; Plummer, E. W. An UPS study of the chemisorption of acetylene and ethylene on Co(0001). *Surf. Sci.* **1984**, *147*, 127–142.

(302) Chen, C.; Wang, Q.; Wang, G.; Hou, B.; Jia, L.; Li, D. Mechanistic Insight into the C 2 Hydrocarbons Formation from Syngas on fcc-Co(111) Surface. *J. Phys. Chem. C* **2016**, *120*, 9132–9147.
(303) Dae Bok Kang; Anderson, A. B. Adsorption and structural rearrangements of acetylene and ethylene on Pt(111); Theoretical study. *Surf. Sci.* **1985**, *155*, 639–652.
(304) Carter, E. A.; Koel, B. E. A method for estimating surface reaction energetics. *Surf. Sci.* **1990**, *226*, 339–357.
(305) Cheng, J.; Song, T.; Hu, P.; Lok, C. M.; Ellis, P.; French, S. A density functional theory study of the α-olefin selectivity in Fischer–Tropsch synthesis. *J. Catal.* **2008**, *255*, 20–28.
(306) Zijlstra, B. Modeling the Fischer-Tropsch reaction on Cobalt surfaces; Eindhoven University of Technology, 2015.
(307) Lorenz, M. P. A.; Fuhrmann, T.; Streber, R.; Bayer, A.; Bebensee, F.; Gotterbarm, K.; Kinne, M.; Tränkenschuh, B.; Zhu, J. F.; Papp, C.; Denecke, R.; Steinrück, H.-P. Ethene adsorption and dehydrogenation on clean and oxygen precovered Ni(111) studied by high resolution x-ray photoelectron spectroscopy. *The Journal of chemical physics* **2010**, *133*, 14706.
(308) Chen, H.; Zhu, W.; Zhang, Z. Contrasting behavior of carbon nucleation in the initial stages of graphene epitaxial growth on stepped metal surfaces. *Physical review letters* **2010**, *104*, 186101.
(309) Avery, N. R. Adsorption and reactivity of acetylene on a copper (110) surface. *J. Am. Chem. Soc.* **1985**, *107*, 6711–6712.
(310) Lambert, R. M.; Ormerod, R. M. Tricyclisation and Heterocyclisation Reactions of Ethyne over Well-Defined Palladium Surfaces. In *Surface Reactions*; Madix, R. J., Ed.; Springer Series in Surface Sciences 34; Springer Berlin Heidelberg: Berlin, Heidelberg, 1994; pp 89–134.
(311) Rucker, T. G.; Logan, M. A.; Gentle, T. M.; Muetterties, E. L.; Somorjai, G. A. Conversion of acetylene to benzene over palladium single-crystal surfaces. 1. The low-pressure stoichiometric and the high-pressure catalytic reactions. *J. Phys. Chem.* **1986**, *90*, 2703–2708.
(312) Patterson, C. H.; Lambert, R. M. Molecular pathways in the cyclotrimerization of ethyne on palladium. *J. Am. Chem. Soc.* **1988**, *110*, 6871–6877.
(313) Xu, L.; Jin, Y.; Wu, Z.; Yuan, Q.; Jiang, Z.; Ma, Y.; Huang, W. Transformation of Carbon Monomers and Dimers to Graphene Islands on Co(0001). *J. Phys. Chem. C* **2013**, *117*, 2952–2958.
(314) Diehl, F.; Khodakov, A. Y. Promotion of cobalt Fischer-Tropsch catalysts with noble metals. *Oil Gas Sci. Technol. – Rev. IFP Energies nouvelles* **2009**, *64*, 11–24.
(315) Qian, W.; Zhang, H.; Ying, W.; Fang, D. The comprehensive kinetics of Fischer–Tropsch synthesis over a Co/AC catalyst on the basis of CO insertion mechanism. *Chem. Eng. J.* **2013**, *228*, 526–534.
(316) Haarlemmer, G.; Bensabath, T. Comprehensive Fischer–Tropsch reactor model with non-ideal plug flow and detailed reaction kinetics. *Comput. Chem. Eng.* **2016**, *84*, 281–289.
(317) La Osa, A. R. de; Lucas, A. de; Romero, A.; Valverde, J. L.; Sánchez, P. Fischer–Tropsch diesel production over calcium-promoted Co/alumina catalyst. *Fuel* **2011**, *90*, 1935–1945.
(318) Yates, I. C.; Satterfield, C. N. Hydrocarbon selectivity from cobalt Fischer-Tropsch catalysts. *Energy Fuels* **1992**, *6*, 308–314.
(319) Todic, B.; Ma, W.; Jacobs, G.; Davis, B. H.; Bukur, D. B. Effect of process conditions on the product distribution of Fischer–Tropsch synthesis over a Re-promoted cobalt-alumina catalyst using a stirred tank slurry reactor. *J. Catal.* **2014**, *311*, 325–338.

(320) Kwack, S.-H.; Bae, J. W.; Park, M.-J.; Kim, S.-M.; Ha, K.-S.; Jun, K.-W. Reaction modeling on the phosphorous-treated Ru/Co/Zr/SiO2 Fischer–Tropsch catalyst with the estimation of kinetic parameters and hydrocarbon distribution. *Fuel* **2011**, *90*, 1383–1394.
(321) Bukur, D. B.; Pan, Z.; Ma, W.; Jacobs, G.; Davis, B. H. Effect of CO Conversion on the Product Distribution of a Co/Al2O3 Fischer–Tropsch Synthesis Catalyst Using a Fixed Bed Reactor. *Catal. Lett.* **2012**, *142*, 1382–1387.
(322) Yang, J.; Ma, W.; Chen, D.; Holmen, A.; Davis, B. H. Fischer–Tropsch synthesis. *Appl. Catal., A* **2014**, *470*, 250–260.
(323) M-C. Marion, F. Hugues. *Diesel yield according to Fischer-Tropsch process conditions*, DGMK Conference; Future Feedstocks for Fuels and Chemicals, 2008.
(324) Schulz, H.; Nie, Z.; Ousmanov, F. Construction of the Fischer–Tropsch regime with cobalt catalysts. *Catal. Today* **2002**, *71*, 351–360.
(325) van Dijk, H.A.J.; Hoebink, J.H.B.J.; Schouten, J. C. A Mechanistic Study of the Fischer–Tropsch Synthesis Using Transient Isotopic Tracing. Part-1. *Top. Catal.* **2003**, *26*, 111–119.
(326) Lögdberg, S.; Lualdi, M.; Järås, S.; Walmsley, J. C.; Blekkan, E. A.; Rytter, E.; Holmen, A. On the selectivity of cobalt-based Fischer–Tropsch catalysts. *J. Catal.* **2010**, *274*, 84–98.
(327) Carvalho, A.; Ordomsky, V. V.; Luo, Y.; Marinova, M.; Muniz, A. R.; Marcilio, N. R.; Khodakov, A. Y. Elucidation of deactivation phenomena in cobalt catalyst for Fischer-Tropsch synthesis using SSITKA. *J. Catal.* **2016**, *344*, 669–679.
(328) Thybaut, J. W.; Sun, J.; Olivier, L.; van Veen, A. C.; Mirodatos, C.; Marin, G. B. Catalyst design based on microkinetic models. *Catal. Today* **2011**, *159*, 29–36.
(329) McQuarrie, D. A. *Statistical thermodynamics;* University Science Books: Mill Valley Calif., 1973.
(330) Pathria, R. K.; Beale, P. D. *Statistical mechanics;* Butterworth-Heinemann; Elsevier: Boston, Amsterdam, 2011.
(331) Congbiao Chen; Qiang Wang; Riguang Zhang; Bo Hou; Debao Li; Litao Jia; Baojun Wang. High coverage CO adsorption and dissociation on the Co(0001) and Co(100) surfaces from DFT and thermodynamics [Online].
(332) Wang, J.-H.; Liu, M. Computational Study of Sulfur–Nickel Interactions. *Electrochem. Commun.* **2007**, *9*, 2212–2217.
(333) Reuter, K.; Scheffler, M. Composition and Structure of the RuO2(110) Surface in an O2 and CO Environment: Implications for the Catalytic Formation of CO2. *Phys. Rev. B* **2003**, *68*, 368.
(334) Reuter, K.; Scheffler, M. Composition, Structure, and Stability of RuO2(110) as a Function of Oxygen Pressure. *Phys. Rev. B* **2001**, *65*, 1038.
(335) Xie, J.; Gironcoli, S. de; Baroni, S.; Scheffler, M. Temperature-Dependent Surface Relaxations of Ag(111). *Phys. Rev. B* **1999**, *59*, 970–974.
(336) Avantium, R&D Systems. https://www.catalysis.avantium.com/flowrence-technology-platform/.

# List of Figures

# List of Tables